Springer Series in Geomechanics and Geoengineering

Wei Wu *Editor*

Desiderata Geotechnica

Springer

Springer Series in Geomechanics and Geoengineering

Series editor

Wei Wu, Universität für Bodenkultur, Vienna, Austria
e-mail: wei.wu@boku.ac.at

Geomechanics deals with the application of the principle of mechanics to geomaterials including experimental, analytical and numerical investigations into the mechanical, physical, hydraulic and thermal properties of geomaterials as multiphase media. Geoengineering covers a wide range of engineering disciplines related to geomaterials from traditional to emerging areas.

The objective of the book series is to publish monographs, handbooks, workshop proceedings and textbooks. The book series is intended to cover both the state-of-the-art and the recent developments in geomechanics and geoengineering. Besides researchers, the series provides valuable references for engineering practitioners and graduate students.

More information about this series at http://www.springer.com/series/8069

Wei Wu
Editor

Desiderata Geotechnica

Springer

Editor
Wei Wu
Institut für Geotechnik
Universität für Bodenkultur
Vienna, Austria

ISSN 1866-8755 ISSN 1866-8763 (electronic)
Springer Series in Geomechanics and Geoengineering
ISBN 978-3-030-14986-4 ISBN 978-3-030-14987-1 (eBook)
https://doi.org/10.1007/978-3-030-14987-1

Library of Congress Control Number: 2019933216

This Springer imprint is published by the registered company Springer Nature Switzerland AG
The registered company address is: Gewerbestrasse 11, 6330 Cham, Switzerland

Contents

Prologue

This book presents contributions to a workshop dedicated to Prof. Gerd Gudehus on occasion of his 80th birthday. The workshop was organized within the China-Europe Conference on Geotechnical Engineering at the Universität für Bodenkultur, Vienna, Austria. There was a cocktail dinner given by Prof. Gudehus for the workshop participants on 13 August 2018. The workshop lasted for three full days from 14 to 16 August 2018 with presentations and subsequent discussions. The workshop also attracted many conference participants. The lively discussions reminded me of the good old times with Gerd in Karlsruhe.

The book title "Desiderata Geotechnica" was suggested by Gerd, who has been opposing trivialization and canonization in research because such mind-setting may eventually undermine any development in our profession. In his own contribution and the epilogue in this book, Gerd draws our attention to the so-called critical phenomena and their fractal nature, which are highly relevant for many problems in geo-engineering and geoscience. The research is challenging yet rewarding, and may bring about a paradigm change in our perception for safety and the observational method. In this sense, our workshop offered an excellent opportunity for a much desired discourse.

All workshop participants deserve my heartfelt thanks for their contributions and their diligence to deliver their publications on time. I am indebted to the workshop chairs Prof. Alexander Scheuermann (Queensland, Australia) and Prof. Torsten Wichtmann (Weimar, Germany), and to Prof. Dimitrios Kolymbas (Innsbruck, Austria) for his laudation. The articles in this book, many written by former students, friends, and colleagues of Gerd, cover a diverse range of topics that reflect the breadth and depth of geomechanics research. The cocktail dinner was sponsored in part by the foundation engineering contractor Keller Grundbau, Germany, represented by their CEO Dr. Venu Raju. This book is a humble tribute to Prof. Gudehus, who has made such a profound impact on our profession.

Gudehus with Wichtmann during the Workshop

Gerd Gudehus was born on 23 July 1938 in Hamburg, Germany. His father was an electrical engineer and his mother an artist. Gerd read civil engineering at the Technical University Berlin and obtained his diploma and Dr.-Ing. there. In 1968, Gerd joined the soil mechanics group of Karlsruhe University in South Germany, now Karlsruhe Institute of Technology. Only some five years later in 1973, the then 35-year-old Gudehus was offered the chair professor of soil mechanics in Karlsruhe. He set a record as the youngest chair professor of geotechnical engineering in the history of German universities. Since then, Gerd was at the helm of the largest research institute in geotechnical engineering for more than three decades until his retirement in emeritus status in 2006. In its prime time, the institute had up to 100 people on staff. The leadership of the large institute of strong individuals called for hard work and ingenuity. Besides the position as head of the institute, Gerd served as the dean of the faculty of civil engineering and as the vice president for research of the university.

This reads like a storybook career. However, Gudehus is no ordinary man. Ordinary people make career themselves, and extraordinary people establish a school of thought with profound impact on a whole generation. Gerd, with his passion for rational mechanics, established the Karlsruhe school of soil mechanics with the hallmark of rational approach to geotechnical engineering, an otherwise much empiricism-dominated engineering discipline. In spite of his management responsibilities, Gerd's research output has been very impressive. More impressive is his ability to inspire young fellows at various stages of their career. During the past 33 years as chair professor, Gerd supervised some 75 theses leading to the degree of Dr.-Ing. and Dr. Sci. (habilitation). This set another record of most supervised theses of our trade. Those who have ever worked under his tutelage were instilled with the Karlsruhe esprit of passion and rationale for research to follow one day his footsteps and pursue an academic career. Some 16 of his students became chair professors in Germany and abroad. Yet another record! This is phenomenal

and serves as a testament to the enormous impact of Gerd and his Karlsruhe school in our community.

Over the years, the institute developed into a powerhouse for both fundamental and applied research with a superb laboratory. Gerd acquired, as PI and as main applicant, 7 SFBs (large research projects funded by the German Research Foundation with a budget of double digit millions Euros for each project). However, I choose to leave out the many groundbreaking achievements in fundamental research in Karlsruhe, for which the institute is well known, and mention instead his capacity in delivering bespoke solutions to problems from engineering practice. A perusal of the publication series of the institute shows the great diversity of the research topics from practice, such as soil nailing, jet grouting, ground freezing, slope stabilization with piles, soil dynamics in high-speed railway, granular flow in silos, soil improvement with bacteria, open pit mine, and preservation of historical monuments, covering virtually the whole spectrum of geotechnical engineering. Many of these research works were pioneering and the outcome often found itself later in norms and standards. In passing, Gerd served as the ombudsman of the German Standard DIN 1054 under the Eurocode EC7 on stability analysis in geotechnical engineering, where he could draw on his wealth of experience from previous projects.

Gerd is well known for his frank sincerity, often straight to the point without frills. This is by no means a lack of empathy. On the contrary, Gerd is an unshakable humanist. He fostered close contact with the scholars from the Eastern bloc countries long before the fall of the iron curtain, e.g. GDR, Poland, Czechoslovakia, Soviet Union, and China. Gerd invited them to carry out joint research in his institute and provided them with much-needed financial support. On a personal note, I myself, as one of the invitees from the then communist countries, owe him as much for his advice and inspiration in research as for his help and encouragement in difficult times. Give credit where credit is due. For his unremitting effort in promoting scientific cooperation between Germany and Poland, Gerd was awarded an honorary doctorate by the Politechnika Gdańska, Poland, in 1995.

With the emeritus status in 2006 came the turning point in Gerd's life. However, you are dead wrong if you assume that he would mothball his research and indulge in his hobbies. And Gerd has many hobbies. He is a passionate piano player and a talented painter with love for pencil sketch. Besides his mother tongue, Gerd speaks English, Russian, Greek, and French. However, none of these seems to exert stronger attraction than his passion for geomechanics research. Exempted from his management responsibility, Gerd has become even more productive. A monograph with the title "Physical Soil Mechanics" was published in 2011, a massive tome with daunting 800 pages. A search in the Scopus database brings out some 20 publications after 2006, which makes about two publications a year. Many of his papers are published in peer-reviewed journals. His latest work with the title: "On the stability of geotechnical systems and its fractal progressive loss" was published in Acta Geotechnica this year. Obviously, this man is still at the forefront of research. As you can see, Gerd is on a good way to set yet another record of most

publications by an emeritus professor, and we wish him success onwards and upwards!

To paraphrase Aristotle, man is at his best when he is doing his best at what he likes doing best. No doubt, Gerd was and is at his best, because he believes that "Soil is matter of its own right" (the very first sentence from his book "Physical Soil Mechanics"). We wish him many happy returns of the day, and we all look forward to being inspired by his contributions to geomechanics research for many more years to come!

October 2018 Wei Wu

Modelling Grain Fragmentation in Hypoplasticity

Erich Bauer(✉)

Institute of Applied Mechanics, Graz University of Technology,
8010 Graz, Austria
erich.bauer@tugraz.at

Abstract. The focus of the present paper is on constitutive modelling of the influence of grain fragmentation on the mechanical behaviour of cohesionless granular materials like sand, gravel or broken rock. To this end the so-called solid hardness of a grain assembly is defined within a continuum description and is a key parameter for modelling the effect of both grain fragmentation and grain rearrangement. While in the original version by Bauer the solid hardness is a constant parameter, an extended concept has recently been proposed where the solid hardness is considered as a state dependent quantity. The general format of the evolution equation for the solid hardness allows the modelling of the influence of various factors on grain fragmentation. Such factors are, for instance, an increase in the mean stress, the deviatoric stress and the rotation resistance of particles and also a time dependent process caused by progressive weathering. The embedding of the solid hardness into hypoplasticity follows the consistency condition originally proposed by Gudehus. In this paper the consistency condition is also applied to proposed constitutive equations for time independent as well as rheological material properties. The performance of these different models is verified with experiments.

1 Introduction

Grain fragmentation leads to changes in the particle size distribution and the internal structure of the granular material. Various concepts for analysing experimental investigations and for mathematical modelling have been proposed in the literature, e.g. [2,3,12,15–17,19,20,28,36,41–43,51]. The results of experimental investigations reveal that the amount of grain fragmentation in the form of grain abrasion and grain breakage strongly depends on the grain hardness, the grain shape, the grain size distribution, the packing density and the loading path [47,48]. Enhanced experimental tools allow a deeper insight into the interaction between load states and grain breakage on the micro-level and also provide new opportunities to trace the evolution of grain breakage. For instance, recent investigations with the help of X-ray tomography indicate that under deviatoric loading grain fragmentation becomes dominant within the localized zone [2]. Moreover, grain fragmentation in shear zones can also be detected under lower pressures [49]. The grain hardness is not only a question of the mineralogical

W. Wu (Ed.): *Desiderata Geotechnica*, SSGG, pp. 1–20, 2019.
https://doi.org/10.1007/978-3-030-14987-1_1

composition of the solid material, but also influenced by the state of weathering. The time dependent process of weathering leads to a degradation of the solid hardness which is related to the local evolution of environmental conditions. Depending on the state of weathering of the material the abrasion and breakage resistance of grains can be different for dry or moist states, i.e. the disintegration of the material under higher stresses due to water-induced stress corrosion can be accelerated [46]. Thus, the change of the moisture content of the grain material may have an important influence on the long term behaviour of weathered granular materials. Progressive weathering caused by hydro-chemical reactions and the progressive propagation of micro-cracks is a time dependent process leading to phenomena such as collapse settlements, creep and stress relaxation. For coarse grained and moisture sensitive materials such a mechanical behaviour cannot be explained based on the concept of effective stresses. Grain fragmentation causes a change of the grading, the grain shape, the limit void ratios and the critical void ratio [4,23,39,50].

The focus of the present paper is on constitutive modelling of the influence of grain fragmentation on the mechanical response of cohesionless granular materials like sand, gravel or broken rock. To this end the so-called solid hardness of a grain assembly is defined within a continuum description and is a key parameter for modelling the effect of both grain fragmentation and grain rearrangement. This solid hardness is a parameter in the compression law by Bauer [5,6] and can be applied to an unlimited pressure range. The concept of the solid hardness was embedded into non-polar constitutive models, e.g. [8,9,24,29,44,53], and into micro-polar models, e.g. [18,26,31,32,52]. While in the original version by Bauer the solid hardness is a constant parameter, an extended concept has recently been proposed where the solid hardness is considered as a state dependent quantity [10,12,14,34]. The general format of the evolution equation for the solid hardness allows to account for the influence of various factors on grain fragmentation. In the present paper factors of influence are divided into rate independent factors and rheological factors. Another distinction is made between the description of non-polar and micro-polar effects on grain fragmentation.

The paper is organized as follows: In Sect. 2 the definition of the solid hardness in the sense of a continuum description is summarized first for the original version with a constant solid hardness and second for an extension to a pressure dependent fictitious solid hardness formulation. The latter allows the application of the concept of the soild hardness to cases where experimental data are available only for a limited range of pressures. The embedding of the solid hardness into a hypoplastic constitutive model with help of the consistency condition by Gudehus is outlined in Sect. 3. Section 4 deals with the modelling of the time dependent process of degradation of the solid hardness caused by progressive weathering. The performance of the model is demonstrated by simulation of triaxial compression tests and creep tests under different confining pressures and different deviatoric stresses using only a single set of constants. The numerical results are compared with experiments of a moisture sensitive broken sandstone. An extension of the concept of the solid hardness to account for also micro-polar

effects on grain fragmentation is presented in Sect. 5. In order to illustrate the reduction of the mean grain size depending on particle rotation, shearing of a granular strip under a constant normal stress is investigated using the extended micro-polar hypoplastic model and the finite element method.

Throughout the paper, indices on vector and tensor components refer to an orthonormal Cartesian basis and the symbol δ_{ik} denotes the Kronecker delta. The summation convention by Einstein over repeated indices is employed. A superimposed dot indicates the material time derivative. Compressive stress and strain and their rates are negative as in the sign convention of rational continuum mechanics.

2 Continuum Description of the Solid Hardness

Compression tests carried out with various granular materials show a qualitatively similar behaviour. At lower pressures the reduction of the void ratio is caused by a reorientation of the grains within the grain skeleton while under higher pressures the additional compaction is related to progressive grain crushing. In Fig. 1 it is clearly visible that for different initial void ratios the distance between the compression curves becomes smaller with an increase in the mean pressure. At very high pressures the curves merge together, which means that the memory of the material of the initial density is erased as a result of both grain crushing and a reorientation of particles into a denser state. In a semi-logarithmic representation the compression curves show an S-shape, where the point of inflection is related to the pressure level where grain crushing becomes dominant. Experiments show that the pressure at the point of inflection mainly depends on the mineral composition and the state of weathering of the solid material. Such a behaviour can also be observed for arbitrary granular materials and it is also verified by numerical simulations with the discrete element method, e.g. [22,36]. As the point of inflection shows no noticeable influence on the initial density, it is a well defined state and an appropriate parameter for a constitutive model.

In the following the pressure, $h_s = -\sigma_{mm}$, where the point of inflection appears is termed "solid hardness" and is a material parameter in the compression law by Bauer [5,6]. In particular, the compression law models the reduction of the maximum void ratio e_i under monotonic isotropic compression according to the following exponential function:

$$e_i = e_{i0} \exp\left\{-\left(\frac{3\,p}{h_s}\right)^n\right\}. \tag{1}$$

In Eq. (1) $p = -\sigma_{mm}/3$ denotes the mean pressure. Parameter e_{i0} denotes the maximum void ratio for $p \approx 0$ and n is related to the inclination of the compression curve at the point of inflection. For $p \to \infty$ the void ratio $e_i \to 0$, as illustrated in Fig. 2(a) the compression law (1) reflects the history of grain reorientation and the effect of fragmentation within the whole pressure range in a phenomenological manner.

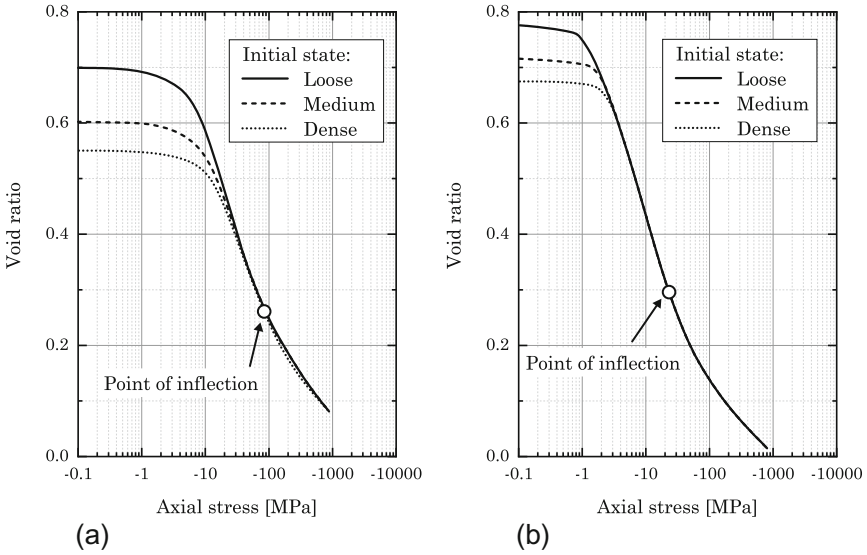

Fig. 1. Oedometric compression experiments by Yamamuro, Bopp and Lade [56] on sands starting from different initial void ratios: (a) Cambra sand; (b) Gybsum sand

It should be noted that for the quantity h_s in the compression law (1) different names are used in the literature. For instance, h_s is termed: "granulate hardness" by Gudehus [24], Herle and Gudehus [29], "granular hardness" by Bauer [5,6] and by Niemunis and Herle [44], and "granular stiffness" by von Wolfferdorff [53]. Already in the paper by Gudehus [24] a distinction is made between "granulate hardness" and "argotropic granulate hardness" for the rate-independence and rate-dependence of granular materials, respectively. Later Gudehust [25] and Gudehus [27] introduced the term "solid hardness" to refer to a rate-dependent h_s. The term "solid hardness" was adopted by Bauer [10] for modelling the time dependent process of degradation of h_s, which can be relevant, for instance, for weathered and moisture sensitive rockfill materials. In any case the parameter h_s in Eq. (1) is related to the grain aggregate under isotropic compression in the sense of a continuum description and should be distinguished from the hardness of an individual grain. For the sake of simplicity the term "solid hardness" is used uniformly in the present paper for both the rate-independent and rate-dependent h_s.

For unweathered granular materials the pressure required to reach the point of inflection is high and it cannot usually be achieved with standard test equipment available for isotropic compression experiments in soil mechanics laboratory. On the other hand oedometer tests under high pressure are more easier to carry out. Investigations show that the solid hardness can also be calibrated with sufficient accuracy if data are used which are obtained from an oedometer test instead of an isotropic test. However, oedometer devices, which allow

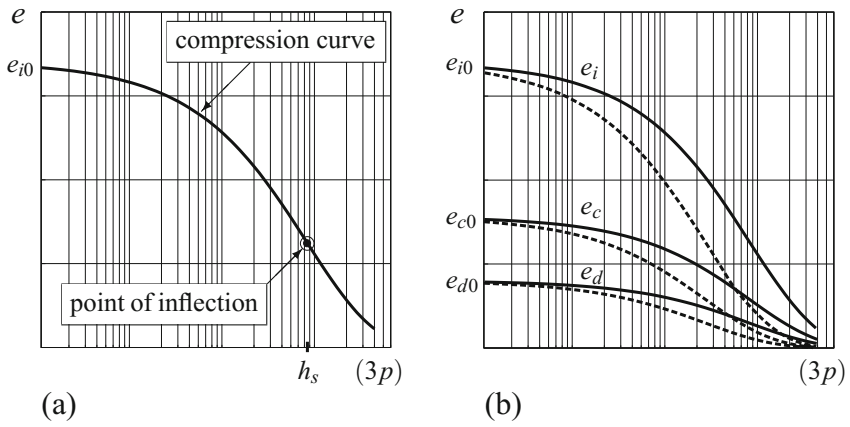

Fig. 2. (a) Monotonic isotropic compression law in a semi-logarithmic representation; (b) pressure dependence of the maximum void ratio e_i , the critical void ratio e_c , and of the minimum void ratio e_d

measuring the lateral stress in addition to the vertical stress are rare [35]. With the vertical stress σ_v from a standard oedometer device the mean pressure p can be estimated with help of the coefficient of the earth pressure at rest K_o, i.e. $p = -\sigma_v\,(1 + 2\,K_o)/3$, where K_0 can be approximated using the formula given by Jaky [33], i.e. $K_o \approx 1 - \sin\varphi_c$. Herein φ_c denotes the critical friction angle.

With respect to the time derivative of the compression law (1)

$$\dot{e}_i = \frac{\mathrm{d}\,e_i}{\mathrm{d}\,t} = -e_i\,n\,\frac{\dot{p}}{p}\left(\frac{3\,p}{h_s}\right)^n \tag{2}$$

and the general relation between the rate of the void ratio $\dot{e}$ and the volume strain rate $\dot{\varepsilon}_{mm}$:

$$\dot{e} = (1 + e)\dot{\varepsilon}_{mm} \tag{3}$$

a pressure dependent compression modulus can be derived, i.e.

$$\frac{\mathrm{d}\,p}{\mathrm{d}\,\varepsilon_v} = -\frac{h_s}{3\,n}\left(\frac{1}{e_i} + 1\right)\left(\frac{3\,p}{h_s}\right)^{1-n}. \tag{4}$$

As discussed by Herle and Gudehus [29] and Bauer and Herle [7] the compression modulus obtained in Eq. (4) formally resembles the oedometric compression law proposed by Ohde [45]:

$$\frac{\mathrm{d}\,p}{\mathrm{d}\,\varepsilon_v} = -\xi\left(-\frac{p}{p_r}\right)^{\eta}. \tag{5}$$

Herein p_r is negative and a reference pressure, e.g. the atmospheric pressure. With $\eta = 1 - n$ Eq. (5) can also be represented as:

$$\frac{\mathrm{d}\,p}{\mathrm{d}\,\varepsilon_v} = -\xi\left(-\frac{h_s}{3\,p_r}\right)^{1-n}\left(\frac{3\,p}{h_s}\right)^{1-n}. \tag{6}$$

The comparison of relation (4) with (6) yields for the parameter ξ:

$$\xi = \frac{h_s}{3\,n}\left(\frac{1}{e_i}+1\right)\left(-\frac{3\,p_r}{h_s}\right)^{1-n}. \tag{7}$$

In contrast to formula (5) for the compression modulus by Ohde the parameter ξ in Eq. (7) is not constant as it depends on the void ratio e_i. Consequently, the compression modulus obtained from the law by Bauer can only be approximated with the law by Ohde for a small range of void ratios.

2.1 Pressure Dependent Solid Hardness

If experimental data from compression tests are only available for a lower pressure range, the calibration using Eq. (1) will lead to an overestimation of the solid hardness. That is justified by the fact that under lower pressures the solid material does not reveal its intrinsic ultimate strength, i.e. the particles behave like rigid bodies and densification is only related to the reorientation of grains. For instance, for medium quartz sand a solid hardness of $h_s = 5800\,\mathrm{MPa}$ was reported by Herle and Gudehus [29], which reflects the experimental data for a low pressure range. For the same material a value of $h_s = 190\,\mathrm{MPa}$ was identified for the data obtained from a high pressure test by Bauer [6]. It is obvious that the pressure range considered in experiments has a great influence on the adaptation of h_s using Eq. (1). If the maximum pressure applied in the experiment does not reach the point of inflection, only a fictitious value of h_s can be obtained. In order to model a smooth transition of the compression behaviour from the lower to the higher pressure range the constant solid hardness h_s in Eq. (1) is replaced by the pressure dependent quantity h_{sp}. The evolution of the solid hardness with increasing mean pressure can be computed from the following equation:

$$\dot{h}_{sp} = -\frac{\dot{p}}{p}\left(\frac{3\,p}{b_p}\right)^{n_p} h_{sp} \qquad \text{for} \qquad \dot{\mathrm{p}} > 0. \tag{8}$$

Herein $\dot{h}_{sp}$ denotes the rate of the solid hardness, i.e. $\dot{h}_{sp} = \mathrm{d}h_{sp}/\mathrm{d}t$, $\dot{p}$ is the rate of the mean pressure, i.e. $\dot{p} = \mathrm{d}p/\mathrm{d}t$, and b_p and n_p are material parameters. Relation (8) also permits the adaptation of the solid hardness to an arbitrary range of experimental data available, provided that the pressure range is relevant to the practical application. It is worth noting that although Eq. (8) is of the rate type, the reduction of the solid hardness is rate independent. With respect to the initial state, i.e. $h_{sp}(p = p_0) = h_{s0}$, the integration of Eq. (8) yields for the pressure dependent solid hardness h_{sp}:

$$h_{sp} = h_{s0}\,\exp\left\{-\frac{1}{n_p}\left[\left(\frac{3\,p}{b_p}\right)^{n_p} - \left(\frac{3\,p_0}{b_p}\right)^{n_p}\right]\right\}. \tag{9}$$

Relation (8) is also part of the more extended concept for modelling grain fragmentation outlined in Sect. 5.

3 Embedding the Solid Hardness into Hypoplasticity

The strategy implementing of the concept of solid hardness into the framework of hypoplasticity is demonstrated for a particular non-polar hypoplastic constitutive model proposed by Bauer [6] and Gudehus [24]. The constitutive equations for the components of the objective stress tensor have the following form:

$$\mathring{\sigma}_{ij} = f_s \left[\hat{a}^2 \, \dot{\varepsilon}_{ij} + (\hat{\sigma}_{kl} \, \dot{\varepsilon}_{kl}) \, \hat{\sigma}_{ij} + f_d \, \hat{a} \, (\hat{\sigma}_{ij} + \hat{\sigma}^d_{ij}) \, \sqrt{\dot{\varepsilon}_{kl} \, \dot{\varepsilon}_{kl}} \right]. \tag{10}$$

The relation between the rate of the void ratio $\dot{e}$, the current void ratio e, and the volume strain rate $\dot{\varepsilon}_v = \dot{\varepsilon}_{mm}$ reads:

$$\dot{e} = (1 + e) \, \dot{\varepsilon}_{mm}. \tag{11}$$

The quantities in Eq. (10) are defined as:

$\mathring{\sigma}_{ij}$ ... objective stress rate,
$\dot{\varepsilon}_{ij}$ ... rate of deformation,
σ_{ij} ... Cauchy stress,
$\hat{\sigma}_{ij}$ ... normalized Cauchy stress σ_{ij}, i.e. $\hat{\sigma}_{ij} = \sigma_{ij}/\sigma_{kk}$,
$\hat{\sigma}^d_{ij}$ ... deviatoric part of $\hat{\sigma}_{ij}$, i.e. $\hat{\sigma}^d_{ij} = \hat{\sigma}_{ij} - \delta_{ij}/3$,
$\hat{a}$ ... critical stress state factor,
f_d ... pressure dependent relative density factor,
f_s ... stiffness factor.

The critical stress state factor $\hat{a}$ can be adjusted to arbitrary stress limit conditions with a conical shape in the principal stress space and is generally a function of the stress deviator and the so-called critical friction angle φ_c [6]. In the present paper the adaptation of $\hat{a}$ to the stress limit condition by Matsuoka and Nakai [40] is considered, i.e. [8]:

$$\hat{a} = \frac{\sin \varphi_c}{3 - \sin \varphi_c} \left[\sqrt{\frac{8/3 - 3 \, \hat{\sigma}^d_{kl} \, \hat{\sigma}^d_{kl} + g \sqrt{(3/2) \, (\hat{\sigma}^d_{kl} \, \hat{\sigma}^d_{kl})^3}}{1 + g \sqrt{(3/2) \, \hat{\sigma}^d_{kl} \, \hat{\sigma}^d_{kl}}}} - \sqrt{\hat{\sigma}^d_{kl} \, \hat{\sigma}^d_{kl}} \right] \tag{12}$$

with:

$$g = -\frac{\sqrt{6} \, \hat{\sigma}^d_{kl} \, \hat{\sigma}^d_{lm} \, \hat{\sigma}^d_{mk}}{\left(\hat{\sigma}^d_{pq} \, \hat{\sigma}^d_{pq} \right)^{3/2}}.$$

The density factor f_d is a function of the current void ratio e, the critical void ratio e_c and the minimum void ratio e_d, i.e.:

$$f_d = \left(\frac{e - e_d}{e_c - e_d} \right)^{\alpha}, \tag{13}$$

where α is a material parameter. The critical void ratio e_c and the minimum void ratio e_d are pressure dependent and related to the maximum void ratio e_i according to the postulate by Gudehus [24], i.e.:

$$\frac{e_i}{e_{i0}} = \frac{e_d}{e_{d0}} = \frac{e_c}{e_{c0}} = \exp \left\{ - \left(\frac{3 \, p}{h_s} \right)^n \right\}, \tag{14}$$

where the material parameters n and h_s are defined according to Eq. (1). The values of the corresponding material parameters e_{i0}, e_{d0} and e_{c0} are related to $p \approx 0$. Although the equations for the pressure dependency of e_c and e_d are affine to the one for e_i, it is worth noting that only the pressure dependency of the maximum void ratio e_i is related to the monotonic isotropic compression. Moreover, the isotropic compression relation (1) defines the upper bound of possible void ratios. Compared to previous constitutive models for the density factor f_d, e.g. [54,55], the enhanced version of f_d by Bauer [5] together with the postulate by Gudehus expressed in Eq. (14) has two advantages. First, the definition of the range of possible void ratios depending on the mean pressure is defined consistently as illustrated in Fig. 2(b) and, second, the number of material parameters required is reduced.

The stiffness factor f_s is the product of three parts, i.e.:

$$f_s = f_e \, f_\sigma \, f_b \, . \tag{15}$$

Herein the density dependent part f_e is defined as the ratio of the maximum void ratio e_i to the current void ratio e, i.e.

$$f_e = \left(\frac{e_i}{e} \right)^\beta , \tag{16}$$

where β is a material parameter. In relation (15) factor f_σ was suggested by von Wolfferdorff [53] and takes into account a decrease in the incremental stiffness with an increase in $\hat{\sigma}_{kl}\hat{\sigma}_{kl}$, i.e.

$$f_\sigma = \frac{1}{\hat{\sigma}_{kl}\hat{\sigma}_{kl}} . \tag{17}$$

Factor f_b in Eq. (15) is called barotropy factor and is obtained from a consistency condition as outlined in the following section.

3.1 Consistency Condition by Gudehus

For embedding the compression Eq. (1) into the hypoplastic constitutive Eq. (10) the response of both equations must coincide for a monotonic isotropic compression starting from the pressure dependent maximum void ratio e_i. This requirement can be fulfilled using the consistency condition proposed by Gudehus [24]. In particular, for isotropic compression the rates of the mean pressures obtained from the compression law, i.e. $\dot{p}\,(\text{comp} - \text{law})$, and from the hypoplastic constitutive equation, i.e. $\dot{p}\,(\text{hypo} - \text{isotrop})$, must coincide. Thus, the consistency condition by Gudehus reads:

$$\dot{p}\,(\text{comp} - \text{law}) = \dot{p}\,(\text{hypo} - \text{isotrop}). \tag{18}$$

For a constant solid hardness h_s the time derivative of the compression law (1) yields:

$$\dot{p}\,(\text{comp} - \text{law}) = -\frac{\dot{e}_i}{e_i} \frac{h_s}{3\,n} \left(\frac{3\,p}{h_s} \right)^{1-n} . \tag{19}$$

For isotropic compression, i.e. $\sigma_{11} = \sigma_{22} = \sigma_{33}$, $\dot{\varepsilon}_{11} = \dot{\varepsilon}_{22} = \dot{\varepsilon}_{33}$ and $\dot{\sigma}_{11} = \dot{\sigma}_{22} = \dot{\sigma}_{33}$, $f_e(e = e_i) = 1$, $f_\sigma(\sigma_{11} = \sigma_{22} = \sigma_{33}) = 3$, $f_d(e = e_i) = [(e_{i0} - e_{d0})/(e_{c0} - e_{d0})]^\alpha$, and with respect to $\dot{e}_i = (1 + e_i)\dot{\varepsilon}_{mm}$, the rate of the mean pressure calculated from the constitutive Eq. (10) reads:

$$\dot{p}\,(\text{hypo} - \text{isotrop}) = -\dot{\sigma}_{kk}/3 = -f_b\, h_i\, \frac{\dot{e}_i}{3\,(1 + e_i)} \tag{20}$$

with the constant quantities

$$h_i = 3\,\hat{a}_o^2 + 1 - \sqrt{3}\,\hat{a}_o \left(\frac{e_{i0} - e_{d0}}{e_{c0} - e_{d0}}\right)^\alpha$$

and

$$\hat{a}_o = \hat{a}(\sigma_{11} = \sigma_{22} = \sigma_{33}) = \sqrt{\frac{8}{3}}\frac{\sin\varphi_c}{3 - \sin\varphi_c}.$$

As the barotropy factor f_b is the only free quantity in Eq. (20) it can be determined with help of the consistency condition. Substituting Eqs. (19) and (20) into the consistency condition (18) yields:

$$f_b = \frac{h_s}{n\, h_i} \left(\frac{1 + e_i}{e_i}\right) \left(\frac{3\,p}{h_s}\right)^{1-n}. \tag{21}$$

Herein e_i denotes the pressure dependent maximum void ratio according to Eq. (1). It can be noted that for a solid hardness h_s, which is not a material constant, the barotropy factor f_b may differ from Eq. (21) as discussed in the following sections.

3.2 Barotropy Factor for the Pressure Dependent Solid Hardness

In order to determine the barotropy factor f_b relevant to the pressure dependent solid hardness given in Eq. (9), the equation for the rate of the mean pressure, i.e. $\dot{p}\,(\text{comp} - \text{law})$, must be updated before the consistency condition (18) can be applied. Replacing the constant solid hardness h_s in Eq. (1) with the pressure dependent solid hardness h_{sp} of Eq. (9), the time derivative of the compression law yields:

$$\dot{p}\,(\text{comp} - \text{law}) = -\frac{\dot{e}_i}{e_i}\frac{h_{sp}}{3\,n}\left(\frac{3\,p}{h_{sp}}\right)^{1-n}\left[1 + \left(\frac{3\,p}{b_p}\right)^{n_p}\right]^{-1}. \tag{22}$$

Substituting Eqs. (22) and (20) into the consistency condition (18) yields the relevant barotropy factor:

$$f_b = \frac{h_{sp}}{n\, h_i}\left(\frac{1 + e_i}{e_i}\right)\left(\frac{3\,p}{h_{sp}}\right)^{1-n}\left[1 + \left(\frac{3\,p}{b_p}\right)^{n_p}\right]^{-1}, \tag{23}$$

where e_i is the pressure dependent maximum void ratio depending on h_{sp}.

4 Degradation of the Solid Hardness Caused by Weathering

Grain fragmentation not only depends on the load applied. Even under constant load progressive weathering of the solid material can lead to degradation of the strength of the solid grains and consequently to grain breakage. The reduction of the solid hardness is a time dependent process and it is influenced by the state of weathering and the evolution of environmental conditions. Depending on the state of weathering the abrasion and breakage resistance of grains can be different for dry or water-saturated states. Experiments and field observation show that a change of the moisture content can accelerate the degradation of the solid hardness due to water-induced stress corrosion at micro-cracks, which subsequently leads to grain breakage and so-called wetting deformations, e.g. [37,38,48]. For coarse-grained materials like sandy gravel and rockfills the effect of capillary forces on the effective stresses are negligibly small and not considered in the following. In order to model the time dependent reduction of the strength of the solid material the constant solid hardness h_s in the compression law (1) is replaced by the state dependent solid hardness h_{st}. The degradation of the solid hardness is assumed to be irreversible and modelled by the following evolution equation proposed by Bauer [10]:

$$\dot{h}_{st} = -\frac{1}{c}\,(h_{st} - h_{sw}). \tag{24}$$

Herein $\dot{h}_{st}$ denotes the rate of the solid hardness, h_{st} is the current value of the solid hardness, h_{sw} denotes the value of the solid hardness in the asymptotic state, and c scales the velocity of degradation and has the dimension of time. Parameter h_{sw} and c may depend on the evolution of the environmental conditions and are usually not material constants. For a more complex evolution history the proposed concept of the solid hardness can also be extended to drying and wetting cycles.

Equation (24) can be integrated and, with respect to the initial state $h_{st}(t = 0) = h_{so}$, one obtains:

$$h_{st} = h_{sw} + (h_{so} - h_{sw})\,\exp\left[-\frac{t}{c}\right]. \tag{25}$$

For general 3-D problems the state dependent solid hardness h_{st} was implemented into hypoplasticity. To this end the hypoplastic constitutive Eq. (10) was extended with an additional term depending on the current stresses σ_{ij}, the solid hardness h_{st} and its rate $\dot{h}_{st}$, i.e.

$$\begin{aligned}\mathring{\sigma}_{ij} \;=\; & f_s\Big[\,\hat{a}^2\,\dot{\varepsilon}_{ij} + (\hat{\sigma}_{kl}\,\dot{\varepsilon}_{kl})\,\hat{\sigma}_{ij} + f_d\,\hat{a}\,(\hat{\sigma}_{ij} + \hat{\sigma}^d_{ij})\,\sqrt{\dot{\varepsilon}_{kl}\,\dot{\varepsilon}_{kl}}\,\Big] \\ & + \frac{\dot{h}_{st}}{h_{st}}\left(\frac{1}{3}\sigma_{kk}\,\delta_{ij} + \kappa\,\sigma^d_{ij}\right).\end{aligned} \tag{26}$$

With $\dot{h}_{st}$ in the second term on the right-hand side of Eq. (26) the hypoplastic constitutive equation is rate dependent, i.e. the mechanical response is also influenced by the loading velocity. In the second term the stress is decomposed into its isotropic part and its deviatoric part. The latter, scaled with parameter κ, allows a refined modelling of creep strain and stress relaxation [10,21]. For states where the degradation of the solid hardness has been completed, i.e. for $\dot{h}_{st} = 0$, the rate independent hypoplastic model (10) for a constant solid hardness is obtained. It is obvious that the constitutive model (26) captures both the behaviour of the material under dry and wet condition.

The corresponding barotropy factor f_b can again be determined from the consistency condition (18). Replacing in Eq. (1) the constant solid hardness h_s with the state dependent solid hardness h_{st} of Eq. (25), the time derivative of the compression law yields:

$$\dot{p}\,(\text{comp} - \text{law}) = p \left[\frac{\dot{h}_{st}}{h_{st}} - \frac{\dot{e}_i}{n\, e_i} \left(\frac{3\,p}{h_{st}} \right)^{-n} \right] . \tag{27}$$

For isotropic compression, the rate of the mean pressure calculated from the constitutive Eq. (26) reads:

$$\dot{p}\,(\text{hypo} - \text{isotrop}) = -\,\dot{\sigma}_{kk}/3 = -f_b\, h_i\, \frac{\dot{e}_i}{3\,(1+e_i)} + p\, \frac{\dot{h}_{st}}{h_{st}}. \tag{28}$$

Substituting Eqs. (27) and (28) into the consistency condition (18) yields:

$$f_b = \frac{h_{st}}{n\, h_i} \left(\frac{1+e_i}{e_i} \right) \left(\frac{3\,p}{h_{st}} \right)^{1-n}, \tag{29}$$

where e_i is the maximum void ratio depending on the state dependent solid hardness h_{st}.

To demonstrate the performance of the hypoplastic model (26) the experimental results carried out by Li [37] for a moisture sensitive broken sandstone under triaxial compression are compared with the numerical simulations [11]. For the calibration of the dry material the hypoplastic model for a constant solid hardness can be considered. The following set of material parameters is obtained: $\varphi_c = 40^\circ$, $h_{so} = 47\,\text{MPa}$, $n = 0.3$, $e_{io} = 0.59$, $e_{co} = 0.48$, $e_{do} = 0.20$, $\alpha = 0.18$ and $\beta = 2.50$. After water saturation degradation of the solid hardness takes place and the second part on the right-hand side of Eq. (26) is also active. The material parameters for modelling the degradation of the solid hardness according to Eqs. (25) and (26) are: $h_{sw} = 11.5\,\text{MPa}$, $\kappa = 0.7$ and $c = 72\,\text{h}$. With the same set of material parameters numerical simulations are carried out for the dry and wet states of the material and for two different lateral stresses. Figure 3 shows the comparison of the numerical results with experiments, i.e. Figure 3(a) and (b) show the results for a lateral stress of $-100\,\text{kPa}$ and Fig. 3(c) and (d) show the results for a lateral stress of $-1000\,\text{kPa}$. The mechanical behaviour under monotonic triaxial compression is shown in Fig. 3(a) and (c) for both the

dry and water saturated states of the material. For the water saturated case the degradation of the solid hardness has already been completed under the corresponding initial isotropic state befor deviatoric loading starts. As can be seen in Fig. 3(a), the deviatoric stress $(\sigma_{11} - \sigma_{33})$ and the volumetric strain ε_v against the axial strain ε_{11} is different for the dry and the water saturated materials. In particular the compaction at the beginning of deviatoric loading are significantly higher for the water saturated material, while the maximum deviatoric stress is higher for the dry material. Moreover, the subsequent dilation is considerably lower for the saturated material, which can be attributed to the more pronounced particle disintegration. Creep behaviour after water saturation is investigated under different deviatoric stress states as shown in Fig. 3(b) and (d). As can be seen, the axial creep deformation is more pronounced for a higher deviatoric stress while the volume strain curve is steeper under a lower deviatoric stress. The creep paths are almost linear and in good agreement with the experimental results.

5 Micropolar Extension of the Concept of Solid Hardness

To take into account micropolar effects like abrasion under large shearing and grain crushing caused by the rotation resistance of grains the concept of modelling grain fragmentation has recently been extended. Within a micropolar continuum description the change of the grading can also be reflected in a simplified manner by the reduction of the mean grain diameter d_{50}, which enters the present constitutive model as the characteristic length. Consequently, an evolution equation for the reduction of the mean grain diameter d_{50} is required in addition to the evolution equation for the solid hardness h_{st}. According to the concept proposed by Bauer et al. [12] a more refined modelling of the evolution equation for the change of the mean grain diameter and the solid hardness can be outlined as:

$$\dot{d}_{50} = -\left[b_\kappa \sqrt{\dot{\bar{\kappa}}_{ij}\, \dot{\bar{\kappa}}_{ij}} + b_\omega \sqrt{(\dot{\omega}^c_{ij} - \dot{\omega}_{ij})\,(\dot{\omega}^c_{ij} - \dot{\omega}_{ij})} + b_{dp} \frac{\dot{p}}{p} \left(\frac{3p}{h_{st}} \right)^{n_{dp}} + b_{dd} \sqrt{\mathring{\hat{\sigma}}^{ds}_{ij}\, \mathring{\hat{\sigma}}^{ds}_{ij}} \sqrt{\hat{\sigma}^{ds}_{kl}\, \hat{\sigma}^{ds}_{kl}} \right] d_{50}, \tag{30}$$

$$\dot{h}_{st} = -\left[b^*_\kappa \sqrt{\dot{\bar{\kappa}}_{ij}\, \dot{\bar{\kappa}}_{ij}} + b^*_\omega \sqrt{(\dot{\omega}^c_{ij} - \dot{\omega}_{ij})\,(\dot{\omega}^c_{ij} - \dot{\omega}_{ij})} + \frac{\dot{p}}{p} \left(\frac{3p}{b_p} \right)^{n_p} + b_d \sqrt{\mathring{\hat{\sigma}}^{ds}_{ij}\, \mathring{\hat{\sigma}}^{ds}_{ij}} \sqrt{\hat{\sigma}^{ds}_{kl}\, \hat{\sigma}^{ds}_{kl}} \right] h_{st}, \tag{31}$$

The quantities in Eqs. (30) and (31) are defined as:

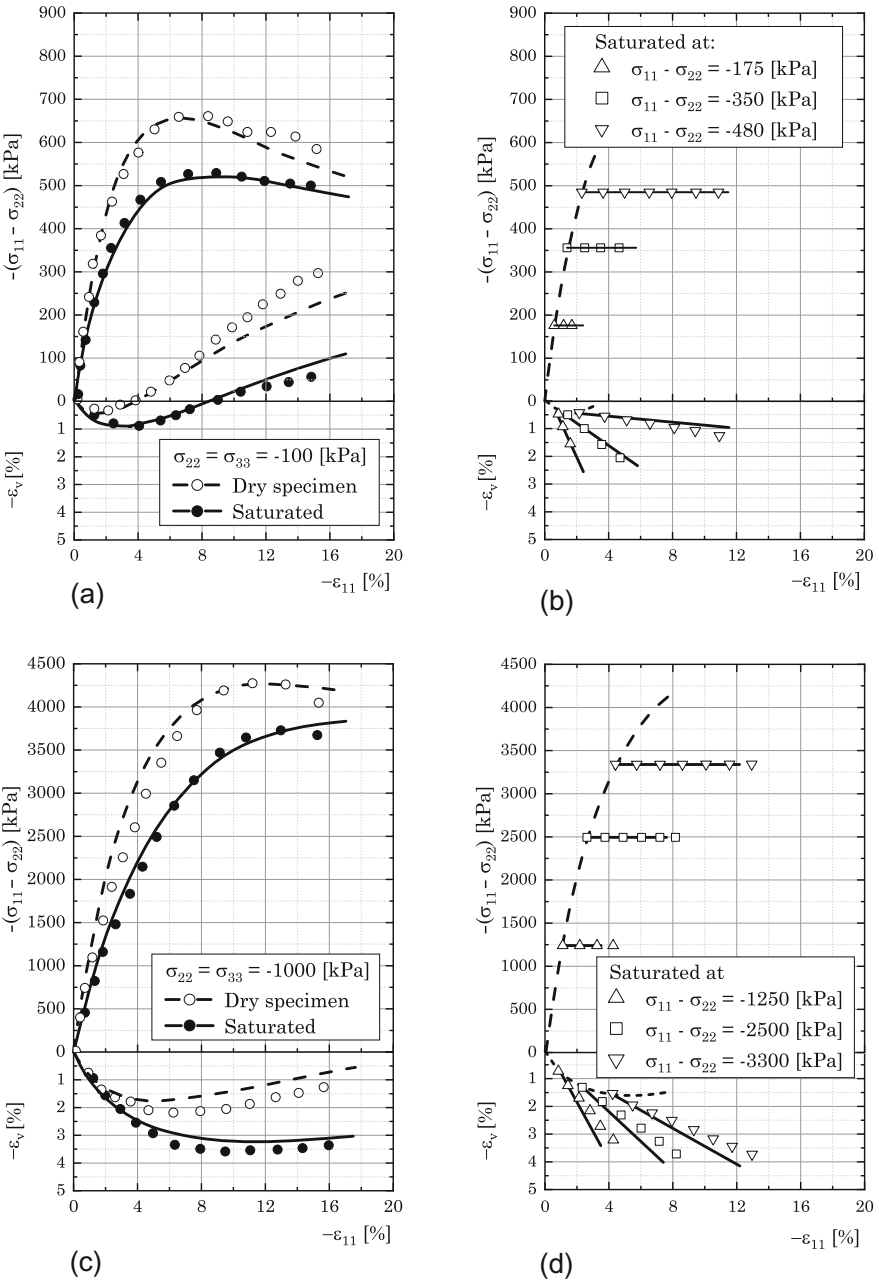

Fig. 3. Response of rockfill material under triaxial compression: dashed curves and solid curves are numerical responses for the dry and the water saturated specimens, respectively [11]; shapes denote the experimental data by Li [37]

$\dot{\bar{\kappa}}_{ij}$ ... normalized rate of curvature, i.e. $\dot{\bar{\kappa}}_{ij} = d_{50}\,\dot{\kappa}_{ij}$,
$\dot{\omega}^c_{ij}$ ... rate of the micro-rotation,
$\dot{\omega}_{ij}$ ... rate of the macro-rotation,
$\mathring{\sigma}^c_{ij}$ ... objective stress rate of the non-symmetric Cauchy stress σ^c_{ij},
$\mathring{\sigma}^{cd}_{ij}$ ... deviatoric part of $\mathring{\sigma}^c$, i.e. $\mathring{\sigma}^{cd}_{ij} = \mathring{\sigma}^c_{ij} - \mathring{\sigma}^c_{kk}\delta_{ij}/3$,
$\mathring{\hat{\sigma}}^{cd}_{ij}$ ... normalized deviatoric part of $\mathring{\sigma}^c_{ij}$, i.e. $\mathring{\hat{\sigma}}^{cd}_{ij} = \mathring{\sigma}^{cd}_{ij}/\sigma^c_{mm}$,
$\mathring{\sigma}^{ds}_{ij}$ ... symmetric part of $\mathring{\sigma}^{cd}_{ij}$, i.e. $\mathring{\sigma}^{ds}_{ij} = (\mathring{\sigma}^{cd}_{ij} + \mathring{\sigma}^{cd}_{ji})/2$,
σ^{cd}_{ij} ... deviatoric part of σ^c_{ij}, i.e. $\sigma^{cd}_{ij} = \sigma^c_{ij} - \sigma^c_{kk}\delta_{ij}/3$,
$\hat{\sigma}^{cd}_{ij}$ ... normalized deviatoric part of σ^c_{ij}, i.e. $\hat{\sigma}^{cd}_{ij} = \sigma^{cd}_{ij}/\sigma^c_{mm}$,
$\hat{\sigma}^{ds}_{ij}$ ... symmetric part of $\hat{\sigma}^{cd}$, i.e. $\hat{\sigma}^{ds}_{ij} = (\hat{\sigma}^{cd}_{ij} + \hat{\sigma}^{cd}_{ji})/2$.

The scalar factors b_κ, b_ω, $b_p\,b^*_\kappa$, b^*_ω and b_η are material parameters. Equations (30) and (31) are slightly modified versions of the one proposed in [14]. In both equations the first two terms are related to micropolar effects and the third and fourth terms consider an increase in the stress. In particular, the first term is related to an increase in the curvature, the second term is relevant for abrasion under large particle rotation even under low stresses, and the third and fourth take into account an increase in the mean pressure and the stress deviator, respectively. As grain fragmentation is irreversible, a reduction of h_{st} and d_{50} takes place only for $\dot{h}_{st} < 0$ and $\dot{d}_{50} < 0$. In both functions the third term only leads a contribution for $\dot{p} > 0$, while the second term takes into account an increase in the deviatoric stress. This distinction also allows an easier calibration of the material parameters involved.

For applications the proposed evolution equations for d_{50} and h_{st} must be included into an appropriate constitutive model which is based on a micropolar continuum. To this end the following micropolar hypoplastic model by Huang et al. [31] is considered in the present paper:

$$\mathring{\sigma}^c_{ij} = f_s \Big[\, \hat{a}^2\,\dot{\varepsilon}^c_{ij} + (\hat{\sigma}^c_{kl}\,\dot{\varepsilon}^c_{kl} + \hat{\mu}_{kl}\,\dot{\bar{\kappa}}_{kl})\,\hat{\sigma}^c_{ij} + f_d\,(\hat{\sigma}^c_{ij} + \hat{\sigma}^{cd}_{ij})\,\sqrt{\hat{a}^2\dot{\varepsilon}^c_{kl}\,\dot{\varepsilon}^c_{kl} + a^2_m\,\dot{\bar{\kappa}}_{kl}\,\dot{\bar{\kappa}}_{kl}}\,\Big], \tag{32}$$

$$\mathring{\mu}_{ij} = f_s\,d_{50}\Big[\, a^2_m\,\dot{\bar{\kappa}}_{ij} + \hat{\mu}_{ij}\,(\hat{\sigma}^c_{kl}\,\dot{\varepsilon}^c_{kl} + \hat{\mu}_{kl}\,\dot{\bar{\kappa}}_{kl} + 2\,f_d\,\sqrt{\hat{a}^2\dot{\varepsilon}^c_{kl}\,\dot{\varepsilon}^c_{kl} + a^2_m\,\dot{\bar{\kappa}}_{kl}\,\dot{\bar{\kappa}}_{kl}}\,)\,\Big]. \tag{33}$$

The quantities in Eqs. (32) and (33) are defined as:

$\mathring{\sigma}^c_{ij}$ ... objective stress rate (non-symmetric)
$\mathring{\mu}_{ij}$ ... objective couple stress rate
σ^c_{ij} ... Cauchy stress (non-symmetric)
$\hat{\sigma}^c_{ij}$ ... normalized stress, i.e. $\hat{\sigma}^c_{ij} = \sigma^c_{ij}/\sigma^c_{mm}$
$\hat{\sigma}^{cd}_{ij}$ ... normalized deviatoric part of σ^c_{ij}, i.e. $\hat{\sigma}^{cd}_{ij} = \hat{\sigma}^c_{ij} - \delta_{ij}/3$
$\dot{\varepsilon}^c_{ij}$ ... rate of deformation (non-symmetric)
$\dot{\overline{\kappa}}_{ij}$ ... normalized rate of curvature, i.e. $\dot{\overline{\kappa}}_{ij} = d_{50}\,\dot{\kappa}_{ij}$
$\hat{\mu}_{ij}$ ... normalized couple stress, i.e. $\hat{\mu}_{ij} = \mu_{ij}/(d_{50}\,\sigma_{kk})$
a_m ... micro-polar constant
$\hat{a}$ ... critical stress state factor according to Eq. (12), but with respect to the symmetric part of $\hat{\sigma}^{cd}_{ij}$, i.e. $\hat{\sigma}^{ds}_{ij} = (\hat{\sigma}^{cd}_{ij} + \hat{\sigma}^{cd}_{ji})/2$.

5.1 Simplified Version

For particular loading paths and in cases where experimental data are limited, it could be convenient to consider a simplified version of Eq. (30) and Eq. (31) as discussed for instance by Bauer et al. [12] and Bauer [13]. In the simplified version the reduction of h_s is directly linked to the reduction of d_{50} according to the following evolution equation:

$$\dot{h}_{st} = b_s \frac{\dot{d}_{50}}{d_{50}} h_{st} \qquad \text{for } \dot{d}_{50} < 0, \tag{34}$$

where b_s is a material parameter. With respect to the initial state, i.e. $h_{st}(d_{50\_0}) = h_{s0}$, the integration of Eq. (34) leads to h_{st} as a function of d_{50}:

$$h_{st} = h_{s0} \left(\frac{d_{50}}{d_{50\_0}} \right)^{b_s}. \tag{35}$$

The current value of d_{50} depends on the history of grain fragmentation and can be obtained for instance by the numerical integration of Eq. (30).

As an example of micropolar effects in shear zones, plane shearing of a lateral infinite granular strip under a constant vertical load is considered in the following. It is assumed that the granular layer is located between two parallel very rough walls, so that no sliding and no particle rotation can occur along the bottom and top boundaries [12]. With respect to an initially homogeneous state of the granular material, the state quantities are independent of the coordinate in the direction of shearing [32]. For a larger shear displacement, the change of the stress is small, so that the first, third and forth terms in Eq. (30) will be neglected in the present study. Then the evolution equation for the mean grain diameter reduces to:

$$\dot{d}_{50} = -\,b_\omega \sqrt{(\dot{\omega}^c_{ij} - \dot{\omega}_{ij})\,(\dot{\omega}^c_{ij} - \dot{\omega}_{ij})}\; d_{50}\,. \tag{36}$$

For the numerical simulation a four node plane strain Cosserat element developed by Huang [30] and the present set of micropolar constitutive equations were implemented into the finite element program ABAQUS [1]. The material

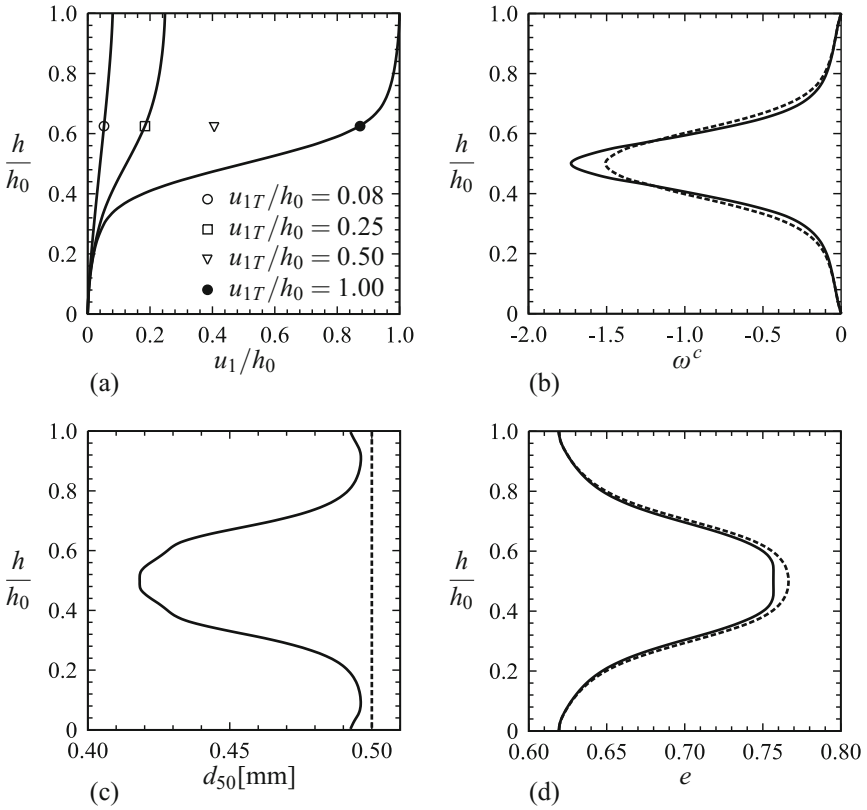

Fig. 4. Mechanical response of micro-polar effects shown across the normalized height h/h_0 in a laterally infinite granular strip under monotonic shearing (solid curves and dashed curves represent the response obtained with grain fragmentation and without grain fragmentation, respectively): (a) displacement field for different horizontal shear displacements u_T prescribed at the top of the shear layer; (b) distribution of the micro-rotation ω^c ; (c) reduction of the mean grain diameter d_{50} ; (d) distribution of the void ratio e

parameters relevant to the constitutive Eqs. (32, 33, 34, 35, 36) are: $\varphi_c = 30°$, $e_{io} = 1.02$, $e_{co} = 0.82$, $e_{do} = 0.51$, $\alpha = 0.14$, $\beta = 1.05$, $n = 0.35$, $h_{s0} = 10^4$ MPa, $a_m = 0.8$, $b_\omega = 2.0$, $b_s = 5.0$ and $d_{50\_0} = 0.5$ mm. The initial height of the granular strip is $h_o = 4$ cm, and the value of the initial void ratio is $e = 0.62$. At the top surface a constant vertical stress of -1 MPa is applied. Shearing is initiated by horizontal node displacements prescribed at the top surface, while the displacements and rotations of the nodes at the bottom are locked. Micro-rotations of the top nodes are also locked. The numerical results obtained are shown in Fig. 4. To visualize the effect of grain fragmentation on the mechanical behaviour, the solid curves and dashed curves represent the response obtained with grain fragmentation and without grain fragmentation, respectively. At the beginning

of shearing the displacement field is almost linear as it is in the non-polar continuum. From Fig. 4(a) it is clearly visible that for larger shear displacements of the top surface the shear deformation within the granular layer localizes and the displacement field becomes non-linear across the height of the granular strip. Because of the symmetric boundary conditions for the rough surfaces at the top and at the bottom, shear strain localization occurs in the middle of the granular layer. It is obvious that shear strain-localization is combined with large micro-rotations ω^c (Fig. 4(b)) and a pronounced reduction of the mean grain diameter d_{50} (Fig. 4(c)). A similar behaviour can also be observed in experiments. For instance, under large shearing in a ring shear device, grain breakage is concentrated in the shear band while almost no grain damage occurs outside the shear band [50]. Within the shear band a higher void ratio is visible due to pronounced dilatancy of the initially medium dense specimen as shown in Fig. 4(d). However, as a consequence of grain fragmentation during shearing, the void ratio is somewhat smaller compared to the results obtained with constant values of the solid hardness and the mean grain diameter. For a more realistic quantification of the constitutive parameters involved appropriate experimental methods are needed to analyse the distribution of grain crushing across the shear band.

Acknowledgements. The author wishes to thank Professor W. Huang and Dr. Z. Fu for the fruitful discussion of extended numerical tools used for the simulations. The assistance of Dr. L. Li and Mr. S. Safikhani in preparing the drawings presented in the paper is gratefully acknowledged.

References

1. ABAQUS Software. Dassault Systèmes (2017)
2. Alikarami, R., Andò, E., Gkiousas-Kapnisis, M., Torabi, A., Viggiani, G.: Strain localisation and grain breakage in sand under shearing at high mean stress: insights from in situ X-ray tomography. Acta Geotechnica **10**, 15–30 (2015)
3. Alonso, E.E., Cardoso, R.: Behavior of materials for earth and rockfill dams: perspective from unsaturated soil mechanics. Front. Archit. Civ. Eng. China **4**(1), 1–39 (2010). https://doi.org/10.1007/s11709-010-0013-6
4. Ando, E., Hall, S.A., Viggiani, G., Desrues, J., Besuelle, P.: Grain-scale experimental investigation of localised deformation in sand: a discrete particle tracking approach. Acta Geotechnica **7**, 1–13 (2012)
5. Bauer, E.: Constitutive modelling of critical states in hypoplasticity. In: Proceedings of the Fifth International Symposium on Numerical Models in Geomechanics, pp. 15–20. Balkema, Davos (1995)
6. Bauer, E.: Calibration of a comprehensive hypoplastic model for granular materials. Soils Found. **36**(1), 13–26 (1996)
7. Bauer, E., Herle, I.: Stationary states in hypoplasticity. In: Kolymbas, D. (ed.) Constitutive Modelling of Granular Materials, pp. 167–192. Springer, Heidelberg (2000)
8. Bauer, E.: Conditions for embedding Casagrande's critical states into hypoplasticity. Mech. Cohesive-Frictional Mater. **5**, 125–148 (2000)
9. Bauer, E., Huang, W., Wu, W.: Investigation of shear banding in an anisotropic hypoplastic material. Solids Struct. **41**, 5903–5919 (2004)

10. Bauer, E.: Hypoplastic modelling of moisture-sensitive weathered rockfill materials. Acta Geotechnica **4**, 261–72 (2009)
11. Bauer, E., Fu, Z., Liu, S.: Influence of pressure and density on the rheological properties of rockfills. Front. Struct. Civil Eng. **6**, 25–34 (2012). https://doi.org/10.1007/s11709-012-0143-0
12. Bauer, E., Li, L., Huang, W.: Hypoplastic constitutive modelling of grain damage under plane shearing. In: Bifurcation and Degradation of Geomaterials in the New Millennium, pp. 181–187 (2015)
13. Bauer, E.: Simulation of the influence of grain damage on the evolution of shear strain localization. In: Albers, B., Kuczma, M. (eds.) Continuous Media with Microstructure, vol. 2, pp. 231–244. Springer, Cham (2016). ISBN 978-3-319-28239-8
14. Bauer, E., Li, L., Khosravi, M.: Modelling grain damage under plane strain compression using a micro-polar continuum. In: Papamichos, E., Papanastasiou, P., Pasternak, E., Dyskin, A. (eds.) Proceedings of the 11th International Workshop on Bifurcation and Degradation in Geomaterials Dedicated to Hans Muhlhaus, Limassol, Cyprus, May 21–25 2017. Geomechanics and Geoengineering, pp. 539-546. Springer, Heidelberg (2017). https://doi.org/10.1007/978-3-319-56397-8, ISBN 978-3-319-56396-1
15. Bolton, M.D., Nakata, Y., Cheng, Y.P.: Micro- and macro-mechanical behavior of DEM crushable materials. Géotechnique **58**(6), 471–480 (2008)
16. Coop, M.R., Sorensen, K.K., Freitas, T.B., Georgoutsos, G.: Particle breakage during shearing of a carbonate sand. Géotechnique **58**(6), 471–480 (2004)
17. Daouadji, A., Hicher, P.Y., Rahma, A.: An elastoplastic model for granular materials taking into account grain breakage. Eur. J. Mech. A/Solids **20**, 113–137 (2001)
18. Ebrahimian, B., Bauer, E.: Numerical simulation of the effect of interface friction of a bounding structure on shear deformation in a granular soil. Int. J. Numer. Anal. Methods Geomech. **36**, 1486–1506 (2012)
19. Einav, I.: Breakage mechanics-part I: theory. J. Mech. Phys. Solids **55**(6), 1274–1297 (2007)
20. Einav, I.: Breakage mechanics-Part II: modelling granular materials. J. Mech. Phys. Solids **55**(6), 1298–1320 (2007)
21. Fu, Z.Z., Bauer, E.: Hypoplastic constitutive modelling of the long term behaviour and wetting deformation of weathered granular materials. In: Bauer, E., Semprich, S. Zenz, G. (eds.) Proceedings of the 2nd International Conference on Long Term Behaviour of Dams, Graz, Austria, pp. 473–478 (2009). ISBN 978-3-85125-070-1
22. Fu, R., Hua, X., Zhou, B.: Discrete element modeling of crushable sands considering realistic particle shape effect. Comput. Geotech. **91**, 179–191 (2017)
23. Garga, V.K., Infante Sedano, J.A.: Steady state strength of sands in a constant volume ring shear apparatus. Geotech. Test. J. **25**, 414–421 (2002)
24. Gudehus, G.: A comprehensive constitutive equation for granular materials. Soils Found. **36**(1), 1–12 (1996)
25. Gudehus, G.: A visco-hypoplastic constitutive relation. Soils Found **44**(4), 11–25 (2004)
26. Gudehus, G., Nübel, K.: Evolution of shear bands in sand. Géotechnique **54**, 187–201 (2004)
27. Gudehus, G.: Physical Soil Mechanics. Advances in Geophysical and Environmental Mechanics and Mathematics. Springer, Heidelberg (2011)
28. Hardin, B.O.: Crushing of soil particles. J. Geotech. Eng. **111**(10), 1177–1192 (1985)
29. Herle, I., Gudehus, G.: Determination of parameters of a hypoplastic constitutive model from grain properties. Mech. Cohesive-Frictional Mater. **4**, 461–486 (1999)

30. Huang, W.: Hypoplastic modelling of shear localisation in granular materials. Ph.D. thesis, Graz University of Technology, Austria (2000)
31. Huang, W., Nübel, K., Bauer, E.: A polar extension of hypoplastic model for granular material with shear localization. Mech. Mater. **34**, 563–576 (2002)
32. Huang, W., Bauer, E.: Numerical investigations of shear localization in a micro-polar hypoplastic material. Int. J. Numer. Anal. Methods Geomech. **27**, 325–352 (2003)
33. Jaky, J.: Pressure in silos. In: 2nd ICSMFE, London, vol. 1, pp. 103–107 (1948)
34. Khosravi, M., Linke Li, L., Bauer E.: Numerical simulation of post construction deformation of a concrete face rockfill dam. In: Noorzad, A., Bauer, E., Ghaemian, M., Ebrahimian, B. (eds.) Proceedings of the 4th International Conference on Long-Term Behaviour and Environmentally Friendly Rehabilitation Technologies of Dams, LTBD 2017, pp. 307–314. Verlag der Technischen Universität Graz (2017). ISBN 978-3-85125-564-5
35. Kolymbas, D., Bauer, E.: Soft oedometer – a new testing device and its application for the calibration of hypoplastic constitutive laws. Geotech. Test. J. GTJODJ **16**(2), 263–270 (1993)
36. Laufer, I.: Grain crushing and high-pressure oedometer tests simulated with the discrete element method. Granul. Matter **17**, 389 (2015). https://doi.org/10.1007/s10035-015-0559-z
37. Li, G., X.: Triaxial wetting experiments on rockfill materials used in Xiaolangdi earth dam. Research report from Tsinghua University (1988)
38. Li, L., Wang, Z., Liu, S., Erich Bauer, E.: Calibration and performance of two different constitutive models for rockfill materials. Water Sci. Eng. **9**(3), 227–239 (2016). https://doi.org/10.1016/j.wse.2016.11.005
39. Luzzani, L., Coop, M.R.: On the relationship between particle breakage and the critical state of sand. Soils Found. **42**(2), 71–82 (2002)
40. Matsuoka, H., Nakai, T.: Stress-strain relationship of soil based on the 'SMP'. In: Proceedings of Speciality Session 9, IX International Conference on Soil Mechanics and Foundation Engineering, Tokyo, pp. 153–162 (1977)
41. McDowell, G.R., Bolton, M.D.: On the micromechanics of crushable aggregates. Geóeteehnique **4S**(5), 667–679 (1998)
42. Nakata, Y., Hyodo, M., Hyde, A.F., Kato, Y., Murata, H.: Microscopic particle crushing of sand subjected to high pressure one-dimensional compression. Soils Found. **41**(1), 69–82 (2001)
43. Nguyen, G.D., Einav, I.: Numerical regularization of a model based on breakage mechanics for granular materials. Int. J. Solids Struct. **47**(10), 1350–1360 (2010)
44. Niemunis, A., Herle, I.: Hypoplastic model for cohesionless soils with elastic strain range. Mech. Cohesive-Frictional Mater. **2**(4), 279–299 (1997)
45. Ohde, J.: Zur Theorie der Druckverteilung im Baugrund. Bauingenieur **20**, 451–459 (1939)
46. Oldecop, L.A., Alonso, E.E.: Theoretical investigation of the time-dependent behaviour of rockfill. Géotechnique **57**(3), 289–301 (2007)
47. Ovalle, C., Frossard, E., Dano, C., Hu, W., Maiolino, S., Hicher, P.-Y.: The effect of size on the strength of coarse rock aggregates and large rockfill samples through experimental data. Acta Mechanica **225**(8), 2199–2216 (2014)
48. Ovalle, C., Dano, C., Hicher, P.Y., Cisternas, M.: An experimental framework for evaluating the mechanical behavior of dry and wet crushable granular materials based on the particle breakage ratio. Can. Geotech. J. **52**, 1–12 (2015)
49. Sadrekarimi, A., Olson, S.M.: Particle damage observed in ring shear tests on sands. Can. Geotech. J. **47**(5), 497–515 (2010)

50. Sadrekarimi, A., Olson, S.M.: Critical state friction angle of sands. Géotechnique **61**(9), 771–783 (2011)
51. Salim, W., Indraratna, B.: A new elastoplastic constitutive model for coarse granular aggregates incorporating particle breakage. Can. Geotech. J. **41**, 657–671 (2004)
52. Tejchman, J., Bauer, E.: Numerical simulation of shear band formation with a polar hypoplastic constitutive model. Comput. Geotech. **19**, 221–44 (1996)
53. von Wolffersdorff, P.A.: A hypoplastic relation for granular materials with a predefined limit state surface. Mech. Cohesive-Frictional Mater. **1**, 251–271 (1996)
54. Wu, W., Bauer, E.: A hypoplastic model for barotropy and pyknotropy of granular soils. In: Kolymbas, D. (ed.) Proceedings of the International Workshop on Modern Approaches to Plasticity, pp. 225–245. Elsevier Press, Amsterdam (1992–1993)
55. Wu, W., Bauer, E., Kolymbas, D.: Hypoplastic constitutive model with critical state for granular materials. Mech. Mat. **23**, 45–69 (1996)
56. Yamamuro, J.A., Bopp, P.A., Lade, P.V.: One-dimensional compression of sands at high pressures. J. Geotech. Eng. ASCE **122**(2), 147–154 (1996)

The Development of the Material Point Method for Simulating Nonlocal Failure Evolution Involved in Multi-phase Interactions

Zhen Chen[1,2(✉)]

[1] Department of Civil and Environmental Engineering, University of Missouri, Columbia, MO 65211, USA
chenzh@missouri.edu
[2] Department of Engineering Mechanics, Faculty of Vehicle Engineering and Mechanics, Dalian University of Technology, Dalian 116024, China

Abstract. The evolution of interfacial failure between different materials such as concrete and soil has the nonlocal feature. As a result, local constitutive models cannot predict the real physics associated with the interfacial failure evolution. Since its first journal paper was published in 1994, the Material Point Method (MPM, http://en.wikipedia.org/wiki/Material_Point_Method), which is a spatial discretization extension from computational fluid dynamics to solid dynamics, has evolved with applications to different areas in Simulation-Based Engineering Science (SBES). We are developing a particle-based computer test-bed for multiscale and multiphysics modeling and simulation to advance SBES, with a focus on the multiphase interactions involving failure evolution. In this conference, the very recent results in improving the MPM will be presented with applications to nonlocal failure events, and future research and development directions will be discussed to promote international collaboration.

Keywords: Nonlocal failure · Interface · Material point method

1 Introduction

Multi-phase (solid-liquid-gas) or multi-material (soft-hard material interfacial) interactions play an important role in geotechnical engineering applications such as drilling, hydrofracturing, impact and penetration into geologic media. It has been shown that the evolution of interfacial failure between different materials has the nonlocal feature [4, 5], namely, the stress state at a material point depends on the strain distribution around that point in a representative volume of certain size. Hence, local constitutive models cannot predict the real physics associated with interfacial failure evolution.

Higher order continuum models, such as nonlocal integral or strain gradient models, have been formulated to predict the evolution of localized failure with applications to interfacial problems, as reviewed by Chen and Schreyer [5]. However, the use of higher order models yields higher order governing equations with the ambiguity in the physics behind additional boundary conditions and with the difficulty in large-scale computer simulations. On the other hand, it has been demonstrated that

W. Wu (Ed.): *Desiderata Geotechnica*, SSGG, pp. 21–24, 2019.
https://doi.org/10.1007/978-3-030-14987-1_2

the jumps of certain kinematic variables in a complete failure process can be related to the transition between local governing equations of different types [2]. By taking the initial point of material failure as one at which the change of local governing equation type occurs (e.g., a hyperbolic type to an elliptic one for dynamic problems or an elliptic type to another one for quasi-static problems), a moving material surface of discontinuity can be defined through the jump forms of conservation laws across the surface. Jumps in mass density, velocity, strain and stress can be determined on this moving surface of discontinuity between two material domains. As a result, both continuum-based and discontinuity-based approaches could be employed to model the evolution of localization, with different types of applicability and limitation for different cases, depending on the scale of the problem and the degrees of discontinuity considered [1].

Since the discontinuous bifurcation identifies the transition from continuous to discontinuous failure modes, it appears that a local continuum elastoplasticity/damage model in combination with a decohesion model via discontinuous bifurcation analysis could be sound in physics and efficient in computation [6, 13]. Thus, the gap between the continuous and discontinuous approaches could be bridged to simulate a complete failure evolution process without invoking higher order terms in space. To effectively simulate localized large deformations and discontinuities of various types, however, a robust spatial discretization procedure is a necessity to accommodate both continuous and discontinuous modeling approaches in a single computational domain.

Due to the use of master/slave nodes at the contact surface of (assumed) zero thickness, the mesh-based methods such as the finite element method (FEM) and finite difference method (FDM) cannot describe the real physics involved in the nonlocal interfacial problems, in addition to re-meshing as required for the simulation of failure evolution. To better simulate the multi-material interactions, such as those in impact, explosion and penetration, the material point method (MPM) has evolved over the last two and a half decades, and been applied to many areas of Simulation-based Engineering Science (SBES) since its first journal paper was published [11]. The MPM is an extension to solid dynamics problems of a hydrodynamics code called FLIP which, in turn, evolved from the particle-in-cell Method for computational fluid dynamics. The essential idea is to take advantage of both the Eulerian and Lagrangian methods while avoiding the shortcomings of each so that it could effectively integrate computational fluid dynamic with solid dynamics. In comparison with the other recently developed numerical procedures, the MPM appears to be less complex with a cost factor of at most twice that associated with the use of corresponding finite elements. In addition, the use of the single-valued mapping functions in the MPM results in a natural no-slip contact/impact scheme such that no inter-penetration would occur. The slip condition could also be implemented based on the physics involved in the interfacial failure evolution without invoking master/slave nodes at the contact surface. Furthermore, the MPM and FEM could be easily combined in a single computational domain for efficient large-scale computer simulation because both methods are developed based on the same weak formulation of continuum mechanics.

Because the MPM has the common feature of both discrete [such as molecular dynamics (MD) and smoothed particle hydrodynamics (SPH)] and mesh-based (such as FEM and FDM) spatial discretization procedures, a particle-based multiscale

simulation approach has been proposed via the mapping-remapping process within the MPM framework, in which MD at nano scale is linked with dissipative particle dynamics (DPD) at meso scale hierarchically, and the DPD and MPM at microscale are employed concurrently in a single computational domain [3, 9]. It has been shown that the MPM mapping-remapping process could effectively coarse-grain the DPD, and that the multi-phase interactions under extreme loading conditions could be simulated at different scales. The recent MPM book provides a comprehensive review of the research and development efforts made by many international teams to promote the MPM in the evolution of SBES [14].

2 Proposed Approach

To improve the solution accuracy for large deformation cases, very recent efforts have been made to enhance the MPM with B-spline basis functions [7], and time-discontinuous mapping operation [10] with additional computational expenses. Based on the conservation laws of mass, momentum and energy, the generalized interpolation material point (GIMP) method has also been improved for simulating and evaluating the fully coupled thermomechanical responses, such as the failure evolution in a snowy slope [12]. The fully coupled thermomechanical GIMP method (CTGIMP) considers the effects of both the temperature on deformation and the deformation on temperature so that geothermal problems might be better treated with high fidelity. However, the CTGIMP remains to be validated against experimental data.

Each spatial discretization procedure has its own strength and limitation so that a robust model-based simulation tool for multiscale and multiphysics problems should take advantage of the strengths of different procedures for different problem domains. We are developing the smoothed MPM by integrating the strengths of SPH and MPM to better handle the impact problems, in which the smoothed MPM mapping operation is employed only around the impact surface without invoking master/slave nodes while either the MPM or SPH could be used in other parts of the problem domain [8]. As a result, no artificial viscosity is required to eliminate the problem-specific choice for simulating transient problems. As the smoothed mapping operation is in fact a nonlocal process, it might be feasible for us to combine nonlocal interfacial constitutive modeling with the smoothed operator for efficient multiscale model-based simulation.

3 Conclusion

In this workshop, recent advances in improving the MPM for better simulating nonlocal failure evolution will be presented, with applications to the nonlocal failure evolution in heterogeneous materials that includes complex microstructure such as cement-based materials. Future research and development directions will also be discussed.

References

1. Bazant, Z.P., Chen, E.P.: Scaling of structural failure. Appl. Mech. Rev. **50**, 593–627 (1997)
2. Chen, Z.: Continuous and discontinuous failure modes. J. Eng. Mech. **122**, 80–82 (1996)
3. Chen, Z., Jiang, S., Gan, Y., Liu, H., Sewell, T.D.: A particle-based multiscale simulation procedure within the material point method framework. Comput. Part. Mech. **1**, 147–158 (2014)
4. Chen, Z., Schreyer, H.L.: Simulation of soil-concrete interfaces with nonlocal constitutive models. J. Eng. Mech. **113**(11), 1665–1677 (1987)
5. Chen, Z., Schreyer, H.L.: On nonlocal damage models for interface problems. Int. J. Solids Struct. **31**(9), 1241–1261 (1994)
6. Chen, Z., Shen, L., Mai, Y.-W., Shen, Y.-G.: A bifurcation-based decohesion model for simulating the transition from localization to decohesion with the MPM. J. Appl. Math. Phys. (ZAMP) **56**, 908–930 (2005)
7. Gan, Y., Sun, Z., Chen, Z., Zhang, X., Liu, Y.: Enhancement of the material point method using B-spline basis functions. Int. J. Numer. Meth. Eng. **113**, 411–431 (2018)
8. He, L., Gan, Y., Chen, Z.: Preliminary effort in developing the smoothed material point method for impact. Comp. Part. Mech. (2018, submitted)
9. Jiang, S., Chen, Z., Sewell, T.D., Gan, Y.: Multiscale simulation of the responses of discrete nanostructures to extreme loading conditions based on the material point method. Comput. Meth. Appl. Mech. Eng. **297**, 219–238 (2015)
10. Lu, M., Zhang, J., Zhang, H., Zheng, Y., Chen, Z.: Time-discontinuous material point method for transient problems. Comput. Meth. Appl. Mech. Eng. **328**, 663–685 (2018)
11. Sulsky, D., Chen, Z., Schreyer, H.L.: A particle method for history-dependent materials. Comput. Meth. Appl. Mech. Eng. **118**, 179–196 (1994)
12. Tao, J., Zhang, H., Zheng, Y., Chen, Z.: Development of generalized interpolation material point method for simulating fully coupled thermomechanical failure evolution. Comput. Meth. Appl. Mech. Eng. **332**, 325–342 (2018)
13. Yang, P., Gan, Y., Zhang, X., Chen, Z., Qi, W., Liu, P.: Improved decohesion modeling with the material point method for simulating crack evolution. Int. J. Fract. **186**, 177–184 (2014)
14. Zhang, X., Chen, Z., Liu, Y.: The Material Point Method: A Continuum-Based Particle Method for Extreme Loading Cases. Academic Press, Elsevier (2016)

Modelling of Shaking-Induced Slope Displacements During Strong Earthquakes

Roberto Cudmani(✉)

Zentrum Geotechnik, Technical University of Munich, Munich, Germany
r.cudmani@tum.de

Abstract. A nonlinear wave propagation model, which is based on the theory of Hypoplasticity developed at the Institute of Soil Mechanics and Rock Mechanics at the KIT (former TU Karlsruhe) under the guidance of Prof. Gudehus, is applied for the simulation of the dynamic response of slopes during strong earthquakes. The model captures the main features of mechanical behavior of coarse and fine-grained soils under seismic-induced alternating shearing and is an alternative to the *Newmark method*, which simply assumes ideal-plastic Coulomb-friction sliding, for the estimation of earthquake-induced displacements of buildings and slopes during earthquakes. After a short introduction and validation, the capabilities of the model to predict the magnitude of permanent displacements as a function of the slope inclination, the intensity of the seismic excitation and the drainage conditions of the slope are shown exemplarily.

Keywords: Ground response analysis · Earthquake · Slope · Dynamic soil behavior

1 Introduction

During the course of history, earthquake-induced landslides have been responsible for as much, or even more damage than all other seismic hazards combined. In spite of scientific advances in the theory and applications of numerical methods and constitutive modeling of soil behavior in the past, pseudo-static limit equilibrium analyses and sliding block analyses are the most frequently applied methods in practice to judge the stability and to estimate the motion of slopes under earthquake excitation, respectively.

The main shortcomings of the pseudo-static limit equilibrium analysis in the case of strong earthquakes are the choice of the ground acceleration to evaluate the pseudo-static seismic forces and the choice of the shear strength of the soil, which is not a soil constant as it is often assumed. In the sliding block analysis proposed by Newmark [4], slope sliding starts when the inertial forces cause driving forces to exceed the available shear strength at the slip surface. The motion of the slope is driven by the unbalanced force until the driving forces drop below the resisting forces and the relative velocity between the sliding mass (rigid body) and the underlying ground vanishes. By integration of the equation of motion of a rigid block for a given ground acceleration and friction angle at the failure surface, the displacement of the block induced by the earthquake can be calculated.

Newmark's approach assumes that a slip surface develops at the beginning of the earthquake. Furthermore, the block slides on this slip surface with the interface behaviour

W. Wu (Ed.): *Desiderata Geotechnica*, SSGG, pp. 25–31, 2019.
https://doi.org/10.1007/978-3-030-14987-1_3

prescribed by the Coulomb friction law. Nevertheless, as the shear strength changes during a strong earthquake, e.g. due to pore pressure generation, an objective evaluation of the friction angle to be used in the analysis is not possible. In addition, it is not clear whether the calculated displacements correspond to the displacement at the ground surface or at any point within the slope. Therefore, both approaches can only very roughly take into account the real mechanisms controlling earthquake-induced slope displacements and the onset of landslides. An evaluation of slope behavior based on these methods appears to be insufficient for the case of strong earthquakes. To overcome these shortcomings, an effective-stress ground response analysis for layered soils developed by Osinov [6] and validated by Cudmani et al. [1] has been extended to the case of an infinite slope. In the following, the original and the extended models are called (*HGSM: Horizontal Ground Surface Model)* and (*ISM: Infinite Slope Model*), respectively.

2 The Wave Propagation Model

The HGSM and ISM are shown in Fig. 1. The unknown variables are the horizontal and vertical material velocities, the non-zero components of the stress tensor (σ_{11}, σ_{22}, σ_{33}, τ_{12}) and the pore pressure. These variables are functions of the depth and time. The governing system of equations consists of the equation of motion, the constitutive equations for the solid skeleton and the pore fluid and the mass balance equation. The constitutive equation for the pore pressure considers the compressibility of the pore fluid, which depends on the degree of saturation. Both drained and undrained conditions can be considered in the calculations. In the numerical simulations, seepage is taken into account by using the so-called u-p formulation [7], which assigns different velocities but same accelerations to the solid and fluid phases. The initial vertical stresses and the initial pore pressures result from the densities of the solid and fluid phases and gravity. The initial horizontal stress is related to the vertical stress via the earth pressure coefficient at rest. The upper surface is assumed to be free of traction. In the case of saturated soil, the pore pressure at the water table and above is assumed to be zero and the lower boundary is assumed to be impermeable.

In order to consider an infinite slope, the equations of motions for the soil skeleton and the pore fluid were modified to account for the component of gravity acting in the direction of the slope. This component is controlled by the angle of the slope ϑ and the acceleration of gravity g.

To solve the dynamic boundary-value problems sketched in Fig. 1, the soil layers are discretised into sublayers with lumped masses. The constitutive parameters, initial void ratios, initial stresses and hydraulic permeability are assigned to each discrete sublayer. The differential equations are solved with the Finite Difference Method. The calculation is carried out in two stages. In the first stage, the driving force $\rho \cdot g \cdot z \cdot \sin \vartheta$ is applied to the soil, while inertial forces are switched off. In the second stage, horizontal (in-plane, anti-plane) and vertical velocities are prescribed at the base of the model to simulate the earthquake. In the case of the ISM, the results are transformed to the rotated Cartesian coordinate system with x-axis parallel to the slope for better visualization of the slope motion.

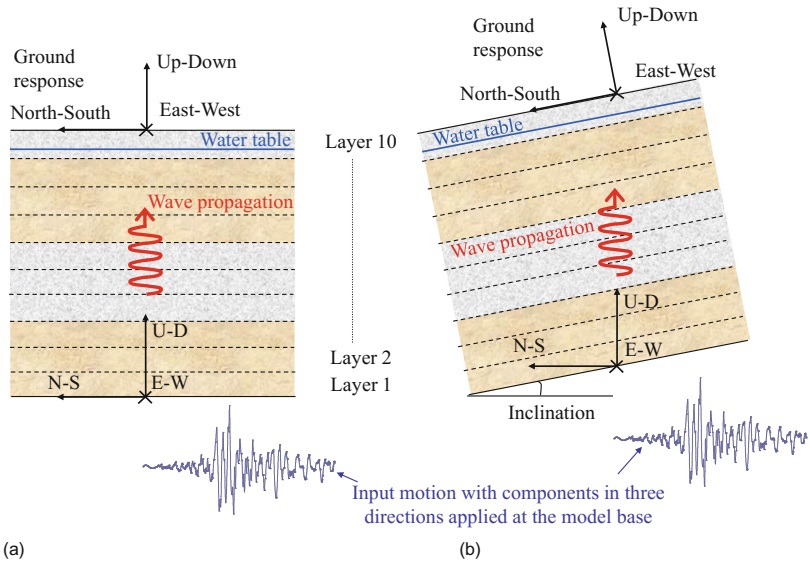

Fig. 1. Wave propagation models (a) HGSM (b) ISM.

3 Constitutive Models

Two hypoplastic constitutive relations are employed in the present study. One describes the rate-independent behaviour of granular soils (e.g. sand), and the other one takes into account viscous effects and is used for the modelling of clayey soils. Both relations describe plastic deformations of a solid skeleton under monotonic as well as cyclic loading for drained and undrained conditions. They incorporate the critical state concept of soil mechanics and the dependence of the stiffness on the current stress, density and history of deformation.

As it is known from elastoplasticity theories, the description of the plastic deformation through hypoplasticity does not require the introduction of a yield surface and a flow rule, and the decomposition of the deformation into elastic and plastic parts. A detailed description of the hypoplastic relations can be found in Niemunis [5]. The solution of a boundary value problem requires both material parameters and initial values of the state variables. The constitutive equation contains 13 model parameters. They are independent of the state variables, that is, the material behaviour can be modelled in a wide range of stresses and densities with the same set of parameters.

4 Validation of the Wave Propagation Model

The wave propagation model was validated by comparing measured and calculated ground responses during strong earthquakes for well-documented sites [1, 3]. For each considered site, a 1D-ground model that included the soil layers, the ground water table, the initial density and stress state as well as the parameters was developed based

on available field investigations and laboratory tests. Thereafter, the earthquake was simulated by applying three velocity components (two horizontal and one vertical) at the base of the model simultaneously, which are obtained by integration of the actual ground acceleration records. In all cases, the base of the model was set at the deepest point in which the acceleration was recorded during the earthquake. Exemplarily, Fig. 2 shows the comparison between the experimental and predicted velocities at two different depths for Port Island during the 1995 Kobe earthquake.

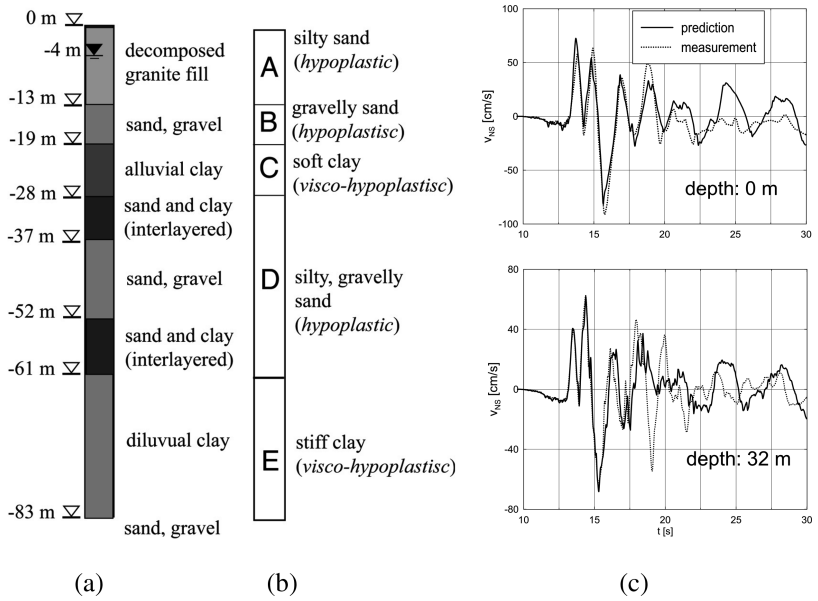

Fig. 2. Port Island: real (a) and idealized (b) soil profiles; (c) measured and predicted velocities at the surface and at depth and 32 m in the North-South direction [1].

5 Shaking-Induced Slope Displacement

In order to investigate the behavior of an infinite slope using the model Fig. 1(b), the same base excitation as before was used. The subsoil data from the Sunamachi experimental site close to the Tokyo Bay [2] and the acceleration recorded in the depth of 18.3 m in December 17, 1987, during the Chiba-Toho-Oki earthquake (magnitude M = 6.7) were used. The subsoil data and the idealized soil profile are presented in Fig. 3.

In Fig. 4, the permanent displacement induced by the earthquake in N-S-direction are shown for inclinations of 0°, 5°, 10°, 15° and 20° (slope in N-S (in-plane) direction).

The permanent displacements in the slope direction (N-S) increase with increasing slope inclination. It almost reaches 3 cm at the end of the earthquake for an inclination of 5°. For the inclinations 10°, 15° and 20°, the permanent displacements increase to

approximately 7 cm, 11 cm and 36 cm, respectively. The pronounced jump of permanent displacements when increasing the slope inclination from 15° to 20° shows that the permanent displacements increase above average when the inclination approaches the value leading to the failure of the slope.

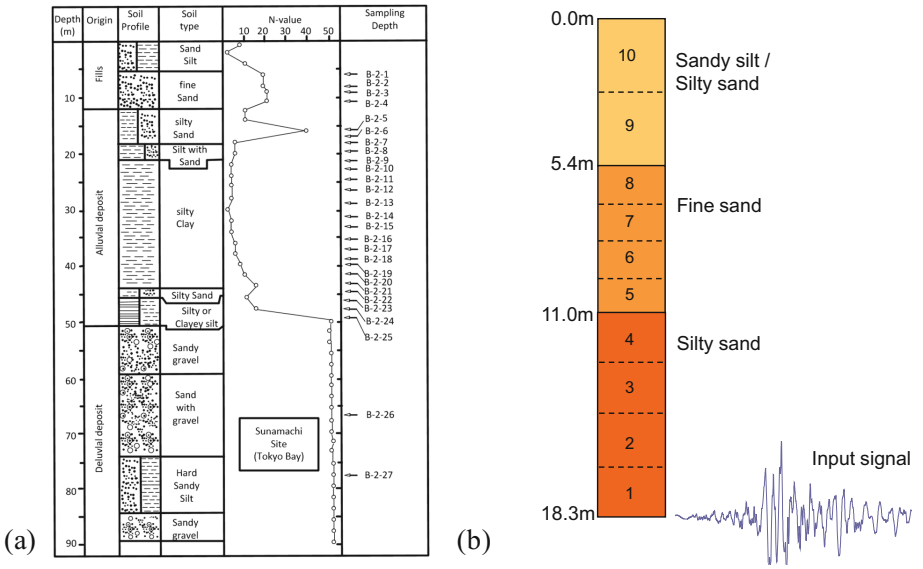

Fig. 3. (a) Typical soil profile at the Sunamachi test site [2]; (b) ground model considered in the numerical simulation.

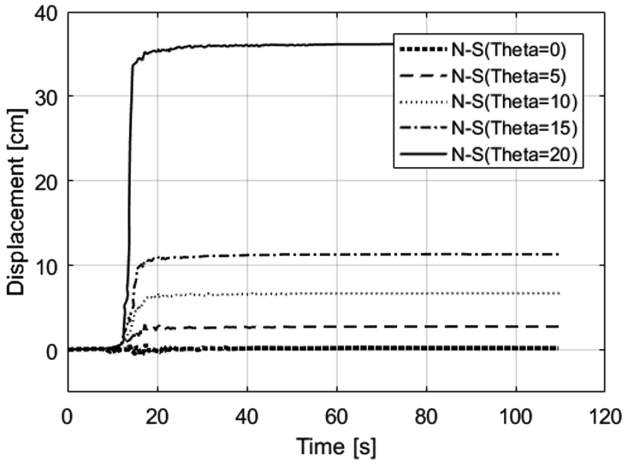

Fig. 4. Displacements in N-S direction for inclinations of 0°, 5°, 10°, 15° and 20°.

Figure 5 compares the response of the slope for dry and fully saturated subsoil conditions. The larger displacements for the condition of fully saturation result from the excess pore pressure induced by the shear waves, which causes a decay of the mean effective stresses and a reduction of shear strength and shear stiffness in comparison with the soil response of the dry slope. However, the inclination of the slope and the initial stress state affect the dynamic response of the slope as well as the location of soil liquefaction. Therefore, there is no simple correlation between the initial slope inclination and the induced displacements.

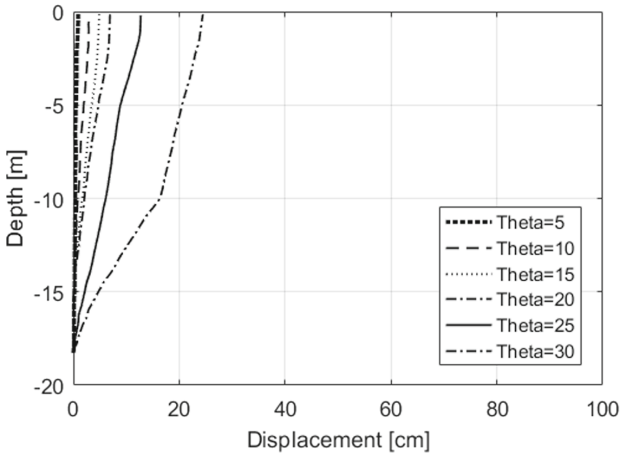

(a) Water table at the surface

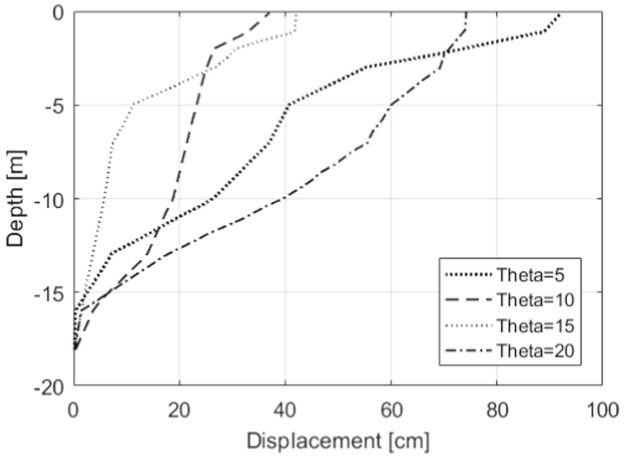

(b) Subsoil without ground water

Fig. 5. Permanent displacements in N-S direction at the end of the earthquake

6 Conclusions

In comparison with the Newmark's sliding block analyses, which assumes a rigid soil mass and perfectly plastic shear failure at the sliding interface, the proposed 1D- wave propagation model takes into account the actual soil behaviour much more realistically, allowing a soil mechanically reliable assessment of the permanent displacements of infinite slopes induced by strong earthquakes.

References

1. Cudmani, R., Osinov, V., Bühler, M., Gudehus, G.: A model for the evaluation of liquefaction susceptibility in layered soils due to earthquakes. In: 12th Panamerican Conference on Soil Mechanics and Geotechnical Engineering, pp. 969–976 (2003)
2. Ishihara, K., Muroi, T., Towhata, I.: In-situ pore water pressures and ground motions during the 1987 Chiba-Toho-Oki earthquake. Soils Found. **29**(4), 75–90 (1989)
3. Kluge, K., Cudmani, R.: Modelling the response of horizontal and sloped ground during strong earthquakes. In: Proceedings from the 2nd International Conference on Performance-Based Design in Earthquake Geotechnical Engineering, Taormina-Italy, vol. 08, no. 03, pp. 975–985 (2012)
4. Newmark, N.M.: Effects of earthquakes on dams and embankments. Géotechnique **15**(2), 139–160 (1965)
5. Niemunis, A.: Extended hypoplastic models for soils. Institut für Grundbau und Bodenmechanik der Ruhr-Universität Bochum, No. 34 (2003)
6. Osinov, V.A.: Cyclic shearing and liquefaction of soil under irregular loading: an incremental model for the dynamic earthquake-induced deformation. Soil Dyn. Earthq. Eng. **23**, 535–548 (2003)
7. Zienkiewicz, O.C., Chang, C.T., Bettess, P.: Drained, undrained, consolidating and dynamic behaviour assumptions in soil. Géotechnique **30**(4), 385–395 (1980)

On the Simulation of the Cyclic Mobility Effect with an ISA-Hypoplastic Model

W. Fuentes(✉) and C. Lascarro

University del Norte, Barranquilla, Colombia
{fuentesw,cjlascarro}@uninorte.edu.co

Abstract. The ISA-Hypoplasticity corresponds to an extended version of conventional Hypoplasticity to enable the simulation of some observed effects on cyclic loading. This extension offers novel features compared to the intergranular strain theory by Herle and Niemunis [4], including the incorporation of an elastic strain amplitude, to separate the elastic and plastic response, and the ability to reduce the plastic accumulation rate upon a larger number of cycles ($N > 10$). In the present work, a modification to the ISA-hypoplastic model is described in order to enable the simulation of cyclic mobility effects exhibited by granular materials. The modification is based on a new state variable, able to detect paths at which the cyclic mobility effect is activated. With this information, some factors of the ISA-hypoplastic model are modified to deliver the proper response on paths showing cyclic mobility effects. Simulations examples are given to illustrate the new mechanism and a short analysis of the new parameters is also included.

1 Introduction

The Intergranular Strain Anisotropy (ISA) can be considered as a mathematical extension of conventional Hypoplasticity for sands [9] or clays [3,7], to improve cyclic loading simulations. Originally, it was proposed to consider three observed effects on cyclic paths [2]: a strain amplitude dividing the plastic and elastic regime, the increase of the stiffness upon reversal loading and the reduction of the plastic strain rate under the same conditions. Successful simulations of cyclic loading for a low number of cycles ($N < 10$) were achieved [2]. Nevertheless, some inspections on the formulation revealed the weakness of the model to predict the behavior of the accumulated plastic behavior upon a higher number of repetitive cycles ($N > 10$). This motivated Poblete et al. [5] to modify the model to account for the effect of repetitive cycles. For a large number of cycles ($N > 10$), the new relations were now able to simulate the observed reduction of the plastic accumulation rate, and showed to work well, not only on undrained cyclic triaxial tests, but also on complex multidimensional cyclic loading under drained conditions [5]. Despite of all these achievements, some issues related to the absence of cyclic mobility effects, and thus the liquefaction analysis, were not addressed by the existent relations given the fact, that this effect were considered to be related to the

W. Wu (Ed.): *Desiderata Geotechnica*, SSGG, pp. 32–39, 2019.
https://doi.org/10.1007/978-3-030-14987-1_4

reference hypoplastic equation, and not to the extension provided by ISA. As a matter of fact, despite the vast amount of works studying hypoplastic models under several cyclic tests, scarce works are devoted to propose relations encompassing the cyclic mobility effect.

The current work describes an extension of an ISA-hypoplastic model to enable the simulation of the cyclic mobility effect, and thus to permit the analysis of liquefaction under undrained conditions. To that end, a strain-type sate variable $\mathbf{z}$ is introduced to detect paths at which the cyclic mobility effect is activated. This information is then considered to modify some factors of the constitutive equation. It will be shown, that the modifications presented herein permit the simulation of cyclic mobility, without altering other former capabilities of hypoplastic models related to the stress-dilatancy behavior under drained conditions.

2 New Modifications of the ISA-Hypoplastic Model

The equations of the reference model are described in the appendices. It corresponds to the Hypoplastic equation by Wollfersdorff [9] extended by the ISA relations according to [2,5]. Evaluation of the model capabilities under cyclic loading can be found in [5]. Its extension to consider cyclic mobility effects is described in the following lines.

In order to detect paths at which the cyclic mobility effect is activated, we introduce a new state variable, denoted with $\mathbf{z}$, with an evolution equation similar to [1]:

$$\dot{\mathbf{z}} = c_z \langle \eta / (M_c f_{d0} F) - 1 \rangle (\mathbf{N} - \mathbf{z}) \|\dot{\boldsymbol{\varepsilon}}\| \tag{1}$$

whereby c_z is a new material parameter controlling the rate of $\mathbf{z}$, $M_c = 6\sin(\varphi_c)/(3 - \sin\varphi_c)$ is the critical state slope, $\eta = q/p$ is the stress ratio, and the factors F and f_{d0} are scalar functions, the first described in the appendices, and the second defined in the sequel. Let denote z the scalar function defined as:

$$z = \langle \mathbf{z} : \mathbf{N} \rangle \tag{2}$$

where $\mathbf{N}$ is a unit tensor ($\|\mathbf{N}\| = 1$) providing information about the intergranular strain rate direction, see Eq. 8. According to Eq. 2, factor z is bounded by $0 \leq z \leq 1$. A value of $z = 0$ indicates that the effect of the cyclic mobility is not accounted by the model, while a value of $z = 1$ means that it is fully considered. Intermediate values of $0 < z < 1$ intend to simulate a transition between these two states. For the case of $z = 1$, we propose that the model reproduces a contractant behavior as by looses states $e \approx e_c$. Specifically, we propose to consider the following characteristics:

- For $z = 1$, the scalar factors f_e and f_d are set to one, i.e. $f_e = f_d = 1$. This is equivalently to evaluate these factors at $e = e_c$.
- For the same condition ($z = 1$), the strain amplitude $\Delta\boldsymbol{\varepsilon}$ at which the intergranular strain effect is reproduced is reduced.

The first requirement is considered through the introduction of the following modifications to the scalar factors f_e and f_d:

$$f_e = f_{e0} - z\langle f_{e0} - 1\rangle, \quad \text{with} \quad f_{e0} = \left(\frac{e_c}{e}\right)^{\beta} \tag{3}$$

$$f_d = f_{d0} + z\langle 1 - f_{d0}\rangle, \quad \text{with} \quad f_{d0} = \left(\frac{e - e_d}{e_c - e_d}\right)^{\alpha} \tag{4}$$

Note that for $z = 1$, they give $f_e = f_d = 1$. For the second requirement, we propose that the former parameter β_h is converted into a function:

$$\beta_h = \beta_{\max} + (\beta_0 - \beta_{\max})(1 - z) \tag{5}$$

which now depends on parameters β_0 and $\beta_{\max}$. For $z = 0$, it gives $\beta_h = \beta_0$, coinciding with its original definition. On the other hand, the relation $\beta_h = \beta_{\max}$ holds for $z = 1$ conditions. At that state ($z = 1$), the new parameter $\beta_{\max}$ allows to control the strain amplitude $\|\Delta\boldsymbol{\varepsilon}\|$ at which the intergranular strain effect is considered. Hence, simulation of the cyclic mobility effect requires the calibration of the new parameters c_z and $\beta_{\max}$.

We now present some simulations examples. The Karlsruhe fine sand parameters reported in [5] are borrowed for the following simulations ($e_{\max} = 1.054$, $e_{\min} = 0.677$). Consider a drained triaxial test with constant mean pressure $p =$ constant, such as the tests by [6]. The test is performed under $p = 100\,\text{kPa}$ (constant), with an initial void ratio of $e_0 = 0.6$ (dense state). Three different simulations are presented in Fig. 1, whereby the variation of the parameter $c_z = \{0, 100, 300\}$ is considered. From the results one may see, that for higher values of c_z, a higher degradation of the shear stiffness accompanied with an increase of the compressive volumetric strains are obtained. Hence, c_z may be calibrated by trial and error, to provide accurate simulations of these effects under cycles of large strain amplitudes ($\|\Delta\boldsymbol{\varepsilon}\| > 0.001$). Notice that the stress-dilatancy response exhibited in Fig. 1d, is not spoiled by the current modification.

A cyclic undrained triaxial test with constant deviator stress amplitude ($q^{\text{amp}} = 40\,\text{kPa}$) is shown in Fig. 2. For this simulation, c_z is set to $c_z = 300$. The results show that the model is able to reproduce the cyclic mobility effect observed on the last cycles. This is better noted on Fig. 3, whereby the simulation of the reference model lacking of the current extension is included. The proposed extension assesses to simulate the "butterfly-type" paths in the $p - q$, see Fig. 3a, while the accumulation of the pore water pressure p_w upon the number of cycles N is well reproduced, see Fig. 3b.

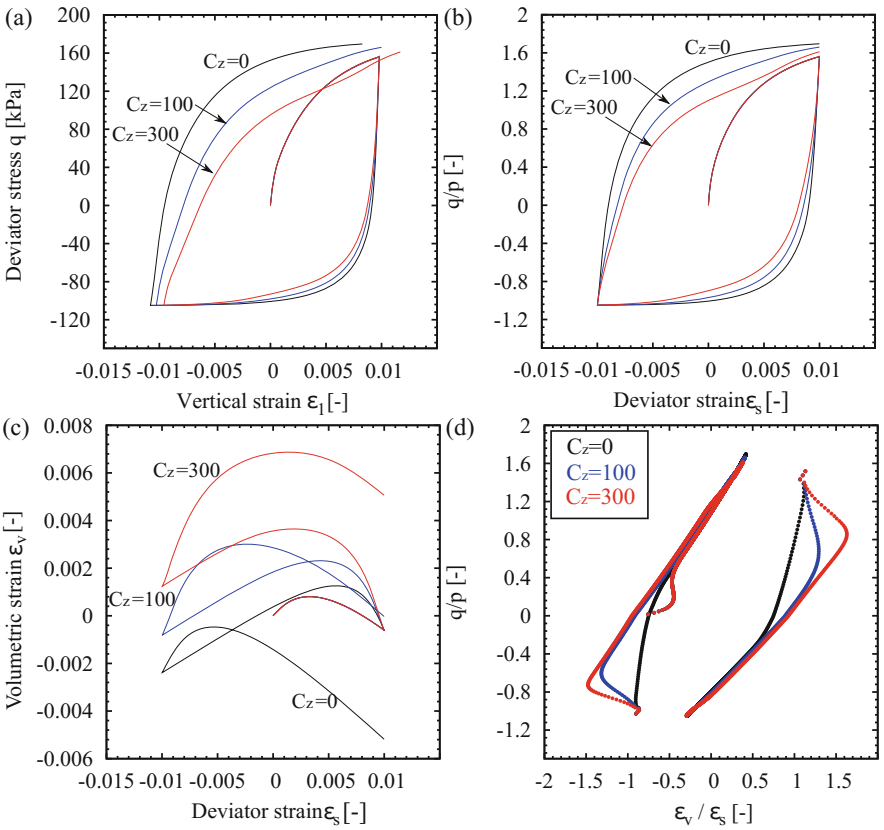

Fig. 1. Simulation of a p = const triaxial test under drained conditions. Karlsruhe fine sand parameters. $p = 100\,\text{kPa}$.

Closure

The present work described an extended version of the ISA-hypoplastic model able to simulate cyclic mobility effects. To that end, an additional state variable $\mathbf{z}$ has been introduced, able to detect paths at which the cyclic mobility effect is activated. This information is used on factors f_e and f_d of the hypoplastic model, and on factor β_h from the ISA model. The proposed methodology requires the calibration of two parameters, namely, c_z which controls the rate of $\mathbf{z}$ and $\beta_{\max}$ controlling the strain amplitude upon cyclic mobility wherein the intergranular strain influences the response. The current extension is simple, and provides fair simulations of cyclic undrained tests while keeping its capabilities on the stress-dilatancy response under drained conditions.

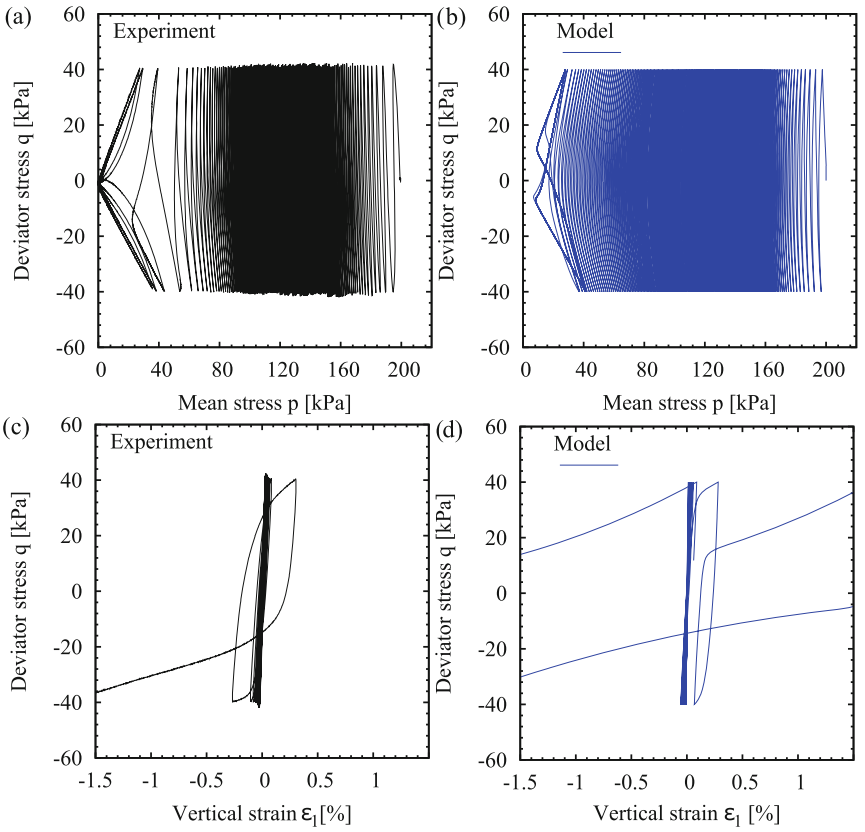

Fig. 2. Simulation of a cyclic undrained triaxial test. Deviator stress amplitude of $q^{\text{amp}} = 40\,\text{kPa}$. Experiment using Karlsruhe fine sand, data by [8]

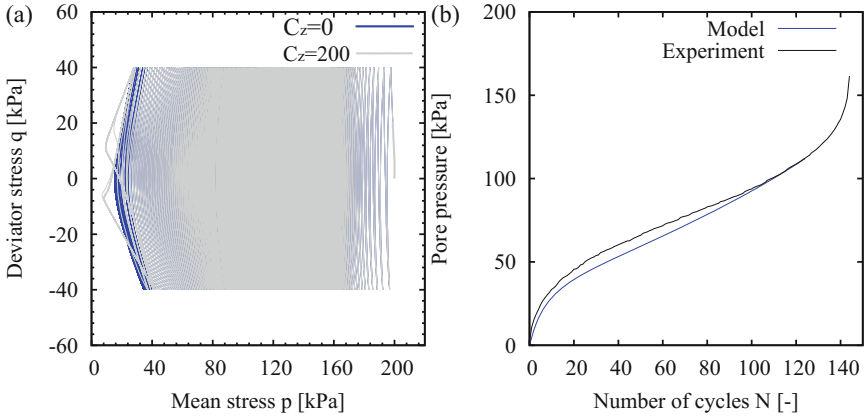

Fig. 3. Accumulated pore pressure p_w against number of cycles N. Parameters of Karlruhe fine sand

Notation and Conventions
The notation and convention of the present work is as follows: italic fonts denote scalar magnitudes (e.g. a, b), bold lowercase letters denote vectors (e.g. $\mathbf{a}, \mathbf{b}$), bold capital letters denote second-rank tensors (e.g. $\mathbf{A}, \boldsymbol{\sigma}$), and special fonts are used for fourth-rank tensors (e.g. E, L). Indicial notation can be used to represent components of tensors (e.g. A_{ij}), and their operations follow the Einstein's summation convention. The Kronecker delta symbol is represented by δ_{ij}, i.e. $\delta_{ij} = 1$ when $i = j$ and $\delta_{ij} = 0$ otherwise. The symbol $\mathbf{1}$ denotes the Kronecker delta tensor ($1_{ij} = \delta_{ij}$). The unit fourth-rank tensor for symmetric tensors is denoted by I, where $\mathsf{I}_{ijkl} = \frac{1}{2}\left(\delta_{ik}\delta_{jl} + \delta_{il}\delta_{jk}\right)$. Multiplication with two dummy indices (double contraction) is denoted with a colon ":" (e.g. $\mathbf{A} : \mathbf{B} = A_{ij}B_{ij}$). The symbol "$\otimes$" represents the dyadic product (e.g. $\mathbf{A} \otimes \mathbf{B} = A_{ij}B_{kl}$). The brackets $\| \sqcup \|$ extract the Euclidean norm (e.g. $\| \mathbf{A} \| = \sqrt{A_{ij}A_{ij}}$). Normalized tensors are denoted by $\overrightarrow{\sqcup} = \frac{\sqcup}{\|\sqcup\|}$, or in general as $\sqcup^{\rightarrow}$. The superscript $\sqcup^{\text{dev}}$ extracts the deviatoric part of a tensor (e.g. $\mathbf{A}^{\text{dev}} = \mathbf{A} - \frac{1}{3}(\text{tr}\mathbf{A})\mathbf{1}$). Components of the effective stress tensor $\boldsymbol{\sigma}$ or strain tensor $\boldsymbol{\varepsilon}$ in compression are negative. Roscoe variables are defined as $p = -\sigma_{ii}/3$, $q = \sqrt{\frac{3}{2}}\|\boldsymbol{\sigma}^{\text{dev}}\|$, $\varepsilon_v = -\varepsilon_{ii}$ and $\varepsilon_s = \sqrt{\frac{2}{3}}\|\boldsymbol{\varepsilon}^{\text{dev}}\|$. The stress ratio η is defined as $\eta = q/p$. The deviator stress tensor is defined as $\boldsymbol{\sigma}^{\text{dev}} = \boldsymbol{\sigma} + p\mathbf{1}$ and the stress-ratio tensor with $\mathbf{r} = \boldsymbol{\sigma}^{\text{dev}}/p = \sqrt{\frac{2}{3}}\,\eta\,\overrightarrow{\boldsymbol{\sigma}^{\text{dev}}}$.

Appendix 1

Appendix 1 presents a summary of the constitutive equations of the ISA-hypoplastic model. Details of the equations below are found in [2,5,9].

$$\dot{\boldsymbol{\sigma}} = \mathsf{M} : \dot{\boldsymbol{\varepsilon}} \tag{6}$$

$$\mathsf{M} = \begin{cases} [m_R + (1 - m_R)y_h](\mathsf{L}^{\text{hyp}} + \rho^{\chi}\mathbf{N}^{\text{hyp}} \otimes \mathbf{N}) & \text{for } F_H \geq 0 \\ m_R\mathsf{L}^{\text{hyp}} & \text{for } F_H < 0 \end{cases} \tag{7}$$

$$\dot{\mathbf{h}} = \dot{\varepsilon} - \dot{\lambda}_H\mathbf{N}, \quad \text{with} \quad \mathbf{N} = \frac{\mathbf{h} - \mathbf{c}}{R/2} \tag{8}$$

$$\dot{\lambda}_H = \frac{\langle \mathbf{N} : \dot{\varepsilon} \rangle}{1 - \left(\dfrac{\partial F_H}{\partial \mathbf{c}}\right) : \bar{\mathbf{c}}} \tag{9}$$

$$\dot{\mathbf{c}} = \dot{\lambda}_H\bar{\mathbf{c}}, \quad \text{with} \quad \bar{\mathbf{c}} = \beta_h(\mathbf{c}_b - \mathbf{c})/R, \quad \text{and} \quad \mathbf{c}_b = (R/2)\,\overrightarrow{\dot{\boldsymbol{\varepsilon}}} \tag{10}$$

$$\rho = 1 - \frac{\|\mathbf{h}_b - \mathbf{h}\|}{2R}, \quad \text{with} \quad \mathbf{h}_b = R\mathbf{N} \tag{11}$$

$$y_h = \rho^{\chi}\langle \mathbf{N} : \overrightarrow{\dot{\boldsymbol{\varepsilon}}} \rangle \tag{12}$$

$$m = m_R + (1 - m_R) y_h \tag{13}$$

$$\dot{\varepsilon}_{\text{acc}} = \frac{C_a}{R}(1 - y_h - \varepsilon_{\text{acc}})\|\dot{\boldsymbol{\varepsilon}}\| \tag{14}$$

$$\chi = \chi_0 + \varepsilon_{\text{acc}}(\chi_{\max} - \chi_0) \tag{15}$$

The set of parameters are R, χ_0, $\chi_{\max}$, m_R, β_0, $\beta_{\max}$ and C_a.

Appendix 2

In the present appendix, the remaining equations of the reference hypoplastic model [9] are given:

$$\mathsf{L}^{\text{hyp}} = f_b f_e \frac{1}{\hat{\boldsymbol{\sigma}} : \hat{\boldsymbol{\sigma}}}(F^2 \mathsf{I} + a^2 \hat{\boldsymbol{\sigma}}\hat{\boldsymbol{\sigma}}) \tag{16}$$

$$\mathbf{N}^{\text{hyp}} = f_d f_b f_e \frac{Fa}{\hat{\boldsymbol{\sigma}} : \hat{\boldsymbol{\sigma}}}(\hat{\boldsymbol{\sigma}} + \hat{\boldsymbol{\sigma}}^{\text{dev}}) \tag{17}$$

$$\begin{aligned} f_e &= \left(\frac{e_c}{e}\right)^{\beta} \\ f_b &= \frac{h_s}{n_B}\left(\frac{1+e_i}{e_i}\right)\left(\frac{e_{i0}}{e_{c0}}\right)^{\beta}\left(-\frac{\text{tr}\boldsymbol{\sigma}}{h_s}\right)^{1-n_B}\left[3 + a^2 - \sqrt{3}a\left(\frac{e_{i0} - e_{d0}}{e_{c0} - e_{d0}}\right)^{\beta}\right]^{-1} \\ f_d &= \left(\frac{e - e_d}{e_c - e_d}\right)^{\alpha} \end{aligned} \tag{18}$$

$$F = \sqrt{\frac{1}{8}\tan^2(\psi) + \frac{2 - \tan^2(\psi)}{2 + 2\sqrt{2}\tan(\psi)\cos(3\theta)}} - \frac{1}{2\sqrt{2}\tan(\psi)} \tag{19}$$

$$\begin{aligned} a &= \frac{\sqrt{3}(3 - \sin(\varphi_c))}{2\sqrt{2}\sin(\varphi_c))} \\ \tan\psi &= \sqrt{3}\|\hat{\boldsymbol{\sigma}}^{\text{dev}}\| \\ \cos(3\theta) &= \sqrt{6}\frac{\text{tr}(\hat{\boldsymbol{\sigma}}^{\text{dev}}\hat{\boldsymbol{\sigma}}^{\text{dev}}\hat{\boldsymbol{\sigma}}^{\text{dev}})}{(\hat{\boldsymbol{\sigma}}^{\text{dev}} : \hat{\boldsymbol{\sigma}}^{\text{dev}})^{3/2}} \end{aligned} \tag{20}$$

$$\begin{aligned} e_i &= e_{i0}\exp\left(-(3p/h_s)^{n_B}\right) \\ e_d &= e_{d0}\exp\left(-(3p/h_s)^{n_B}\right) \\ e_c &= e_{c0}\exp\left(-(3p/h_s)^{n_B}\right) \end{aligned} \tag{21}$$

The set of parameters are φ_c, h_s, n_B, e_{i0}, e_{c0}, e_{d0}, α and β.

References

1. Dafalias, Y., Manzari, M.: Simple plasticity sand model accounting for fabric change effects. J. Eng. Mech. ASCE **130**(6), 622–634 (2004)
2. Fuentes, W., Triantafyllidis, T.: ISA model: a constitutive model for soils with yield surface in the intergranular strain space. Int. J. Numer. Anal. Meth. Geomech. **39**(11), 1235–1254 (2015)
3. Mašín, D.: A hypoplastic constitutive model for clays. Int. J. Numer. Anal. Meth. Geomech. **29**(4), 311–336 (2005)
4. Niemunis, A., Herle, I.: Hypoplastic model for cohesionless soils with elastic strain range. Mech. Cohesive-frictional Mater. **2**(4), 279–299 (1997)
5. Poblete, M., Fuentes, W., Triantafyllidis, T.: On the simulation of multidimensional cyclic loading with intergranular strain. Acta Geotech. **11**(6), 1263–1285 (2016)
6. Pradhan, T., Tatsuoka, F., Sato, Y.: Experimental stress-dilatancy relations of sand subjected to cyclic loading. Soils Found. **29**(1), 45–64 (1989)
7. Weifner, T., Kolymbas, D.: A hypoplastic model for clay and sand. Acta Geotech. **2**(2), 103–112 (2007)
8. Wichtmann, T.: Karlsruhe fine sand data-base. Technical report, Institute of Soil and Rock Mechanics (IBF). Karlsruhe Institute of Technology (KIT) (2015). http://www.torsten-wichtmann.de
9. Wolffersdorff, V.: A hypoplastic relation for granular materials with a predefined limit state surface. Mech. Cohesive-frictional Mater. **1**(3), 251–271 (1996)

Fractality in Geomechanics

Gerd Gudehus(✉)

Emeritus, Institute of Soil and Rock Mechanics,
Karlsruhe Institute of Technology, Karlsruhe, Germany
gerd.gudehus@ibf.uni-karlsruhe.de, gerd.gudehus@kit.edu

Abstract. The cognition of natural soil and rock, called geomatter as it is not a simple material, is impeded by opaqueness and wild randomness so that Aristoteles' induction and Popper's demarcation of theories are seemingly insufficient. This can be attributed to critical phenomena with seismogeneous chain reactions which exhibit fractal features, leave back permanent traces and elude mathematical treatment in general. In the stable range of grain fabrics buckling force chains cause a heat-like micro-seismicity which activates redistributions and can be captured mathematically. This is no more possible for chain reactions due to a positive feedback by seismic waves and pore water diffusion, with sizes from sand-boxes to subduction zones. Successions of them can be captured probabilistically by power laws with lower and upper bounds, which should be estimated in a rational way for keeping the geotechnical risk acceptably low. For this aim one should reduce deficits and avoid defects of cognition.

1 Introduction

The similarity of sand and rock can get visible at the beach (e.g. Fig. 1). It implies self-similar roughness, i.e. geometrical *fractality*. One could estimate fractal dimensions of rims, profiles and surfaces with Mandelbrot's [20] box-counting, but this is left aside as generating mechanisms elude yet mathematical treatment. I focus on internal mechanisms which are intricate enough because of their triple fractality, viz.

- spatial: the solid mass m_s in a cube increases with its length d by $m_s = m_{sr}(d/d_r)^{3\alpha}$ with an exponent ca. $0.9 < \alpha < 1$ as the pore system ($\pi\acute{o}\rho o\varsigma$ = passage) is geometrically fractal;
- temporal: seismic spectra tend often to $v^2 \propto 1/f^{2\beta}$ with ca. $0.9 < \beta < 1$;
- episodic: successions of collapses with released energy E or more occur often with a number $N = N_r(E/E_r)^{-\gamma}$ and an exponent γ near 1.

This holds true approximately within lower and upper cutoffs, and the fractal exponents are not constant. Spatial and temporal distributions of geomechanical quantities may be continuous, but are not differentiable so that gradients and rates do not properly exist. Sets of events are wildly random [21] so that a single event can matter as much as the sum of all smaller ones [22]. Geomatter is not a simple material in [35] sense, and *geomechanics is no continuum mechanics*:

W. Wu (Ed.): *Desiderata Geotechnica*, SSGG, pp. 40–59, 2019.
https://doi.org/10.1007/978-3-030-14987-1_5

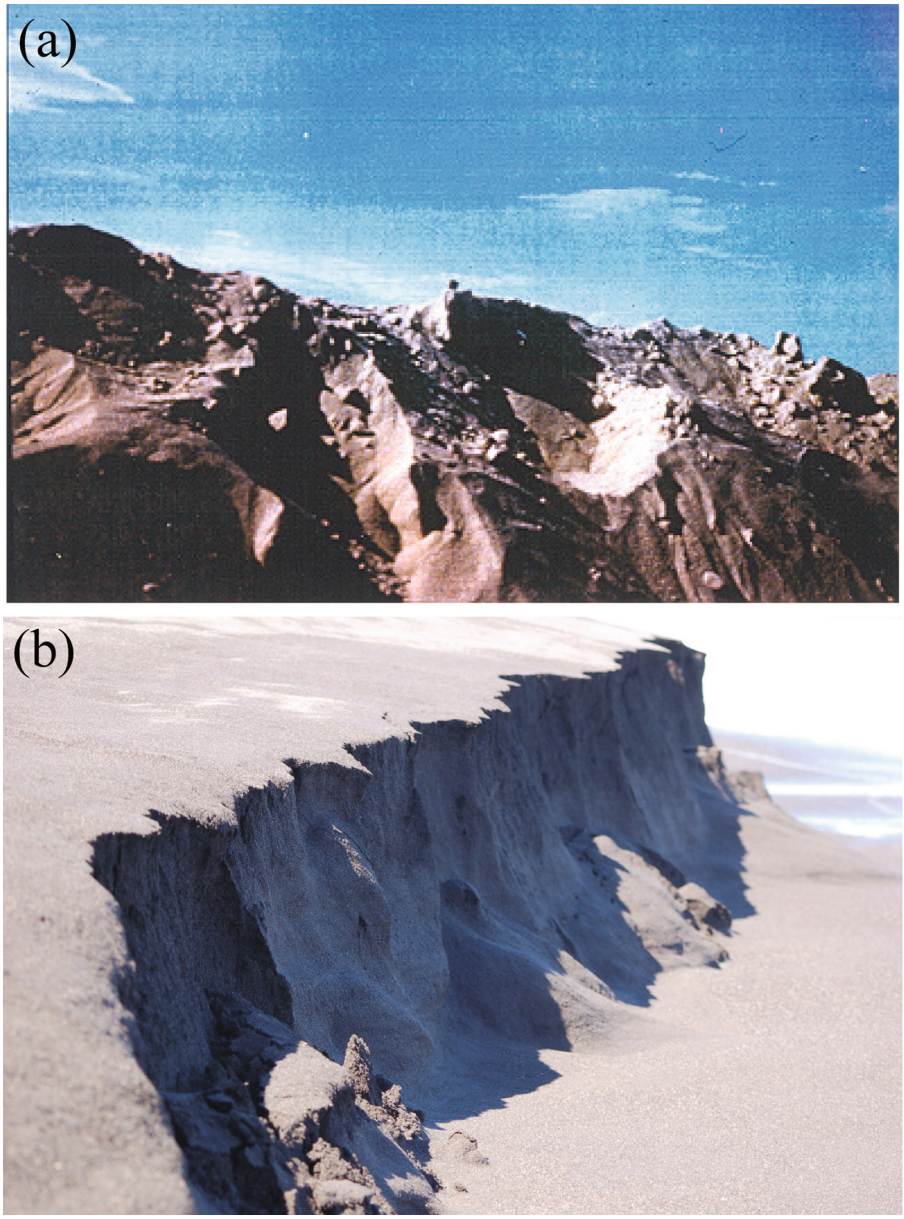

Fig. 1. Self-similarly rough sand structures of ca. 0.3 m height at the beach: (a) mountain ridge (photo R. Gudehus), (b) cliff (photo M. Poblete)

- the solid partial stress, spatially distributed in fractal force chains via contact flats of grains or rock fragments, is no force density in Cauchy's sense;
- rearrangements of the solid fabric are no deformations as displacements are not differentiable, and as there are no unique reference configurations except for the vicinity of solids;
- capillary effects enable metastable fractal fabrics of grains and rock fragments;
- even in a stable range constitutive relations for solid and pore fluid in the usual sense cannot strictly hold true for lack of gradients and rates;
- fractal pore systems force an anomalous diffusion of masses, energies and momentum already in the stable range;
- at the verge of stability geomatter passes through phase transitions in wildly random chain reactions;
- there are no initial states and boundaries in a classical sense.

Nevertheless there are systematic features with the aid of which geotechnical engineers can and should reduce the risk of operations. This is outlined first for the stable range of grain fabrics where a mean-field theory suffices as long as fractal relics matter little (Sect. 2), then for sand deposits with shear bands or liquefaction (Sect. 3). The outline is continued for rock from samples to subduction zones where conventional concepts fail more often (Sect. 4). I turn then to random successions of critical phenomena and to the geomechanical risk (Sect. 5), thereafter my *desiderata* refer to cognition deficits and defects (Sect. 6).

2 Sand in the Stable Range

Fabrics of grains, called *granular solids* by physicists, exhibit fractally distributed stress fields with force chains as no two grains are equal. At equilibrium they have a specific elastic energy w_e, depending on invariants of the elastic strain ϵ^e_{ij} and the void ratio e, which is the potential of stress by $\sigma'_{ij} = \partial w_e / \partial \epsilon^e_{ij}$ [11]. Deforming a fabric causes buckling of force chains in a random succession, e.g. Fig. 2. Audible collapses occur practically synchronous with the drive, i.e. the response is rate-independent, and get more marked with an increasing stress ratio. Up to a critical point each one is accompanied by a minute rearrangement, then a noisy bulging indicates an avalanche-like succession of buckling force chains so that a new equilibrium is attained only after a big rearrangement.

The *micro-seismicity*, with frequencies from an audible part up to eigenvalues of grains, is incoherent in the stable range. It goes over into heat instead of being conserved as the interaction of grains is not conservative like the one of molecules. Coming in jerks due to an imposed deformation or load, it activates rearrangements with a relaxation of elastic energy. This is missed in discrete element simulations with an artificial viscosity, whereas physicists calculated seismic energies and fluctuating parts of elastic energies at equilibrium by means of event algorithms [16]. Thus the force-roughness means a latent seismicity [3] which is waked by deformations imposed to the grain fabric.

The dynamics of granular solids is determined by elastic and micro-seismic energies which go over into heat at dislocating grain contacts. In their 'granular

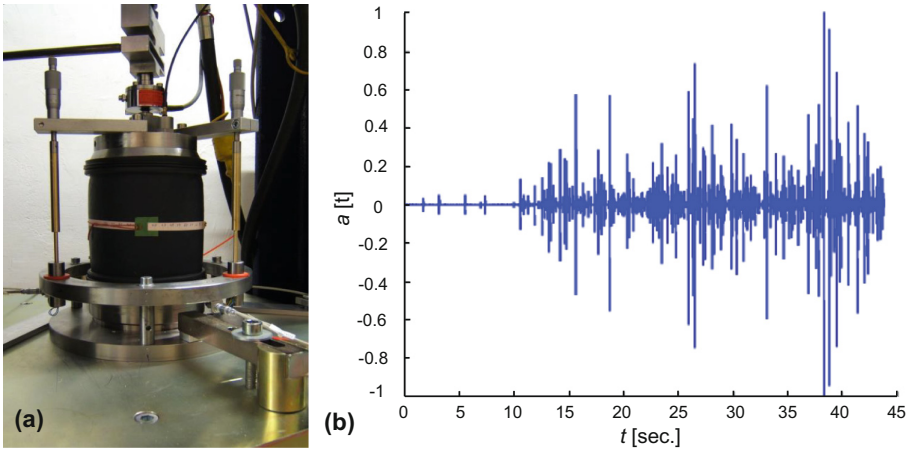

Fig. 2. (a) Rubber mould enclosing corundum grains under vacuum, (b) acoustic emission due to axial loading [10]

solid hydrodynamics' (GSH) [12] proposed a relaxation of elastic energy with a rate proportional to a granular temperature T_g by means of a factor λ, and obtained a hypoplastic relation for monotonous deformations. In a subsequent paper [6] we showed that deformations with cyclic portions cause a kind of plastic flow like in the high cycle accumulation (HCA) model by [27]. However, the differential response at reversals is always elastic as the half-life of T_g is far shorter than the pause of deformation during a reversal. Thus GSH underestimates hysteretic and cumulative effects in general, and numerical simulations with it are intricate.

I propose instead evolution equations with a hidden state variable χ named *eutaraxy* ($\varepsilon\upsilon$ = favouring, $\tau\acute{\alpha}\rho\alpha\xi\iota\varsigma$ = disturbance) [5]. Therein $T_g\lambda$ of GSH is replaced by $\chi d\varepsilon/dt$, with an amount of stretching ε, for the relaxation of ε^e_{ij} so that its evolution is rate-independent. The evolution equation of χ has a term for driving and a second one for halting, both proportional to $d\varepsilon/dt$, with a switch function depending on the sign of $d^2\varepsilon/dt^2$. Thus χ can reach a hypoplastic limit for monotonous deformations and can approach zero for non-monotonous ones with small amplitude. Rates of fabric stress are related with the ones of ε^e_{ij} by an elastic energy w_e and a transfer factor α almost like in GSH, but w_e has a critical point at e_{max} instead of e_{min} and α depends on χ instead of T_g.

This constitutive model, named GSD-EH for brevity, captures the observed sand behavior in the stable range up to its verge with few parameters which can be determined with triaxial tests - but why and how far? The micro-seismicity - observable as crackling noise - arises in fact alongside with an imposed deformation and does not depend on σ'_{ij} and e. It activates intergranular dislocations which are aligned by ε^e_{ij}, i.e. by σ'_{ij} via w_e and α, and with a rate in proportion to the one of strain and to the propensity for micro-seismicity, i.e. to $\chi d\varepsilon/dt$. The transfer factor α is the same for motions and forces, like in a bicycle with

a belt instead of a chain connecting discs instead of toothed wheels. Due to an erratic stick-slip the drive is transferred with a loss factor $0 \leq \alpha < 1$ both kinematically and statically. With driving χ grows up to a saturation value in the hypoplastic range so that it gets constant. An isochoric continuation leads to a critical state with a mean effective pressure $p'(e)$, but no more for $e \to e_{max}$ as then a granular solid collapses into a granular fluid.

Halting of an imposed deformation means a reduction of χ due to its relaxation by the dwindling $\chi d\varepsilon/dt$. The simultaneous reduction of the transfer factor α and the elastic pressure $p^e = \frac{1}{3}\partial w_e/\partial \varepsilon_v^e$ keeps the fabric pressure $p' = (1-\alpha)p^e$ constant, this leads to $\alpha \propto \chi$. $\chi \to 0$ requires a halting deformation which is hardly achieved after a hypoplastic state. However, repeated reversals with a small amplitude lead to χ near zero so that the response gets nearly elastic, except a cumulative part like in the HCA model of [27]. Cyclic attractors - i.e. asymptotic state cycles [3] - are also captured, particularly butterfly-like ones for isochoric cyclic deformations and lenticular ones for isochoric ratchetting.

GSD-EH works at best up to the verge of convexity of w_e as then critical phenomena arise (Sect. 3), but no more with *relics of critical phenomena*. Those with shear bands mean fractal spatial fluctuations of the void ratio e, which are hardly ironed out by seismic actions ($\sigma\varepsilon\acute{\imath}\omega =$ to shake) via attractors in the large [3]. Therefore wave propagations in the stable range are accompanied by an energy diffusion [7] so that power spectra tend to $v^2 \propto f^{-2\alpha}$ with a fractal exponent α just below 1. Fractional derivatives employed in this theory are expected values of classical ones. If relics of critical phenomena are less ironed out the average χ is higher so that the subsequent response is less elastic. As initial χ-fields are unknown in general the eutaraxy in the large causes an inevitable fuzziness of predictions already in the stable range.

The pore system imposes its fractality to the *pore water* already at and near stable equilibria. As water and grain mineral are neutral with respect to changes of pore water pressure p_w the effective or solid partial pressure is $p' = p - p_w$ in case of full saturation. Thus water and solid are isochoric, and so is a grain fabric without drainage. At equilibrium the hydraulic energy height $h \equiv h_g + p_w/\gamma_w$, with geometrical height h_g and specific weight γ_w of water, is constant. Slow deviations are usually captured with Darcy's relation $v_{wi} = k_f \nabla_i h$ of seepage velocity with the hydraulic gradient. However, the thus presumed derivatives do not properly exist with a fractal pore system. Like with the wave propagation indicated above constitutive relation and mass balance of pore water should be written with fractional operators which represent expected values of classical ones in a fractal random set. Then solutions can represent an anomalous diffusion without inadequate notions like laminarity and tortuosity.

The fractality of granular pore systems matters more with *capillary effects*. In case of multiply-connected pore gas Bishop's heuristic relation for p' can still be proven with equilibrium thermodynamics [13], and the authors capture now also the capillary hysteresis. Like with full saturation the transport of pore water and gas could be modelled with fractional derivatives. If pore gas is enclosed its spatial distribution - known as fingering and gas islands - gets less regular so that fractal

random sets require fractional images already at equilibrium. Capillary bridges enable grain fabrics with aggregates and macropores which are metastable for $e > e_{max}$ as they collapse into a suspension after flooding (Sect. 3).

Robust geotechnical systems enable *indifferent limit equilibria*, i.e. dissipative transitions to infinitesimally neighbored configurations with the same overall potential energy. Apart from geometrical effects as with toppling or pull-out, then limit equilibria with a realistic set of mechanisms and with ductile shear resistances τ_f are not only necessary, but also sufficient for overall stability [8]. For undrained loose water-saturated sand τ_f is at least the one determined by GSD-EH from critical states with $(e_{max} - e)/(e_{max} - e_{min})$ and φ_c. Drained sand has at least $\tau_f = \sigma' \tan \varphi_c$, but fabric pressures σ' can be estimated at best for slopes and retaining structures. There are no indifferent limit equilibria for piles, tunnel roofs and similarly confined configurations as pressure fields are far from statically determinate. The bound theorems of ideal plasticity fail also in case of shaking with insufficient drainage, e.g. during earthquakes or offshore.

3 Critical Phenomena with Sand

At the local verge of stability of a grain fabric its elastic energy is at a *saddle point* with respect to ε^e_{ij}. This is a necessary condition for the loss of equilibrium, which is evident with two invariants of ε^e_{ij}, e.g. Fig. 3. Like with a sphere on the wrist of your hand there are two opposite directions with a maximal release of kinetic energy; a collapse occurs with one of them if there is no constraint. An isobarically driven grain fabric dilates then in shear bands, thus polar quantities arise with σ'_{ij}-alignment. Quasi-static simulations with hypoplastic relations, including polar degrees of freedom, yield shear band patterns which come astonishingly close to observed ones [3]. The simulated extension of a dense sand layer yields a fractally hatched shear band pattern and a warped surface, e.g. Fig. 4.

This quasi-static simulation could not be continued beyond the second configuration as the equations got ill-posed. This would also happen with a polar extension of GSD-EH, whereas fictitious viscous terms would constitute a non-physical regularization. Inertial effects should be taken into account, but as yet

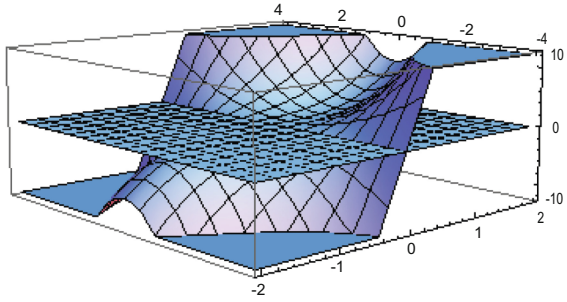

Fig. 3. Blow-up of the elastic energy versus first and second invariants of the elastic energy at a critical point with a tangential plane

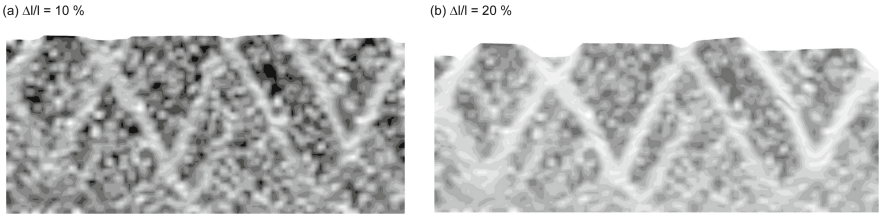

Fig. 4. Simulated quasi-static extension of an initially 10 cm long sand strip with ca. 1 mm grain size and polar quantities. State at the right boundary as at the left one with reflected orientation, configurations after 10% (left) and 20% extension (right), black zones dense, white bands dilated [28]

nobody did that. Fortunately there is an evidence of kinetic effects in model tests. Darwin [1] - second son of Charles Darwin, astronomer and mathematician - checked earth pressure theories by means of a box filled with dry flint powder (Fig. 5). Releasing a wall with hinges by a string he measured the resulting force with a spring balance up to a critical point. This was indicated by a 'hissing noise' and a sudden 'settling' after a slow 'unsettling' during the release. He asked Clerk Maxwell for advice, who stated that 'a *historical element* would enter largely into the nature of the limiting equilibrium of sand', and concluded that this would 'essentially elude mathematical treatment'.

Darwin demonstrated that this 'capricious' behaviour refuted the earth pressure theories of Rankine and Boussinesq. His 'unsettling' was rediscovered by Reynolds as dilatancy, while his conclusions were ignored until present. His hissing noise indicates a coherent seismicity with frequencies of at least ca. $c_s/d \approx 1000/\mathrm{s}$ with $c_s \approx 100\,\mathrm{m/s}$ and $d \approx 0.1\,\mathrm{m}$. This arose in a contractant *chain reaction* within a Coulomb-like shear zone, where the sand got close to critical points with equal stress alignment by the release of the wall. Like with dominoes on a table with equal alignment and suitable distances pressure waves produced a positive feedback towards critical points. This occurred up to a surroundings with less uniform alignment and lower stress ratio. Thus limit stress states arose one after another, not simultaneously in a region as often assumed since Rankine's times.

Model tests with dry sand in a box are irreplaceable for understanding *tectonic deformations* [23]. For sand these are localized in shear bands with stress alignment via a Mohr-Coulomb condition, and they occur similarly with faults in the lithosphere. Initial and boundary conditions in sand-box tests are debatable as the lithosphere has no onset and no walls with imposed displacements. Thus the extension of a sand layer, e.g., can produce lithosphere-like fractal patterns [37], but with lateral artefacts for lack of antimetric boundaries like in Fig. 4. Model tests with periodic boundary conditions are more adequate and yield likewise spatial fractality [31]. One could track contractant chain reactions like those in Darwin's experiments by successive location of seismic sources in a sand-box, though with an inevitable haziness because of energy diffusion [7].

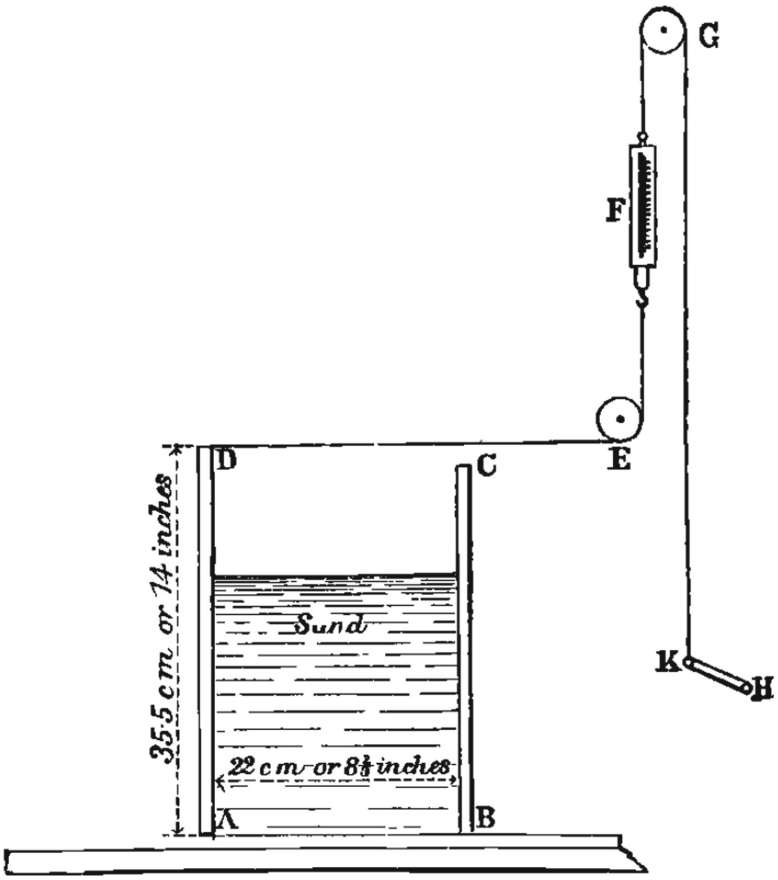

Fig. 5. Model test setup by Darwin [1]

Such investigations could clarify the interplay of slow and fast tectonic processes, and could foster calculation models of seismogeneous chain reactions.

Loose flooded sand deposits demonstrate that seismogeneous chain reactions are also enhanced by the *diffusion of pore water* [4]. Gas-filled macropores enable metastable grain fabrics with an average void ratio $\bar{e} > e_{max}$ which collapse into a suspension after minute disturbances. A collapse front spreads laterally by P-waves up to more than 100 m width so that surface waves arise which are registered up to 100 km away. As the pore pressure p_w attains the total pressure p in the liquefied zone p_w rises in the vicinity by the combination of seepage and compression of enclosed gas, i.e. a kind of diffusion. Thus a next collapse front arises with a progression of ca. 10 m/s, and further ones as far as the deposit is metastable. Combined with a humid cover this led to avalanches with en-échelon offsets (e.g. Fig. 6) with released energies up to ca. 10^9 kNm.

Fig. 6. Loose partly flooded sand deposit from lignite mining after flow slides (courtesy LMBV)

Similar technogeneous avalanches occurred in building and mining sites with released energies from about 10^4 kNm to 10^{10} kNm. Collapses of flooded sand into excavations or tunnels release smaller energies, but can also cause considerable damages. Their 'capricious' dynamics eludes again as yet mathematical treatment. Bigger avalanches of flooded granular solids with gas inclusions occurred naturally. The one triggered at the volcano Huascaran (Peru) 1962 erased a town with 20.000 inhabitants and released about 10^{14} kNm. Another one triggered at the Norwegian continental shelf about 8000 years ago (Storegga) released ca. 10^{16} kNm and produced a tsunami.

4 Critical Phenomena with Rock

For employing the similarity of sand and rock indicated with Fig. 1, I begin with triaxial test results by [18]. Critical points of a cemented grain fabric were attained by axial shortening or lengthening plus increase of pore water pressure p_w. If the effective radial pressure σ'_3 was higher than the tensile strength c' a *shear band pattern* arose at a Mohr-Coulomb limit, Fig. 7 above. It resembles the ones in triaxial tests with sand, and also the simulated one in Fig. 4. The few minutes required for getting a uniform p_w suit to the estimated time needed for a diffusion of pore water [3], and the permeability decreased due to the comminution in shear bands. The confined chain reaction could be tracked by locating seismic sources, also in a series of such experiments, this could help develop mathematical models for such critical phenomena.

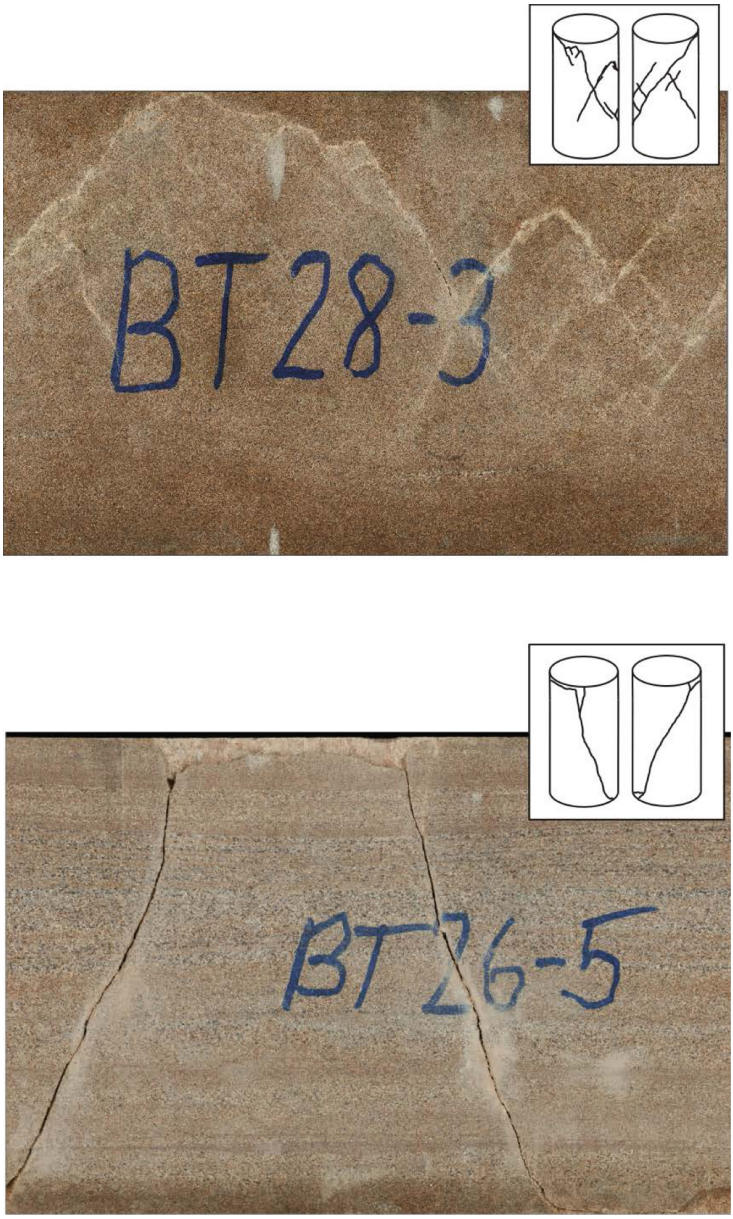

Fig. 7. Shear bands (above) and cracks (below) of water-saturated sandstone samples after triaxial tests with high or low effective radial pressure, respectively (winding-up photographs by Lempp et al. [18])

Critical points with $\sigma_3' < c'$ led to opening cracks, e.g. Fig. 7 below, and thus to a dramatic increase of the overall permeability. This kind of *splitting or discing* by axial shortening or extension, respectively, resembles a Griffith [2] fracture, but eludes as yet mathematical treatment because of its wild randomness. The permeability with cracks is not Darcy-like as temporal and spatial derivatives do not exist, but could be calculated for the linear hydraulic range with a given pore system and boundary conditions. The evolution of crack systems is a more difficult task as the equations for the solid degenerate at critical points, and as random sets of such events should be constructed. Such an approach could help understand rock collapses *in situ* at so low depths that cracks get wider.

Features like in Fig. 7 could also be obtained with humid sand samples at low pressures. Then condensate bridges are no more solid and brittle, but liquid and determined by the vapor pressure so that they dwindle by dilation. The potential energy has an elastic and a capillary part, and at critical points localized state variables come into play. Seismogeneous chain reactions prograde by P-waves and by diffusion of pore water, the latter also via vapor in case of humid geomatter. Like with Darwin's conclusions the loss of stability cannot be captured by conventional limit equilibria because the historical element eludes as yet mathematical treatment. A localized dilation can go over into a crack if the potential energy is at a saddle point like in Griffith's [2] theory, but with spatial and temporal fractality.

The striking similarity of small humid sand structures, e.g. those in Fig. 1, with *rock slopes and mountains* can be explained and employed without calculations. Parts of a steep slope or a cliff collapse suddenly after weathering up to a critical point. Limit equilibria - as conventionally proposed with humid sand and water-filled cracks - may be snapshots, but are insufficient for the judgment of stability [8]. Simulations with finite elements are even more misleading if localizations including capillarity and chain reactions with seismic and hydraulic feedback are not taken into account. This holds also true with erosion and avalanches. A seismo-hydraulic monitoring could serve as early warning if collapse mechanisms are understood with the aid of model and field tests, which could lead to realistic calculation models including the ever-present fractality.

This argument can also be applied to *cavities*. The caving in of boreholes is usually investigated by means of numerical simulations with radial symmetry, but thus the wild randomness of chain reactions with an ever-present fractality is missed. Further damage can arise with erosion along boreholes if this leads to eruptions of mud, gas and/or oil. Natural eruptions from gas inclusions with excess pressure and collapses of sinkholes elude likewise mathematical treatment. The same holds true for excavated cavities, particularly with tunnelling. Limit states are not sufficient for the proof of stability because the shearing resistance is not perfectly plastic as needed for the bound theorems. Presently employed quasi-static finite element simulations require stability so that this cannot be proven with them. Temporal extrapolations of measured displacements and forces are futile as the required differentiability gets lost with the fractality

of critical phenomena. Again a seismo-hydraulic monitoring could serve instead for early warning if the mechanisms are properly understood.

The fractality matters also for the identification of *seismic sources*. In classical models point sources are conceived as momentum tensors with assumed spatio-temporal distribution for getting far-field spectra, and this procedure is tentatively inverted [19]. The classical Green function for a point source can represent speeds and polarizations of wave crests so that the ray approximation is legitimate for far-fields in spite of the energy diffusion due to an inherent fractality in the stable elastic range [7]. Thus momentum tensor inversions can convey at best a diffuse image of propagating dislocations. As outlined further above seismogeneous chain reactions differ from evolutions of regular cracks, and usual stick-slip models are tribologically contestable [9,29].

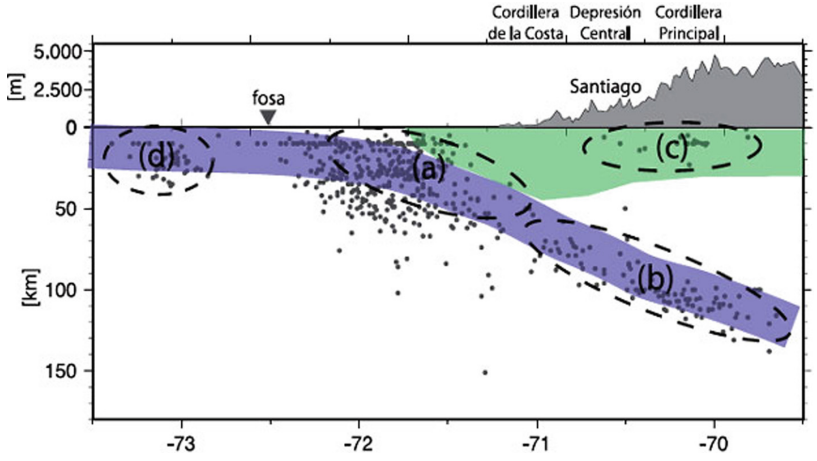

Fig. 8. Cross section of Chile with seismic sources [17]

A possible way out of this conceptual blockade is the transfer of findings with sand to the lithosphere, in particular to *subduction zones*. The biggest one exists under Chile, shown e.g. with a cross section near its capital in Fig. 8. The dots representing seismic sources accumulate in a rather fractal manner in three regions. The Nazca plate (d) dips with a trench (fosa) and hits the continental plate in a thrust zone (a). This may be considered as a passive Coulomb zone with a continued drive. Differently from Darwin's [1] experiments chain reactions - with positive feedback by seismic waves and pore water diffusion - arise repeatedly. The continued shearing of the oceanic plate past the continental one is no more sand-like at bigger depths (b) due to a kind of melting. There mineralogical phase transitions occur in shear bands without pores, but again in a 'capricious' succession of critical points. The horizontally compressed plate under the mountain ridge reaches critical points preferably under its rim (c) due to spreading forces.

5 Successions of Critical Phenomena and Geomechanical Risk

Figure 9 depicts numbers N of earthquakes for the cross section of Fig. 8 which exceed a certain magnitude M. The regression lines confirm the *Gutenberg-Richter relation* with a negative slope or b-value near 1. M is defined as the logarithm of the energy E released in a seismic episode, expressed in energy units. I leave aside the determination of E and M, presuming that disputable details matter little for the sequel. One can represent the straight lines by

$$N = N_r(E/E_r)^{-b}; E_r \leq E \leq E_m \tag{1}$$

with a reference number N_r, a lower cutoff E_r serving also as a reference value, and an upper cutoff E_m. Normalizing N by N_r leads to the cumulative probability

$$P_{\geq E} = (E/E_r)^{-b}; E_r \leq E \leq E_m \tag{2}$$

that an earthquake releases at least the energy E if it happens in a region where E ranges from E_r to E_m. So why does (2) hold, and why with $b \approx 1$?

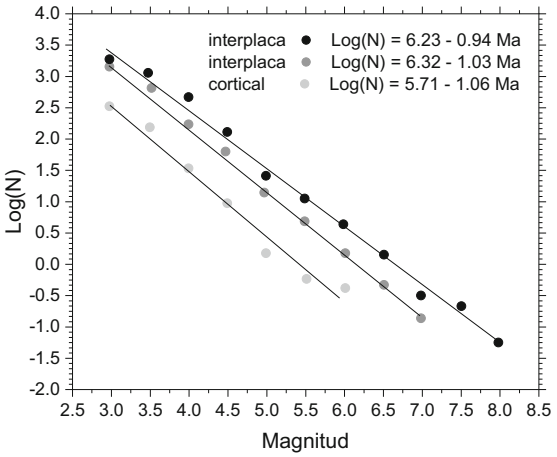

Fig. 9. Seismicity of central Chile [17]: logarithm of number of earthquakes with magnitude M or more. Upper line interplate (thrust), middle one intraplate (subductive shear), lower one crustal (under mountains)

We consider random successions of seismic episodes with released energy E as *stable Lévy processes* [9]. E comes in jumps versus time t as the duration of an episode is far smaller than its recurrence time. Subsequent jumps have variable sizes with a wildly random [21] distribution which changes with time. This property is called 'infinite divisibility', and if the probability distribution is not changed by superimposing distributions of different observation times it is

called 'stable'. Then the cumulative probability $P(\xi, \tau)$ of events with $\xi \equiv E/E_r$ or more at a dimensionless time $\tau \equiv t/t_r$ satisfies the relations

$$P(\xi, a\tau) = P(a^{1/\gamma}\xi, \tau) \tag{3}$$

and

$$P \propto \tau\xi^{-\gamma} \text{ for } \xi/\tau^{1/\gamma} > 1. \tag{4}$$

The wild randomness means that $P(\xi, \tau)$ does not depend on the one of any previous time, which is seemingly at variance with the historical element of seismogeneous chain reactions. However, any subsequent chain reaction occurs in another site than the preceding one as this led to a stabilization so that a continued magma drive leads first other sites close to critical points. This occurs in such a way that the correlation of successive chain reactions arising at different sites gets lost.

If the lithosphere response to the magma drive is *rate-independent* (cf. Fig. 2) P is not changed if either the energy threshold E or the registration time t changes by a certain factor. This means $\gamma = 1$ by (3) and (4), then the stable cumulative Lévy distribution simplifies to the Cauchy distribution

$$P(\xi, \tau) = 1 - \frac{2}{\pi} \arctan(\xi/\tau). \tag{5}$$

Its log-log plot (Fig. 10) exhibits a kind of plateau due to $P \to 1$ for $\xi/\tau \to 0$, a bend near $\xi/\tau = 1$ and a straight line with a slope -1 right of it by (4). Expected value and variance related with (5) diverge, this cannot occur physically and is avoided with an upper cutoff, as assumed also in Fig. 10. A smooth cutoff function instead of an abrupt one widens the range of distributional stability and enables an objective scaling [32]. The convergence to a normal distribution for sums of truncated Lévy distributions is extremely slow [25].

The comparison of (2) and (4) supports a *stationary Gutenberg-Richter relation* with $b = 1$. An upper bound E_m of released energy is determined by the biggest possible chain reaction in a considered region. It could be estimated as $E_m \approx F_m u_m$ by means of the length and depth of a thrust zone with uniform alignment, leading to a Coulomb-like resisting force F_m, and the biggest possible sudden tectonic displacement u_m. This leads to $E \approx 10^{18}$ kNm like for the Valdivia event 1960 with $M = 9.6$, the biggest earthquake ever registered. Due to their long recurrence times such events are rarely observed and hardly representative in a statistical sense. An objective lower cutoff E_r could be related with the log-log bend of an observed distribution near $\xi/\tau = 1$ (cf. Fig. 10). It is inevitably hazy as the theoretical bend is smooth, which corresponds to indiscernible events of a background noise.

$b = 1$ is legitimate if the tectonic conditions are stationary and the lithosphere responds to them without delay, whereas thermally activated dislocations and changing tectonic conditions lead to an *instationary Gutenberg-Richter relation*. Stable Lévy distributions with γ above or below 1 can be approximated by series expansions [24]. With $\gamma \neq 1$ the cumulative probability can again be approximated by (2) due to (4), while it tends to 1 for $(E/E_r)/(t/t_r)^{1/\gamma} \to 0$.

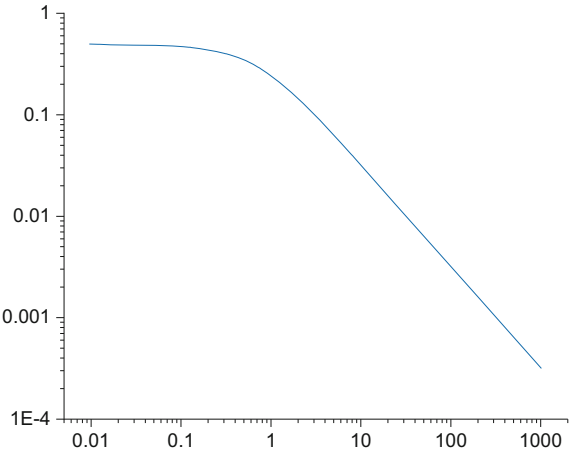

Fig. 10. Log-log plot of a stable cumulative Lévy distribution with $\gamma = 1$. Cumulative probability P versus ξ/τ, cutoffs for $\xi/\tau \to 0$ and $\xi/\tau \to \infty$

Thus the total of released energies beyond a certain E does not grow with the same factor as the registration time. The substitute distribution (2) requires therefore time-dependent bounds E_r and E_m, and the reference number N_r in (1) is no more proportional to the velocity of the magma drive and the registration time.

The Gutenberg-Richter relation with $b \approx 1$ is empirically well established so that it can be used for the validation of stable Lévy processes with γ around 1. Seismically less active regions are left aside as the events constitute a kind of noise which cannot as clearly be related with tectonic mechanisms as with subduction zones. There are *other successions of geomechanical chain reactions* which are seismogeneous and wildly random so that the theory of stable Lévy processes can be of use. Their size, given by the released and dissipated energy, ranges again from a rather diffuse lower cutoff to an upper one which is several orders of magnitudes bigger. This holds true also for collapses of and eruptions from natural cavities, slope collapses from rock falls to avalanches, rupture of retaining structures for excavations and slopes, toppling of high-rise buildings and offshore structures, and combinations of such cases.

A common feature of such mechanisms is an ever-present spatial and temporal fractality, and the impossibility to capture them with presently used computer models. For quantifying the related *geomechanical risk* R, i.e. the expected value of damage D, probabilities of such events and the exposition of men and objects to them is needed. In the simplest rational approach the probability density derived from (2) with $b = \gamma = 1$, and the ansatz $D = VE$ with a constant vulnerability V, leads to the expected value

$$R \equiv \bar{D} = V E_r \ln(E_m/E_r), \tag{6}$$

and with $E_m \gg E_r$ to the variation coefficient

$$V_D = V_E = \frac{\sqrt{E_m/E_r}}{\ln(E_m/E_r)}. \tag{7}$$

An insurance fee is obtained from R by adding an amount for administration and risk of the insurer. The latter is higher than with normal distributions as the law of big numbers works only for at least $n = V_D$ cases [25]. The need of keeping V low and of confining the worst case with $D = VE_m$ is trivial. Less evident is the control of the lower bound E_m so that, alongside with the expenses for reducing it and V, the overall expenses are minimal.

This scheme enables the construction of *fractal random sets* with a minimal number of scenarios. The episodic fractal exponent is $\gamma = 1$ if the geomechanical systems reacts to a drive - from excavation and erosion to tectonic shift - within a time which is several orders of magnitude shorter than the recurrence time. $\gamma > 1$ is adequate if thermally activated relaxation reduces the propensity for chain reactions, e.g. in zones of slow thrust, and the opposite holds true e.g. for excavations in ground with soft mineral. $\gamma < 1$ is also adequate in case of hydraulically activated softening or erosion, and if the damage increases by a delay of remedies.

Systematic estimates of $\gamma \neq 1$ are beyond the present reach, so one should first focus on the *cutoffs* for $\gamma = 1$. The lower one provides an objective scaling by (6) and works as a kind of background noise which can trigger chain reactions. The expected value of released energy $\bar{E} = E_r \ln(E_m/E_r)$ refers to cases where a trigger with E_r is imposed, while the number of events equals the one of such triggers. The vulnerability V depends on exposition, sheltering and monitoring with an erratic component which is but indirectly related with the complexity of geomatter. A paramount objective of geomechanics is the realistic estimation of upper cutoffs E_m or worst cases. As stated further above they cannot be captured by quasi-static computer models as these require stability for being feasible. It is indispensable to take into account inertial effects for modelling seismogeneous chain reactions. Numerical models could be checked and improved by means of sand-box tests with location of seismic sources.

The *eutaraxy in the large* is a bigger challenge. As outlined in Sect. 2 the eutaraxy which has been captured mathematically represents the force-roughness of grain fabrics in the stable range, i.e. the propensity for an incoherent microseismicity due to imposed deformations. This works heuristically as long as relics of former critical phenomena are sufficiently ironed out, but precisely speaking this is a contradiction in terms. Force-roughness means fractal spatial fluctuations so that classical intensive and extensive quantities are objectionable. The postulate of locality for simple materials [35] gets invalid with critical phenomena as then correlation lengths diverge. Thermodynamic critical phenomena yield already fractality, but seismogeneous chain reactions are more intricate as geomatter conserves traces of former critical phenomena as long as they are not swept out - this is Maxwell's historical element. For lack of ergodicity there is a *configurational entropy* which differs from the entropy by Boltzmann and Shannon as fluctuations are rather Lévy- than Gauss-like.

6 Conclusion

The objective of research is to reduce *cognition deficits*. This requires induction ($\varepsilon\pi\alpha\gamma\omega\gamma\acute{\eta}$) in Aristoteles' sense, i.e. hypotheses and logic with empirically limited validity. Popper [30] calls theories nets thrown out for catching parts of reality, emphasizes their refutability and proposes a probabilistic frame for random phenomena. Geomatter is a complex part of reality as it is less continuous than classical solids and fluids, and as its opaqueness impedes observations. In TA ΦYΣIKA Aristoteles mentions that a heap of fragments does not react to an action ($\varepsilon\nu\acute{\varepsilon}\rho\gamma\varepsilon\iota\alpha$) like continuous matter. Müller [26] calls natural rock a discontinuum and points to the self-similarity of crack patterns, Mandelbrot [20] stresses the fractality of earthquakes and the intricacy of Lévy's theory, Turcotte [36] doubts the 'self-organized critically' with cellular automata, Wu and Aki [38] and Shapiro [33] tried to relate wave scattering with the geometrical fractality of geomatter, Tarasov [34] proposed a fractional hydrodynamics for fissured rock. So I am standing on the shoulders of giants in Newton's sense, but their diversity is sometimes frustrating.

My list of contra-continuum arguments (Sect. 1) appears likewise frustrating - so what should and could be done? Maxwell's historical element is a commonplace in geosciences, but does it elude the mathematical treatment of limit equilibria for ever? Small deviations from stable equilibria of solid and pore water with fractality can be captured with the fractional calculus, but how do fractal pore systems evolve? And how to manage the risk even if cumulative probabilities can be captured with truncated power laws or stable Lévy distributions? Briefly speaking: how to cope with the ever-present fractality in geomechanics for research and practice?

One may speak of a new paradigma, but there is no easy answer. Before working out calculation models one should realize how the stability of geomechanical systems gets lost in chain reactions with fractality before, during and after them. Single events should be observed in boxes with sand - dry and water-saturated - and seismometers, and simulated numerically with seismic waves and pore water diffusion. Polar quantities and initial fluctuations should be taken into account. Systematic variations of initial and boundary conditions should reveal expected values and variances of chain reactions, and more generally a data set which is indispensable for developing fractional images of fractal random sets. The range between mild and wild randomness [20,21] is wide and yet hardly explored.

Capillary effects, fracture and erosion including fractality could also be clarified by means of sand-box tests. Kadanoff [14] doubted hydrodynamic theories for sand, Jiang and Liu [12] presented a promising one, I replace their 'hydro' by means of a 'eutaraxy'. Both models cannot yet capture critical phenomena with growing fractality, but extensions should be attempted alongside with sand-box tests. As long as there is no general energetics for fractal phenomena this procedure is inevitably heuristic, but what counts is always the strength of hypotheses. Model experiments with sand and structures can also help to understand the robustness of geotechnical systems, i.e. the ability of harmless redistributions in case of inevitable extreme actions. Model tests with sensitive

systems and location of prograding seismic sources could help to clarify not only tectonic evolutions, but also early warning systems for geotechnical operations.

An objective of psychology is to reveal *cognition defects*. Kahnemann [15] showed that human beings - including scientists and engineers - tend to see patterns even if there are none in reality, and are weak in estimating probabilities even of simple events. No wonder therefore that in geomechanics

- the illusion of limit stress fields and rigid sliding blocks survived until present;
- geotechnical systems with varying arrangement are confused with structures for which the degrees of freedom do not change;
- the probability of failure is considered as sufficiently low by means of safety factors although the then required robustness is not given in general;
- finite element simulations are used for the assessment of stability although the latter is needed for making the former feasible;
- observational methods are used for maintaining stability even if the employed extrapolation gets impossible due to the temporal fractality of stability losses;
- quasi-static finite and discrete element simulations are made with a fictitious viscous damping so that crucial seismic effects are excluded;
- cellular automata are employed for getting look-alikes instead of realistic images of successive events;
- after disasters mysterious anomalies are invented instead of real mechanisms in order to avoid liability suits.

Instead of thus producing or accepting 'alternative realities' and 'fake news' one should go on with Aristoteles' induction by means of an open-minded discourse like in his peripatetic school.

Acknowledgements. I owe stimulations for the present paper particularly to Roberto Cudmani (Munich), Gerhard Huber (Karlsruhe), Demetrios Kolymbas (Innsbruck), Mario Liu (Tübingen), Andrzej Niemunis (Karlsruhe) and Asterios Touplikiotis (Karlsruhe).

References

1. Darwin, G.: On the horizontal thrust of a mass of sand. Proc. Inst. Civ. Eng. **LXXL**, 350–378 (1883)
2. Griffith, A.A.: The phenomena of rupture and flow in solids. Philos. Trans. R. Soc. Lond. Ser. A **221**, 163–198 (1921)
3. Gudehus, G.: Physical Soil Mechanics. Springer, Berlin (2011)
4. Gudehus, G.: Mechanisms of partly flooded loose sand deposits. Acta Geotech. **11**, 505–517 (2016)
5. Gudehus, G.: Granular solid dynamics with eutararaxy and hysteresis. Acta Geotechnica (2018, submitted)
6. Gudehus, G., Jiang, Y., Liu, M.: Seismo- and thermodynamics of granular solids. Granul. Matter **13**, 319–340 (2010)
7. Gudehus, G., Touplikiotis, A.: Wave propagation with energy diffusion in a fractal solid and its fractional image. Soil Dyn. Earthq. Eng. **89**, 38–48 (2016)

8. Gudehus, G., Touplikiotis, A.: On the stability of geotechnical systems and its fractal progressive loss. Acta Geotech. **13**, 317–328 (2017). https://doi.org/10.1007/s11440-017-0549-x
9. Gudehus, G., Touplikiotis, A.: Seismogeneous chain reactions and random successions of them. Soil Dyn. Earthq. Eng. (2018)
10. Huber, G., Wienbroer, H.: Vibro-viscosoity and granular temperature of cylindrical grain skeletons: experiments. In: Powder and Grains, vol. 1, pp. 287–290 (2005)
11. Jiang, Y., Liu, M.: A brief review of "granular elasticity". Eur. Phys. J. E **22**, 255–260 (2007)
12. Jiang, Y., Liu, M.: Granular solid hydrodynamics. Granul. Matter **11**, 139–156 (2009)
13. Jiang, Y., Einav, V., Liu, M.: A thermodynamic treatment of partially saturated soils revealing the structure of effective stress. J. Mech. Phys. Solids **100**, 131–146 (2016)
14. Kadanoff, L.P.: Built upon sand: theoretical ideas inspired by the flow of granular materials. Rev. Mod. Phys. **71**(1), 435–444 (1999)
15. Kahnemann, D.: Thinking, Fast and Slow. Farrar Straus and Giroux, New York (2003)
16. Kondic, L., Behringer, L.P.: Elastic energy, fluctuations and energy for granular materials. Europhys. Lett. **67**(2), 205–211 (2004)
17. Leighton, F., Ruiz, S., Sepulveda, S.A.: Reevaluacion del peligro sismico probabilistico en Chile central. Andean Geol. **37**(2), 455–472 (2010)
18. Lempp, C., Menezes, F., Schöner, A.: Influence of pore fluid pressure on gradual mechanical weakening of permotriassic sandstones in multistep triaxial compression tests (2018, under preparation)
19. Madariaga, R.: Seismic source theory. Treatise Geophys. **4**, 59–82 (2007)
20. Mandelbrot, B.: The Fractal Geometry of Nature. Freeman, New York (1982)
21. Mandelbrot, B.: Multifractals and 1/f-Noise: Wild Self-affinity in Physics. Springer, New York (1999)
22. Mandelbrot, B., Taleb, N.: A focus on the expectations that prove the rule. Financial Times (2006)
23. Mandl, G.: Mechanics of Tectonic Faulting: Models and Basic Concepts. Elsevier, Amsterdam (1988)
24. Mantegna, R.N.: Fast, accurate algorithm for numerical simulation of Lévy stable stochastic processes. Phys. Rev. E **49**(5), 4677–4683 (1993)
25. Mantegna, R.N., Stanley, H.E.: Stochastic process with ultraslow convergence to a Gaussian: the truncated Lévy flight. Phys. Rev. Lett. **73**(22), 2946–2949 (1994)
26. Müller, L.: Der Felsbau 1. Enke, Stuttgart (1963)
27. Niemunis, A., Wichtmann, T., Triantafyllidis, T.: A high-cycle accumulation model for sand. Comput. Geotech. **32**, 245–263 (2005)
28. Nübel, K.: Experimental and numerical investigation of shear localization in granular material. Ph.D. thesis, Veröff. Inst. Bodenmech. u. Felsmech., Univ. Karlsruhe, Heft 159 (2002)
29. Persson, B.: Sliding Friction: Physical Principles and Applications. Springer, Heideberg (1998)
30. Popper, K.: Logik der Forschung. Springer, Wien (1935)
31. Revushenko, A.F.: Mechanics of Granular Media. Springer, Berlin (2006)
32. Schinckus, C.: How physicists made stable Lévy processes physically plausible. Braz. J. Phys. **43**, 281–293 (2013)
33. Shapiro, S.A.: Elastic waves scattering and radiation by fractal inhomogeneity of a medium. Geophys. J. Int. **110**, 591–600 (1992)

34. Tarasov, V.E.: Fractional hydrodynamic equations for fractal media. Ann. Phys. **318**, 286–307 (2005)
35. Truesdell, C., Noll, W.: The Non-Linear Field Theories of Mechanics. Encyclopedia of Physics, III/c. Springer, Berlin (1965)
36. Turcotte, D.L.: Self-organized criticality: does it have anything to do with criticality and is it useful? Nonlinear Process. Geophys. **8**, 193–196 (2001)
37. Wolf, H., Koenig, D., Triantafyllidis, T.: Examination of shear band formation in granular material. J. Struct. Geol. **25**, 1229–1240 (2003)
38. Wu, R.-S., Aki, K.: The fractal nature of the inhomogeneities in the lithosphere evidenced from seismic wave scattering. Pageophys **123**, 805–819 (1985)

Hypoplastic Prediction of Path-Dependent Failure in True Triaxial Tests of Granular Soils

Wenxiong Huang(✉)

Hohai University, Nanjing 210098, China
wh670@hhu.edu.cn

Abstract. Prediction of failure in soil tests is considered based on hypoplastic modelling of soil behavior and bifurcation analysis. With a comprehensive hypoplastic model for granular soils, a bifurcation condition is formulated for general stress state. The possibility of localized failure in true triaxial tests is investigated by examining the bifurcation condition in element tests following different stress paths. Three situations depending on stress path, including no bifurcation, bifurcation in softening regime and bifurcation in hardening regime, are predicted. Concerning shear localization, the predicted failure surfaces differs significantly in shape from the implemented critical state surface.

Keywords: Granular soils · Hypoplasticity · Triaxial test · Failure · Bifurcation

1 Introduction

The granular soils are typical cohesionless frictional materials, whose strengths are usually characterized by a friction angle in term of the Mohr-Coulomb (M-C) failure criterion, or of a more sophisticated failure criterion such as the Matsuoka-Nakai (M-N) criterion which takes into account the influences of the intermediate principal stress. In triaxial tests of soils, two types of failure may be observed, namely, the uniform diffuse failure and the localized failure. In the former cases, soil sample maintains a uniform deformation in a test, reflected by a stress-strain curve with a smooth peak followed by a gradual strain-softening regime, leading to an asymptotic value. In the latter cases, a shear band develops in soil samples, resulting in a relative sharp peak on the stress-strain curves with a more pronounced softening rate.

In constitutive modeling of soil behavior, the critical friction angle is commonly regarded as a material property. By employing the critical friction angle as a strength parameter, the density-dependent peak strengths can be obtained as model predictions. Moreover, by implementing a pre-defined critical state surface (CSS) in the model, prediction of similarly-shaped failure surfaces is assumed. In doing so, the effect of shear localization is usually not considered.

The present work discusses the influence of shear localization on the predicted failure in hypoplastic modelling of granular soils on the basis of bifurcation analysis. Hypoplasticity is a framework for constitutive description of soil behavior developed in

W. Wu (Ed.): *Desiderata Geotechnica*, SSGG, pp. 60–66, 2019.
https://doi.org/10.1007/978-3-030-14987-1_6

Karlsruhe [1, 2]. A comprehensive hypoplastic model for sand-like granular soils formulated by Gudehus [3] and Bauer [4] is used for this discussion. This model can capture the main features of the density-dependent compressibility and the pressure- and density-dependent shear behavior of granular soils. In particular, the concept of the critical state is incorporated. Like many other elastoplastic models for soils, it is also calibrated against experimental data from basic soil tests, namely the oedometer test and the conventional triaxial test. In this paper, the condition for shear bifurcation formulated for the hypoplastic model following the approach by Rudnicki and Rice [5] is presented. The possibility of shear localization is determined by examining the bifurcation condition along various stress paths for true triaxial tests. Path-dependent failure of granular soils in laboratory tests is discussed in the light of prediction of shear bifurcation.

2 Description of the Constitutive Model

The hypoplastic model employed for this analysis is basically as described in [3, 4], which takes the following form:

$$\dot{\sigma}_{ij} = f_s(p,e)[L_{ijkl}\dot{\varepsilon}_{kl} + f_d(p,e)N_{ij}\sqrt{\dot{\varepsilon}_{kl} : \dot{\varepsilon}_{kl}}], \tag{1}$$

with $L_{ijkl} = \hat{a}^2\delta_{ik}\delta_{jl} + \hat{\sigma}_{ij}\hat{\sigma}_{kl}$ and $N_{ij} = \hat{a}(\hat{\sigma}_{ij} + \hat{s}_{ij})$. Here δ_{ij} is the Kronecker delta, $\hat{\sigma}_{ij} = \sigma_{ij}/\sigma_{mm}$ is the normalized stress and $\hat{s}_{ij} = \hat{\sigma}_{ij} - 1/3$ its deviator. The model performances are governed by the stiffness factor f_s and the density factor f_d, which depend on the mean stress p and the void ratio e. In particular, f_d is a power function of the relative void ratio

$$r_e = (e - e_d)/(e_c - e_d). \tag{2}$$

Here e_c and e_d represent, respectively, the pressure-dependent critical and densest void ratio. Factor f_s is basically determined based on consistence condition with the compression law and is amended considering density and deviatoric stress effects as described in [3]. The model contains 8 parameters, which can be determined from basic laboratory tests, as discussed in [4, 6].

For a monotonic shear test, the model predicts a critical state which is characterized by $e = e_c$ and stress satisfying the following critical state condition:

$$\psi_c(\sigma_{ij}) = \hat{s}_{ij}\hat{s}_{ij} - \hat{a}^2 = 0. \tag{3}$$

Equation (3) describes a cone-shaped critical state surface in the stress space. Predefined critical state surfaces may be implemented in the model by expressing $\hat{a}$ as a relevant function of an intermediate principal stress parameter [7]. In this work, this is done alternatively by using the stress transformation technique following Huang et al. [8], i.e., by replacing $\hat{\sigma}_{ij}$ in tensors L_{ijkl} and N_{ij} with the following transformed stress:

$$\hat{\sigma}_{ij}^{*} = [r_\theta \delta_{ik}\delta_{jl} - \frac{1}{3}(1 - r_\theta)\delta_{ij}\delta_{kl}]\hat{\sigma}_{kl}. \tag{4}$$

Here the transformation factor r_θ is a function of angle θ, which is determined with $\cos 3\theta = \sqrt{6}\,(\hat{\sigma}_{ij}\hat{\sigma}_{jk}\hat{\sigma}_{ki})/(\hat{\sigma}_{mn}\hat{\sigma}_{nm})$. For instances, a CSS defined by the M-N or the M-C failure criterion is implemented with the following respective representations for r_θ:

$$r_\theta = \frac{1 - \sqrt{3/2}\|\hat{\mathbf{s}}\|\cos(3\theta)}{1 - \frac{3}{2}\|\hat{\mathbf{s}}\|^2}\left(\sqrt{\frac{3}{8}\|\hat{\mathbf{s}}\|^2 + \frac{1 - \frac{3}{2}\|\hat{\mathbf{s}}\|^2}{1 - \sqrt{3/2}\|\hat{\mathbf{s}}\|\cos(3\theta)}} + \sqrt{\frac{3}{8}}\|\hat{\mathbf{s}}\|\right); \tag{5}$$

$$r_\theta = \sqrt{\frac{8}{3}}\frac{\sin(\theta + \pi/3)}{[\sqrt{2} + \sqrt{3}\|\hat{\mathbf{s}}\|\cos(\theta + \pi/3)] - \|\hat{\mathbf{s}}\|\sin(\theta + \pi/3)}. \tag{6}$$

3 Prediction of Stress Path-Dependent Failure

In this section, prediction of possible uniform diffuse failure or localized failure in true triaxial tests is discussed based on the bifurcation analysis with the above described constitutive model.

3.1 Condition for Shear Bifurcation

In modeling uniformly stressing or straining of soil samples in triaxial tests, a constitutive model may allow non-uniform deformation in the form planar weak discontinuity to enter the solution. For a well-developed constitutive model, such shear bifurcation marks the incipience of shear localization in soil samples in an ideal condition. As a weak discontinuity plane (shear plane) starts to appear, crossing it the velocity gradient exhibits a jump, which can be expressed by the normal vector of the plane n_i and a vector g_i characterizing the relative shear. Correspondingly, the strain rate also exhibits a jump which can be expressed by

$$[[\dot{\varepsilon}_{ij}]] = \frac{1}{2}(g_i n_j + n_i g_j). \tag{7}$$

By considering the equilibrium condition on the discontinuity plane together with the constitutive relation, an equation which should be satisfied by vector g_k is obtained:

$$Q_{ik}g_k = \lambda f_d B_i. \tag{8}$$

where $Q_{ik} = (1/2)(L_{ijkl} + L_{ijlk})n_j n_l$, $B_i = -N_{ij}n_j$, $\lambda = [[\sqrt{\dot{\varepsilon}_{mn}\dot{\varepsilon}_{mn}}]]$. Note that tensor Q_{ik} is positive definite and $\lambda = 0$ is equivalent to $g_k = 0$. Equation (9) is hence a nonlinear homogenous equation for vector g_k. Non-trivial solution exists in case the following condition is fulfilled [9]:

$$\psi_b(\sigma_{ij}, e, n_i) = \frac{f_d^2}{2}[Q_{ij}^{-1} B_j Q_{ik}^{-1} B_k + (Q_{ij}^{-1} n_i B_j)^2] - 1 \geq 0. \tag{9}$$

3.2 Condition for the Peak State

For automatic determination of the smooth peak point on the stress-strain curve in modelling a shear test, a mathematical representation describes the peak state is provided here. This is derived from the constitutive equation by setting:

$$\dot{\sigma}_{ij} = 0 \text{ for } \sqrt{\dot{\varepsilon}_{kl} : \dot{\varepsilon}_{kl}} \neq 0 \text{ with } f_d < 1$$

which leads to the following condition for identifying smooth peak states in shear tests:

$$\psi_p(\sigma_{ij}, e) = \frac{f_d^2}{\hat{a}^2}[\eta^2 \hat{\sigma}_{ij}^* \hat{\sigma}_{ij}^* + (2\eta - 1)\hat{s}_{ij}^* \hat{s}_{ij}^*] - 1 = 0, \tag{10}$$

with $\eta = (\hat{a}^2 - \hat{s}_{kl}^* \hat{s}_{kl}^*)/(\hat{a}^2 + \hat{\sigma}_{kl}^* \hat{\sigma}_{kl}^*)$.

3.3 Prediction of Stress Path-Dependent Bifurcation

The possibility of localized failure in triaxial tests is now investigated by checking the bifurcation condition through element tests along various stress paths starting with an initial state defined by $\sigma_{ij,0} = -p_0 \delta_{ij}$ and $e_0 = e_d + r_{e0}(e_c - e_d)$. That is, the constitutive equation is integrated along each stress path with condition (9) being checked at each increment step. Note that the maximum value of function ψ_b is searched with respect to the varying orientation vector n_i, and the bifurcation point is identified for $\psi_{b,\max} = 0$.

In Fig. 1, some results obtained from a plane strain biaxial compression test are presented. The model with the CSS defined by M-N criterion is used for testing. The stress-strain curve is obtained for $p_0 = 100$ kPa and $r_{e0} = 0.4$. The values of function ψ_b are computed at three marked points and presented against β, the angle between the normal of the searched plane and the maximum compressive stress, which illustrates the dependence of ψ_b on the orientation of the potential discontinuity plane. Point B is on the stress-strain curve is identified as the (earliest) bifurcation point, as $\psi_{b,\max} = 0$ is obtained at this point for some particular values of angle β. The orientation of the discontinuity plane is indicated by β values at which $\psi_{b,\max}$ is achieved.

Figure 2 presents the main results obtained from tests along different stress paths for true triaxial test. The peak and bifurcation points are presented in Fig. 2(a) in terms of the mobilized friction angle ϕ_m against stress path parameter $b = (\hat{\sigma}_2 - \hat{\sigma}_3)/(\hat{\sigma}_1 - \hat{\sigma}_3)$. Three situations can be noted. For tests along stress paths with zero or small values of b or θ, no bifurcation point is obtained. Next to this range there is a narrow band for b (θ), along the stress paths bifurcation points are obtained in the soften regime after a peak. For a larger range with greater b (θ) value, bifurcation points are obtained in the hardening regime before peak. These results agree in general with the experimental observations by Wang and Lade [10] and Sun et al. [11]. These three different situations are further illustrated in Fig. 3, where three stress-strain curves obtained for tests along

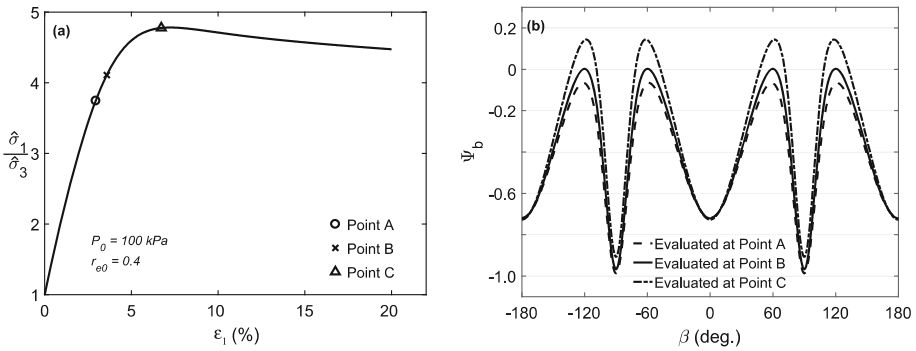

Fig. 1. Shear bifurcation in a biaxial compression test: (a) stress-strain curve and (b) function ψ_b calculated at three marked points (right).

stress paths with $\theta = 0°, 14°$ and $30°$ respectively are presented with variation of corresponding $\Psi_{b,\max}$ against the maximum strain. It can be seen that in the test for stress path $\theta = 0°$, the value of $\Psi_{b,\max}$ never reaches zero, while in other two tests, $\Psi_{b,\max}$ hits zero value in the softening and the hardening regime, respectively.

The normal of the predicted shear plane is found to be always perpendicular to the intermediate principal stress. The shear plane inclination, characterized by β, the angle between the normal of the shear plane and the maximum compressive stress, varies with the stress path parameter b as shown in Fig. 2(b). Influence of soil density is reflected by three curves obtained for different initial relative void ratio.

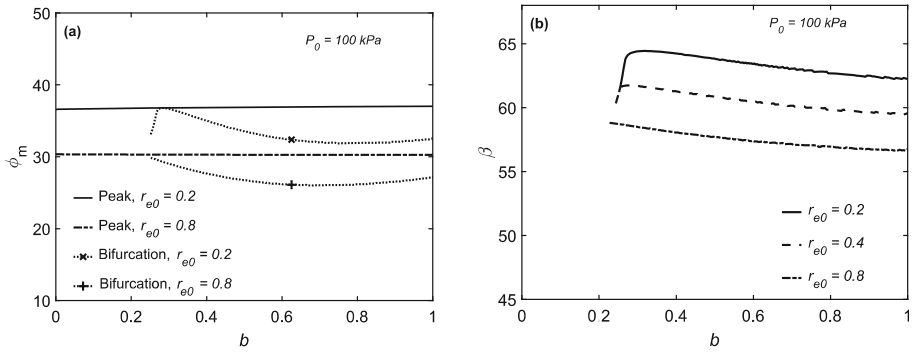

Fig. 2. (a) Path-dependent peak and bifurcation points for true triaxial tests and (b) inclination of the discontinuity for bifurcation.

Tests are also performed for the same hypoplastic model with a different CSS defined by the M-C criterion. The predicted peak points and bifurcation points for different stress paths are presented in Fig. 4 as loci in the deviatoric stress plane, and compared with the results for the model with CSS defined by M-N criterion. Though different in shape, the bifurcation loci in relation to the peak loci for two cases are quite similar. This highlights that bifurcation is basically a model property.

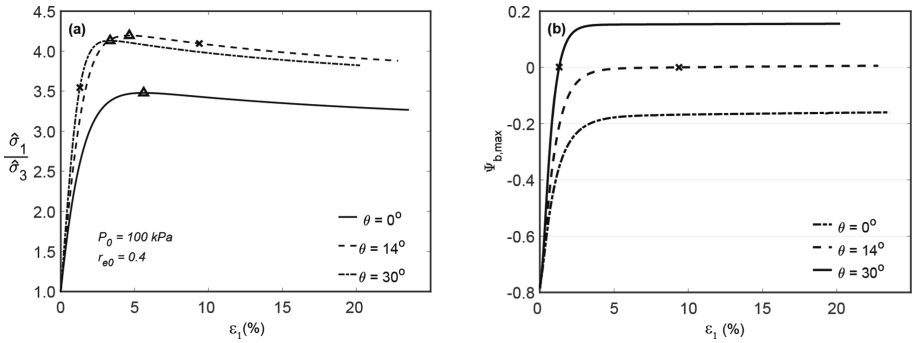

Fig. 3. Illustration of three situations in shear tests: (a) three stress-strain curves with peak and bifurcation points marked; (b) variation of $\psi_{b,\max}$ in three tests.

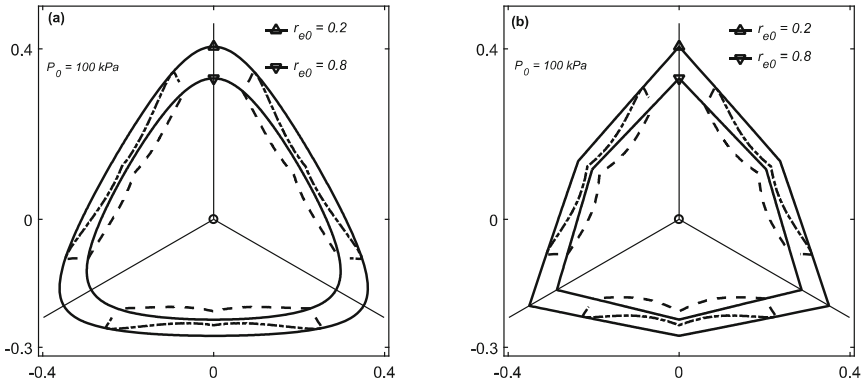

Fig. 4. Predicted peak and the bifurcation loci on the deviatoric stress plane by the model with the CSS defined (a) by the M-N criterion and (b) by the M-C criterion.

4 Concluding Remarks

For hypoplastic description of granular soils, the possibility of localized failure in true triaxial tests has investigated based on a bifurcation condition, which is formulated for general stress condition. Three situations are predicted in element tests following different stress paths: bifurcation does not occur, occurs in the softening regime after peak or occurs in the hardening regime, depending on stress path. For conventional triaxial test or the stress paths close to that, uniform diffused failure is predicted. For stress paths with relative greater value of θ or b, including triaxial extension, localized failure is the prediction. Thus, with the present hypoplastic model, the predicted failure surface differs significantly in shape from the CSS. Then how to predict a targeted failure surface in a model may need a further consideration.

It should be noted that the model prediction of bifurcation refers to tests of soils in ideal conditions. Laboratory test results may be affected by many factors. In general, due to the inevitable heterogeneity of soil samples, shear localization may be more prone to occur. Should shear bifurcation occur in a laboratory test, interpretation of the test result is no longer straightforward. Neither can the result be used for model calibration. Fortunately, the conventional triaxial test is the most stable one among all tests considered in this work and the uniform diffuse failure is achievable in such tests, which is meaningful for model development. However, in a wide range of true triaxial tests, localization failure may not be avoidable. Cautiousness is also needed in application of the experimental data from those tests.

References

1. Kolymbas, D.: Introduction to Hypoplasticity. A.A. Bolkema, Rotterdam (2000)
2. Wu, W., Kolymbas, D.: Hypoplasticity then and now. In: Kolymbas, D. (ed.) Constitutive Modelling of Granular Materials, pp. 57–105. Springer, Berlin (2000)
3. Gudehus, G.: A comprehensive constitutive equation for granular materials. Soils Found. **36** (1), 1–12 (1996)
4. Bauer, E.: Calibration of a comprehensive hypoplastic model for granular materials. Soils Found. **36**(1), 13–26 (1996)
5. Rudnicki, J.W., Rice, J.R.: Conditions for the localization of deformation in pressure-sensitive dilatant materials. J. Mech. Phys. Solids **23**(6), 371–394 (1975)
6. Herle, I., Gudehus, G.: Determination of parameters of a hypoplastic constitutive model from properties of grain assemblies. Mech. Cohesive-Fric. Mater. **4**(5), 461–486 (1999)
7. Bauer, E.: Conditions for embedding Casagrade's critical state into hypoplasticity. Mech. Cohesives-Frict. Mater. **5**(2), 125–148 (2000)
8. Huang, W., Sloan, S.W., Fityus, S.G.: Incorporating a predefined limit condition in a hypoplastic model by means of stress transformation. Mech. Mater. **40**(10), 796–802 (2008)
9. Huang, W., Hjiaj, M., Sloan, S.W.: Bifurcation analysis for shear localization in non-polar and micro-polar hypoplastic continua. J. Eng. Math. **52**, 167–184 (2005)
10. Wang, Q., Lade, P.V.: Shear banding in true triaxial tests and its effect on failure in sand. J. Eng. Mech. ASCE **127**(8), 754–761 (2001)
11. Sun, D., Huang, W., Yao, Y.: An experimental study of failure and softening in sand under three-dimensional stress condition. Granular Matter **10**(3), 187–195 (2008)

Discrete Element Models of Soil-Geogrid Interaction

Alina Irsainova[1], Marcos Arroyo[2], and Jong-Ryeol Kim[1(✉)]

[1] Nazarbayev University, Astana 010000, Kazakhstan
jong.kim@nu.edu.kz
[2] Universitat Politècnica de Catalunya, 08034 Barcelona, Spain

Abstract. Geogrids are the geosynthetics of choice for soil reinforcement applications. To evaluate the efficiency of geogrid reinforcement, several methods are used including field tests, laboratory tests and numerical modeling. Field studies consume long period of time and conducting these investigations may become highly expensive because of the need for real-size structures. Laboratory studies present also significant difficulties: large-size testing machines are required to accommodate realistic geogrid designs. The discrete element method (DEM) may be used as a complementary tool to extend physical testing databases at lower cost. Discrete element models do not require complex constitutive formulations and may be fed with particle scale data (size, strength, shape) thus reducing the number of free calibration parameters. Discrete element models also are well suited to problems in which large displacements are present, such as geogrid pullout. This paper reviews the different approaches followed to model soil-geogrid interaction in DEM and presents preliminary results from pull-out conditions.

Keywords: Discrete element method (DEM) · Soil reinforcement · Geogrids

1 Introduction

1.1 Geogrids

Geosynthetics are synthetically manufactured products used with soil, rock, and earth so overcome civil engineering problems. Geosynthetics can be used in a wide spectrum of fields such as transportation, geotechnical, environmental, hydraulics, and private development [1].

Geogrids are one of the types of geosynthetics that are quickly growing in usage. Its structure consists of plastic ribs forming big apertures. Due to its open-like structure, it can be used for reinforcement and stabilization. Transverse and longitudinal ribs of the geogrids are manufactured from high-modulus polymers; therefore, the strength of geogrid ribs is higher than the strength of geotextiles. Transverse members of the geogrids serve as an abutment or anchor due to their location parallel to the face of structure. Therefore, the main function of longitudinal ribs is to keep the transverse ribs in position [2]. The opening size of geogrids is sufficient enough to allow soil contact and interlocking between particles. Geogrid reinforcement provides higher shear strength of soil mass and higher load bearing capacity. Geogrids are also helpful in

W. Wu (Ed.): *Desiderata Geotechnica*, SSGG, pp. 67–74, 2019.
https://doi.org/10.1007/978-3-030-14987-1_7

preventing soil erosion. Moreover, use of geogrids in construction reflects other advantages such as ease of construction, high durability, resistance to environmental issues, availability of the material, and low cost [3].

1.2 Geogrid Modeling Methods

Modeling of geogrids can be categorized as soil-inclusion problems. Applying finite element method (FEM) for such case is widely practiced [4, 5]. However, using FEM to model soil-inclusion problems faces difficulties in the definition of crucial parameters that represent grid-soil interaction. Application of discrete element method (DEM) may be useful, particularly for cases involving large sized granular materials. There are several studies that describe conventional method of modeling representing soil and soil inclusion as rigid spherical particles [6]. Some studies develop soil-inclusion model by using mix of methods: where soil was modeled by discrete element (DE) and geogrid was modeled by finite element (FE) [7]. A summary example of geogrid modeling methods is given in Table 1.

Table 1. Summary of geogrid modeling methods.

#	Modeling approaches	Applications	Refs.
1	Model by using FEM: where both soil and geogrid was modeled by finite element	Pull-out behavior of the model was investigated	Sugimoto and Alagiyawanna [4]; Khedkar and Mandal [5]
2	DEM model representing soil and soil inclusion as rigid spherical particles	Cyclic triaxial loading simulation with spherical ballast particles	McDowell et al. [6]
3	DEM-FEM models: where soil was modeled by spherical discrete element and geogrid was modeled by finite element (FE)	Pull-out test was performed to define relationships between pull-out force and displacements	Tran et al. [7]
4	DEM model by representing geogrids as deformable cylinders according to the Minkowski sum concept and representing soil as spherical particles	Pull-out test was performed in order to check effectiveness of the model	Thoeni et al. [8]

2 Numerical Modeling

2.1 Numerical Modeling Method

A method to model geogrid-soil interactions through representing geogrids as deformable cylinders according to the concept by Minkowski sum has been recently proposed by Thoeni et al. [8]. Main components of Minkowski sum include rigid

spheres (Fig. 1a) and cylinders represented by sphere and line (Fig. 1b). Each rib of the grid can be modeled by one or more cylinders depending on geometry of grid.

Contacts between each component are treated as sphere-sphere interconnection allowing to use basic mathematical formulation for contact forces.

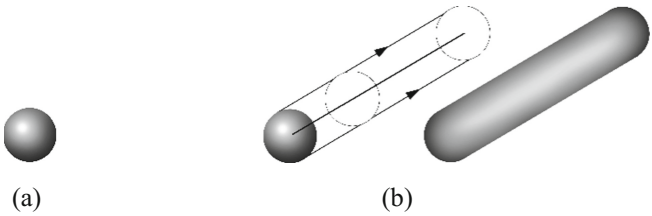

Fig. 1. Minkowski sum components: (a) sphere and (b) cylinder [8]

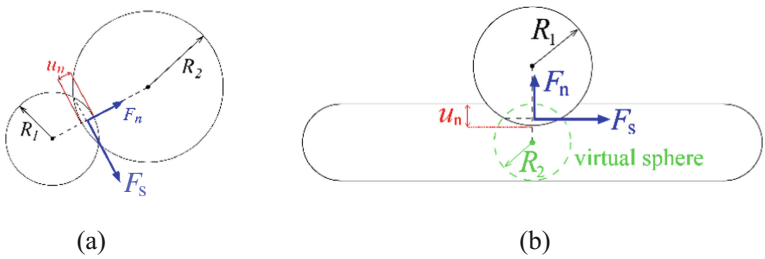

Fig. 2. Contact forces between components: (a) sphere-sphere and (b) sphere and virtual sphere of cylinder or pfacet [8]

2.2 Inter-particle Contact Law

A linear contact stiffness law and Mohr-Coulomb friction were used in the software to describe inter-particle interaction. This law implements the classical linear elastic-plastic law from Cundall Strack [9]. The normal force is (with the convention of positive tensile forces) $F_n = \min(k_n u_n, 0)$, where u_n is the normal distance between two spheres. The shear force is $F_s = k_s u_s$, where u_s is the relative shear displacement. The plasticity condition defines the maximum value of the shear force: $F_s(\max) = F_n \tan(\varphi)$, with φ the friction angle. The linear contact model stiffness is derived from the normal and shear stiffness k_n and k_s assigned to the contacting objects. Linear contact model represents two contacting objects to be in series; hence, normal secant stiffness of contact is defined by following equation:

$$k_n = \frac{k_{n1} k_{n2}}{k_{n1} + k_{n2}} = \frac{2E_1 R_1 E_2 R_2}{E_1 R_1 + E_2 R_2}$$

where, k_{n1}, k_{n2} = normal stiffness of contacting objects. Whereas shear tangent stiffness of the contact is defined by:

$$k_s = \frac{k_{s1}k_{s2}}{k_{s1}+k_{s2}} = \frac{2E_1R_1\nu_1E_2R_2\nu_2}{E_1R_1\nu_1+E_2R_2\nu_2}$$

where, k_{s1}, k_{s2} = shear stiffness of contacting objects, E_1, E_2 = Young's modulus, R_1, R_2 = radii of the contacting spheres, and ν_1, ν_2 = Poisson's ratio. When a soil particle contacts a grid component the same formulas apply, but the grid is assigned the radius of the virtual inscribed sphere (see Fig. 2(b)).

3 Results and Discussion

Ongoing work is directed to apply the discussed geogrid modeling technique in realistic laboratory configurations. A pull-out test was initially modeled in order to observe the potential of the approach chosen. The contact properties of soil and geogrid material are assumed to be the same (Table 2). Note that, for simplicity, no rolling friction was included in the contact model. Square grid mesh of 9.5 cm × 9.5 cm dimensions with 1 cm openings was introduced to the model (Fig. 3a). Pull-out of the grid for cubic soil matrix with sides of 10 cm was performed applying a constant velocity of 0.06 m/s to the grid. All numerical simulation was performed using Yade software [10].

Table 2. Summary of material properties.

Parameter	Value
Young's modulus, *E*	5000 kPa
Density, ρ	2650 kg/m^3
Poisson's ratio, υ	0.3
Friction angle, *φ*	20°

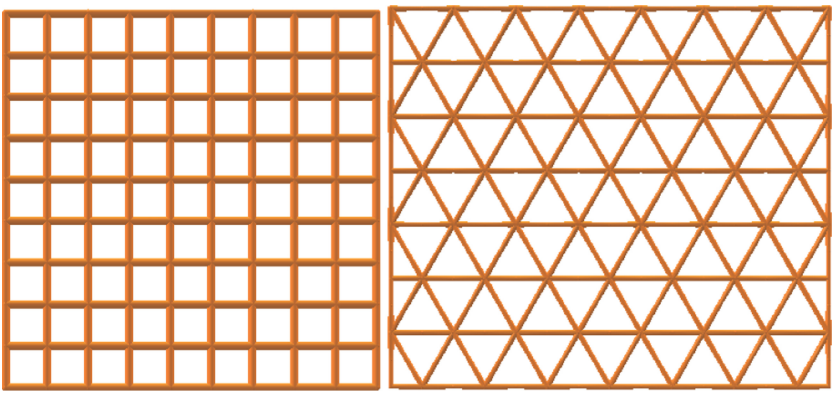

Fig. 3. Geogrid mesh: (a) rectangular and (b) triangular

Figure 4 shows a pull-out test at several stages, with the grid at different positions. Figure 4(a) shows when the displacement of a grid at the initial stage ($\Delta x = 0$), while Fig. 4(b) and (c) present pull-out at the intermediate stage ($\Delta x = 4.75$ cm) and total pullout ($\Delta x = 9.5$ cm) respectively. The entrapment of soil particles can be observed as grey soil columns became mixed with green columns as geogrid is being pulled-out. This is indicative of the interlocking properties of the grid because soil particles are captured in the grid openings and while it is pulled out, the particles move along the movement direction.

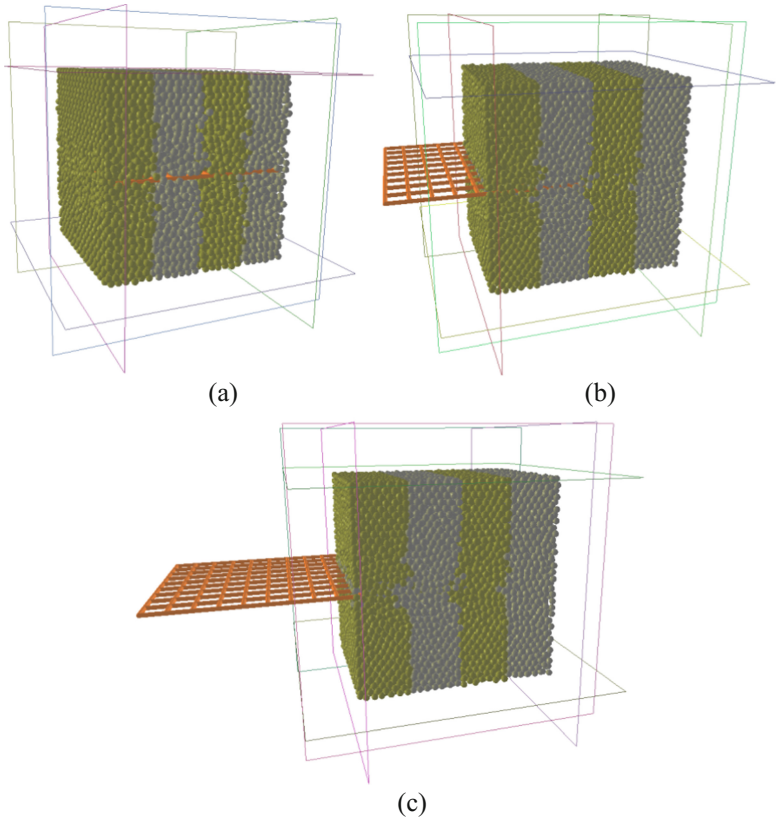

Fig. 4. Pull-out of a grid: (a) $\Delta x = 0$, (b) $\Delta x = 4.75$ cm and (c) $\Delta x = 9.5$ cm

A parametric study was conducted, in which the grid pull-out was performed under different conditions. The parameters explored included the vertical confining pressure at the top wall of the box, size of soil particles and the shape of the grid pulled out. The corresponding values of the parameters are presented in Table 3. It is noted that a uniform sized particle distribution was used in all cases. The schematic view of 10 cm $\times$ 8.7 cm triangular geogrid can be seen in Fig. 3(a) and its geometry is more complex compared to the rectangular. Triangles of the grid are equilateral with the sides of 1.43 cm and vertical components at both sides of the grid are 1.24 cm.

Table 3. Range of parameters considered in the study.

Parameter	Value
Confining pressure, P (kPa)	75, 150 and 300
Radius of soil grains, r (m)	0.001, 0.0015 and 0.0025
Shape of geogrid	Rectangular and triangular

The resultant graph of pull-out force versus displacement is given in Fig. 5 for various confining pressure conditions. This case considers rectangular geogrid with middle (0.0015 m) soil particle dimension. The figure shows that pull-out response slightly increases with increasing vertical confining stress of 75 kPa, 150 kPa and 300 kPa. Average values of pull-out force are 20.11 N, 28.05 N and 31.20 N respectively. Interestingly there seems to be very little effect on the pullout force of the reduction of inserted grid length in the specimen; as long as there is one transversal rib in the box the pull-out force average is closely maintained.

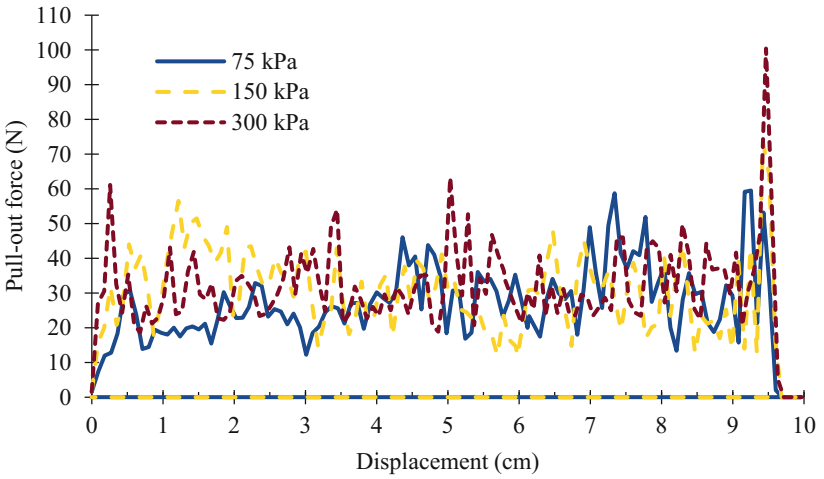

Fig. 5. Pull-out response of square geogrid: r = 0.0015 m

Another figure was built to illustrate variance of response of geogrid pull-out according to different shapes of geogrid. Figure 6 represents the case with vertical confining stress of 150 kPa and with soil grain radius of 0.0025 m. The figure shows that pull-out response for the rectangular grid is higher than triangular grid case, at least until a large displacement has been achieved. Average pull-out forces for rectangular and triangular grid shapes are 36.66 N and 28.05 N respectively.

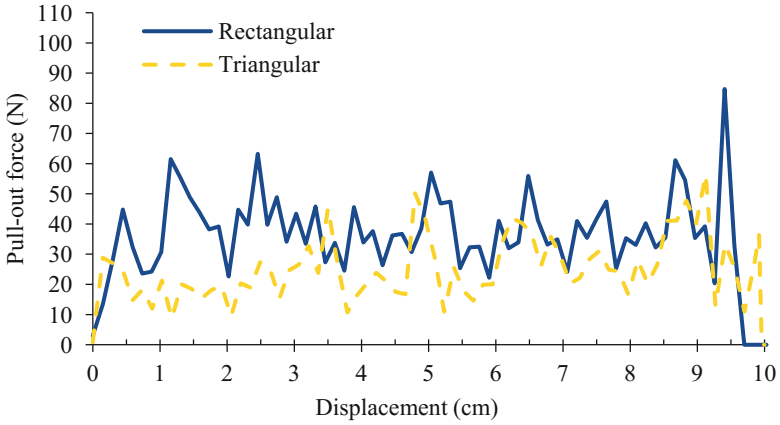

Fig. 6. Pull-out of geogrids: P = 150 kPa and r = 0.0025 m

Average pull-out force values for each case in the study are shown in Table 4. As expected, for all sizes of soil grains the pull-out response of the grid is higher for increased vertical confinement. In order to quantify variation of the pull-out response results, coefficient of variation values were estimated. Table 5 includes coefficient of variation for different particles sizes and for varied vertical confining stress. As a result, variation coefficient decreases with the decreasing particle size for each confinement scenario. This indicates that variation of the pull-out response is smaller for smaller grain size which leads to more precise results. As the model becomes more continuous the variance of the results related to the average value diminishes.

Table 4. Average pull-out force values with different parameters.

Confining pressure (kPa)	Radius of soil particles (m)			Triangular shape (r = 0.0025 m)
	0.0025	0.0015	0.0010	
75	26.29	20.11	41.32	20.11
150	36.66	28.05	42.41	28.05
300	43.56	31.20	44.51	39.23

Table 5. Coefficient of variation of pull-out force with different parameters.

Confining pressure (kPa)	Radius of soil particles (m)		
	0.0025	0.0015	0.0010
75	0.543	0.445	0.242
150	0.434	0.381	0.234
300	0.413	0.406	0.230

4 Conclusions

To conclude, basic soil-geogrid models have been built using the method of representing grids as deformable cylinders defined by Minkowsky sums, as implemented in the Yade open-source DEM code. In order to verify the application of the model, pull-out test was performed. As a result, rearrangement of the particles is noted due to interlock of them within grid openings. Furthermore, several simulations of a pull-out test were performed. The results indicated that pull-out response will increase with the increasing vertical confining stress. It was also deduced that with varying geometry of geogrid, pull-out response will change. As a result, pull-out force is higher for rectangular shape compared to the triangular grid. Moreover, it was estimated that variation of the pull-out response is smaller for smaller grain size which was defined by calculating coefficient of variation for the obtained data. Further tests are planned to verify the accuracy of the model before proceeding to further investigations including triaxial testing.

Acknowledgment. This work has been supported by the REA of the European Union, through grant 645665 "GEO-RAMP", H2020-MSCA-RISE-2014.

References

1. Koerner, R.M.: Designing with Geosynthetics, 5th edn. Xlibris Corporation, Bloomington (2005)
2. Jones, C.J.: Earth Reinforcement and Soil Structures. Elsevier, New York (2013)
3. Chan, D.H., Law, K.T. (eds.) Soft Soil Engineering: Proceedings of the Fourth International Conference on Soft Soil Engineering, Vancouver, Canada, 4–6 October 2006. CRC Press (2006)
4. Sugimoto, M., Alagiyawanna, A.M.N.: Pullout behavior of geogrid by test and numerical analysis. J. Geotech. Geoenvironmental Eng. ASCE **129**(4), 361–371 (2003)
5. Khedkar, M.S., Mandal, J.N.: Pullout behaviour of cellular reinforcements. Geotext. Geomembr. **27**(4), 262–271 (2009)
6. McDowell, G.R., Harireche, O., Konietzky, H., Brown, S.F., Thom, N.H.: Discrete element modelling of geogrid-reinforced aggregates. Proc. Inst. Civ. Eng.-Geotech. Eng. **159**(1), 35–48 (2006)
7. Tran, V.D.H., Meguid, M.A., Chouinard, L.E.: A finite–discrete element framework for the 3D modeling of geogrid–soil interaction under pullout loading conditions. Geotext. Geomembr. **37**, 1–9 (2013)
8. Thoeni, K., Effeindzourou, A., Chareyre, B., Giacomini, A.: Discrete modelling of soil-inclusion problems. In: Applied Mechanics and Materials, vol. 846, pp. 397–402. Trans Tech Publications (2016)
9. Cundall, P.A., Strack, O.D.: A discrete numerical model for granular assemblies. Geotechnique **29**(1), 47–65 (1979)
10. Šmilauer, V.: Yade Documentation, 2nd edn. The Yade Project (2015). https://doi.org/10.5281/zenodo.34073. http://yade-dem.org/doc/

On Why and Where GSH Is Rate-Independent

Yimin Jiang[1] and Mario Liu[2(✉)]

[1] Central South University, Changsha 410083, China
[2] Theoretische Physik, Universität Tübingen, 72076 Tübingen, Germany
marioliu@gmail.com

Abstract. This exposition is dedicated to Professor Gert Gudehus on his 80th Birthday, who was among the first to realise the potential of GSH, presciently and more clearly than we did. In what follows, we shall first generalising the notion of rate-independence to invariance under a scale transformation in time. We then demonstrate this invariance of GSH (granular solid hydrodynamics) at typical shear rates of soil-mechanical experiments, for both slowly varying and suddenly changing rates, and in the presence of shear bands. Scale invariance is lost, and rate-dependence appears, at higher shear rates such as given in chute flows.

Granular phenomena are frequently rate-independent, the observed stress remains the same, however fast the experiment is executed. This has led to the wide-spread believe that rate-independence (RI) is a basic feature of granular media. Hence, constructing constitutive relations, one needs to start from it. Such approaches are efficient, but they prevent an understanding of why RI holds, and where it does (i.e., to what range RI is limited). Moreover, such approaches preclude the construction of constitutive relations that remain valid outside the RI regime, in phenomena such as chute flows.

To get a better understanding of RI, it is useful to first recognise the difference in RI between that of elasticity and hypoplasticity. They are different because the first is a static property, and the second a dynamic one. In elasticity, the strain ε_{ij} is a state variable, and both the elastic energy w and the stress $\pi_{ij} \equiv -\partial w/\partial \varepsilon_{ij}$ are unique functions of it. This is the reason the stress remains the same for a given strain, $\pi_{ij} = \pi_{ij}(\varepsilon_{kl})$, however fast ε_{ij} is built up, whatever the shear rate $\dot{\varepsilon}_{ij}$ is. Dynamics does not enter this consideration. (Of course, if the Cauchy stress has a viscous contribution, $\sigma_{ij} = \pi_{ij} - \eta\dot{\varepsilon}_{ij}$, the stress is not rate-independent.)

In hypoplasticity, the strain ε_{ij} is not a state variable, because the Cauchy stress σ_{ij} is not a unique function of it – think of "incremental nonlinearity". Here, RI is connected to the dynamics, more specifically to the structure of the evolution equation for σ_{ij}. Taking $\dot{\sigma}_{ij}$ as a function of the shear rate $\dot{\varepsilon}_{ij}$, the stress σ_{ij} and density ρ, it is

$$\dot{\sigma}_{ij} = H_{ijkl}\dot{\varepsilon}_{kl} + \Lambda_{ij}\sqrt{\dot{\varepsilon}_{kl}\dot{\varepsilon}_{kl}}, \tag{1}$$

with the two tensors H_{ijkl}, Λ_{ij} functions of σ_{ij} and ρ. (For simplicity, here and below, we always set $\dot{\varepsilon}_{kk} \equiv 0$.) As a result, the stress σ_{ij} remains the same for any given path

W. Wu (Ed.): *Desiderata Geotechnica*, SSGG, pp. 75–78, 2019.
https://doi.org/10.1007/978-3-030-14987-1_8

$\varepsilon_{kl} \equiv \int \dot{\varepsilon}_{kl}(t)\mathrm{d}t$, whatever the rate $\dot{\varepsilon}_{kl}(t)$ is. (We note Eq. (1) is not of the most general form, because terms such as $\sqrt{\dot{\varepsilon}_{ik}\dot{\varepsilon}_{kj}}$ or $\sqrt[3]{\dot{\varepsilon}_{ik}\dot{\varepsilon}_{kl}\dot{\varepsilon}_{lj}}$ would retain RI.)

Mathematically speaking, Eq. (1) is invariant under a transformation rescaling the time,

$$t \to t/A, \tag{2}$$

because all three terms of Eq. (1) get multiplied by the same constant factor A. Therefore, the solution for the stress also needs to be scale invariant and cannot depend on $\dot{\varepsilon}_{kl}$ alone, but may depend on $\varepsilon_{kl} \equiv \int \dot{\varepsilon}_{kl}(t)\mathrm{d}t$.

More generally, the dynamics of neither elasticity nor hypoplasticity is scale invariant. Consider for instance momentum conservation, in which $\rho\dot{v}_i$ scales as A^2, and $\nabla_j\sigma_{ij}$ as A^0. Therefore, wave phenomena are never rate-independent. And when one speaks of RI in the context of resonance column experiments, one needs to carefully spell out what is implied.

GSH (granular solid hydrodynamics [1–3]) is a continuum-mechanical theory capable of qualitatively accounting for a wide range of granular behavior, from elasto-plastic motion to fast dense flow, including shear bands and elastic waves [4,5]. To render GSH quantitatively useful, values for its material parameters are needed. We are at present discussing the complete set of calibrating experiments for obtaining these parameters. And as for any type of grains, part of these experiments are as yet lacking, we infer them from the hypoplastic model and the granular kinetic theory employing some extrapolating assumptions. This work will be reported in a forthcoming publication.

In the present exposition, we discuss when and why GSH is rate-independent, or rather scale invariant. As we shall see, GSH reduces to hypoplasticity, Eq. (1), for constant (or slowly varying) shear rates [6]. GSH is trivially rate-independent then, as hypoplasticity is. If the shear rate oscillates, such as in cyclic loading, GSH is more complicated than hypoplasticity, as more terms appear. As we shall see, it is then less plastic but remains rate-independent. Moreover, the gradient term accounting for shear bands is also scale-invariant and maintains RI.

A minimalist version of GSH is given here [7]. (The complete version renders the description of granular phenomena more realistic. Yet it suffices to consider the former since all conclusions on RI drawn below remain valid for the latter.) The state variables of any granular system are the density ρ, the momentum density ρv_i, the granular entropy density s_g (accounting for granular jiggling), and the elastic strain ε^e_{ij} (accounting for the deformation of grains). Their close set of equations is

$$\partial_t\rho + \nabla_i(\rho v_i) = 0, \tag{3}$$

$$\partial_t(\rho v_i) + \nabla_i(\sigma_{ij} + \rho v_i v_j) = \rho g_i, \tag{4}$$

$$\sigma_{ij} = \pi_{ij} + P_T\delta_{ij} - \eta_1 T_g\dot{\varepsilon}_{ij}, \tag{5}$$

$$\pi_{ij}(\varepsilon^e_{ij}) \equiv -\partial w/\partial\varepsilon^e_{ij},\ P_T \equiv -\partial(w/\rho)/\partial(1/\rho), \tag{6}$$

$$\partial_t T_g = -R_T[T_g(1-\xi_T^2\nabla_i^2)T_g - f^2\dot{\varepsilon}_{ij}\dot{\varepsilon}_{ij}], \tag{7}$$

$$\partial_t\varepsilon^{e*}_{ij} = \dot{\varepsilon}_{ij} - \lambda T_g\varepsilon^{e*}_{ij}, \quad \partial_t\varepsilon^e_{kk} = -\alpha_1\varepsilon^{e*}_{ij}\dot{\varepsilon}_{ij} - \lambda_1 T_g\varepsilon^e_{kk}, \tag{8}$$

where ε^{e*}_{ij} is the traceless part of the elastic strain, and $\dot{\varepsilon}_{kk} = 0$ is again assumed. Equation (3) is the continuity equation, Eq. (4) the momentum balance, with the Cauchy

stress σ_{ij} explicitly given if the free energy $w = w(\rho, T_g, \varepsilon^e_{ij})$ is known. (As the specific form of the free energy we employ is irrelevant to the discussion about RI, it is not reproduced here.)

Equation (7) is the balance of the granular entropy, and Eq. (8) are the evolution equations for the elastic strain. The seven scalar coefficients: $\lambda, \lambda_1, \alpha_1, R_T, \xi_T, f, \eta_1$ are functions of the density alone, providing the only leeway GSH has for fitting experimental data.

For $\dot{\varepsilon}_{kk} = 0$, Eq. (3) is redundant. Excluding acceleration, $\partial_t(\rho v_i) = 0$, and wave propagation leaves the dynamics given by Eqs. (7, 8) alone. They are, as we shall see, invariant under the scale transformation of Eq. (2).

Note first that in the stationary limit, $\partial_t T_g = 0$, and for uniform samples, $\xi_T^2 \nabla_i^2 T_g = 0$, we have

$$T_g = f\sqrt{\dot{\varepsilon}_{ij}\dot{\varepsilon}_{ij}}. \tag{9}$$

Inserted into Eq. (8), this expression yields two equations of hypoplastic structure, implying RI of the elastic strain. Next, we go an important step further. Equation (9) implies that T_g scales with A, same as $\dot{\varepsilon}_{ij}$. Then, clearly, under the scale transformation of Eq. (2), every single term of Eq. (7) scales with A^2, and every one of Eq. (8) with A. This leaves both equations scale invariant. As above, we again conclude that no solution for the elastic strain ε^e_{ij} may depend on $\dot{\varepsilon}_{ij}$ or T_g alone, though $\int \dot{\varepsilon}_{kl}(t)\mathrm{d}t$ or $\int T_g \mathrm{d}t$ are fine.

In the Cauchy stress of Eq. (5), both the viscous contribution and the pressure $P_T \sim T_g^2$ are not scale invariant. However, they are important only at higher shear rates, such as in chute flows or the $\mu(I)$-rheology. At lower shear rates, they may be neglected, rendering the Cauchy stress a function of the elastic strain alone, $\sigma_{ij} = \pi_{ij}(\varepsilon^e_{kl})$, scale and rate invariant.

In cyclic loading, both T_g and $\dot{\varepsilon}_{ij}$ vary with time. If the amplitude is too small for T_g to reach the stationary limit, the term $\partial_t T_g = 0$ becomes important, typically rendering T_g smaller than given by Eq. (9). This reduces the plasticity that is accounted for by the terms $\sim T_g$ in Eq. (8), and is how GSH accounts for cyclic loading rate-independently. A forthcoming paper shows the agreement thus achieved with the data by Wichtmann [8]. Similarly, the term $T_g \xi_T^2 \nabla_i^2 T_g$ in Eq. (7) accounts for shear bands rate-independently.

For thermodynamic consistency, GSH must reduce to elasticity at the very low end of shear rates [4,5], with the transition starting presumably at a shear rate somewhere between 10^{-5} and 10^{-6}/s. Such a transition is necessarily rate-dependent. To account for this, we substitute f^2 with $f^2/(1 + T_0/T_g)$ in Eq. (7), and α_1 with $\alpha_1/(1 + T_0/T_g)$ in Eq. (8). This keeps all above results for $T_g \gg T_0$, but replace Eq. (9) with $T_g = f^2\dot{\varepsilon}_{ij}\dot{\varepsilon}_{ij}/T_0$ for $T_g \ll T_0$, implying T_g is quadratically small and hence negligible. At the same time, Eq. (8) become fully elastic. However, with the present technology, any rate-dependency is hard to observe, because it represents only a tiny portion of the cyclic loading: If the maximal amplitude of the shear rate is 10^{-2}/s, the rate-dependent portion is between 0.1% and 0.01% of a period.

References

1. Jiang, Y.M., Liu, M.: Granular solid hydrodynamics. Granul. Matter **11**, 139 (2009). www.springerlink.com/content/a8016874j8868u8r/fulltext
2. Jiang, Y.M., Liu, M.: The physics of granular mechanics. In: Kolymbas, D., Viggiani, G. (eds.) Mechanics of Natural Solids, pp. 27–46. Springer (2009)
3. Gudehus, G., Jiang, Y.M., Liu, M.: Seismo- and thermodynnamics of granular solids. Granular Matter **1304**, 319–340 (2011)
4. Jiang, Y.M., Liu, M.: Granular Solid Hydrodynamics (GSH): a broad-ranged macroscopic theory of granular media. Acta Mech. **225**, 2363–2384 (2014). https://doi.org/10.1007/s00707-014-1131-3
5. Jiang, Y.M., Liu, M.: Applying GSH to a wide range of experiments in granular media. Eur. Phys. J. E **38**, 15 (2015)
6. Jiang, Y.M., Liu, M.: Similarities between GSH, hypoplasticity and KCR. Acta Geotech. **11**, 519–537 (2016). https://doi.org/10.1007/s11440-016-0461-9
7. Jiang, Y.M., Liu, M.: Why granular media are thermal, and quite normal, after all. Eur. Phys. J. E **40**, 10 (2017). https://doi.org/10.1140/epje/i2017-11497-4
8. Wichtmann, T.: Bauhaus-Universität Weimar. http://www.torsten-wichtmann.de

Mathematical Modeling of Deformation of Self-stress Rock Mass Surrounding a Tunnel

S. V. Lavrikov(✉) and A. F. Revuzhenko

Chinakal Institute of Mining, SB RAS, Novosibirsk 630091, Russia
lvk64@mail.ru

Abstract. The mathematical model of structurally inhomogeneous rock mass, describing the property of rocks to accumulate and release elastic energy is used in the study. The finite element algorithm and programs for solving plane boundary-value problems are developed. The authors solve a problem on deformation of rock mass with a disjunction. It is shown that driving of horizontal tunnel nearby the disjunction can provoke the accumulated elastic energy release, which affects stress state of rock mass around the tunnel.

Keywords: Rock · Internal structure · Internal self-balancing stresses · Modeling · Tunnel · Disjunction

1 Introduction

One of the priority trends in the modern geomechanics is concerned with the studies into internal structure of soil and rock. In the mechanics of soil and granular material, the granular structure governs internal friction, cohesion and dilatancy. During deformation, such properties may give rise to an increase in the pressure applied to enclosing structures, as well as to localization of shears and generation of isolated slip surfaces [1–3]. In the mechanics of rocks, the occurrence of discontinuities and the block structure determine essential nonlinearity and anisotropy of rock mass behavior [4–6].

One of the important properties of rock mass is the capacity to accumulate energy of external forces in the form of internal self-balancing stresses. This property is connected with the hierarchical block structure of rocks, having numerous equilibrium states [7]. Some areas in rock mass can accumulate energy and later, under certain conditions, to release it, i.e. such areas function as energy sources. The energy release process can either be stable relaxation or unstable disaster [8–10].

There exist many approaches to taking into account the hierarchical structure and internal self-balancing stresses of rock mass. Among them there are, for instance, the mathematical apparatus and models with internal variables [11, 12], the approach based on the methods of the non-Archimedean mathematical analysis [13], the discrete element method [14, 15], etc. In this study we used the approach from [11] and the mathematical model from [12] to analyze numerical deformation of rock mass surrounding a horizontal tunnel.

W. Wu (Ed.): *Desiderata Geotechnica*, SSGG, pp. 79–85, 2019.
https://doi.org/10.1007/978-3-030-14987-1_9

2 Mathematical Model

We choose a two-scale model of self-stress rock mass [11, 12] (plane strain deformation). The microscale elastic particles (grains) occur at the points of a square lattice. The pore space is filled with a binding material having elastic characteristics other than the properties of the grains (Fig. 1). In-between the particles plastic shears develop by the nonlinear law, including stages of strengthening, softening and residual strength. The diagram of microslip between grains, connecting tangential microstress t_{12} and microshears ε_{ij}^R (in the general case, it is assumed that $\varepsilon_{12}^R \neq \varepsilon_{21}^R$), is shown in Fig. 2 (piece-wise linear approximation).

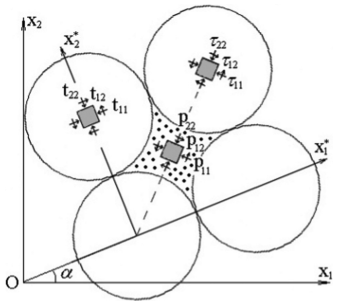

Fig. 1. Internal microstructure of packing

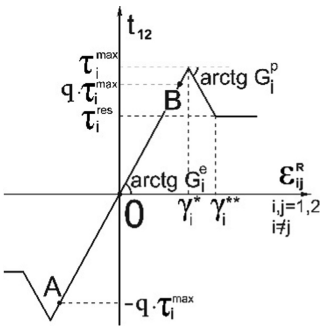

Fig. 2. Diagram of inter-grain slip

The conditions for the slip between grains are approximated by the piecewise-linear diagram (Fig. 2), and for the increments in the microstresses and microshears are given by

$$\Delta\varepsilon_{12}^R = \Delta t_{12}/G_1^s,\ \Delta\varepsilon_{21}^R = \Delta t_{12}/G_2^s \tag{1}$$

The parameters G_1^s, G_2^s in Eq. (1) are the preset moduli of slip for each family of contacts. The moduli G_i^s are defined by the preset constants γ_i^*, γ_i^{**}, $\tau_i^{\max}$, τ_i^{res}, where $i = 1, 2$ is the number of the family of contacts

$$G_i^s = \begin{cases} G_i^e, & 0 \le \gamma_i < \gamma_i^* \\ -G_i^p, & \gamma_i^* \le \gamma_i < \gamma_i^{**} \\ 0, & \gamma_i^{**} \le \gamma_i \end{cases}$$

where, $\gamma_1 = \varepsilon_{12}^R$, $\gamma_2 = \varepsilon_{21}^R$.

The constitutive relations at the macroscale of the model connect the increments of the macrostresses $\Delta\sigma_{ij}$ with the increments of the macrostrains $\Delta\varepsilon_{ij}$:

$$\begin{pmatrix} \Delta\varepsilon_{11} \\ \Delta\varepsilon_{22} \\ \Delta\varepsilon_{12} \end{pmatrix} = W \cdot \left((T+R)^{-1} + 2(T+P)^{-1} \right) \cdot W^{-1} \cdot \begin{pmatrix} \Delta\sigma_{11} \\ \Delta\sigma_{22} \\ \Delta\sigma_{12} \end{pmatrix} \tag{2}$$

The coefficients in Eq. (2) depend on the microproperties of grains (matrix T), pore-filling material (matrix P), moduli of contact slip between grains (matrix R) and on the angle α (see Fig. 1), governing the orientation of regular grain packing in the Cartesian coordinates (matrix $W = W(\alpha)$).

The forces appearing in grains cause deformation of the grains and inter-grain shearing, which results in the deformation of the pore structure. Compression of the pore space is balanced by the tangential forces at the inter-grain contacts, and, in this way, even at zero external stresses, the internal self-balancing stresses can be considerably high. The condition of compatibility of micro- and macroparameters make it possible to connect the macrostresses σ_{ij}^{*} (in the coordinates of regular grain packing, see Fig. 1) and microstresses of grains t_{ij} and pore-filling material p_{ij} in the form of:

$$\sigma_{ij}^{*} = t_{ij} + 2m \cdot p_{ij}, \qquad i, j = 1, 2 \tag{3}$$

where the dimensionless value $0 < m < 1$ acts as a parameter of areal porosity [11].

The conditions (3) mean that one and the same macrostresses σ_{ij}^{*} can agree with the multitude different stress states of grains t_{ij} and pore-filing material p_{ij}. In this regard, zero macrostresses do not imply the absence of the internal microstresses. The microstresses in grains and in pore-filling material may have different signs and may completely balance each other.

The constitutive relations (2) in combination with the Cauchy relations, connecting strains and displacements, is closed by the equations of equilibrium (in terms of increments):

$$\frac{\partial \Delta\sigma_{11}}{\partial x_1} + \frac{\partial \Delta\sigma_{12}}{\partial x_2} + \Delta X_1 = 0, \frac{\partial \Delta\sigma_{12}}{\partial x_1} + \frac{\partial \Delta\sigma_{22}}{\partial x_2} + \Delta X_2 = 0. \tag{4}$$

The formulated quasi-static problem is numerically solved with a help of finite element method by steps of loading with regard to the changing properties of the medium in the course of deformation: $\sigma_{ij}^{k+1} = \sigma_{ij}^{k} + \Delta\sigma_{ij}^{k}$, $\varepsilon_{ij}^{k+1} = \varepsilon_{ij}^{k} + \Delta\varepsilon_{ij}^{k}$, where the superscript k is the number of iteration.

The analysis of the type of the system (2), (4) shows that if the slope of the descending branch of the microslips at the inter-grain contact is less than a critical value (depends on the shear modulus and Poisson's ratio of grains, μ^{t}, ν^{t}, and pore-filling material, μ^{p}, ν^{p}), the system of equations is elliptical. In this case, deformation is a stable process of microstrength loss without jumps. The examples of the numerical calculations in the given range of parameters are discussed below.

3 Numerical Modeling Results

The computational domain is set in the neighborhood of a horizontal tunnel with an arch cross-section (Fig. 3). The initial macrostress state is chosen as the linear distribution according to Dinnik:

$\sigma_{22}^0 = -\gamma(H - x_2)$, $\sigma_{11}^0 = \xi\sigma_{22}^0$, $\sigma_{12}^0 = 0$, where γ is the specific weight of rocks, H is the depth of the tunnel occurrence, ξ is the lateral earth pressure coefficient. Alongside with the macrostresses, it is required to determine initial distribution of microstresses such that satisfy the relations (3). We select distribution of microstresses as function of the parameters $q_i : t_{11}^0 = 0.5\sigma_{11}^0$, $t_{22}^0 = 0.5\sigma_{22}^0$, $t_{12}^0 = \pm q\tau_i^{max}$, $p_{ij}^0 = \left(\sigma_{ij}^0 - t_{ij}^0\right)/2m$, $i, j = 1, 2$ and consider two different problems. In the first problem, it is set that in the whole computational domain the shear microstresses of grains and, accordingly, pore-filling material, are zero:$q_i = 0$, $i = 1, 2$. In the diagram of shearing (see Fig. 2), this state corresponds to the point O. The second problem includes a disjunction nearby the tunnel (grey-colored zone in Fig. 3), and it is assumed that the shear microstresses of grains in the disjunction make a certain portion of the critical value, e.g.$q_i = 0.9$ while $q_i = 0$, $i = 1, 2$ in the surrounding rock mass. This state in the shearing diagram conforms with the points A or B depending on the sign of the shear microstress (see Fig. 2). In this manner, one and the same initial macrostresses are set in the two problems, and the difference is the distribution of the microstresses of the structural elements.

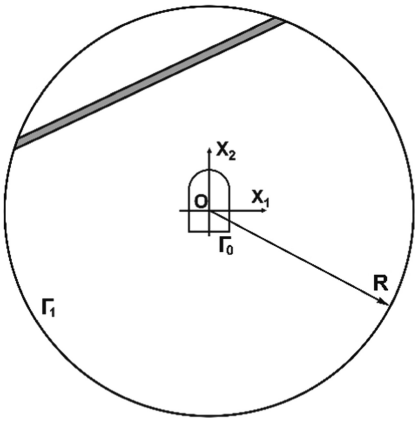

Fig. 3. Computational domain, disjunction is grey-colored

The boundary values are set as a sequential reduction in stresses at the tunnel boundary: $\Delta\sigma_n|_{\Gamma_0} = -\Delta d^k \cdot \sigma_n^0$, $\Delta\tau_n\big|_{\Gamma_0} = -\Delta d^k \cdot \tau_n^0$, where $\Delta\sigma_n, \Delta\tau_n$ are the increments in the normal and shear macrostress, respectively;σ_n^0, τ_n^0 – initial normal and shear macrostresses; Γ_0 is the boundary of the tunnel;$0 \le \Delta d^k \le 1$ is the increment in

the dimensionless loading parameter at a k^{th} step. The condition $\sum_k \Delta d^k = 1$ means complete relieving of the tunnel boundary. The external boundary Γ_1 is assumed immobile: $\Delta u_i|_{\Gamma_i} = 0,\ i = 1,\ 2.$

The input dimensionless parameters (all values of the dimension of stresses are related to the value of the maximum shear microstress τ_1^{max} at the peak of the diagram in Fig. 2) are: $\mu^t = 3.75 \times 10^3$, $\nu^t = 0.2$, $\mu^p = 0.635 \times 10^3 \,.\nu^p = 0.3$, $\gamma_1^* = \gamma_2^* = 0.5 \times 10^{-3}$, $\gamma_1^{**} = \gamma_2^{**} = 10^{-3}$, $\tau_1^{max} = \tau_2^{max} = 1$, $\tau_1^{res} = \tau_2^{res} = 0.5$, $\gamma H = 33.75$, $\Delta X_1 = \Delta X_2 = 0$, $\xi = 0.42$, $m = 0.5$, $\alpha = 0$, $H/R = 100$. The calculations are continued till complete relieving of the tunnel boundary.

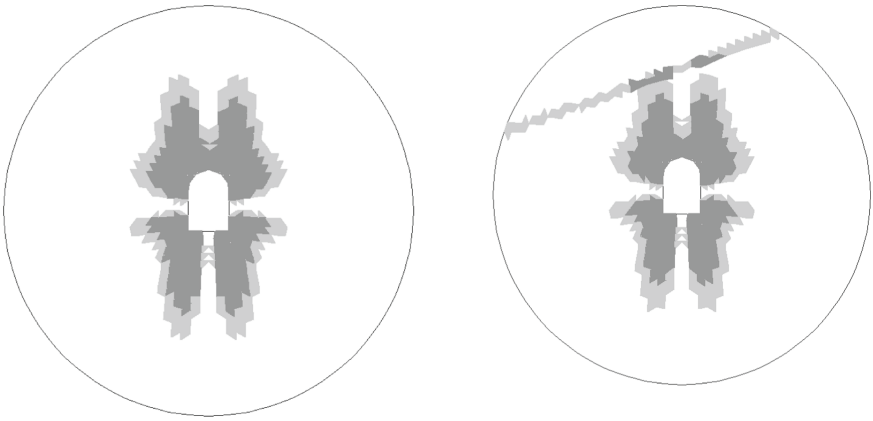

(a) (b)

Fig. 4. Calculated zone of plastic deformation: (a) without disjunction, (b) considering the disjunction

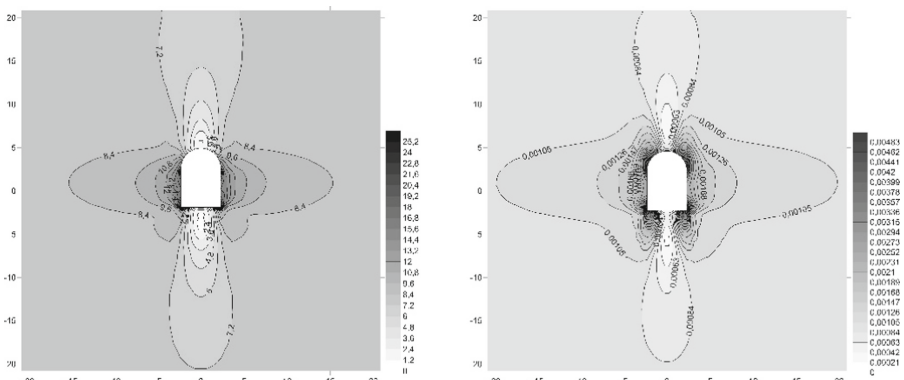

(a) (b)

Fig. 5. Calculation data of the problem without the disjunction: (a) contour lines of the maximum tangential stress τ_0, (b) contour lines of the maximum shear γ_0

Figures 4a and 5 depict the results of the first problem solution without the fracture. Figure 4a illustrates evolution of plastic deformation zones (light-grey are the zones of local softening-the descending branch; dark-grey are the residual strength zones-horizontal branch in Fig. 2). Figures 5a, b show contour lines of the maximum tangential stress $\tau_0 = 0.5\sqrt{(\sigma_{11} - \sigma_{22})^2 + 4\sigma_{12}^2}$, maximum shear $\gamma_0 = \sqrt{(\varepsilon_{11} - \varepsilon_{22})^2 + 4\varepsilon_{12}^2}$, respectively. Apparently, plastic shears initiate from the natural stress raisors at the tunnel boundary and propagate in rock mass predominantly in the vertical direction (since the preset gravity stresses exceed the tectonic stresses).

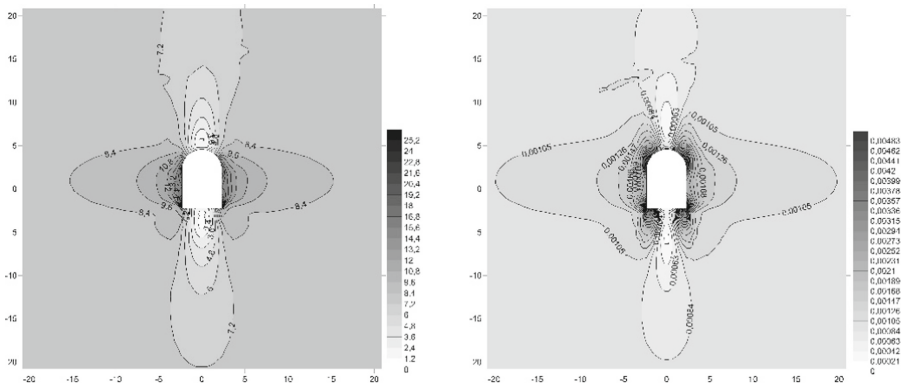

(a) (b)

Fig. 6. Calculation data of the problem taking into account the disjunction: (a) contour lines of the maximum tangential stress τ_0, (b) contour lines of the maximum shear γ_0

Figures 4b and 6 present the results of the second problem solution with regard to the disjunction. It is seen (Fig. 4b) that during deformation the material inside the disjunction zone relatively rapidly passes to plastic state and exerts influence on the stress state of surrounding rocks (Figs. 6a and b).

Overall, under the same initial macrostresses, the release of the accumulated energy in a relatively narrow section of the disjunction in the course of the tunnel driving induces macroshear of the fracture edges and the related change in the macrostress state of surrounding rock mass. The influence of the disjunction will even more increase in case of unstable deformation, when the release of the accumulated elastic energy will have the uncontrollable dynamic behavior.

4 Conclusions

- The developed approach enables problems on deformation of structurally inhomogeneous geo-materials to be solved regarding internal self-balancing stresses.
- Driving of a tunnel nearby a disjunction can result in relief of internal self-balancing stresses, which affects stress state of surrounding rock mass.

Acknowledgements. The study has been supported by the Russian Science Foundation, Project No. 16-17-10121.

References

1. Gudehus, G.: Physical Soil Mechanics, 835p. Springer, Heidelberg (2011)
2. Wu, W., Bauer, E., Niemunis, A., Herle, I.: Visco-hypoplastic models for cohesive soils. In: Kolymbas, D. (ed.) Modern Approaches to Plasticity, pp. 365–383. Elsevier, Amsterdam (1993)
3. Borja, R.I., Song, X., Rechenmacher, A.L., Abedi, S., Wu, W.: Shear band in sand with spatially varying density. J. Mech. Phys. Solids **61**, 219–234 (2013)
4. Kolymbas, D.: Tunneling and Tunnel Mechanics. A Rational Approach to Tunneling, 437 p. Springer, Heidelberg (2005)
5. Kolymbas, D., Lavrikov, S.V., Revuzhenko, A.F.: Deformation of anisotropic rock mass in the vicinity of a long tunnel. J. Min. Sci. **48**(6), 962–974 (2012)
6. Kocharyan, G.G.: Geomechanics of Faults, 422 p. GEOS, Moscow (2016, in Russian)
7. Kurlenya, M.V., Oparin, V.N., Revuzhenko, A.F., Shemyakin, E.I.: Some features of rock mass response to near-range blasting. In: Proceedings of the USSR Academy of Sciences, vol. 293, no. 1, pp. 67–70 (1987, in Russian)
8. Bobryakov, A.P., Kosyh, V.P., Revuzhenko, A.F.: Trigger initiation of elastic energy relaxation in high-stress geomedium. J. Min. Sci. **51**(1), 10–16 (2015)
9. Moroz, A.I.: Self-Stress State of Rocks, 288 p. MGGU, Moscow (2004, in Russian)
10. Stavrogin, A.N., Shirkes, O.A.: Aftereffect in rocks caused by preexisting irreversible deformations. J. Min. Sci. **22**(4), 235–244 (1986)
11. Revuzhenko, A.F.: Mechanics of Elastoplastic Media and Nonstandard Analysis, 426 p. NGU, Novosibirsk (2000, in Russian)
12. Lavrikov, S.V., Revuzhenko, A.F.: Modeling deformation processes in self-stressed rock specimens. J. Min. Sci. **53**(1), 12–20 (2017)
13. Lavrikov, S.V., Mikenina, O.A., Revuzhenko, A.F.: Rock mass deformation modeling using the non-Archimedean analysis. J. Min. Sci. **44**(1), 1–14 (2008)
14. Klishin, S.V., Revuzhenko, A.F.: 3D discrete element approach to the problem on abutment pressure in a gently dipping coal seam. In: IOP Conference Series: Earth and Environmental Science, vol. 84, p. 012003 (2017)
15. Lavrikov, S.V., Revuzhenko, A.F.: Numerical modeling of elastic energy accumulation and release in structurally heterogeneous geomaterials. J. Min. Sci. **52**(4), 632–637 (2016)

Constitutive Relations from Particle Simulations

Stefan Luding(✉)

Multi-Scale Mechanics (MSM), Faculty of Engineering Technology,
MESA+, University of Twente,
POBox 217, 7500 AE Enschede, The Netherlands
s.luding@utwente.nl

Abstract. Particulate systems like powders, soil or granular matter are discrete, disordered systems displaying dynamic and static, fluid - and solid-like states. The transients between fluid - and solid-like behavior can be intermittent and sometimes both states coexist in steady-state. Bridging the gap between the particulate, microscopic picture (velocities, forces) on the particle scale and their continuum description (strain and stress) via a so-called micro-macro transition is the goal of this paper. The generalized local constitutive relation for the stress in critical state granular flows involves not only density and strain rate but also the jamming-density and the granular temperature.

Keywords: Particle models · Micro-macro transition · Continuum rheology

1 Introduction

Particulate systems are interesting and challenging for academia and of practical relevance for industry, civil engineering and geo-sciences. Molecular dynamics-like discrete particle simulations provide in-depth microscopic insight and allow to extract scalar fields like density or granular temperature, vector fields like the flow velocity, or tensors like stress, strain-rate, and structure (fabric) [1–13]. Either one carries out many simulations of a homogeneous representative volume element (REV) for each state-point [7] or one performs local micro-macro coarse graining on an inhomogeneous system, in which case a few simulations might be sufficient. Given satisfactory statistics, such data-sets can have a quality that allows deriving constitutive relations that describe the local rheology and flow behavior of fluids (e.g. atoms confined in a nano-scale channel [4]) or granular systems, which are non-Newtonian, with particular relaxation behavior, anisotropy, etc. [1–3, 5, 6]. Attractive forces, like van-der Waals adhesion or liquid-bridges, lead to macro-cohesion added on top of the already non-trivial dynamics of granular matter [2, 6, 8, 9]. Dependent on the energy input (e.g., through an applied shear-rate), the particles can flow like a fluid, jam or un-jam, or be solid with interesting anisotropic structure (contact-and force-networks) [10, 11, 13].

The goal of the present paper is by using particle simulation data and the local coarse graining (micro-macro transition) procedure proposed by Isaac Goldhirsch [12, 13] to determine three-dimensional local rheology laws (in steady state shear in a split-bottom ring shear cell [1, 2, 5, 6, 8, 9]) that go beyond the classical $\mu(I)$-rheology [14].

W. Wu (Ed.): *Desiderata Geotechnica*, SSGG, pp. 86–92, 2019.
https://doi.org/10.1007/978-3-030-14987-1_10

This constitutive relation can predict surprisingly well (neglecting all but one non-Newtonian mechanism [3] and not accounting for very small strain-rates [5, 15]) the steady-state flow behavior of rigid, cohesionless particles, where the inertial number is the only relevant dimensionless number relating shear-rate to the confining pressure time-scale. However, for real particles also the effect of large confining stress or, inversely, softness has to be taken into account as additional control parameter [5–9]. As new ingredients to the generalized rheology that complements the static contributions to stress, also the dynamic time-scale set by the so-called granular temperature [7] or fluidity [16–18] has to be considered. For a discussion of many of the relevant time-scales of the involved micro-mechanisms and the dimensionless numbers formed by ratios of those see Refs. [9, 19], and for experiments see Ref. [20] and references therein.

In granular systems, the interplay between strain, stress and microstructure (including anisotropy) is one micro-mechanism that can lead to dilatancy [21–23], related to the 'memory' of the packing. The transitions of granular systems from (jammed) solid to fluid and, oppositely, from un-jammed to (shear) jammed was studied in detail in Refs. [7, 23]. The evolution of the steady state anisotropy (micro-structure) is independent from the direction-dependency ("anisotropy") of stress, both in rates as well as in principal directions, i.e., tensorial eigen-system orientations [3–5]. In steady state, a certain proportionality and relative orientation of the tensors establishes, which is subject of ongoing research [5, 6].

Besides the anisotropy of the micro-structure [11, 23] an additional (isotropic) state-variable was identified as a necessary ingredient to describe the slow, quasi-static transitions between fluid - and solid-like states. As mind-changing concept, the transition point itself was proposed as the new state-variable [22, 23]; however, it could be related to various other possible variables like contact/coordination number, isotropic fabric, or the fraction of rattlers [23] and is thus not a unique choice but rather a question of convenience and matter of taste which variable one choses to use.

Starting from a static, dense packing, shear motion is only possible if the grains "unlock" from their dense, jammed arrangement. Shearing for long time, the initial state is forgotten and a steady state (critical state) is reached. The dynamics of the tails of shear bands involves a very slow approach to steady state due to the small strain rate [5, 9, 15]. The local steady state rheology was shown to be valid also in transient states [24] but requires corrections for very small strain rates [5, 9, 25].

In a particular geometry, i.e., the split bottom ring shear cell, see Refs. [1, 2, 5, 6, 8, 9] and references therein, the fields are functions of position (height and radial distance from the symmetry axis), so that a wide range of local densities, strain-rates and pressures are covered by data from a single (inhomogeneous) simulation [5, 6, 8, 9]. Having available this information, the next step is to formulate general, local constitutive relations [9] that allow to predict the systems flow behavior in more general inhomogeneous systems and applications. Similar methods and approaches can also be applied to solid-like systems [11] – all are based on the original ideas of coarse-graining from micro-to-macro [3, 12, 13], following the ideas of Isaac Goldhirsch [12]. Macroscopic data can then be related to microscopic particle - and contact-properties like particle size distributions, stiffness, friction as well as system state parameters like strain-rate (the scale of which is set by the externally applied shear-rate).

2 Theory

In the following, a short summary of recent results and some new insights on formulating a generalized local granular rheology are presented, starting with the shear rheology, but then focusing more on the hydrostatic stress, density, jamming density, strain-rate and granular temperature. Note that the rheology (constitutive relations) are expressed in dimensionless form to make them generally applicable. When parameters are given in dimensional form, those are input parameters for the simulations and to give an indication of what physical experiments the simulations are supposed to model.

When formulating a granular rheology, the starting point is the surprisingly simple and elegant so-called $\mu(I)$-rheology [5, 14] that relates – in a sheared particulate system – the so-called macroscopic (bulk) friction, i.e., the shear-stress to pressure ratio $\mu = \tau/p$, to the inertial number, i.e., the dimensionless strain-rate $I = \dot{\gamma}\, d_0/\sqrt{p'/\rho}$ with local shear rate $\dot{\gamma}$, diameter $d_0 = 0.0022$ m, particle mass-density $\rho = 2000\,\mathrm{kg/m^3}$, and dimensional pressure p'. The relation that describes nicely a surprisingly wide variety of flows [14] of rigid and cohesion-less particles at various strain rates is:

$$\mu(I) = \mu_0 + (\mu_\infty - \mu_0)\frac{1}{1 + I_0/I} \tag{1}$$

where $\mu_0 = 0.15$ and $\mu_\infty = 0.42$ represent the zero and infinite strain rate limits, respectively, and the characteristic dimensionless strain-rate, where inertial effects considerably kick in, is $I_0 = 0.06$. Note that the simulations presented below only concern particle simulations with a very small coefficient of particle contact friction, $\mu_p = 0.01$; the dependence of the coefficients in Eq. (1) on friction are considered elsewhere [21].

Corrections to the $\mu(I)$-rheology become necessary for soft particles and/or high confining stress, as shown by Singh et al. [5]; originally, linear terms were added to the above rheology for small strain-rates [5], however, these can better be re-phrased as multiplicative correction factors [9] allowing for more elegant mathematical treatment so that the original rheology is modified by multiplicative forms that tend to $f \sim 1$ if the respective mechanism is not active. The pressure/softness correction f_p appears as:

$$\mu(I,p) = \mu(I) f_p(p) = \mu(I)\exp\left(-\left(\frac{p}{p_0}\right)^{1/2}\right) \cong \mu(I)\left(1 - \left(\frac{p}{p_0}\right)^{1/2}\right) \tag{2}$$

with the dimensionless pressure $p = p'\, d_0/k$ (corresponding to the typical overlap/deformation of particles relative to their diameter), the characteristic pressure at which this correction becomes considerable, $p_0 = 0.9$, and the particle contact stiffness $k = 100$ N/m. In Ref. [5], where the linear correction was calibrated by local ring-shear

cell data, it was shown that this correction accounts for a wide range of particle stiffness (or softness), but also for different magnitudes of gravity, as in a centrifuge or on the moon.[1]

Note that the pressure dependent correction function, in its linear form, has an unreasonable zero-crossing; this is avoided by the exponential form in Eq. (2); both forms are identical in first order and thus practically identical for all values of confining pressures considered in the particle simulations [5, 9]; a decision about the functional form is not really possible with the available data and remains an open issue for future research. Several additional corrections functions f were presented in Ref. [9] but are dropped here for the sake of brevity; also cohesion involves a dimensionless number, the so-called Bond-number (Bo), as studied elsewhere [6, 7, 9, 19] and ignored in the following. The two dimensionless numbers in Eq. (2) can be expressed as ratios of time-scales, namely $I = t_p/t_{\dot{\gamma}}$ and $p = \left(t_c/t_p\right)^2$, where the subscripts refer to strain-rate, $\dot{\gamma}$, pressure, p, and contact duration, c, respectively [19]. There are many ways of constructing the dimensionless numbers that control the flow behavior and to implement the correction terms they are responsible for, however, here we choose multiplicative functions that are in first order proportional additive corrections, as shown in Ref. [5].

In order to complete the rheology for soft, compressible particles, a relation for the density as function of pressure and shear rate is missing:

$$\phi(I,p) = \phi_c \left(1 + \frac{p}{p_\phi^c}\right)\left(1 - \frac{I}{I_\phi^c}\right) \tag{3}$$

with the critical or steady state density under shear, in the limit of vanishing pressure and inertial number, $\phi_c = 0.648$, valid for a given material with a certain polydispersity [9, 19], the strain rate for which dilation would turn to fluidization, $I_\phi^c = 0.85$, and the typical pressure level for which softness leads to huge densities, $p_\phi^c = 0.33$. Note that both correction terms in Eq. (5) were first determined as additive corrections [5], identical to the multiplicative form for sufficiently small arguments. Too large inertial numbers are not allowed since they would lead to negative densities; large I would fully fluidize the system so that the rheology should be that of a granular fluid, for which standard kinetic theory applies [7]. Too large pressures would lead to enormous deformations/overlaps (or even breakage), for which the contact model and the particle simulation become questionable.

Two small adaptations of the correction functions in Eq. (3) remove the invalidity for large I, and uses an analogous but not necessarily plausible correction form for pressure, p, while remaining identical to first order Taylor expansion for small arguments:

$$\phi(I,p) = \phi_c \exp\left(\frac{p}{p_\phi^c}\right) \exp\left(-\frac{I}{I_\phi^c}\right) \tag{4}$$

[1] Using either one of the correction terms alone, without the other, leads to slightly different coefficients in Eqs. (1) and (2), e.g., when the I-dependence is neglected for the case of very small gravity and thus very small confining stress, one observes a slightly different $\mu_0 = 0.17$ due to the considerable inertial number at small p, see Eq. (14) and Fig. 5 in Ref. [5]. Thus, correction functions should always be applied together!

This new form, Eq. (4), allows for an elegant rephrasing (inversion) and express pressure as a function of density, critical state density, and inertial number, yielding:

$$p = p(\phi, I) = p_\phi^c \left(\log\left(\frac{\phi}{\phi_c}\right) - \left(-\frac{I}{I_\phi^c}\right)\right) = p_\phi^c \varepsilon_V + \frac{I}{I_p} \tag{5}$$

with the implicit definition of the (virtual, elastic) volumetric strain, $\varepsilon_V = \log(\phi/\phi_c)$, and the dynamic strain-rate non-Newtonian pressure dilatancy coefficient $I_p = I_\phi^c / p_\phi^c$. The volumetric (elastic) strain ε_V in the first term is defined relative to the stress-free reference state, where ϕ_c, is also termed the critical state density (in the zero-pressure limit of a very slowly sheared system in steady state). The factor $p_\phi^c \sim \phi C$ hides its dependence on the coordination number and can be seen as the dimensionless bulk modulus in the static limit. For the dimensional pressure $p' = pk/d_0$, all contributions should in fact be additive, which allows for further contributions (anisotropy is not considered here, but discussed in detail elsewhere [6, 11, 23]) as, e.g., the pressure from standard kinetic theory, $p'_{SKT}(\phi, T_g)$, proportional to the granular temperature, T_g [7]:

$$p'(\phi, \phi_c, I, T_g) = p'(\phi, \phi_c, I) + p'_{SKT}(\phi, \phi_c, T_g) \tag{6}$$

When the system is left at rest, $I = 0$, for vanishing T_g, the *SKT* correction vanishes, and the first term in Eq. (5) survives, for $\phi > \phi_c$ representing a linearly elastic stress-strain relation, as introduced in Ref. [21] for non-sheared systems, and confirmed later in [10, 11, 23] under shear. For $I > 0$, the second term in Eq. (5) represents the (non-Newtonian) pressure-dilatancy, i.e., an over-pressure due to the applied shear, as defined for dense fluids in Ref. [4]; for more details see references therein. Note that the rheological property dilatancy (decrease of density or increase of volume) in pressure-controlled systems, is equivalent to this pressure-dilatancy in a volume-controlled system. The dependence of the last term in Eq. (6) on the softness was studied in Ref. [7], but is not visible here, as it is subject to ongoing research.

3 Conclusions

Particle scale simulations and the micro-macro transition can guide the development of new rheological constitutive models that include and combine various mechanisms as quantified by dimensionless numbers. The original rheology for hard, cohesionless particles [14] was generalized to include the effect of large confining stress or softness (or compressibility) [5] as well as various other effects [9]. Both density and shear stress ratio are well predicted by the improved, inertial - and pressure-dependent rheology model, at least in the center of the shear band [5, 6, 9]. In the tails, however, deviations still occur, which can be due to several reasons: *(i)* the statistics is much worse in areas where the strain rate is small, *(ii)* the system has not yet reached the true steady state – as reported in Refs. [5, 9, 15], *(iii)* there can be non-local effects as encompassed, e.g., by a "fluidity" variable, as used in Refs. [16–18, 25], or there are additional local corrections needed, as proposed in Refs. [9, 21–24] and reported as

relevant for the present system in Refs. [5, 9]. The present paper was adding a kinetic contribution to the hydrostatic stress that allows to link the elastic regime to the standard kinetic theory of collisional granular gases in the respective dense/static/solid and dilute/collisional/fluid cases.

Ongoing research is aiming at finding and calibrating all the necessary additional corrections for very small strain rates [5, 9, 21], for very small pressure close to the free surface [9, 19], and also for cohesive particles [9, 19]. The next step is the implementation of such multi-purpose, generalized scalar flow/rheology models into continuum solvers. The final challenge is the development of fully tensorial flow models, as shown in Refs. [3, 4], that are needed to account for a variety of non-Newtonian aspects of atomistic, particulate and granular matter and include not only the microstructure (fabric) tensor [5, 11] but also the granular temperature [7] as introduced above, as well as other ratios of time-scale or other combinations of dimensionless numbers in the correction functions.

References

1. Luding, S.: The effect of friction on wide shear bands. Part. Sci. Tech. **26**, 33–42 (2008)
2. Luding, S., Alonso-Marroquin, F.: The critical-state yield stress (termination locus) of adhesive powders from a single experiment. Granular Matter **13**, 109–119 (2011)
3. Weinhart, T., Hartkamp, R., Thornton, A.R., Luding, S.: Coarse-grained local and objective continuum description of 3D granular flows down an inclined surface. Phys. Fluids **25**, 070605 (2013)
4. Hartkamp, R., Todd, B., Luding, S.: A constitutive framework for the non-Newtonian pressure tensor of a simple fluid under planar flows. J. Chem. Phys. **138**, 244508 (2013)
5. Singh, A., Saitoh, K., Magnanimo, V., Luding, S.: Role of gravity or confining pressure and contact stiffness in granular rheology. New J. Phys. **17**, 043028 (2015)
6. Singh, A., Magnanimo, V., Saitoh, K., Luding, S.: Effect of cohesion on shear banding in quasi-static granular material. Phys. Rev. E **90**(2), 022202 (2014)
7. Vescovi, D., Luding, S.: Merging fluid & solid granular behavior. Soft Matter **12**, 8616 (2016)
8. Roy, S., Singh, A., Luding, S., Weinhart, T.: Micro-macro transition and simplified contact models for wet granular materials. Comp. Part. Mech. **3**(4), 449–462 (2016)
9. Roy, S., Luding, S., Weinhart, T.: A general(ized) local rheology for wet granular materials. New J. Phys. **19**, 043014 (2017)
10. Göncü, F., Luding, S.: Effect of particle friction and polydispersity on the macroscopic stress-strain relations of granular materials. Acta Geotech. **8**, 629–643 (2013)
11. Kumar, N., Luding, S., Magnanimo, V.: Macroscopic model with anisotropy based on micro-macro informations. Acta Mech. **225**(8), 2319–2343 (2014)
12. Goldhirsch, I.: Stress, stress asymmetry and couple stress: from discrete particles to continuous fields. Granular Matter **12**, 239–252 (2010)
13. Weinhart, T., Thornton, A.R., Luding, S., Bokhove, O.: From discrete particles to continuum fields near a boundary. Granular Matter **14**, 289–294 (2012)
14. Midi, G.D.R.: On dense granular flows. Eur. Phys. J. E **14**, 367–371 (2004)
15. Ries, A., Wolf, D.E., Unger, T.: Shear zones in granular media: three-dimensional contact dynamics simulations. Phys. Rev. E **76**, 051301 (2007)

16. Nguyen, V.B., Darnige, T., Bruand, A., Clément, E.: Creep and fluidity of a real granular packing near jamming. Phys. Rev. Lett. **107**, 138303 (2011)
17. Kamrin, K., Koval, G.: Nonlocal constitutive relation for steady granular flow. Phys. Rev. Lett. **108**, 178301 (2012)
18. Hennan, D.L., Kamrin, K.: A predictive, size-dependent continuum model for dense granular flows. Proc. Natl. Acad. Sci. USA **110**, 6730–6735 (2013)
19. Shi, H., Luding, S., Magnanimo, V.: Limestone powders yielding and steady state resistance under shearing with different testers. In: Mallick, S.S. (ed.) Proceedings of PGBSIA 2016, 1–3 December 2016
20. Shi, H., et al.: Effect of particle size and cohesion on powder yielding and flow. KONA 2018014 (2017)
21. Göncü, F., Duran, O., Luding, S.: Constitutive relations for the isotropic deformation of frictionless packings of polydisperse spheres. C. R. Mecanique **338**(10–11), 570–586 (2010)
22. Luding, S.: Granular matter: so much for the jamming point. Nat. Phys. **12**, 531 (2016)
23. Kumar, N., Luding, S.: Memory of jamming – multiscale models for soft and granular matter. Granular Matter **18**, 58 (2016)
24. Pons, A., Darnige, T., Crassous, J., Clement, E., Amon, A.: Spatial repartition of local plastic processes in different creep regimes in a granular material. EPL **113**(2), 28001 (2016)
25. Koval, G., Roux, J.N., Corfdir, A., Chevoir, F.: Annular shear of cohesionless granular materials: from the inertial to quasistatic regime. Phys. Rev. E **79**, 021306 (2009)

Modelling of Bentonite for Nuclear Waste Disposal Facilities with Hypoplasticity

David Mašín(✉)

Charles University, Prague, Czech Republic
masin@natur.cuni.cz

Abstract. Summary of a coupled thermo-hydro-mechanical model based on hypoplasticity principles combined with the concept of double structure, aimed to predict bentonite behaviour in the simulations of planned nuclear waste repositories, is presented in this paper. The model has been developed by Mašín [11] by a hierarchical enhancement of the earlier model from [9], which did not consider the effects of temperature. That model, in turn, was a double structure enhancement of earlier models for unsaturated and saturated soils. Predictive performance of the model is presented by comparing model predictions with experiments.

Keywords: Bentonite · Clay · Hypoplasticity · Waste disposal

1 Background

Bentonite is considered as a buffer material in most design versions of planned nuclear waste repositories, separating canister with spent nuclear fuel from the host rock. It has been selected for its favourable sealing and self-healing properties: very low permeability ensures slow radionuclide migration; high swelling tendency ensures self-healing of any technological gaps or other disturbances caused by geological movements during lifetime of the repository. For this reason, bentonite represents a high-priority application of geomechanical models internationally. It is, however, also remarkably complex, as bentonite is compacted at partially saturated states, it is thermally loaded by the heat generated by the spent nuclear fuel and it is being saturated by water entering the system from the host rock. The hydraulic, thermal and mechanical properties influence each other (thermo-hydro-mechanical coupling). In this paper, a model for bentonite based on hypoplasticity principles is described to demonstrate capabilities of this modelling approach.

The model has been developed using a double-structure framework originally proposed by Gens and Alonso [3], who introduced the double structure concept, and Alonso et al. [1], who developed a complete constitutive model. Double-structure models are based on an assumption, supported by various micro-mechanical studies, that in expansive soils one can identify two levels of structure: a macrostructure, which represents an assembly of silt-size aggregates of the clay particles, and a microstructure, which represents the internal structure of these aggregates. A conceptual sketch of these two levels of structure is shown in Fig. 1. In the model by Mašín [9], separate

W. Wu (Ed.): *Desiderata Geotechnica*, SSGG, pp. 93–98, 2019.
https://doi.org/10.1007/978-3-030-14987-1_11

models are considered for the mechanical and hydraulic responses of the microstructure and of the macrostructure. These responses are coupled at each structural level, and the behavior of the two structural levels is linked through the double-structure coupling function. A schematic of the adopted modeling approach is in Fig. 1. The individual models are denoted as G^M, G^m, H^M, and H^m, respectively.

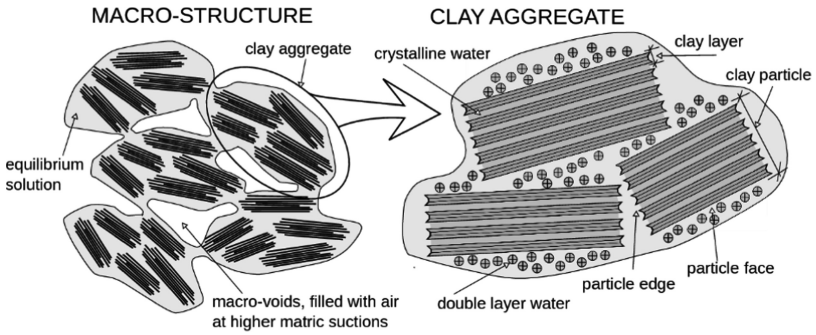

Fig. 1. Schematic representation of double structure concept (Mašín [9, 11]).

The mechanical behavior of the macrostructure (G^M) was described using the model for unsaturated soils developed by Mašín and Khalili [2], which itself was based on a hypoplastic model for saturated clays from Mašín [6, 8, 10]. The hydraulic response of the macrostructure (H^M) was based on the void ratio–dependent water retention model from Mašín [7]. The microstructure has always been considered as fully saturated (thus the H^m model is very simple), with its mechanical behavior (G^m) reversible volumetric, governed by the Terzaghi effective stress principle (see Mašín and Khalili [13] for a thorough discussion). The $G^M H^M$ coupling was accomplished by the dependency of H^M on volume change and by the dependency of the effective stress on degree of saturation of the macrostructure Sr^M. The $G^m H^m$ coupling was introduced through the adoption of the Terzaghi effective stress for the mechanical behavior of the microstructure. Finally, the double-structure coupling was controlled by a function of relative void ratio, which evolved from the original proposition by Alonso et al. [1].

The model by Mašín [11] evolved from the Mašín [9] model by including the thermal component. To accomplish this task, additional thermal dependency has been introduced for water retention curves, volumetric behaviour of microstructure and normal compression behaviour of macrostructure. The final model is a comprehensive model capable of predicting complex THM behaviour of bentonites.

2 Mathematical Formulation

Mathematical formulation of the model is based on the principles of hypoplasticity, combined with the effects of partial saturation, temperature and double structure. The primary rate equation of the model reads:

$$\overset{\circ}{\boldsymbol{\sigma}}^{M} = f_s[\mathcal{L} : (\dot{\epsilon} - f_m\dot{\epsilon}^m) + f_d\|\mathrm{N}\dot{\epsilon} - f_m\dot{\epsilon}^m\|] + f_u(\boldsymbol{H}_s + \boldsymbol{H}_T) \tag{1}$$

In Eq. (1), the primary structure of hypoplastic equation follows from critical state-based model by Gudehus [4], while the main additional components are as follows:

Behaviour of *macrostructure* is defined using the hypoplastic approach. Thus, Eq. (1) defines the effective stress rate of macrostructure $\overset{\circ}{\boldsymbol{\sigma}}^{M}$. It is defined using Bishop equation, in which the factor χ is equal to the degree of saturation of macrostructure.

$$\boldsymbol{\sigma}^{M} = \boldsymbol{\sigma}^{net} - 1S_r^M s \tag{2}$$

where $\boldsymbol{\sigma}^{net}$ is net stress, s is suction and S_r^M is degree of saturation of macrostructure defined using a hysteretic macrostructural void ratio-dependent water retention model of Brooks and Corey [2] type.

Behaviour of *microstructure* is defined using elastic volumetric model, which can be written as

$$\dot{\epsilon}^m = \frac{1}{3}\left(\alpha_s\dot{T} - \frac{\kappa_m}{p^m}\dot{p}^m\right) \tag{3}$$

where $\dot{\epsilon}^m$ is microstructural strain, $\dot{T}$ is temperature rate, p^m is microstructural mean effective stress and α_s and κ_m are parameters. Microstructure is always assumed to be fully saturated and its behaviour governed by the Terzaghi effective stress, that is

$$\boldsymbol{\sigma}^m = \boldsymbol{\sigma}^{net} - 1s \tag{4}$$

The double structure coupling is accomplished through the factor f_m appearing in Eq. (1). This factor depends or relative density, such that for the most dense state $f_m = 1$ and for the most loose state $f_m = 0$. These values mean that at the loose state microstructural strain does not cause any macrostructural deformation, because microstructural units (aggregates) swell into the macrovoids. Contrary, at the densest possible state macrostructure is basically closed, and any microstructural strain causes equivalent strain macrostructural. The factor f_m is defined as

$$f_m = 1 - (r_{em})^m \tag{5}$$

where m is a parameter and r_{em} is relative void ratio defined as

$$r_{em} = \frac{e - e_d}{e_i - e_d} \tag{16}$$

where e_d is minimum void ratio (equal to microstructural void ratio) and e_i is maximum void ratio (equal to the void ratio at the isotropic normal compression line).

Equation (1) contains two tensors $\boldsymbol{H}_s$ and $\boldsymbol{H}_T$ and a scalar factor f_u. The factors $\boldsymbol{H}_s$ and $\boldsymbol{H}_T$ are denoted as wetting- and heating-induced compaction ("collapse") factors, calculated to ensure that during wetting and heating of specimen whose state is close to the isotropic normal compression line (NCL), its state remains at NCL and thus

wetting- and heating-induced compaction is predicted. The factor f_u depends on relative density and decreases the effect of $\boldsymbol{H}_s$ and $\boldsymbol{H}_T$ for higher overconsolidation ratios.

Last, Eq. (1) contains two scalar factors f_s and f_d. These are denoted as barotropy- and pyknotropy factors and they control the effect of stress and void ratio on macrostructural soil stiffness. They were taken over from the basic hypoplastic model for clays from Mašín [6].

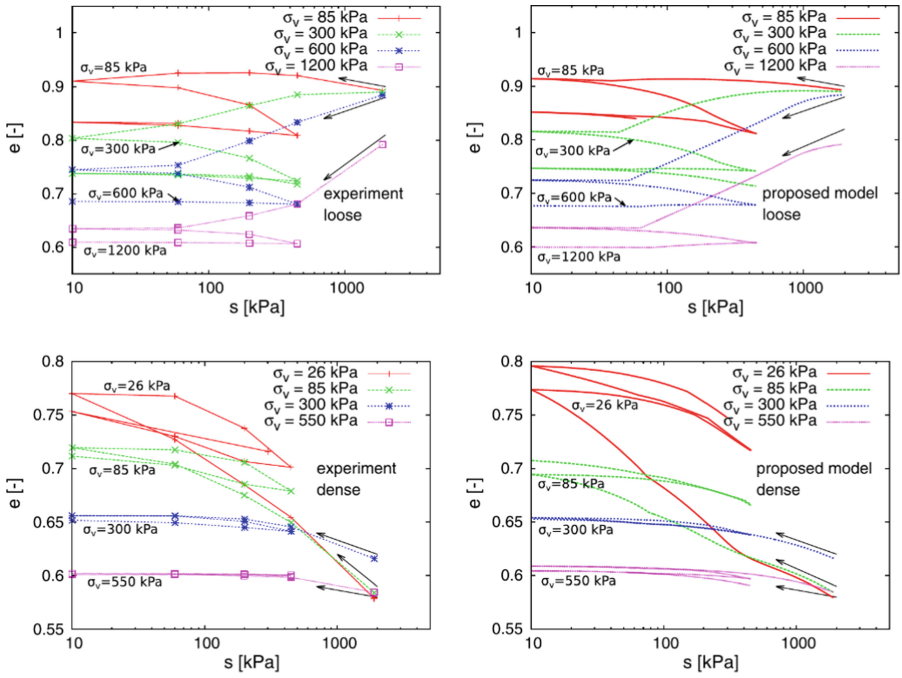

Fig. 2. Simulations of oedometric wetting-drying tests at various initial densities and vertical loads. Model performance compared with experimental data on Boom clay (Romero [14]). Figure from Mašín [9].

3 Examples of Model Predictions

Model performance for experiments relevant for modelling of bentonite in nuclear waste repository facilities is demonstrated in this section. Figure 2 shows simulations of oedometric wetting-drying tests at various initial densities and vertical loads. This figure is taken over from Mašín [9] and represents the behaviour of compacted Boom clay (data by Romero [14]). The model predicts increase of swelling strains with decrease of vertical load and increase of swelling potential with increasing relative density. For very loose samples, wetting-induced compaction is predicted instead of swelling.

Dependency of swelling pressure on the initial dry density is shown in Fig. 3 representing the data on Czech B75 bentonite (data by Hausmannová, [5]). Swelling pressures are very well reproduced.

Finally, Fig. 4 shows heating-cooling experiments at various suctions and mean stresses, simulated by Mašín [11] and compared with experimental data by Tang et al. [15] on MX80 bentonite. The thermally-induced strains depend on both suction and stress levels. The samples at lowest suction exhibit initial thermally-induced compaction, whereas the other samples exhibit thermally-induced expansion. During cooling, all the samples contract.

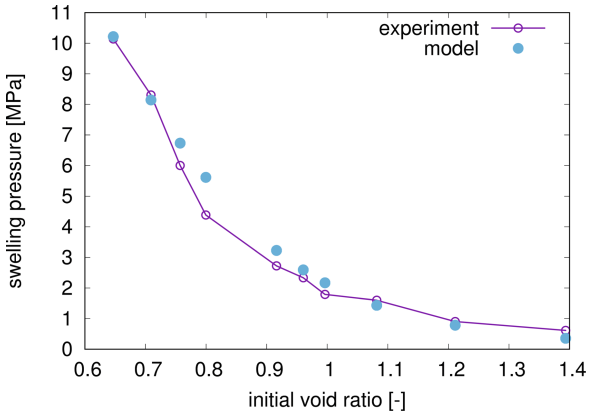

Fig. 3. Predictions of the dependency of swelling pressures on the initial void ratio (dry density). Experimental data on B75 bentonite by Hausmannová [5].

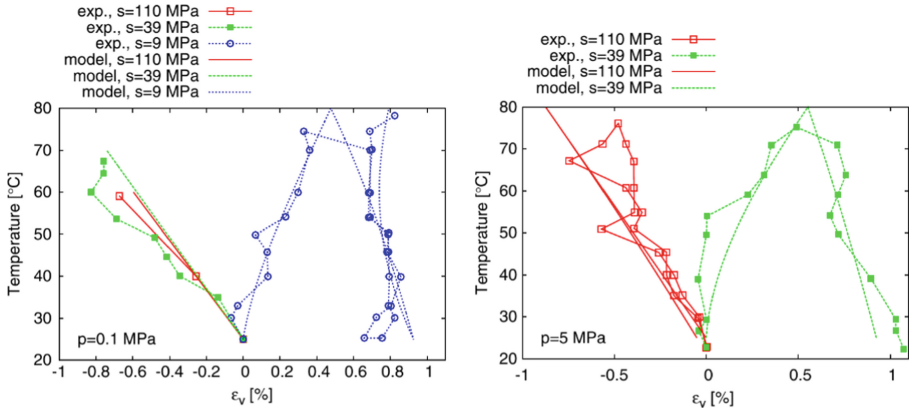

Fig. 4. Volume change during isotropic tests due to heating-cooling cycles at various suctions and mean net stresses. Experimental data by Tang et al. [15], figure from Mašín [11].

Acknowledgement. This project receives funding from the Euratom research and training programme 2014–2018 under grant agreement No. 745942. Institutional support by Center for Geosphere Dynamics (UNCE/SCI/006) is greatly appreciated.

References

1. Alonso, E.E., Vaunat, J., Gens, A.: Modelling the mechanical behaviour of expansive clays. Eng. Geol. **54**, 173–183 (1999)
2. Brooks, R., Corey, A.: Hydraulic properties of porous media. Hydrology paper no. Colorado State University (1964)
3. Gens, A., Alonso, E.: A framework for the behaviour of unsaturated expansive clays. Can. Geotech. J. **29**, 1013–1032 (1992)
4. Gudehus, G.: A comprehensive constitutive equation for granular materials. Soils Found. **36** (1), 1–12 (1996)
5. Hausmannová, L.: The influence of water pressure on the hydraulic conductivity and swelling pressure of Czech bentonites. Ph.D. thesis, Faculty of Civil Engineering, Czech Technical University (2017)
6. Mašín, D.: A hypoplastic constitutive model for clays. Int. J. Numer. Anal. Meth. Geomech. **29**(4), 311–336 (2005)
7. Mašín, D.: Predicting the dependency of a degree of saturation on void ratio and suction using effective stress principle for unsaturated soils. Int. J. Numer. Anal. Meth. Geomech. **34**, 73–90 (2010)
8. Mašín, D.: Hypoplastic Cam-clay model. Géotechnique **62**(6), 549–553 (2012)
9. Mašín, D.: Double structure hydromechanical coupling formalism and a model for unsaturated expansive clays. Eng. Geol. **165**, 73–88 (2013)
10. Mašín, D.: Clay hypoplasticity model including stiffness anisotropy. Géotechnique **64**(3), 232–238 (2014)
11. Mašín, D.: Coupled thermohydromechanical double structure model for expansive soils. ASCE J. Eng. Mech. **143**(9), 04017067 (2017)
12. Mašín, D., Khalili, N.: A hypoplastic model for mechanical response of unsaturatedsoils. Int. J. Numer. Anal. Meth. Geomech. **32**(15), 1903–1926 (2008)
13. Mašín, D., Khalili, N.: Swelling phenomena and effective stress in compacted expansive clays. Can. Geotech. J. **53**(1), 134–147 (2016)
14. Romero, E., Gens, A., Lloret, A.: Water permeability, water retention and microstructure of unsaturated compacted Boom clay. Eng. Geol. **54**, 117–127 (1999)
15. Tang, A.M., Cui, Y.J., Barnel, N.: Thermo-mechanical behaviour of a compacted swelling clay. Géotechnique **58**(1), 45–54 (2008)

Concepts of Barodesy

Gertraud Medicus(✉), Wolfgang Fellin, Dimitrios Kolymbas, and Fabian Schranz

Geotechnik und Tunnelbau, Universität Innsbruck, Innsbruck, Austria
Gertraud.Medicus@uibk.ac.at

Abstract. Barodesy is a frame for constitutive modeling of soils based on their asymptotic properties. This frame allows to derive the constitutive relation by reasoning on general properties of granular materials. The so obtained constitutive relation is a single tensorial equation that expresses the evolution of stress in dependence of the deformation. Common concepts of soil mechanics, such as critical states, barotropy (i.e. the dependence of stiffness and strength on the stress level), pyknotropy (i.e. the dependence of stiffness and strength on density) and a stress-dilatancy relation are comprised in the presented model.

1 Introduction

Compared with elastoplasticity, barodesy is an alternative frame of constitutive models for soils. The structure of the theory and a simple calibration procedure are outlined in this article, and some results of simulations of element tests are also presented. Barodesy holds, with small adjustments, for both types of soil, sand and clay. Clay, being also a particulate material consisting of minute particles has a behavior very similar to sand. Both exhibit critical states. In addition, an asymptotic behavior similar to the one described by Goldscheider for sand (see Sect. 4) was observed by Topolnicki in experiments with Kaolin clay in a Hambly type biaxial apparatus [25]. However, there are some differences that mainly arise from the fact that the stiffness of sand in monotonic compression is much higher than that of normally consolidated clay. In other words, sand has the tendency to jam at monotonic compression.

2 On the Name 'barodesy'

Usually the word 'plasticity' is used with prefixes such as hypo-, para-, hyper- etc. to denote the various constitutive models. For granular materials, however, the words 'elasticity' and 'plasticity' (to the extend the latter is associated with

W. Wu (Ed.): *Desiderata Geotechnica*, SSGG, pp. 99–112, 2019.
https://doi.org/10.1007/978-3-030-14987-1_12

notions such as yield surface, elastic regime etc., originally created for metals) can be avoided. Yield surfaces and the other concepts of plasticity theory may prejudice our perception and sometimes obscure soil mechanics, which suffers from a long lasting fragmentation in constitutive modelling [12]. The name 'barodesy' has therefore been coined by Kolymbas motivated by the fact that granular materials gain their stiffness ($\delta\acute{\varepsilon}\sigma\iota\varsigma$ = bond, hence stiffening, hardening) from externally applied pressure ($\beta\acute{\alpha}\rho o\varsigma$). Thus, the names 'barodesy' and 'barodetic' are proposed for granular materials to distinguish them from what traditionally is denoted as 'elastic' or 'plastic'.

2.1 Barodesy and Hypoplasticity

As in hypoplasticity [1,2,7,9–11,15,20,21,27–29], the barodetic constitutive equation has the general form

$$\mathring{\boldsymbol{T}} = \boldsymbol{h}(\boldsymbol{T}, \boldsymbol{D}, e) \tag{1}$$

to describe the co-rotational stress rate $\mathring{\boldsymbol{T}}$ as a function of stress $\boldsymbol{T}$, stretching $\boldsymbol{D}$ and void ratio e. However, barodesy has a different design than hypoplasticity. In the original versions of hypoplasticity published by Kolymbas, trial and error was applied by general principles of objectivity and representation theorems for tensor-valued functions. In barodesy, the amount of trial and error has been reduced in favour of reasoning on asymptotic behaviour of granulates. Asymptotic states matter not only from conceptual reasons but also from the experimental viewpoint: With long monotonic deformations, initial disturbances, related e.g. with sample preparation, fade out and do no more influence the results.

3 Symbols and Notation

As usual in mechanics, the symbols σ and $\boldsymbol{T}$ denotes the stress, and ε denotes the strain. Tensors are usually denoted either in the index notation or in the symbolic notation with boldface letters. Compared to the index notation, the symbolic notation facilitates insight into the prevailing relationships. Therefore, in this paper the symbolic notation, as introduced in [26], is mainly followed. Table 1 summarizes the symbols and notation used in this article.

Table 1. Symbols and notation

Symbol	Description
$\boldsymbol{T}$	Cauchy-stress. Its components are σ_{ij}. Its principal components are denoted as $\sigma_1, \sigma_2, \sigma_3$
$\boldsymbol{D}$	Stretching tensor, i.e. the symmetric part of the velocity gradient $\nabla \boldsymbol{v}$. It can be set approximately equal to the strain rate, $D_{ij} \approx \dot{\varepsilon}_{ij}$
$\operatorname{tr} \boldsymbol{D}$	Trace of $\boldsymbol{D}$ is the scalar quantity $\operatorname{tr} \boldsymbol{D} = D_{11} + D_{22} + D_{22}$, which denotes the rate of volume change: $\operatorname{tr} \boldsymbol{D} = \dot{\varepsilon}_{\mathrm{v}} = \dot{\varepsilon}_{11} + \dot{\varepsilon}_{22} + \dot{\varepsilon}_{33}$
e	Void ratio, i.e. the ratio V_p/V_s, where V_p and V_s are the volumes of pores and solids (grains), respectively
$\|\boldsymbol{A}\|$	The value of a tensor is its Euclidean norm: $\|\boldsymbol{A}\| = \sqrt{\operatorname{tr} \boldsymbol{A}^2}$
$\boldsymbol{A}^0$	Normalized tensor, i.e. $\boldsymbol{A}^0 = \boldsymbol{A}/\|\boldsymbol{A}\|$. Clearly, $\boldsymbol{A}^0$ is a unit tensor with $\|\boldsymbol{A}^0\| = 1$
$\delta = \operatorname{tr} \boldsymbol{D}^0$	This quantity is a measure of dilatancy
$\mathring{\boldsymbol{T}}$	Objective stress rate
c_i	Constants. It facilitates reading to clearly denote the constants in mathematical functions as such and to distinguish them from quantities that depend on other variables

4 Empirical Basis of Barodesy

Of basic importance for the following is the notion of a *proportional path*. Proportional stress and strain paths are characterized by constant ratios of the principal values $\sigma_1 : \sigma_2 : \sigma_3$ and $\varepsilon_1 : \varepsilon_2 : \varepsilon_3$, respectively.

There are two basic experimental findings for sand:

1. Starting from the stress-free state, proportional strain paths lead to proportional stress paths.
2. Starting from a non-vanishing stress state and applying a proportional strain path leads asymptotically to the proportional stress path that would be obtained starting from the stress-free state.

These two rules are inferred by Goldscheider from his test results obtained with rectilinear extensions of sand [6] (cf. also [16]). These tests have been carried out in a so-called true triaxial apparatus, which allows to apply rectilinear extensions (i.e. motions without rotation of the principal axes of deformation) independently in all three directions of space.

5 Virgin Proportional Paths

We first consider proportional strain paths starting form the stress-free state. Such paths can be volume-decreasing (we will call them 'consolidations'), characterized by $\operatorname{tr} \boldsymbol{D} < 0$, or volume preserving ('isochoric' or 'undrained'), characterized by $\operatorname{tr} \boldsymbol{D} = 0$, or volume increasing, characterized by $\operatorname{tr} \boldsymbol{D} > 0$. Clearly, the latter are not feasible with cohesionless sand.

Let us denote with $\boldsymbol{R}$ a tensor that has the direction of a proportional stress path. The question arises, how does $\boldsymbol{R}$ depend on the direction of the corresponding proportional strain path? The latter is characterized by the direction of stretching $\boldsymbol{D}$, i.e. by the normalized stretching $\boldsymbol{D}^0$. How can we determine the relation $\boldsymbol{R}(\boldsymbol{D}^0)$? This question can be easily answered if we observe that all consolidations are mapped into a specific part of the principal stress space, which is formed by the stress components σ_1, σ_2 and σ_3. This part is the octant, where all principal stresses are compressive, i.e. negative. Hence, the product $\sigma_1\sigma_2\sigma_3$ must also be negative. Now, for a proportional stress path we have $\sigma_i = \mu R_i(\boldsymbol{D}), i = 1, 2, 3$, where μ simply denotes the proportionality of σ_i and R_i.[1] With $R(D_i) := R_i$, the following condition must hold:

$$R(D_1)R(D_2)R(D_3) < 0 \qquad \text{for} \quad \operatorname{tr}\boldsymbol{D} = D_1 + D_2 + D_3 < 0 \tag{2}$$

This implies that the product $R(D_1)R(D_2)R(D_3)$ must be a function of the sum $D_1 + D_2 + D_3$, a requirement which is fulfilled by the exponential mapping

$$\boldsymbol{R}(\boldsymbol{D}) = -\exp(a\boldsymbol{D}^0) \tag{3}$$

a depends on dilatancy δ, and for $\delta = 0$ it obtains the value a_0. It should be added that Goldscheider's rules have, as every rule, some exceptions in detail. Thus, it is known that stress paths obtained with oedometric deformation are not strictly proportional, i.e. $K_0 := \sigma_2/\sigma_1$ is not strictly constant. Such 'details' can be captured by slight modifications of barodesy [4], but they are omitted here for simplicity.

5.1 Critical State Surface

Equation (3) maps all volume-reducing ($\operatorname{tr}\boldsymbol{D} < 0$) proportional strain paths into a cone in the stress space with appex at $\boldsymbol{T} = \boldsymbol{0}$, which can be called the $\boldsymbol{R}$-cone. Its boundary corresponds to paths with $\operatorname{tr}\boldsymbol{D} = 0$ and is thus the critical state surface. Consider the intersection of the $\boldsymbol{R}$-cone with a plane $\operatorname{tr}\boldsymbol{T} = \text{const}$, as shown in Fig. 1. This curve expresses the critical limit state in a so-called deviatoric plane of the stress space. The mathematical representation of this curve can be easily derived from Eq. (3): Eliminating $\boldsymbol{D}^0$ from (3) we obtain:

$$\boldsymbol{D}^0 = \frac{1}{a}\ln(-\boldsymbol{R})\ . \tag{4}$$

The requirement $\operatorname{tr}\boldsymbol{D}^0 = 0$ results in $\ln(-R_1R_2R_3) = 0$ or $R_1R_2R_3 = -1$. From the additional requirement $\|\boldsymbol{D}^0\| = 1$ we obtain:

$$[\ln(-R_1)]^2 + [\ln(-R_2)]^2 + [\ln(-R_3)]^2 = a_0^2\ . \tag{5}$$

[1] Herein, $R_i(\boldsymbol{D})$ are the principal values of $\boldsymbol{R}(\boldsymbol{D})$.

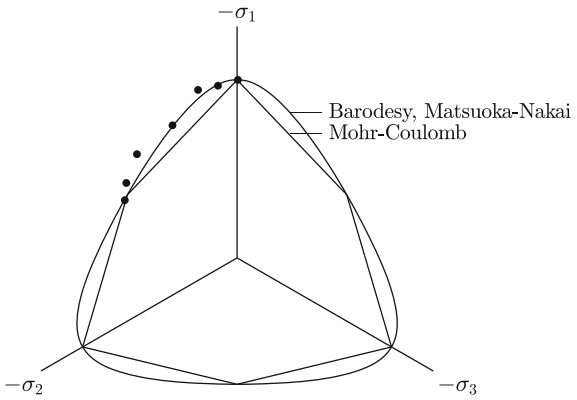

Fig. 1. Critical stress states in the deviatoric plane ($\mathrm{tr}\,\boldsymbol{T} = -500$ kPa): normally consolidated San Francisco Bay Mud (•, $\varphi_c = 30.6°$) [14] is compared with Matsuoka-Nakai, Mohr-Coulomb and barodesy. Barodesy and Matsuoka-Nakai practically coincide [5].

For the here considered proportional paths holds: $\boldsymbol{T} = \mu \boldsymbol{R}$, $0 < \mu < \infty$, hence we can replace in this equation $\boldsymbol{R}$ by $\boldsymbol{T}/\mu$ and obtain finally the equation of critical states in the stress space[2]:

$$\left(\ln \frac{\sigma_1}{\sqrt[3]{\sigma_1\sigma_2\sigma_3}}\right)^2 + \left(\ln \frac{\sigma_2}{\sqrt[3]{\sigma_1\sigma_2\sigma_3}}\right)^2 + \left(\ln \frac{\sigma_3}{\sqrt[3]{\sigma_1\sigma_2\sigma_3}}\right)^2 = a_0^2 \,. \tag{6}$$

Equation (6) is homogeneous of the 0-th degree in $\boldsymbol{T}$ and describes thus a conical surface in the stress space with apex at $\boldsymbol{T} = \boldsymbol{0}$. Its intersection with a plane $\mathrm{tr}\,\boldsymbol{T} = \mathrm{const}$ is shown in Fig. 1. Its shape *practically coincides* [5] with the curve obtained by the well-known expression of Matsuoka & Nakai:

$$\frac{(\sigma_1+\sigma_2+\sigma_3)(\sigma_1\sigma_2+\sigma_1\sigma_3+\sigma_2\sigma_3)}{\sigma_1\sigma_2\sigma_3} = \mathrm{const} \,. \tag{7}$$

Equation (3) maps not only isochoric but also volume-reducing and volume increasing proportional strain paths to the corresponding proportional stress paths. It proves that this mapping gets more realistic if we let a depend on dilatancy δ, e.g. as

$$a(\delta) = -30 + c_3 \frac{\left|\delta - \sqrt{2}\right|^{c_2}}{\left(1 + |\delta - \sqrt{2}|\right)^{c_1}} . \tag{8}$$

This modification does not affect isochoric (i.e. undrained) proportional strain paths with $\delta = 0$. Thus, we replace Eq. (3) by equation

$$\boldsymbol{R}(\boldsymbol{D}) = -\exp\left[\left(-30 + c_3 \frac{\left|\delta - \sqrt{2}\right|^{c_2}}{\left(1 + |\delta - \sqrt{2}|\right)^{c_1}}\right) \boldsymbol{D}^0\right] . \tag{9}$$

[2] From $\sigma_1\sigma_2\sigma_3 = -1/\mu^3$ we obtain $\mu = -1/\sqrt[3]{\sigma_1\sigma_2\sigma_3}$ and replace in Eq. (5) R_i by T_i/μ.

This equation is capable to map arbitrary proportional paths (cf. Fig. 2).

For the calibration of c_1, c_2 and c_3 the stress ratios $K = \sigma_1/\sigma_2$ from the oedometer test (e.g. Jáky's law $K_0 = 1 - \sin\varphi_c$), the critical state $\left(K_c = \frac{1-\sin\varphi_c}{1+\sin\varphi_c}\right)$ and a dilatant stress state (e.g. according to Chu and Lo [3]) can be used (marked with circles in Fig. 2). All these stress states can be calculated with the critical friction angle φ_c. For a critical friction angle of 30° the constants yield $c_1 = 0.1005$, $c_2 = 0.0782$ and $c_3 = 30.9483$.

In Fig. 2, results of (9) are compared with the relation found by Chu and Lo [3]

$$\eta = \frac{q}{p'} = M + \frac{M}{3}\tan\beta \qquad \text{with} \qquad M = \frac{6\sin\varphi_c}{3-\sin\varphi_c} \tag{10}$$

Here $\tan\beta = \frac{-\dot{\varepsilon}_{11}}{\dot{\varepsilon}_v}$ is an alternative measure of dilatancy with

$$\delta = \frac{\tan\beta}{\sqrt{1+\frac{(1+\tan\beta)^2}{2}}} \quad . \tag{11}$$

This relationship is experimentally well proofed.

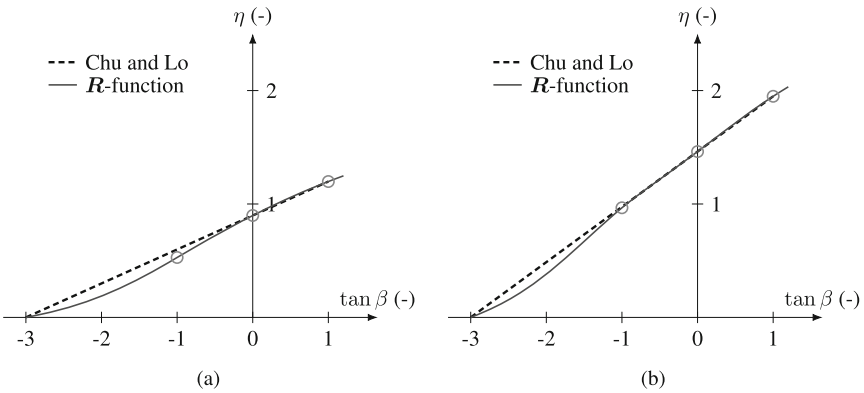

Fig. 2. Comparison of the stress-dilatancy relation from Chu and Lo with results obtained with the $\boldsymbol{R}$-function for $\varphi_c = 23°$ (a) and $\varphi_c = 36°$ (b).

6 Proportional Paths and Fading Memory

Now we start from a stress state $\boldsymbol{T} \neq \boldsymbol{0}$ and apply the stretching $\boldsymbol{D}$. In order to asymptotically approach the corresponding proportional stress path $\boldsymbol{T} = \mu\boldsymbol{R}(\boldsymbol{D})$, the stress rate $\mathring{\boldsymbol{T}}$ must be oriented towards a point of the proportional stress path with the direction $\boldsymbol{R}(\boldsymbol{D})$, i.e.

$$\boldsymbol{T} + \lambda\mathring{\boldsymbol{T}} = \mu_1\boldsymbol{R}(\boldsymbol{D}), \tag{12}$$

where the positive constants μ, μ_1 and λ need not be further specified at the moment. If we eliminate $\mathring{\boldsymbol{T}}$ we obtain an *evolution equation for the stress:*

$$\mathring{\boldsymbol{T}} = \nu_1 \boldsymbol{R}(\boldsymbol{D}) + \nu_2 \boldsymbol{T} \tag{13}$$

with scalar quantities ν_1 and ν_2. Equation (13) is already the general form of the barodetic constitutive relation. To comply with barotropy (i.e. dependence on σ), pyknotropy (i.e. dependence on e) and rate independence, ν_1 and ν_2 can be further specified, such that the barodetic constitutive equation obtains the following specific form:

$$\mathring{\boldsymbol{T}} = h \cdot (f \boldsymbol{R}^0 + g \boldsymbol{T}^0) \cdot \|\boldsymbol{D}\| \quad . \tag{14}$$

where $\boldsymbol{R}$ is given by Eq. (9). The quantities f and g will be specified below. h is responsible for the stiffness and depends on $\|\boldsymbol{T}\|$. Subsequently it will be shown how all known concepts of soil mechanics can be cast in the frame given by Eq. (14).

7 Limit States and Peaks

At limit states the stress rate vanishes:

$$\mathring{\boldsymbol{T}} = \boldsymbol{0}. \tag{15}$$

Limit states are manifested either as peak or residual (critical) limit states, where the stress-strain curves obtain a horizontal slope. In barodesy, $\dot{\boldsymbol{T}} = \boldsymbol{0}$ implies:

$$f \boldsymbol{R}^0 + g \boldsymbol{T}^0 = \boldsymbol{0}. \tag{16}$$

This tensorial equation implies[3]:

$$\boldsymbol{R}^0 = \boldsymbol{T}^0 \tag{17}$$

$$f + g = 0 \tag{18}$$

Interestingly, Eq. (17) contains a flow rule, i.e. a stress-dilatancy relation for peak states. Critical limit states are obtained with $\delta = 0$ **and** $e = e_c$, whereas peak limit states are obtained with $\delta > 0$ **and** $e < e_c$.

8 Incremental Non-linearity

Different stiffnesses at loading and unloading and, consequently, irreversible or hysteretic mechanical behaviour imply incremental non-linearity. Both, elasto-plastic and hypoplastic relations exhibit incremental non-linearity. The elasto-plastic approach consists in introducing (at least) two different stiffnesses, one

[3] The other two possibilities, (i) $\boldsymbol{R}^0 = -\boldsymbol{T}^0$ and $f - g = 0$, as well as (ii) $f = 0$ and $g = 0$, can be excluded, because $\boldsymbol{R}$ always points to the compression octant, and f and g cannot vanish simultaneously, see Eqs. 20 and 21.

for loading and one for unloading. A criterion has to be added to distinguish loading from unloading. In the frame of hypoplasticity and barodesy, a unique expression for the stress rate (or stiffness) is used, and the distinction between loading and unloading is accomplished by the non-linearity of this equation. In barodesy, the difference of stiffness at loading and unloading is modelled by the fact that the second term (i.e. $g\boldsymbol{T}^0$) in Eq. (14) is not changed if $\boldsymbol{D}$ is switched to $-\boldsymbol{D}$, whereas the first term (i.e. $f\boldsymbol{R}^0$) undergoes a change.

9 Barodetic Constitutive Equations

The main equation of barodesy is given by Eq. 14. The scalar functions h, f and g obtain different representation for sand and clay.

9.1 Sand

For sand the scalar functions h, f and g of the barodetic constitutive equation are [13]:

$$h = -\frac{c_4 + c_5\|\boldsymbol{T}\|}{e - e_{\min}} \tag{19}$$

$$f = \delta + c_6 e_c \tag{20}$$

$$g = -c_6 e \tag{21}$$

e_c is a stress-dependent critical void ratio. Further details are given in [13]. The calibration must take into account the critical state line $e_c(p)$, the determination of which is still extremely difficult for sand.

9.2 Clay

In the open access article [19] a detailed description of the equations of barodesy for clay can be found. The scalar functions h, f and g in Eq. (14) are:

$$h = c_4\|\boldsymbol{T}\| \tag{22}$$

$$f = c_6 \cdot \beta \cdot \delta - \frac{1}{2} \tag{23}$$

$$g = (1 - c_6) \cdot \beta \cdot \delta + \left(\frac{1+e}{1+e_c}\right)^{c_5} - \frac{1}{2} \tag{24}$$

$$\text{with} \qquad e_c = \exp\left(N - \lambda^* \ln \frac{2\,p}{\sigma^*}\right) - 1 \tag{25}$$

$$\text{and} \qquad \beta = -\frac{1}{c_4 \Lambda} + \frac{1}{\sqrt{3}} 2^{c_5 \lambda^*} - \frac{1}{\sqrt{3}} \tag{26}$$

$$\text{with} \qquad \Lambda = -\frac{\lambda^* - \kappa^*}{2\sqrt{3}}\delta + \frac{\lambda^* + \kappa^*}{2} \tag{27}$$

The constants c_i can be calibrated on the basis of the critical state soil mechanics parameters φ_c, N, λ^* and κ^*.

Isotropic loading and unloading of Weald clay is shown in Fig. 3. The calibration of the parameters N, λ^* and κ^* is illustrated in the $\ln(1+e)$ - $\ln p'$ plot Fig. 3(b). The critical friction angle φ_c' is calibrated by a normally consolidated CU test. The four soil parameters N, λ^*, κ^* and φ_c' are sufficient to calibrate barodesy for clay [18,19].

10 Simulation of Element Tests

In this section simulations of element tests with and without rotation of principal axes are shown. Element tests in general are idealizations and, in reality inhomogenities occur. Especially with shearing, localization takes place and the loss of homogeneity is unavoidable.

10.1 Rectilinear Extensions

Proportional Paths
Applying various proportional strain paths starting at a non-vanishing stress state produces a fan of curved stress paths, all of which have to stay within the allowed range (fan) in the stress space. The corresponding graph (Fig. 4) is a visualisation of the performance of a constitutive equation.

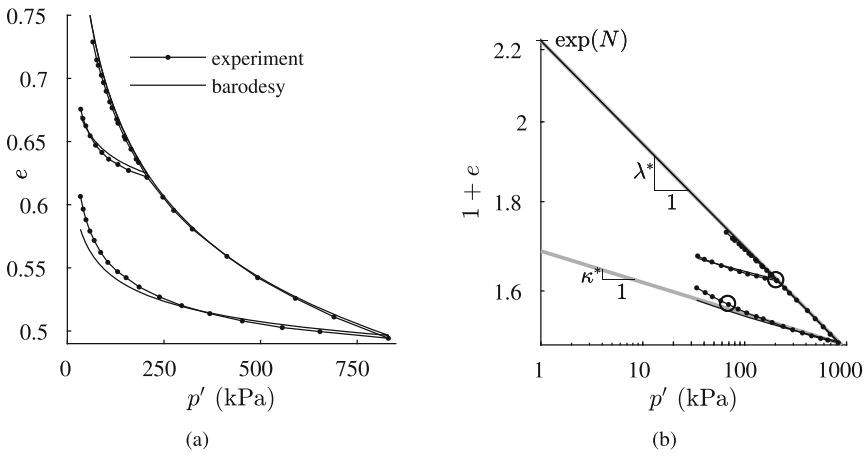

Fig. 3. Isotropic loading and unloading: Experimental results of Weald clay ([17], data from [8]) and numerical simulation with barodesy.

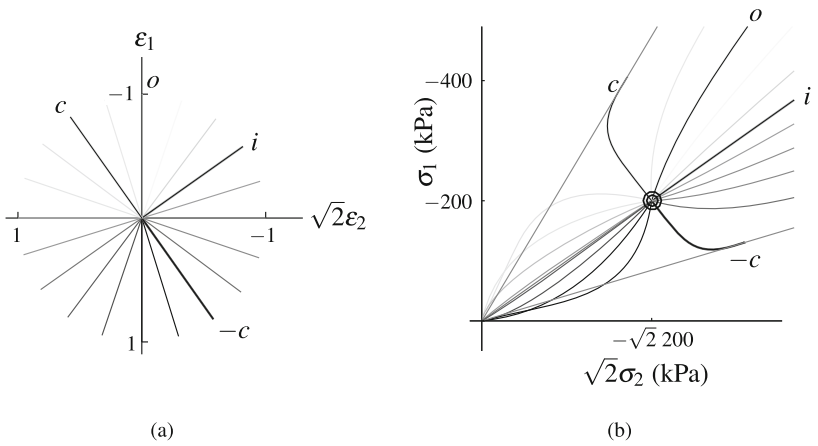

Fig. 4. Stress paths (b) corresponding to proportional strain paths (a) starting from a non-vanishing stress state. Note that stress paths asymptotically approach corresponding proportional stress paths. Weald clay ($\varphi_c = 24°$) is simulated.

Drained Triaxial Tests

In Figs. 5 and 6 simulations of drained triaxial tests with barodesy are shown. The highly overconsolidated/dense samples dilate to reach the critical state line. The normal and slightly overconsolidated/loose samples contract to reach the CSL. In Fig. 6 the highly overconsolidated samples (gray backed area) reach peak friction angles which are higher than the critical friction angle of $\varphi_c = 24°$.

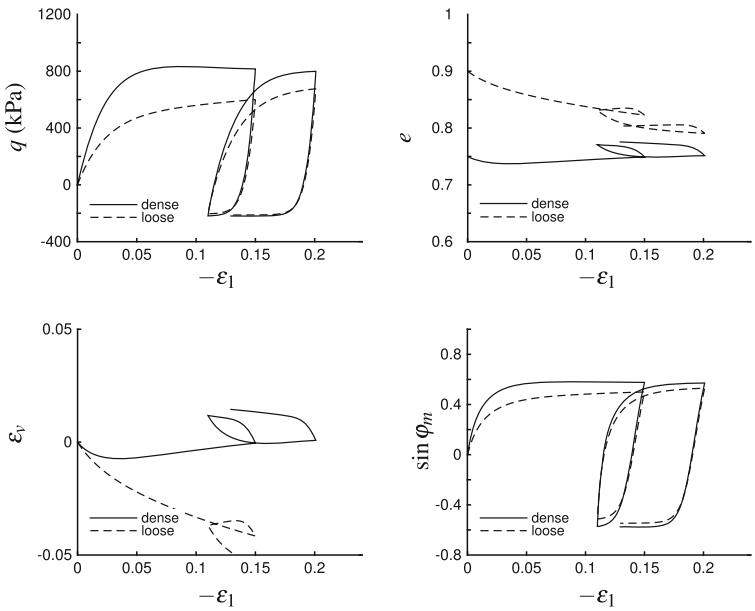

Fig. 5. Simulations with barodesy of drained triaxial tests

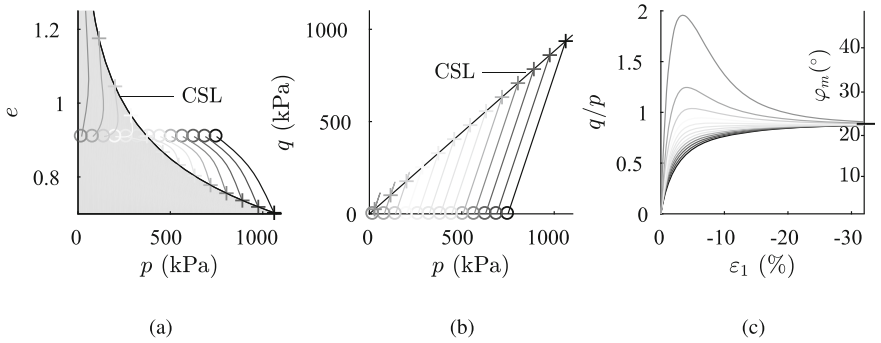

Fig. 6. Simulations with barodesy of drained triaxial tests of London clay ($\varphi_c = 24°$).

10.2 Rotation of Principal Stress and Strain Axes

Figures 7 and 8 present a simulation from [19] of a simple shear test with a constant vertical stress of $\sigma_y = -100\,\text{kPa}$. The evolution of the shear stress τ_{xy} is plotted over the shear strain γ. The angle α_σ denotes the inclination of major principal stress to the horizontal direction x, and α_D is the inclination of major principal stretching. In Fig. 7a Weald clay sample with initial stress $\boldsymbol{T} = \begin{pmatrix} T_{\text{ini}} & 0 & 0 \\ 0 & K_0 \cdot T_{\text{ini}} & 0 \\ 0 & 0 & K_0 \cdot T_{\text{ini}} \end{pmatrix}$ is sheared. The major principal stress direction α_σ is 90° at zero shear strain and decreases to $\approx 45°$ with ongoing shear strain. The difference between the angles α_D and α_σ, i.e., the *angle of non-coaxiality* $\alpha_D - \alpha_\sigma$ becomes very small,[4] i.e., $\alpha_\sigma \approx \alpha_D \approx 45°$ at the critical state. Similar results with hypoplasticity and an elasto-plastic model are shown in [23]. Experiments on sand according to [22] and DEM simulations [24,31] yield similar results, cf. [30].

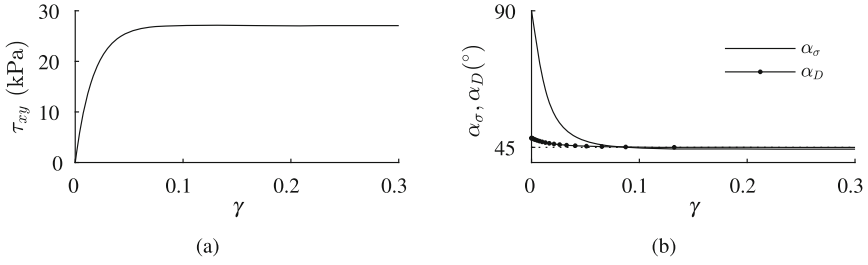

Fig. 7. Simple shear test with a constant vertical stress of $\sigma_y = -100\,\text{kPa}$, the initial radial stress is $\sigma_x = (1 - \sin\varphi_c) \cdot \sigma_y = -59.33\,\text{kPa}$. In (b) directions of principal stress α_σ and principal stretching α_D are shown. Weald Clay with an initial void ratio $e_{\text{ini}} = 0.68$ is simulated with barodesy. Figure from [19].

[4] At critical states $\alpha_D - \alpha_\sigma \approx 0.5°$. Neglecting the Zaremba/Jaumann terms $-\boldsymbol{W}\boldsymbol{T} + \boldsymbol{T}\boldsymbol{W}$ yields $\dot{\boldsymbol{T}} = \mathring{\boldsymbol{T}}$. It follows that $\alpha_D - \alpha_\sigma = 0°$ at failure.

In Fig. 8, the evolution of the *angle of non-coaxiality* with ongoing shear strain is shown for different initial K_0 values. In Fig. 8(a), DEM simulations from [24,31] show that the angle of non-coaxiality is small for $K_0 = 1$. For $K_0 = 2$, the angle of non-coaxiality decreases with ongoing shear strain to $\approx 0°$; and for $K_0 = 0.5$ it increases to $\approx 0°$. Zhang [31] states that non-coaxiality is significant before 10% shear strain. The predictions with barodesy in Fig. 8(b) are in good agreement with the DEM simulations in Fig. 8(a), which indicates that barodesy is applicable for general deformation, i.e., rotation of principal stress and strain axes.

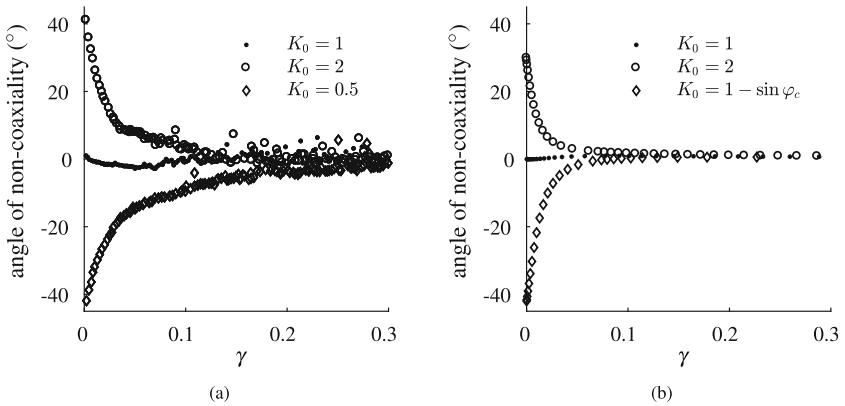

Fig. 8. Evolution of the angle of non-coaxiality in a simple shear test with different initial K_0 values: in (a), DEM simulations from [24,31] are shown, in (b), Weald Clay with $e_{\text{ini}} = 0.68$ is simulated with barodesy. Figure from [19].

11 Conclusions

In total, barodesy may be considered as attractive for its simplicity and elegance but has still potential for improvement, which should however preserve simplicity.

The present version of barodesy cannot cover all aspects of soil behavior. The memory of past loading is stored only in the actual stress $\boldsymbol{T}$ and the actual porosity e, and this is not sufficient to cover all aspects of re-loading, in particular the so-called aspects of 'small strain stiffness'. Though, it is interesting to note how many aspects of memory can be covered with $\boldsymbol{T}$ and e only.

Acknowledgements. The first author is supported by a research grant of the Austrian Science Fund (FWF): P 28934-N32

References

1. Bauer, E.: Calibration of a comprehensive hypoplastic model for granular materials. Soils Found. **36**(1), 13–26 (1996)
2. Bauer, E.: The critical state concept in hypopasticity. In: Yuan, J.X. (ed.), Computer Methods and Advances in Geomechanics, pp. 691–696. Balkema (1997)
3. Chu, J., Lo, S.C.R.: Asymptotic behaviour of a granular soil in strain path testing. Géotechnique **44**, 65–82 (1994)
4. Fellin, W.: Extension to barodesy to model void ratio and stress dependency of the K0 value. Acta Geotech. **8**(5), 561–565 (2013)
5. Fellin, W., Ostermann, A.: The critical state behaviour of barodesy compared with the Matsuoka-Nakai failure criterion. Int. J. Numer. Anal. Methods Geomech. **37**, 299–308 (2011)
6. Goldscheider, M.: Grenzbedingung und Fließregel von Sand. Mech. Res. Comm. **3**, 463–468 (1976)
7. Gudehus, G.: A comprehensive constitutive equation for granular materials. Soils Found. **36**(1), 1–12 (1996)
8. Henkel, D.: The effect of overconsolidation on the behaviour of clays during shear. Géotechnique **6**, 139–150 (1956)
9. Herle, I., Kolymbas, D.: Hypoplasticity for soils with low friction angles. Comput. Geotech. **31**, 365–373 (2004)
10. Kolymbas, D.: A rate-dependent constitutive equation for soils. Mech. Res. Comm. **4**, 367–372 (1977)
11. Kolymbas D.: A generalised hypoelastic cosntitutive law. In: Proceedings of XI International Conference on Soil Mechanics and Foundation Engineering, vol. 5, p. 2626, Balkelma, San Francisco (1985)
12. Kolymbas, D.: The misery of constitutive modelling. In: Kolymbas, D. (ed.) Constitutive Modelling of Granular Materials, pp. 11–24. Springer, Heidelberg (2000)
13. Kolymbas, D.: Introduction to barodesy. Géotechnique **65**, 52–65 (2015)
14. Lade P.V.: Effects of consolidation stress state on normally consolidated clay. In: Rathmayer, H. (ed.), Proceedings of NGM-2000: XIII Nordiska Geoteknikermötet, Helsinki, Finland, Building Information Ltd., (2000)
15. Mašín, D.: Hypoplastic Cam-clay model. Géotechnique **62**, 549–553 (2005)
16. Mašín, D.: Asymptotic behaviour of granular materials. Granular Matter **14**(6), 759–774 (2012)
17. Mašín, D.: Clay hypoplasticity with explicitly defined asymptotic states. Acta Geotech. **8**, 481–496 (2013). Springer, Berlin Heidelberg
18. Medicus, G., Kolymbas, D., Fellin, W.: Proportional stress and strain paths in barodesy. Int. J. Numer. Anal. Methods Geomech. **40**, 509–522 (2016)
19. Medicus, G., Fellin, W.: An improved version of barodesy for clay. Acta Geotech. **12**, 365–376 (2017)
20. Niemunis A.: Extended hypoplastic models for soils. Heft 34, Schriftenreihe des Inst. f. Grundbau u. Bodenmechanik der Ruhr-Universitaet Bochum (2003)
21. Niemunis, A., Herle, I.: Hypoplastic model for cohesionless soils with elastic strain range. Mech. Cohesive-Frict. Mater. **2**(4), 279–299 (1997)
22. Roscoe K., Bassett R., Cole E.: Principal axes observed during simple shear of a sand. In: Proceedings of the 4th European Conference on Soil Mechanics and Geotechnical Engineering, vol. 1, pp. 231–237 (1967)
23. Schranz, F., Fellin, W.: Stability of infinite slopes investigated with elastoplasticity and hypoplasticity. Geotechnik **39**(3), 2190–6653 (2016)

24. Thornton, C., Zhang, L.: A numerical examination of shear banding and simple shear non-coaxial flow rules. Philos. Mag. **86**, 3425–3452 (2006)
25. Topolnicki M.: Observed stress-strain behaviour of remolded saturated clay and examination of two constitutive models. Veröffentlichungen des Instituts für Bodenmechanik und Felsmechanik der Universität Fridericiana in Karlsruhe (1987)
26. Truesdell C., Noll W.: The non-linear field theories of mechanics. In: Encyclopedia of Physics, vol. IIIc. Springer (1965)
27. von Wolffersdorff, P.A.: A hypoplastic relation for granular materials with a predefined limit state surface. Mech. Cohesive-Frict. Mater. **1**(1), 251–271 (1996)
28. Wu, W.: Hypoplastizität als mathematisches Modell zum mechanischen Verhalten granularer Stoffe. Veröffentlichungen des Instituts für Bodenmechanik und Felsmechanik der Universität Fridericiana in Karlsruhe, Heft 129 (1992)
29. Wu, W., Bauer, E., Kolymbas, D.: Hypoplastic constitutive model with critical state for granular materials. Mech. Mater. **23**, 45–69 (1996)
30. Yu, H.S.: Plasticity and Geotechnics. Springer, US (2006)
31. Zhang L.: The behaviour of granular material in pure shear, direct shear and simple shear. Aston University (2003)

A Model for Trap Door Flow from a Deep Container

H.-B. Muhlhaus[1(✉)] and L. N. Moresi[2]

[1] School of Earth and Environmental Science, The University of Queensland, Brisbane 4071, Australia
h.muhlhaus@uq.edu.au
[2] Earth Sciences, The University of Melbourne, Melbourne 3010, Australia

Abstract. Computational simulations of trap door flow in cohesive frictional, materials are presented. We focus on flows where the extraction volume is generated by dilatancy. The dilatancy is caused by micro-cracking associated with the loss of cohesion at the onset of flow and/or the transition of the granulate into a more mobile, more loose packing order. The material behavior is modelled as a non-Newtonian fluid including rigid plastic behavior as a limit case. A rate dependent cohesion term considers the fluid like behavior if collisions dominate the intergranular momentum transfer. The simulations are based on an implicit particle-in-cell finite element code [1] developed by the second author. The implementation of the model equations is benchmarked against an analytical solution for gravity driven flow in an infinite chute.

Keywords: Dilatancy · Rate dependent granular flow · Moving particle method · Plasticity

1 Introduction

Granular flow from man-made or natural containers occurs in numerous industrial applications related to bulk materials handling, silo flows and mass mining techniques such as block caving. In this paper the focus is on the case where the discharge volume is not provided by surface subsidence or other external sources but by inelastic volume expansion the so called dilatancy observed in dense granular materials (e.g. Gudehus [3]; Hejko and Tejchman [9]). The situation is nicely illustrated in the experiment depicted in Fig. 1. A rectangular container with a trapdoor at the bottom surface is filled with dense granular material. As the trapdoor is lowered (Fig. 1a) two narrow zones of intense shearing develop forming roughly a triangle above the outlet. The dilatancy associated with the shearing produces the extraction volume corresponding to the trapdoor displacement. As the volume produced by dilatancy is exhausted, continued lowering of the trapdoor requires propagation of the dilatant deformation zone as depicted in Fig. 1b, c. In the following section we propose a simple, rigid plastic, non-associated plasticity model.

The model forms the basis for a numerical simulation of the trapdoor problem (Sect. 3) in which the influence of the model parameters on the evolution of the deformation pattern and the extraction volume is investigated.

W. Wu (Ed.): *Desiderata Geotechnica*, SSGG, pp. 113–118, 2019.
https://doi.org/10.1007/978-3-030-14987-1_13

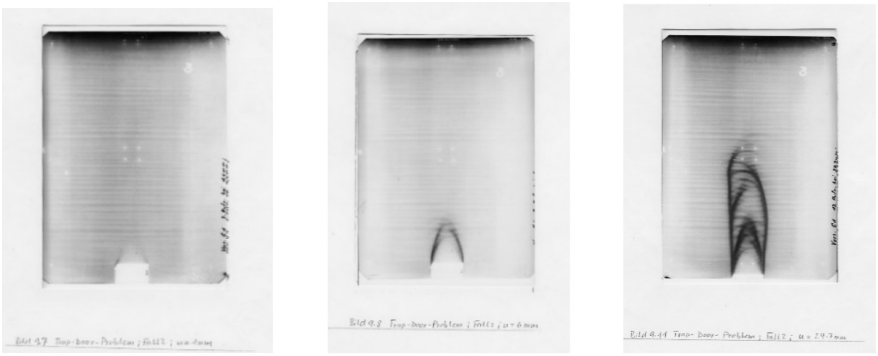

(a) (b) (c)

Fig. 1. Evolving deformation pattern as trap door is lowered (Experimental results by Vardoulakis 2002, private communication)

2 Granular Flow

In granular flows such as flows from containers, silos or, on a larger scale, in caving operations (mining), particle movements are large and are associated with large velocity gradients in zones between active and stagnant flow. Elastic deformations are unimportant in such a situation and the deformation can be described, in principle, by a rigid-plastic model. The internal boundary value problem associated with a strictly rigid-plasticity model however is difficult to solve for non-trivial problems. Conforming to tradition, then, we weaken the rigidity constraint by keeping elastic- or introducing viscous terms whereby the elastic moduli or viscosities play the role of penalty parameters, penalizing, (i.e. suppressing) non-plastic contributions to the deformation.

We describe the non-plastic part of the flow as an isotropic, viscous fluid with shear viscosity η and bulk viscosity η_B. The viscous formulation turns out to be more robust (no stress advection) computationally than the usual elastic models. Our viscous-plastic model for rigid-plastic flow reads:

$$D_{ij} = \frac{\sigma'_{ij}}{2\eta} - \frac{p}{9\eta_{\mathbf{B}}}\delta_{ij} + \dot{\gamma}^p\left(\frac{\sigma'_{ij}}{2\tau} + \frac{v}{3}\delta_{ij}\right) \tag{1}$$

In Eq. (1), D_{ij} designates the stretching, σ_{ij} the stress, $p = -1/3\sigma_{kk}$ is the pressure, $\tau = \sqrt{1/2\sigma'_{ij}\sigma'_{ij}}$ is the equivalent stress deviator, v is the dilatancy parameter, and the prime denotes the deviator of a tensor The equivalent plastic strain rate reads $\dot{\gamma}^p = \sqrt{2D^{'p}_{ij}D^{'p}_{ij}}$ and the total equivalent strain rate $\dot{\gamma}$ is defined accordingly. In combination with (1) we assume a Drucker-Prager type yield criterion:

$$F = \tau - \mu p - \tau_Y \leq 0. \tag{2}$$

The friction and the dilatancy function μ and ν as well as the cohesive strength τ_Y may depend on the equivalent plastic strain and strain rate γ^p and $\dot{\gamma}^p$ respectively. While the focus in engineering geo-mechanics is mainly on rate independent behavior, rate dependence is considered in geophysics mainly in the context of earthquake research (key word: rate and state friction, e.g. Rice [6]). There is a significant, mainly theoretical literature in physics and engineering on fast granular flows (e.g. [7, 8], Gudehus [4]) inspired by the mathematical theories of non-uniform gases by Chapman and Cowling [2]. These theories lead to relationships similar to the rheology of a thermo-viscous fluid. Rate dependence of μ in the context of granular flow down an incline was considered by Jop et al. [5]. In the present case, fluid-like granular behavior needs to be included into the constitutive model in order to capture the flow in the vicinity of the outlet (the trapdoor, assumed open, allowing free outflow) in the simulations presented here. The simplest possibility to introduce fluid-like behavior in our model is to assume rate dependence of the cohesive strength by assuming

$$\tau_Y = \tau_0(\gamma^p) + \eta^p \dot{\gamma}^p \tag{3}$$

The plastic viscosity η^p, assumed as constant for simplicity, is related to the intergranular collisions in the vicinity of the trapdoor. Viscous effects in the friction- and dilatancy functions are not considered. Specific forms are considered in Sect. 3. From Eqs. 1 and 2 we derive

$$\dot{\gamma} = \tau/\eta + \dot{\gamma}^p \tag{4}$$

$$\dot{\gamma}^p = F^v(\eta(1+\eta^p/\eta) + \mu\nu\eta_B)^{-1} \text{ where } F^v = \eta\dot{\gamma} + \mu\eta_B D_{kk} - \tau_0 \tag{5}$$

In (4) the equivalent plastic strain rate is positive if $F^v > 0$. Combining (1)–(5) the constitutive relationships may be written as:

$$\sigma'_{ij} = 2(\mu p + \tau_Y)\dot{\gamma}^{-1} D'_{ij}, p = -\eta_B(D_{kk} - \nu\dot{\gamma}^p) \text{ for } F^v > 0 \text{ and} \tag{6}$$

$$\sigma'_{ij} = 2\eta D'_{ij}, \quad p = -\eta_B D_{kk} \quad \text{for} \quad F^v \leq 0 \tag{7}$$

Insertion of (3) into the first of the relations (6) yields:

$$\sigma'_{ij}(1+\eta^p/\eta) = 2(\mu p + \tau_0)\dot{\gamma}^{-1} D'_{ij} + 2\eta^p D'_{ij} \tag{8}$$

In our trapdoor application, the viscous term in (8) is important only in the vicinity of the trapdoor where p and τ_0 approach zero so that fluid like behavior prevails. The effective shear viscosity $\eta_{eff} = \tau/\dot{\gamma}$ approaches an upper bound $\eta_{eff} = \eta$ for $\dot{\gamma} \to 0$ and the lower bound $\eta_{eff} = \eta^p$ is obtained as $\dot{\gamma} \to \infty$.

3 Trap Door Flow

Trap door models may serve as an analogue for gravity induced fracture and flow in the so-called cave mining methods, gravity flow induced by chemical erosion at depth (e.g. sink holes) or deformation of soft structures such as pipelines through the overburden load.

The geometry, boundary and initial conditions of the trapdoor model considered here are shown in Fig. 2. The ratio of the height to trapdoor width is assumed large enough to ensure that the outflow volume is provided mainly by dilatancy and not by surface deformation.

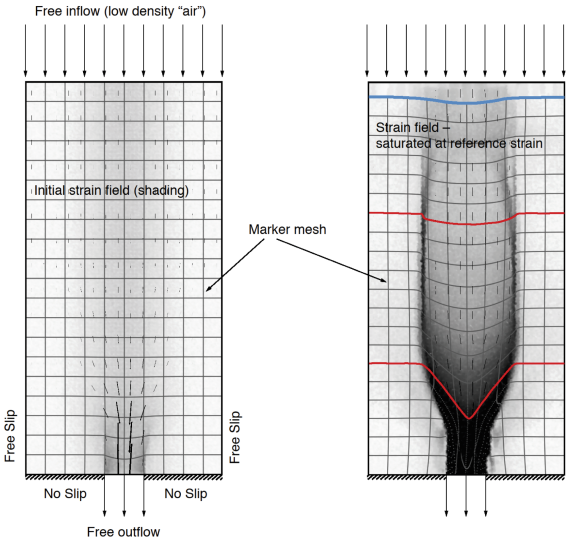

Fig. 2. Gravity flow from open trap door: geometry and boundary conditions. Grid lines shown are not identical to finite element grid

As indicated in Fig. 2 we consider free flow from an open trapdoor. In preparation for the computational simulations we consider rigid plastic, granular flow in a vertical (direction of gravity) chute. The solution of this problem provides us with useful time and velocity scales for the computational simulation. The flow in the infinite chute ($|x_1| < W/2, |x_2| < \infty$) is similar to the one in a trap door problem in a sufficient distance from the trap door and the propagating flow front (e.g. Fig. 3E, F). The fields depend on x_1 only. The velocity field is divided in two shear zones adjacent to the boundaries $|x_1| = W/2$ of width W_S each and rigid zone $|x_1| < W/2 - W_S$ where $v_{2,1} = 0$ and $v_2 = -v_{2\max} = const$. Within the shear zones the strain rate varies linearly between 0 and $\pm v_{2,1\max}$ on the boundaries. From Eqs. (6, 7) and stress equilibrium

$$2W_S/W = 1 - 2\mu p/(\rho g W), v_{2,1\max} = \rho g W_S/\eta \text{ and } v_{2\max} = \rho g W_S^2/2\eta. \qquad (9)$$

Gravity flow is possible if $W_S > 0$, or $0 < \mu p < \rho g W/2$. For the definition of time and velocity scales we substitute $p = \rho g W/4\mu$.

The model equations of the computational simulation are based on an implicit, moving particle method and solved by means of a geometric multi grid solver (Moresi et al. [1]). The pressure sensitivity, dilatancy and the rate independent part of the cohesive strength (cp. Eq. 3) decrease linearly with γ^p from the initial values μ_0, ν_0 and τ_0 resp. until, for $\gamma^p \geq \gamma^0_{res}$ the residual values μ_{res}, 0 and 0 resp. are reached. It turns out that the smaller initial the dilatancy ν_0 the larger (wider) the active flow domain has to be in order to provide the outflow volume necessary to maintain continuous flow.

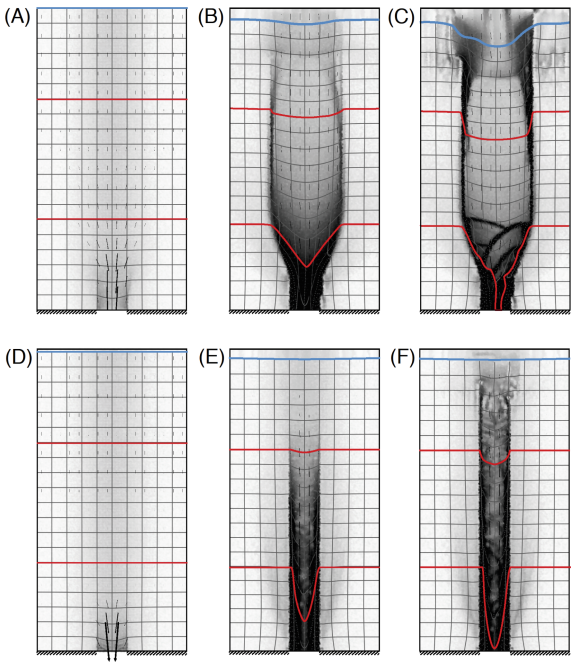

Fig. 3. Successive stages of gravity flow from open trap door. Top row (A–C), $v = 0.1$ second row (D–F) $v = 0.35$

4 Conclusions

In the main application of this paper we considered the gravity driven transformation of the static deformation of an initially cohesive-frictional material into a flowing granular, purely frictional material. The domain considered is a rigid container filled with the initially cohesive-frictional material with a free flow boundary condition at the bottom center (open trap door). The breakdown of the cohesive strength was initiated by gradually lowering the trap door pressure from overburden stress level to zero.

The main observations are:

- The smaller the initial dilatancy v_0 the larger (wider) the active flow domain has to be in order to provide the outflow volume necessary to maintain continuous flow
- The mass flux at the trap door scales with $\bar{v} = \rho g W^2/8\eta$.

The modeling scenario considered clearly represents a strong simplification of real mining operations: In cave mining for instance often an air gap forms between the cave front and the mobile, granular domain. This happens if the volume provided by dilatancy doesn't match the volume extracted at the draw point. This case is not considered here. Also important, but not considered here is the fact that the cave front has a finite width, the so called seismic zone. This effect may be considered by including a diffusion like term-e.g. proportional to the Laplacian of the equivalent plastic strain- into the dilatancy constraint. This would introduce a length scale, scaling the seismic zone as well as an additional time scale, beside the one introduced by the rate dependent cohesion in (3). These effects will be considered in the full version of this extended abstract.

References

1. Moresi, L., Dufour, F., Muhlhaus, H.B.: A Lagrangian integration point finite element method for large deformation modeling of viscoelastic geomaterials. J. Comput. Phys. **184**, 476–497 (2003)
2. Chapman, S., Cowling, T.G.: The Mathematical Theory of Non-uniform Gases. Cambridge University Press, Cambridge (1970)
3. Gudehus, G.: Elastoplastische Stoffgleichungen fuer trockenenen Sand. Ing. Arch. **42**(3), 151–169 (1973)
4. Gudehus, G., Jiang, Y., Liu, M.: Seismo- and thermodynamics of granular solids. Granular Matter **13**(4), 319–340 (2011)
5. Jop, P., Forterre, Y., Pouliquen, O.: A constitutive law for dense granular flows. Nature **44**, 727–730 (2006)
6. Rice, J.R., Lapusta, N., Ranjith, K.: Rate and state dependent friction and the stability of sliding between elastically deformable solids. J. Mech. Phys. Solids **49**, 1865–1898 (2001)
7. Franklin, S.V., Shattuck, M.D.: Kinetic theories for collisional grain flow. In: Handbook of Granular Materials, pp. 155–186 (2016)
8. Savage, S.B.: The mechanics of fast granular flows. Adv. Appl. Mech. **24**, 289–366 (1984)
9. Hajko, P., Tejchman, J.: Modelling of shear localization during granular flow within non-local hypoplasticity using material point method, pp. 593–598. Springer, Cham (2017)

Desiderata Geotechnica: Halting Steps

David Muir Wood(✉)

University of Dundee, Dundee, UK
d.muirwood@dundee.ac.uk

Abstract. Apparatus regularly used for extraction of stress – strain response of soils all contain internal variations of strain and stress. The inhomogeneous state is the natural state of many soils. Where the repeated cell size of heterogeneities is uniform it is simple to define a reference volume element. Study of triaxial samples, however, reveals mechanisms which are not individually axially symmetric.

Keywords: Laboratory testing · Heterogeneities · Reference volume element

1 Introduction

What are the desirable geotechnical findings which would improve the quality of our geotechnical research life without achieving so much progress that we are left wise and useful with no further challenges?

Perhaps the most desirable geotechnical advance might be to have a constitutive model or suite of constitutive models which are generally accepted and which can be reliably deployed for most of the soils that we encounter. Such a group of models would desirably be constructed around a series of plausible and comprehensible and refutable hypotheses. These models would require the availability of experimental data sufficient in quantity and quality to tune the parameters of our models and to support the modelling hypotheses. A subsidiary desirable geotechnical advance would be the identification of one or more ideal configurations for laboratory element tests with which to gather reliable data of soil behaviour. Some testing configurations have some desirable features, but are likely to remain research apparatus - true triaxial and directional shear cell fall into this category.

Possible candidates might be: conventional triaxial, simple shear, hollow cylinder apparatus.

In summary, our list of geotechnical desirables becomes: perfect element testing; elegant constitutive models, data from well-controlled laboratory or full scale $1g$ or multiple gravity boundary value problems. Is that such an unreasonable list?

W. Wu (Ed.): *Desiderata Geotechnica*, SSGG, pp. 119–124, 2019.
https://doi.org/10.1007/978-3-030-14987-1_14

2 Triaxial Test

The conventional triaxial apparatus tests a cylindrical sample. We know that the sample is subjected to an all-round *pressure* supplied by a pressurised cell fluid, together with an axial *displacement* though an axial loading ram. However, if we interpret the observations through conventional measures of stress and strain: axial stress σ_a and radial stress σ_r, axial strain ε_a and radial strain ε_r, then it has been found convenient to divide perturbations and response into volumetric and distortional components: volumetric stress $p = (\sigma_a + 2\sigma_r)/3$, distortional stress $q = \sigma_a - \sigma_r$ and corresponding work-conjugate strain increments: volumetric strain increment $\delta\varepsilon_p = \delta\varepsilon_a + 2\delta\varepsilon_r$ and distortional strain increment $\delta\varepsilon_q = 2(\delta\varepsilon_a - \delta\varepsilon_r)/3$. Each of these variables combines one part of which we are confident with one part which is more speculative.

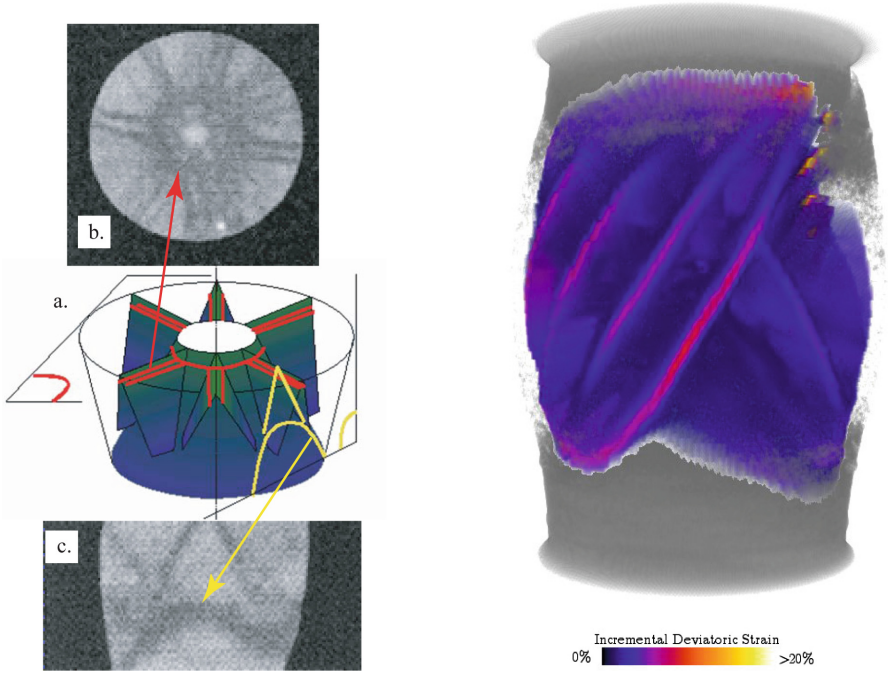

Fig. 1. (a) (left) Volumetric strain variations in triaxial sample ; (b) (right) distortional strain variations in triaxial sample

Scanning procedures are improving rapidly and with each step of improvement new surprises become visible. The x-ray imaging of Desrues [4] revealed patterns of dilation bands which combined to form clear mechanisms of deformation, some of which were directly consistent with an overall axisymmetric interpretation but most of which were not (Fig. 1a). The dilation bands indicate

a series of shearing mechanisms controlled by the boundaries of the sample and the constraints that the boundaries impose.

Other scanning techniques have been used recently [3] to reveal the variation of distortional strains within triaxial samples (Fig. 1b). The lack of significant correspondence between the deformation mechanisms and the supposed axial symmetry is clear.

3 Plane Strain Probing

There are various devices that can be used for plane testing of granular materials and which permit the full-field determination of displacements. The Grenoble $1\gamma 2\varepsilon$ apparatus can be used for plane stress testing of a Schneebeli rod material with the possibility of controlling all three plane strain components,and permitting rotation of principal axes of strain. Photographic techniques can follow the movements of individual rods to discover a pattern of shear and volumetric deformation which has a clear structure and regularity (Fig. 2) [5]. It is clearly legitimate to speculate on the size of sample needed to provide a homogeneous heterogeneity for which the unit of observation is the cell formed by neighbouring shear or dilation bands rather than by individual particles (rods) being tested. Such speculation is evidently out of place for the mechanisms observed in the triaxial sample. The heterogeneity is not the result of a regular patterning but is a response to the boundaries.

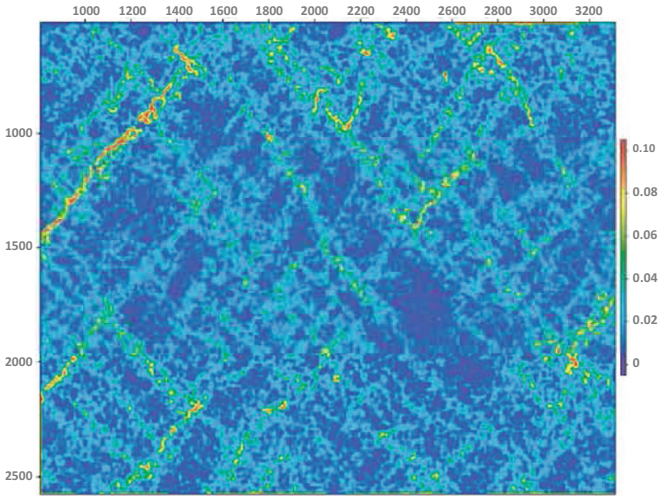

Fig. 2. Distortional strain variations in $1\gamma 2\varepsilon$ sample

4 Torsional Hollow Cylinder Test Apparatus

The torsional hollow cylinder apparatus has, in principle the desirable ability to impose controlled variation of four stress components out of six. These components are imposed through axial force applied over the whole cross-section of the hollow cylinder; through internal and external pressures; and through a torque applied at the upper boundary. There are evidently challenges in creating the sample for testing - carving the sample to the correct geometry or raining a granular material into the space between the outer and inner walls. There are inevitable variations of shear strain with radius: the thinner the walls of the hollow cylinder the better but thin walls produce other difficulties. Differences between internal and external pressures obviously imply a radial variation of radial stress and some control of circumferential stress. The apparatus is a boundary value problem which we can use to compare with finite element simulations but cannot be interpreted as a test on a single homogeneous element.

5 Caterpillar Continuous Shearing Device

A variant of the simple shear apparatus is provided by Allersma's caterpillar device in which a continuous toothed belt - rather like the caterpillar tracks of a site vehicle - completely contains the sample (Fig. 3) [1,2]. Pulling the lower part of the belt to one side while maintaining a vertical pressure on the top of the sample develops a continuous simple shearing of the sample. Allersma tested crushed glass. Immersing the material in a fluid of the same refractive index as the glass and then observing the sample with polarised light provides the unique possibility of obtaining some information concerning the stress state in the sample using the photoelastic properties of the granular material. Photographic observation can be used to produce a continuous field of displacements.

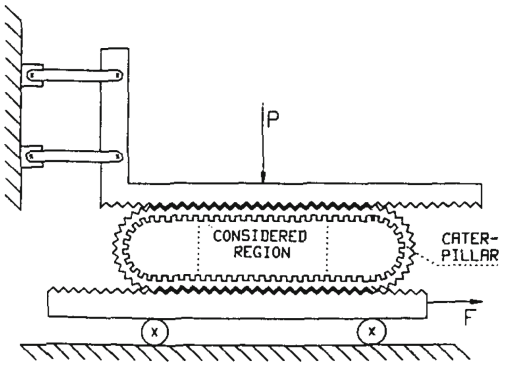

Fig. 3. Caterpillar continuous shearing device.

6 Desiderata: Incremental Data - Infinite Possibilities

Soils are in general nonlinear and history dependent in their mechanical response. The gathering of experimental data needs to cover a wide range of stress histories and paths, relying on the constitutive framework to fill in the gaps.

7 Yielding and Response Envelopes

Response envelopes - describing incremental response to a series of strain or stress probes from a common history serves two purposes. The variation of incremental stiffness with history provides basic data to test the simulatory abilities of the constitutive model. Response envelopes can also be inspected to seek evidence for (or against) constitutive conjectures. For example, it becomes quickly evident that any region of high incremental stiffness - which might be interpreted as a region of elastic response enclosed within a yield surface - is very local to the current stress state. Plasticity is kinematic (Fig. 4) [6].

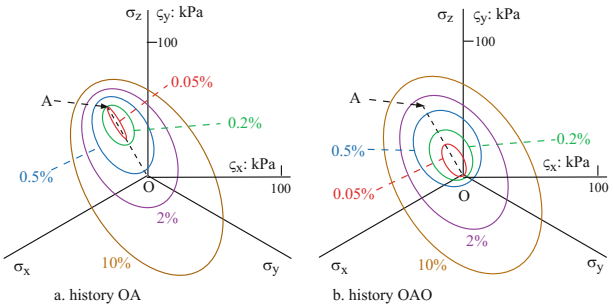

Fig. 4. Response envelopes in true triaxial shearing of sand.

8 Conclusion

The success of the models in simulating geotechnical performance needs to be demonstrated against well-controlled boundary value problems - field trials or centrifuge modelling of typical geotechnical configurations.

References

1. Allersma H.G.B.: Optical analysis of stress and strain in photoelastic particle assemblies. Ph.D. thesis, Delft University of Technology (1987)
2. Allersma H.G.B., Dijkstra J., Muir Wood, D.: Continuous shear of granular materials. Géotechnique (2018, submitted)
3. Desrues J.: Distortionsl localisation in triaxial sample. Private Commmunication (2017)

4. Desrues, J., Chambon, R., Mokni, M., Mazarolle, F.: Void ratio evolution inside shear bands in triaxial sand specimens studied by computed tomography. Géotechnique **46**(3), 529–546 (1996)
5. Hall, S.A., Muir Wood, D., Ibraim, E., Viggiani, G.: Localised deformation patterning in 2D granular materials revealed by digital image correlation. Granular Matter **12**(1), 1–14 (2010)
6. Muir Wood, D.: Geotechnical Modelling. Taylor & Francis, London (2004)

Significance and Usefulness of the t_{ij} Concept

Teruo Nakai(✉)

Geo-Research Institute and Chubu University, Nagoya, Japan
nakai.teruo@nitech.ac.jp

Abstract. Constitutive models formulated using the stress invariants (p and q) cannot describe uniquely the deformation and strength of geomaterials under three principal stresses [1]. Then, the concept of t_{ij} has been proposed to describe uniquely the stress-strain behaviors in general three-dimensional (3D) stress conditions [2]. This concept was found out from the idea that the frictional law essentially governs soil behavior. Since the formulation of elastoplastic model using this concept was described in the previous papers [3, 4], the meaning of this concept and its usefulness are presented in this paper.

Keywords: Constitutive modeling · Spatially mobilized plane · Concept of t_{ij}

1 Stress Invariants in 2D Condition

Figure 1 shows the Mohr's stress circle on τ-σ plane in two-dimensional (2D) condition. Now, 2D soil models are usually formulated using the normal stress $\sigma_{45^\circ}(=s)$ and shear stress $\tau_{45^\circ}(=t)$ on the plane where shear stress is maximized (called $\tau_{\max}$ plane or 45° plane). On the other hand, Murayama [5] paid his attention not to this plane but to the plane where the shear normal stress ratio is maximized (called $(\tau/\sigma_N)_{\max}$ plane or mobilized plane), because it is considered appropriate that soil behavior during shear is governed by the frictional law. The shear normal stress ratios on these planes are expressed as follows:

$$\frac{\tau_{45^\circ}}{\sigma_{45^\circ}} = \frac{t}{s} = \sin\phi_{mo} = \frac{\sigma_1 - \sigma_3}{\sigma_1 + \sigma_3} \tag{1}$$

$$\frac{\tau}{\sigma_N} = \tan\phi_{mo} = \frac{\sigma_1 - \sigma_3}{2\sqrt{\sigma_1\sigma_3}} \tag{2}$$

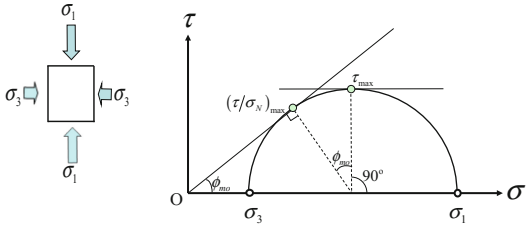

Fig. 1. Two reference planes ($\tau_{\max}$ plane and $(\tau/\sigma_N)_{\max}$ plane) expressed on Mohr's stress circle

W. Wu (Ed.): *Desiderata Geotechnica*, SSGG, pp. 125–131, 2019.
https://doi.org/10.1007/978-3-030-14987-1_15

It is noticed that when the principal stress ratio σ_1/σ_3 changes from 1 to infinite (the mobilized angle ϕ_{mo} changes from 0° to 90°), the stress ratio τ/σ_N in Eq. (2) can take a value of 0 to infinite, but the value of stress ratio $\tau_{45°}/\sigma_{45°}$ expressed by Eq. (1) should be between 0 and 1. Although 2D model can be formulated using stress invariants, it is necessary that the stress ratio $\tau_{45°}/\sigma_{45°}(=t/s)$ is less than 1 when the model is formulated by the stresses on 45° plane.

2 Octahedral Plane and Spatially Mobilized Plane

In 3D condition, three Mohr's stress circles between respective two principal stresses can be drawn. So, there are three 45° planes on which the shear stresses are maximized between two principal stresses as shown in Fig. 2(a). The plane where these three 45° planes are combined is called the octahedral plane, which has been usually employed as the reference plane in constitutive modeling of metals and geomaterials [1]. On the other hand, three mobilized planes where shear normal stress ratio is maximized between respective two principal stresses are also described as shown in Fig. 2(b). The specially mobilized plane (SMP) is defined as the combined plane of these three mobilized planes [6]. Although the direction cosines of octahedral plane are given by $\left(1/\sqrt{3},\ 1/\sqrt{3},\ 1/\sqrt{3}\ \right)$, the direction cosines of SMP are given as a function of stress ratio by

$$(a_1,\ a_2,\ a_3) = \left(\sqrt{I_3/(I_2\sigma_1)},\ \sqrt{I_3/(I_2\sigma_2)},\ \sqrt{I_3/(I_2\sigma_3)}\right) \tag{3}$$

Here, I_2 and I_3 are the second and third invariants of the Cauchy stress σ_{ij}. Also, the unit symmetric tensor, a_{ij}, whose principal values are given by these direction cosines, can be defined.

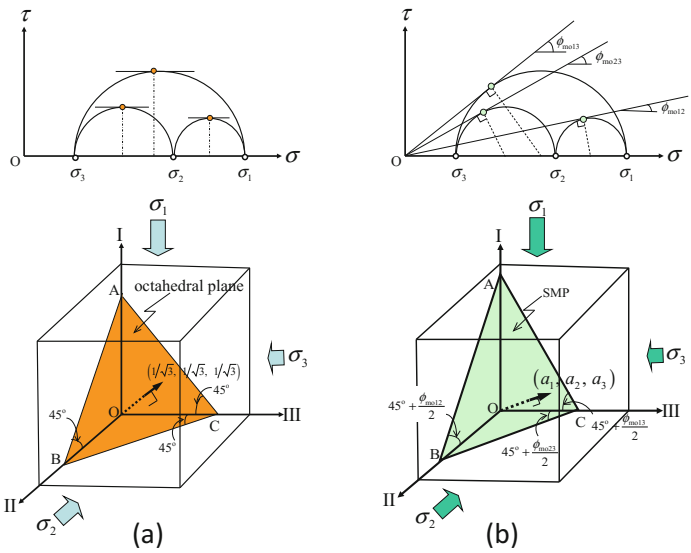

Fig. 2. (a) Octahedral plane and (b) Spatially mobilized plane (SMP)

3 Formulation of 3D Elastoplastic Models

3.1 Ordinary Modeling Using Stress Invariants (p and q) [1]

The mean stress p and the deviatoric stress q correspond to the normal and in-plane components of the stress with respect to the octahedral plane as shown in Fig. 3, and are expressed by Eq. (4) using three principal stresses.

$$\begin{cases} p = \sqrt{\frac{1}{3}}\mathrm{ON} = \frac{1}{3}(\sigma_1 + \sigma_2 + \sigma_3) = \sigma_{oct} \\ q = \sqrt{\frac{3}{2}}\mathrm{NP} = \frac{1}{\sqrt{2}}\sqrt{(\sigma_1 - \sigma_2)^2 + (\sigma_2 - \sigma_3)^2 + (\sigma_3 - \sigma_1)^2} = \frac{3}{\sqrt{2}}\tau_{oct} \end{cases} \tag{4}$$

The yield function (plastic potential) $f = 0$ is formulated using these stress invariants, and the plastic strain increments is calculated assuming flow rule (normality condition) in the Cauchy stress σ_{ij}.

$$d\varepsilon_{ij}^{p} = \Lambda \frac{\partial f}{\partial \sigma_{ij}} = \Lambda \left(\frac{\partial f}{\partial p}\frac{\partial p}{\partial \sigma_{ij}} + \frac{\partial f}{\partial \eta}\frac{\partial \eta}{\partial \sigma_{ij}} \right) \quad (\text{where } \eta = q/p) \tag{5}$$

Figure 4 shows the yield surface and normality rule in (p, q) plane under triaxial compression ($\sigma_1 > \sigma_2 = \sigma_3$; upper half) and triaxial extension ($\sigma_1 = \sigma_2 > \sigma_3$; lower half). The yield surface is symmetric with respect to p-axis. Also, stress condition without tension stress is limited in gray color area. Then, some normal stress becomes negative when stress ratio q/p becomes larger than the broken lines ($\sigma_3 = 0$) during elastic deformation or elastoplastic deformation, even if p is positive.

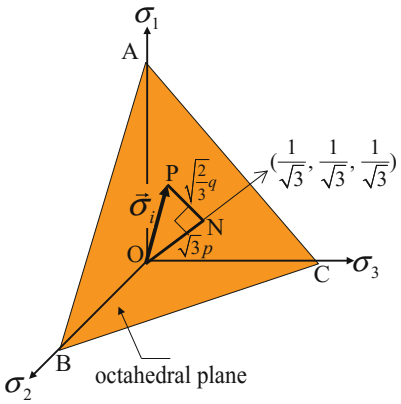

Fig. 3. Definitions of (p and q)

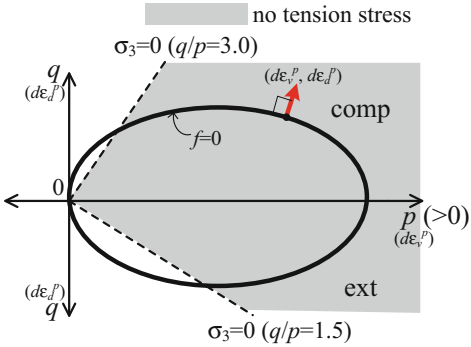

Fig. 4. Yield surface on p-q plane and no tension area

3.2 Modeling Based on t_{ij} Concept [2]

The modified stress tensor t_{ij} is defined by the product of a_{ik} and $\boldsymbol{\sigma}_{kj}$ as follows:

$$t_{ij} = a_{ik}\sigma_{kj} \tag{6}$$

Its principal values are given by

$$t_1 = a_1\sigma_1, \quad t_2 = a_2\sigma_2, \quad t_3 = a_3\sigma_3 \tag{7}$$

The invariants of modified stress (t_N and t_S) used in t_{ij} concept are defined as the normal and in-plane components of t_{ij} to the SMP as shown in Fig. 5.

$$\begin{cases} t_N = \mathrm{ON} = t_1a_1 + t_2a_2 + t_3a_3 = 3I_3/I_2 \\ t_S = \mathrm{NT} = \sqrt{(t_1a_2 - t_2a_1)^2 + (t_2a_3 - t_3a_2)^2 + (t_3a_1 - t_1a_3)^2} \end{cases} \tag{8}$$

The yield function $f = 0$ based on the t_{ij} concept is formulated using the stress invariants (t_N and t_S) instead of (p and q).

$$d\varepsilon_{ij}^p = \Lambda\frac{\partial f}{\partial t_{ij}} = \Lambda\left(\frac{\partial f}{\partial t_N}\frac{\partial t_N}{\partial t_{ij}} + \frac{\partial f}{\partial X}\frac{\partial X}{\partial t_{ij}}\right) \qquad (\text{where } X = t_S/t_N) \tag{9}$$

Figure 6 shows schematically the yield surface in $t_N - t_S$ plane under triaxial compression (upper half) and triaxial extension (lower half) in the same way as Fig. 4. The yield surface is symmetric with respect to the t_N-axis. The area where tension stress does not occur is indicated by gray color area, because σ_3 is always positive in case of $t_N > 0$ (see Eq. (8)). Also, there is no tension zone inside of the yield surface. This is because $\sigma_3 = 0$ condition is satisfied on the vertical axis (t_S axis) in Fig. 6.

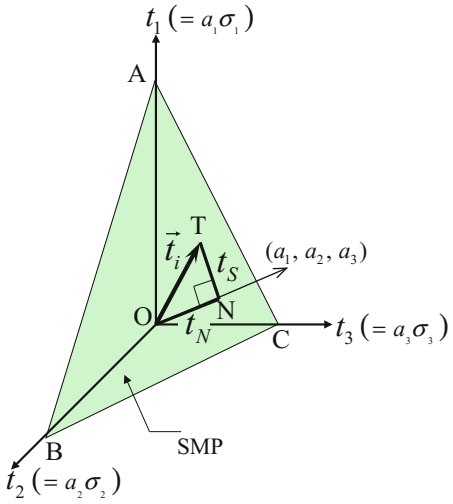

Fig. 5. Definitions of (t_N and t_S)

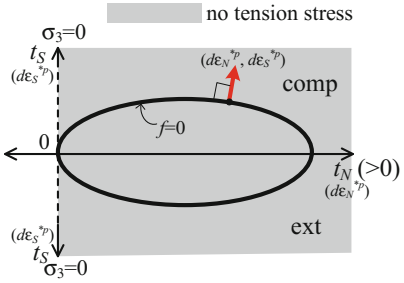

Fig. 6. Yield surface on $t_N - t_S$ plane and no tension area

4 Meaning of t_{ij} Concept

From microscopic observation, Oda [7] showed that, as the stress ratio increases, the average directions normal to the inter-particle contacts gradually concentrate in the same direction as the major principal stress (σ_1). Satake [8] pointed out that the principal values (φ_1, φ_2) of the so-called fabric tensor φ_{ij}, which represents the relative distribution of the number of vectors normal to the inter-particle contacts, is approximately proportional to the square root of the corresponding principal stresses.

$$\frac{\varphi_1}{\varphi_2} \approx \left(\frac{\sigma_1}{\sigma_2}\right)^{0.5} \tag{10}$$

Employing a fabric tensor, Satake [9] also proposed a modified stress tensor σ^*_{ij}

$$\sigma^*_{ij} = \frac{1}{3}\varphi^{-1}_{ik}\sigma_{kj} \tag{11}$$

Figure 7(a) shows schematically the distribution of inter-particle contacts in 2D condition. Considering an equivalent continuum, such material exhibits anisotropy since the stiffness in the σ_1 direction should be larger than that in the σ_2 direction with the increase of stress ratio (see diagram (b)). When adopting an elastoplastic theory, it is reasonable to treat the soil as an isotropic material by introducing the modified stress t_{ij} in which induced anisotropy is already considered. This is because the normality rule should hold in the isotropic space, like the transformed space used to analyze seepage problems in anisotropic ground and others. From Eq. (3), the principal values of a_{ij} are inversely proportional to the square root of the principal stresses, therefore:

$$a_1 : a_2 = 1/\sqrt{\sigma_1} : 1/\sqrt{\sigma_2} \tag{12}$$

It can be noted that a_{ij} corresponds to the inverse of the fabric tensor in Eq. (10), and t_{ij} defined by Eq. (6) corresponds to the modified stress in Eq. (11). As shown in diagram (c), the stress ratio t_1/t_2 in the modified stress space is smaller than stress ratio σ_1/σ_2 in the ordinary stress space. Then, it is reasonable to assume that the flow rule (normality condition) holds not in the σ_{ij} space but in the t_{ij} space, because the

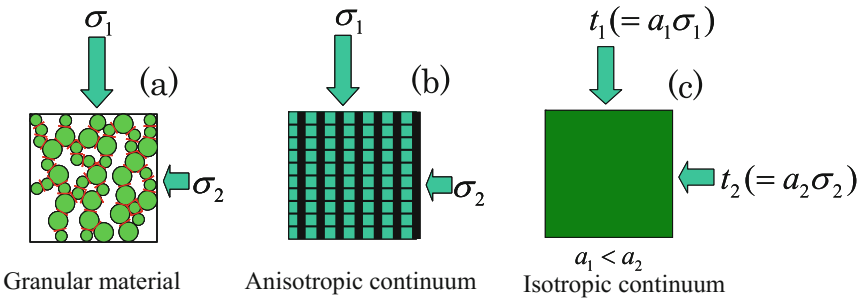

Fig. 7. Induced anisotropy during shear loading and meaning of t_{ij} concept

condition of the anisotropic material in diagram (b) can be considered to be the same as that of the isotropic material in diagram (c).

5 Verification by Test Data

Figure 8 shows the observed results (dots) of drained triaxial compression and extension tests on normally consolidated clay and the corresponding calculated results (curves) based on t_{ij} concept. Although models using (p, q) invariants cannot describe the difference between triaxial compression and extension tests, the model based on t_{ij} concept describes well the observed results. The unique relation between d_N^*/d_S^* and t_S/t_N in Fig. 9, which is independent of intermediate principal stress, means that the shape of yield surface is symmetric with respect to t_N axis as shown in Fig. 6. Figure 10 shows the observed and calculated directions of the shear strain increments on the octahedral plane for true triaxial ($\sigma_1 > \sigma_2 > \sigma_3$) tests. The calculated directions

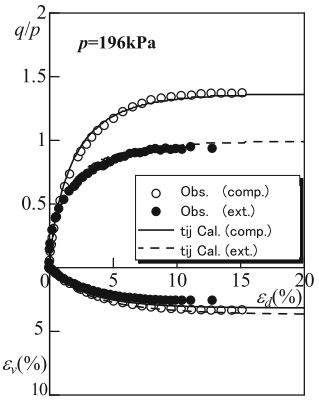

Fig. 8. Stress-strain relation

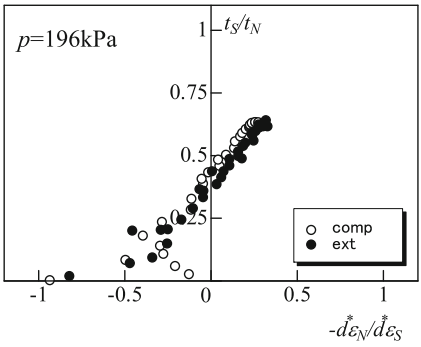

Fig. 9. Observed stress-dilatancy relation

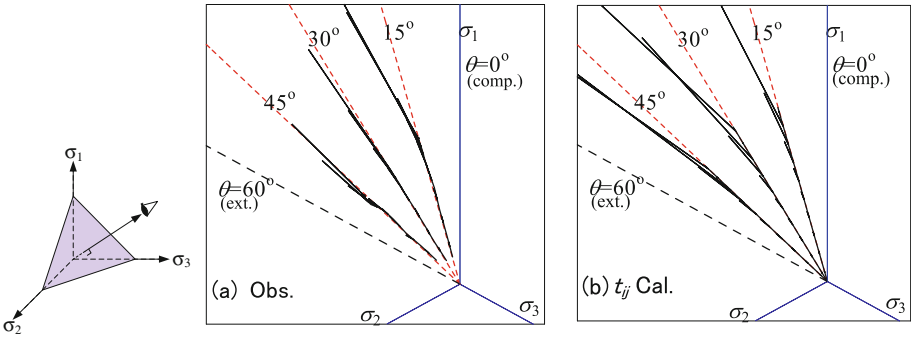

Fig. 10. Observed and calculated directions of shear strain increment on octahedral plane

describe well the observed tendency that the direction of the shear strain increments deviates leftward from that of shear stress (radial direction) with the increase in stress ratio under three different principal stresses. On the other hand, the calculated directions by ordinary (p, q) model are always radial.

References

1. Schofield, A.N., Wroth, C.P.: Critical State Soil Mechanics. McGrow-Hill, London (1968)
2. Nakai, T., Mihara, Y.: A new mechanical quantity for soils and its application to elastoplastic constitutive models. Soils Found. **24**(2), 82–94 (1984)
3. Nakai, T., Hinokio, T.: A simple elastoplastic model for normally and over consolidated soils with unified material parameters. Soils Found. **44**(2), 53–70 (2004)
4. Nakai, T.: Constitutive Modeling of Geomaterials: Principles and Applications. CRC Press, Boca Raton (2012)
5. Murayama, S.: A theoretical consideration on a behavior of sand. In: Proceedings of IUTAM Symposium on Rheology and Soil Mechanics, Grenoble, pp. 146–159 (1964)
6. Matsuoka, H., Nakai, T.: Stress-deformation and strength characteristics of soil under three different principal stresses. Proc. JSCE **232**, 59–70 (1974)
7. Oda, M.: The mechanism of fabric changes during compressional deformation of sand. Soils Found. **12**(2), 1–18 (1972)
8. Satake, M.: Anisotropy in ground and soil materials. Tsuchi Kiso **32**(11), 5–12 (1984, in Japanese)
9. Satake, M.: Fabric tensor in granular materials. In: Proceedings of IUTAM Conference on Deformation and Failure of Granular Materials, Delft, pp. 63–68 (1982)

Essential Concepts of Neohypoplasticity

Andrzej Niemunis(✉) and Carlos E. Grandas Tavera

Institute of Soil Mechanics and Rock Mechanics, Karlsruhe Institute of Technology, Karlsruhe, Germany
andrzej.niemunis@kit.edu

Abstract. The neohypoplastic model [12] eliminates several shortcomings of the hypoplastic vW-HP model [17]. The most important improvements are presented here. The general form of the constitutive equation $\dot{\sigma} = \bar{\mathsf{E}} : (\dot{\varepsilon} + \mathbf{m}Y\|\dot{\varepsilon}\|)$ is slightly modified by two additional terms in brackets. The functions $\mathsf{E}(\sigma,e), \mathbf{m}(\sigma,e)$ and $Y(\sigma,e)$ are completely reformulated in order to deal with numerous problems of the old model: perpetuum mobile of the second kind, too small dilatancy during triaxial tension paths, poor predictions of peak stress and inconsistent behaviour of the model at the upper density limit. A new state variable $\mathbf{z}$ similar to the one from the *Sanisand* model [3] is introduced. The hitherto used state variables: the stress and the void ratio are preserved, of course. Moreover, a new kind of nonlinearity is proposed: the rotation of the deviatoric stress response. The problems connected to the extension intergranular-strain extension are not discussed here.

1 Hyperelastic Response

The most important deficiencies of the linear part of the vW-HP model are:

- non-conservative (hypoelastic) stiffness
- too small ratio of shear stiffness to volumetric stiffness

The new hyperelastic stiffness of the model is based on an expression $\bar{\psi}(\sigma)$ for the complementary energy. The strain function $\varepsilon_{ij}(\sigma)$ and the compliance $C_{ijkl}(\sigma)$ are obtained as partial derivatives,

$$\varepsilon^{\mathrm{el}}_{ij} = \frac{\partial \bar{\psi}}{\partial \sigma_{ij}} \qquad \text{and} \qquad \dot{\varepsilon}^{\mathrm{el}}_{ij} = \frac{\partial^2 \bar{\psi}}{\partial \sigma_{ij} \partial \sigma_{kl}}\, \dot{\sigma}_{kl} = C_{ijkl}\dot{\sigma}_{kl} \tag{1}$$

In geotechnical materials, the tangential compliance $C_{ijkl}(\sigma)$ should decrease with pressure. For sand we postulate that the tangential stiffness $E_{ijkl} = C^{-1}_{ijkl}$ is a homogeneous stress function of order $n \approx 0.6$, i.e. $\forall \lambda > 0 : \mathsf{E}(\lambda\sigma) = \lambda^n \mathsf{E}(\sigma)$, and hence $C_{ijkl}(\sigma)$ is homogeneous of order $-n$.

W. Wu (Ed.): *Desiderata Geotechnica*, SSGG, pp. 132–142, 2019.
https://doi.org/10.1007/978-3-030-14987-1_16

Analogously to Euler's theorem $m\bar{\psi} = (\partial\bar{\psi}/\partial\sigma) : \sigma$, for the first derivative of an m-th order homogeneous function, we formulate[1] a similar relation with the second derivative,

$$m(m-1)\bar{\psi} = \sigma : \frac{\partial^2\bar{\psi}}{\partial\sigma\partial\sigma} : \sigma = \sigma : \mathsf{C} : \sigma \tag{2}$$

Judging by the product on the right-hand side of (2) our potential $\bar{\psi}$ should be homogeneous of order $2-n$. This condition is sufficient (but not necessary) for the n-th-order homogeneous stiffness. The related degrees of homogeneity are given in the following table

Function	$\mathsf{E}(\sigma)$	$\mathsf{C}(\sigma)$	$\mathsf{E}(\varepsilon)$	$\mathsf{C}(\varepsilon)$	$\varepsilon(\sigma)$	$\sigma(\varepsilon)$	$\bar{\psi}(\sigma)$	$\bar{\psi}(\sigma)$	$\psi(\varepsilon)$	$\psi(\varepsilon)$
Degree of homogeneity	n	$-n$	$\frac{n}{1-n}$	$\frac{-n}{1-n}$	$1-n$	$\frac{1}{1-n}$	$2-n$	$2-n$	$\frac{2-n}{1-n}$	$\frac{2-n}{1-n}$

The complementary energy formulas of the general form

$$\bar{\psi}(\sigma) = \sum_{\alpha} c_\alpha P^\alpha R^{2-n-\alpha} \qquad \text{with} \qquad \alpha \in \mathscr{R} \tag{3}$$

have been tested because degree of homogeneity of each summand is $2-n$, is desired. The Vermeer's hyperelasticity [16] can be obtained as a special case with just one summand and with $\alpha = 0$. After numerous experiments with fine sand [5, 10], we could simplify (3) to just a single summand

$$\bar{\psi} = cP^\alpha R^{2-n-\alpha} \quad \text{with} \quad \begin{array}{|c|c|c|} \hline n & c & \alpha \\ \hline 0.6 & 1.517\cdot 10^{-4} & 0.100 \\ \hline \end{array} \tag{4}$$

The total elastic strain $\varepsilon_{ij}^{\mathrm{el}}$ is

$$\varepsilon_{ij}^{\mathrm{el}} = \frac{\partial\bar{\psi}}{\partial\sigma_{ij}} = c\alpha P^{\alpha-1}R^{2-n-\alpha}(-\delta_{ij}) + c(2-n-\alpha)P^\alpha R^{1-n-\alpha}\sigma_{ij} \tag{5}$$

and the compliance is $\mathsf{C} = (\partial^2\bar{\psi}/\partial\sigma\partial\sigma)$, viz.

$$C_{ijkl} = A\delta_{ij}\delta_{kl} + B(\delta_{ij}\sigma_{kl} + \sigma_{ij}\delta_{kl}) + C\sigma_{ij}\sigma_{kl} + DI_{ijkl}, \tag{6}$$

wherein

$$A = c(\alpha-1)\alpha P^{\alpha-2}R^{2-n-\alpha} \tag{7}$$

$$B = -c\alpha(2-n-\alpha)P^{\alpha-1}R^{1-n-\alpha} \tag{8}$$

$$C = c(2-n-\alpha)(-n-\alpha)P^\alpha R^{-n-\alpha} \tag{9}$$

$$D = c(2-n-\alpha)P^\alpha R^{-n-\alpha} \tag{10}$$

[1] We substitute $\tau = \sigma\lambda$ into $\bar{\psi}$ and then differentiate the equation $\bar{\psi}(\tau) = \lambda^m\bar{\psi}(\sigma)$ twice with respect to λ using the chain rule on the left-hand side. The resulting equation $\sigma : \dfrac{\partial^2\bar{\psi}(\tau)}{\partial\tau\partial\tau} : \sigma = m(m-1)\lambda^{m-2}\bar{\psi}(\sigma)$ holds for any λ. In particular, it holds for $\lambda = 1$ and hence (2) can be concluded.

1.1 Scaling of Stiffness for Transversal Isotropy (TI)

Graham and Houlsby [6] introduced a simplified version of the TI stiffness claiming that three material constants (instead of the usual five ones) are sufficient for soils. They proposed a TI stiffness H_{ijkl} with two additional assumptions

$$a = G_h/G_v = (E_h/E_v)^{1/2} = (\nu_h/\nu_{vh}) \tag{11}$$

leaving us with just three material constants a, E_v, ν_h (note that $G_h = E_h/(2+2\nu_h)$ holds). After some manipulations one may notice that the simplified TI stiffness H_{ijkl} from [6] can be obtained from a special *scaling transformation* of the isotropic elastic stiffness E_{abcd}, namely

$$H_{ijkl} = Q_{ijab} E_{abcd} Q_{cdkl}, \tag{12}$$

$$\text{where} \qquad Q_{ijkl} = \mu_{ik}\mu_{jl} \qquad \text{with} \qquad \mu_{ij} = \sqrt{a}\delta_{ij} + (1-\sqrt{a}) m_i m_j \tag{13}$$

and where m_i is the unit vector along the sedimentation axis. The scaling (12) has one major advantage over (11): it can be applied to *any* hyperelastic stiffness. From the existence of the function, $\bar{\psi}(\sigma)$, and from the 1-1 elastic relation $\sigma(\varepsilon)$ we may conclude the existence of the elastic energy $\psi(\varepsilon) = \sigma_{ij}(\varepsilon)\ \varepsilon_{ij} - \bar{\psi}(\sigma(\varepsilon))$ with the help of Legendre transformation. The scaling (12) can be interpreted in the following way: we define a scaled strain with

$$\bar{\varepsilon}_{ij} = Q_{ijkl}\varepsilon_{kl} = \mu_{ik}\varepsilon_{kl}\mu_{lj} \tag{14}$$

and we write the elastic energy with the new argument $\psi(\bar{\varepsilon})$. Using twice the chain rule $(\partial \sqcup/\partial \varepsilon_{ij}) = (\partial \sqcup/\partial \bar{\varepsilon}_{ab})(\partial \bar{\varepsilon}_{ab}/\partial \varepsilon_{ij})$ we obtain (12). The function $\psi(\bar{\varepsilon})$ is a new potential taking into accound a and m_i. The advantage of the above method is that we can "add" some a-type anisotropy to an arbitrary hyperelastic stiffness *a posteriori*, without spoiling the conservation of energy etc.

2 Nonlinear Part $f_d Y$

The following deficiencies have been revealed testing the vW-HP model:

1. At max. density, $e = e_d$ i.e. for $f_d = 0$ the elastic response allows for tension.
2. Tension could be reached even if $f_d < 0.66$ for $\varphi = 30°$.
3. Peak strength corresponds to axial strain $\varepsilon_a \approx 1\%$ (instead of at least 5%) in the conventional triaxial compression despite well calibrated initial stiffness.
4. Extreme densities $e < e_d$ beyond the validity of the model can be numerically arrived at.

The new nonlinearity function $f_d(p,e)Y(\sigma) \to Y(e,\sigma)$ uses the following stress invariant

$$H(\sigma) = \sigma_{ii}\ \ \sigma_{jj}^{-1} - 9 \quad H(\sigma) \in (0,\infty), \tag{15}$$

The yield criterion by Matsuoka and Nakai [11] takes with $H(\sigma)$ a simple form

$$F_{M-N}(\sigma) = H(\sigma) - \phi \le 0 \qquad \text{with} \qquad \phi = 8\tan^2\varphi \tag{16}$$

If any principal stress vanishes, $\sigma_i = 0$, then $H(\sigma) = \infty$. The ansatz $Y = H/\phi(e,p)$ is insufficient although $Y = 0$ for the hydrostatic stress, $Y = 1$ corresponds to (16) as desired and $\phi = \phi(e,p)$ could easily match the barotropy and pycnotropy of the peak friction angle φ_{peak}. The third deficiency requires more sophisticated description: we need a longer range of $h = Q/P$ for which the degree of nonlinearity is close to unity, say $Y \in (0.9,1)$. Hence the degree of nonlinearity is proposed in the following form

$$Y(x) = A_Y \exp(-1/(B_Y x^{n_Y} + C_Y)) \tag{17}$$
$$\text{with} \qquad x = H/\phi(e,P) \qquad \text{and} \qquad Y(1) = 1$$

From four material constants A_Y, B_Y, C_Y, n_Y only three B_Y, C_Y, n_Y are available for fitting whereas A_Y is determined from the constraint $Y(1) = 1$, i.e. from $A_Y = \exp(1/(B_Y + C_Y))$. A reasonable first guess could be $B_Y = 20$, $C_Y = 0.3$, $n_Y = 2$. The function $\phi(e,p)$ can be related to the peak friction angle. Here it is simply interpolated between three values

	Loose	Critical	Dense
Max. friction angle	$\varphi_i = 32$	$\varphi_c = 33$	$\varphi_d = 50$
Void ratio	e_{i0} = 1.1	e_{c0} = 1.0	e_{d0}= 0.6

using the void ratio e and pressure dependent characteristic void ratios, viz (Fig. 1).

$$\phi(e,p) = 8\tan^2[\varphi(e,p)] \qquad \text{where} \qquad \varphi(e,P) = \varphi_c + \begin{cases} (\varphi_d - \varphi_c)\dfrac{e_c - e}{e_c - e_d} \\ (\varphi_c - \varphi_i)\dfrac{e - e_c}{e_i - e_c} \end{cases} \tag{18}$$

and choosing the positive fraction. The characteristic void ratios $e_i(p), e_c(p), e_d(p)$ are found from the Bauer's [1] compression line $e_\sqcup(P) = e_{\sqcup 0}\exp[-(3p/h_s)^{n_B}]$ with $\sqcup = d,i,c$ known from the vW-HP model. The material constants [7] are $e_{i0} = 1.1$, $e_{c0} = 1.0$, $e_{d0} = 0.6$, $h_s = .8 \cdot 10^5$, $n_B = 0.28$.

3 Flow Rule m_{ij}

The most striking deficiency of the vW-HP model is too little dilatancy on the side of triaxial extension, no matter how dense the soil is or how large friction angle is mobilized. All FE calculations of a strip foundation on the dense subsoil showed punching failure. Lateral bulging of soil could never be reproduced.

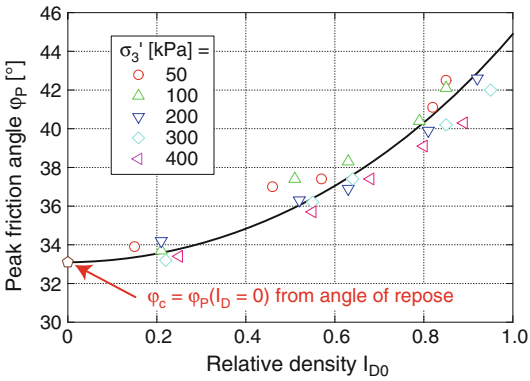

Fig. 1. Peak friction angles reached in drained tests at different void ratios, data provided by T. Wichtmann

The hypoplastic flow rule is described by the unit tensor m_{ij}. It dictates the dilatancy. First, the flow rule is formulated for three special cases

$$m_{ij} = \begin{cases} m^a_{ij} = (\partial H/\partial \sigma_{ij})^{\rightarrow} = \left[\delta_{ij}\ \ \sigma_{kk}^{-1} - \sigma_{kk}\ \sigma_{ij}^{-2}\right]^{\rightarrow} & \text{if} \quad H \geq \phi_a \\ m^c_{ij} = \left[\delta_{ij}\ \ \sigma_{kk}^{-1} - \sigma_{kk}\ \sigma_{ij}^{-2}\right]^{*\rightarrow} & \text{if} \quad H = \phi_c \\ m^i_{ij} = (\delta_{ij})^{\rightarrow} & \text{if} \quad H = 0 \end{cases} \tag{19}$$

corresponding to AFR, isochoric flow and purely volumetric flow, respectively. Next, the interpolation rules with respect to H are defined

$$\mathbf{m} = x\mathbf{m}^c + (1-x)\mathbf{m}^i \quad \text{with} \quad x = (H/\phi_c)^{n_1} \tag{20}$$

$$\mathbf{m} = x\mathbf{m}^a + (1-x)\mathbf{m}^c \quad \text{with} \quad x = [(H-H_c)/(\phi_a - \phi_c)]^{n_2}, \tag{21}$$

with the following material constants $\varphi_a = 36$, $n_1 = 0.1$, $n_2 = 1.0$ Note that the extension $m_{ij}(\sigma) \rightarrow m_{ij}(\sigma, e)$ would not be difficult if high quality experimental data were available.

3.1 Density Limit

The flow rule in neohypoplasticity is extended by the term $\mathbf{m}^d Y_d \|\dot{\varepsilon}\|$

$$\dot{\sigma} = \mathsf{E} : \left(\dot{\varepsilon} - \mathbf{m}\, Y \|\dot{\varepsilon}\| - \mathbf{m}^d Y_d \|\dot{\varepsilon}\|\right) \quad \text{with} \quad \mathbf{m}^d = \mathbf{1} \tag{22}$$

in order to prevent $e < e_d(p)$ i.e. the surpassing of upper density limit. It turns out that a long monotonic isotropic extension or some stress cycles could violate this condition. It became evident in numerical test of thermodynamic admissibility of the neohypoplasticity in which only positive energy dissipation was allowed for upon an arbitrary closed cycle in state space.

4 Rotation of Elastic Deviatoric Response

Experimental evidence shown in [12] suggests that after a long monotonic shearing the elastic deviatoric response of sand is rotated on the isometric $P-Q$ plane.

$$\begin{Bmatrix} \dot{P} \\ \dot{Q} \end{Bmatrix} = \begin{Bmatrix} \dot{P}^{\mathrm{el}} \\ 0 \end{Bmatrix} + \begin{bmatrix} c & -s \\ s & c \end{bmatrix} \cdot \begin{Bmatrix} 0 \\ \dot{Q}^{\mathrm{el}} \end{Bmatrix} \tag{23}$$

In the general case we need an operator R_{ijkl} that rotates the stress rate $\dot{\sigma}^*_{ij}$ as if it was a vector in 9 dimensional space, i.e. the Frobenius norm $\|\mathscr{R} : \dot{\sigma}^*\| = \|\dot{\sigma}^*\|$ does not change. However, neither the eigenvectors nor the eigenvalues of $\dot{\sigma}^*_{ij}$ are preserved.

Rotation can be generalized using operators

$$A_{ijkl} = \delta_{ij}\delta_{kl} \qquad \text{and} \qquad D_{ijkl} = I_{ijkl} - A_{ijkl} \tag{24}$$

which extract the hydrostatic part $\mathscr{A} : \sigma$ and the deviatoric part $\mathscr{D} : \sigma$ from a 2nd rank tensor σ, respectively. The rotation operator $\dot{\sigma}^*$ is obtained using an analogy to the Rodriguez formula

$$R_{ijkl} = I_{ijkl} + (c-1)(u_{ij}u_{kl} + v_{ij}v_{kl}) - \sqrt{1-c^2}(u_{ij}v_{kl} - v_{ij}u_{kl}), \tag{25}$$

wherein $u_{ij} = -\delta_{ij}$ and $v_{ij} = \sigma^*_{ij}$ are perpendicular unit tensors and $c = \cos\beta$ is the cosine of the rotation angle β. Tensor R_{ijkl} rotates from u_{ij} to v_{ij}, i.e. from P-axis via current Q towards $-P$. In particular, the same strain increment is rotated counterclockwise at $Q > 0$ and clockwise at $Q < 0$ in the P, Q plane. The rotation is objective and $\mathscr{R}$ is a 4th rank tensor. The stiffness is rotated for the deviatoric portion only using $\mathsf{E}^{\mathrm{rot}} = \mathscr{A} : \mathsf{E} + \mathscr{R} : \mathscr{D} : \mathsf{E}$. In the elastic case (Fig. 2)

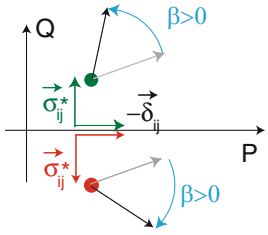

$$\dot{\sigma} = (\mathscr{A} : \mathsf{E} + \mathscr{R} : \mathscr{D} : \mathsf{E}) : \dot{\varepsilon} = \bar{E} : \dot{\varepsilon} \tag{26}$$

The idea of rotation of the deviatoric response is illustrated in Fig. 3. The rotation of the deviatoric portion of stress rate only is justified by the test, Fig. 3-left. Identical dense sand samples as described in [12], Sect. 3.1, are subjected to different isotropic compression cycles 1–2 after a long undrained shearing path 0–1. The corresponding strain increments, Fig. 3-right, are only slightly rotated off the isotropic direction.

The rotation is applied depending on the length of the monotonic deformation[2] and on the density.

5 Phase Transition and Rolling of Grains

Modelling of cyclic mobility and the butterfly-like stress path observed in undrained cycles can be simulated introducing an additional contractancy at the cost of an additional tensorial state variable $\mathbf{z}$. Some authors, e.g. [4], attribute this contractancy effect

[2] Given by the new state variable $\mathbf{z}$ which decays upon cyclic loading.

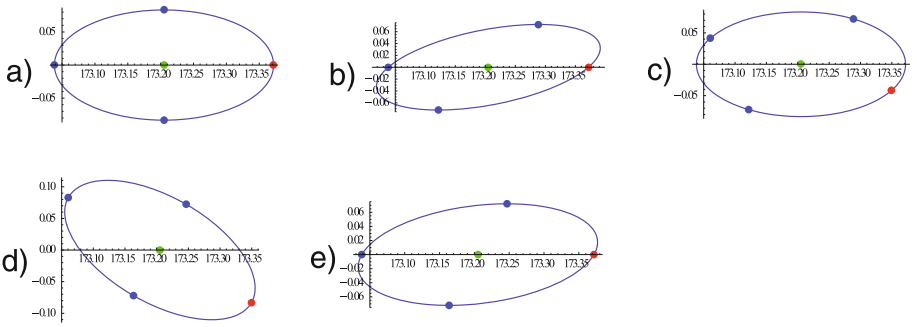

Fig. 2. Modifications of an isotropic elastic (Poisson number 0.2 shown in all pictures) response envelope in the PQ-diagram. Red point corresponds to the isotropic compression. (a) basic response envelope $\dot{\sigma} = \mathsf{E} : \dot{\varepsilon}$, (b) deviatoric strain rate rotated CW by 30 i.e. $\dot{\sigma} = \mathsf{E} : (\mathscr{A} + \mathscr{R} : \mathscr{D}) : \dot{\varepsilon}$, (c) total strain rate rotated CW by 30 i.e. $\dot{\sigma} = \mathsf{E} : \mathscr{R} : \dot{\varepsilon}$, (d) total stress rate rate rotated CW by 30 i.e. $\dot{\sigma} = \mathscr{R} : \mathsf{E} : \dot{\varepsilon}$ (e) deviatoric stress rate rotated CW by 30 i.e. $\dot{\sigma} = (\mathscr{A} + \mathscr{R} : \mathscr{D}) : \mathsf{E} : \dot{\varepsilon}$. The latter modification has been confirmed by the tests.

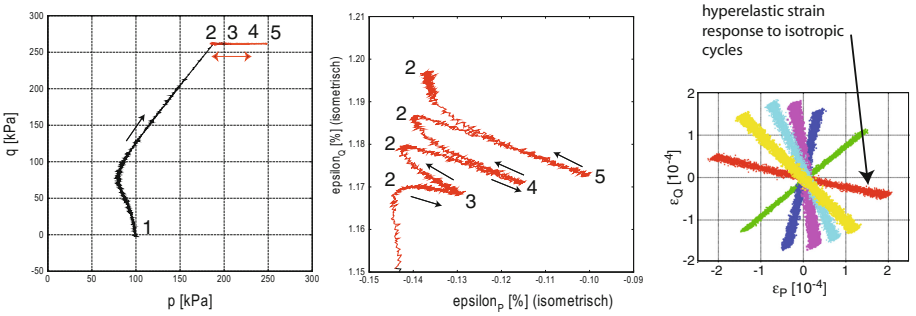

Fig. 3. Left: $p - q$ stress path consisting of several isotropic compression cycles 2-3-2-4-2-5-2 preceded by a long monotonic undrained shearing 1–2. Inclination of the strain response in the middle is similar to Strain paths in the $\varepsilon_{\text{vol}} - \varepsilon_q$ obtained from isotropic compression after conditioning (shake-down). The tests (left) were done by T. Wichtmann and L. Knittel [10].

to the rolling of grains during shearing at large stress obliquity, Fig. 4. After a 180° reversal of shearing the direction of rolling changes. Such backwards rolling is associated with strong contractancy. On the microscopic level one can think of grains which roll into the holes from which they have been rolled out. During undrained shearing, this contractancy manifests itself as a strong relaxation of P after stress reversals. Under undrained symmetric stress cycles, such relaxation accumulates. Finally, the stress is passing through the origin of the stress space and a characteristic shape of the stress path can be observed. This shape is sometimes called a "butterfly" and the phenomenon is known as the "cyclic mobility".

In order to describe this additional contractancy, we need information, how much dilatancy has been accumulated due to rolling. Moreover, we must know, what direction of shearing caused this accumulation. A further continuation of such shearing leads to

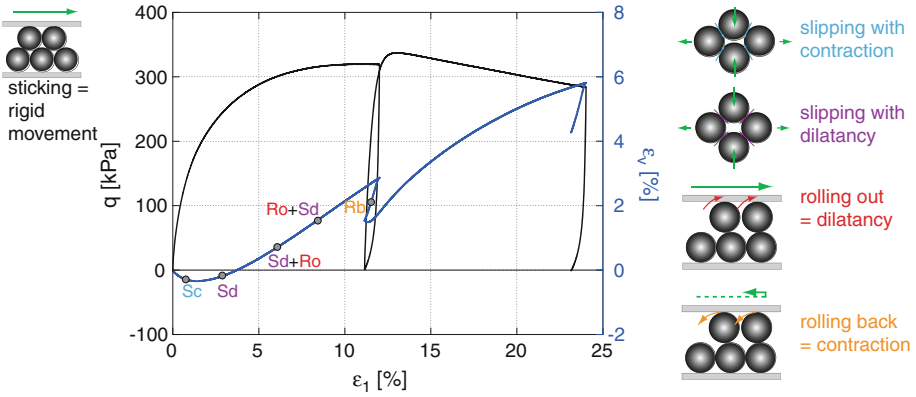

Fig. 4. Micromechanical interpretation of drained triaxial shear deformation for different states on the conventional stress-strain-dilatancy diagram.

further accumulation. A shearing in the opposite direction correspond to rolling back and causes contractancy. For mathematical description of these phenomena we introduce, similarly as in [15], a structural variable (a deviator) $\mathbf{z}$. Its norm $\|\mathbf{z}\|$ should grow during dilatant rolling and decline with contractant rolling back. Its direction should be used as indicator:

- rolling out with dilatancy for $\mathbf{z} : \dot{\varepsilon} > 0$
- rolling back with contractancy for $\mathbf{z} : \dot{\varepsilon} < 0$

The proposed evolution equations for $\mathbf{z}$ and for the rate of contractancy due to rolling $\dot{\varepsilon}_P^r$ are

$$\dot{\mathbf{z}} = \left(1 + \frac{\|\mathbf{z}\|}{z_{\max}}\right)\left(\dot{\boldsymbol{\varepsilon}}^* - \frac{\mathbf{z}}{z_{\max}}\|\dot{\boldsymbol{\varepsilon}}^*\|\right) \quad \text{with} \quad z_{ii} = 0 \tag{27}$$

$$\dot{\sigma} = \bar{\mathbf{E}} : \left(\dot{\boldsymbol{\varepsilon}} - \mathbf{m}\, Y\|\dot{\boldsymbol{\varepsilon}}\| - \omega \mathbf{m}^z \langle -\mathbf{z} : \dot{\boldsymbol{\varepsilon}}\rangle - \mathbf{m}^d Y_d \|\dot{\boldsymbol{\varepsilon}}\|\right) \quad \text{with} \quad \mathbf{m}^z = -\mathbf{1} \tag{28}$$

The factor ω grows at small pressures p in accordance to the observation that the cyclic accumulation at a constant strain amplitude accelerates with decreasing p, viz.

$$\omega(p) = \frac{p_{\text{ref}} f_e(e)}{z_{\max}(p_{\min} + p)}, \quad \text{where} \quad f_e = 1 - 1/\left[1 + \exp(k_d(e - e_d))\right] \tag{29}$$

The function f_e suppresses the rolling-type contractancy at $e \approx e_d$. The material constants are $z_{\max} = 0.05$, $P_{\min} = 3$, $P_{\text{ref}} = 100\sqrt{3}$, $k_d = 200$.

6 Viscosity

The neohypoplastic model has been supplemented by two rheological effects:

- Slow decay of the back strain $\mathbf{e}$,

$$\dot{\mathbf{e}} = -\frac{1}{\tau}\mathbf{e} \tag{30}$$

  used in the paraelastic part of the model. With the relaxation time[3] $\tau(\sigma)$. After the deformation is stopped, $\dot{\varepsilon} = \mathbf{0}$, the decay $\mathbf{e} \to \mathbf{0}$ leads to $\varepsilon_c \to \varepsilon$. Hence, (30) may lead to an overshooting. However, transient overshooting is acceptable for sands, cf. the TESRA model [2]. This relaxation can be used to simulate aging, however paraelasticity is beyond the scope of this text.
- Fast Bagnold viscosity for high rates of shear deformations, which can be of importance during liquefaction (at $\sigma \approx \mathbf{0}$).

  Both effects can be deactivated.

6.1 Bagnold Viscosity

Another viscous effect is proposed for very fast deformation. It may be of importance for vanishing hypoplastic stress $\sigma^{\mathrm{HP}} = \mathbf{0}$ because the barotropic stiffness may vanish due to $\mathsf{E} \sim P^n$. The Bagnold viscosity is similar to the well known Newtonian viscosity $\sigma^* = \mu\dot{\varepsilon}^*$ but beside shear stress σ^* it implements the normal stress components which is called *dispersive pressure*. Several models for debris flow or magma flow have been proposed basing on this kind of viscosity, [9]. The total viscous stress is proposed to be calculated from

$$\sigma^{\mathrm{vis}} = \eta_{\mathrm{Bag}}\left[\dot{\varepsilon}^* - k_{\mathrm{Bag}}\mathbf{1}\|\dot{\varepsilon}^*\|\right], \tag{31}$$

wherein minus is due to the mechanical sign convention. Only linear dependence[4] is used in (31) with[5] dynamic friction $k_{\mathrm{Bag}} \approx 0.7$ and dynamic viscosity $\eta_{Bag} \approx 0.02$ kPa s. Formally, the stress rate $\mathring{\sigma}^{\mathrm{vis}}$ obtained from time differentiation of (31) can be added (parallel coupling) to the hypoplastic rate $\mathring{\sigma}^{\mathrm{HP}}$

$$\mathring{\sigma} = \mathring{\sigma}^{\mathrm{HP}} + \mathring{\sigma}^{\mathrm{vis}} \quad \text{with} \quad \mathring{\sigma}^{\mathrm{vis}} = \eta_{\mathrm{Bag}}\left[\ddot{\varepsilon}^* - k_{\mathrm{Bag}}\mathbf{1}(\dot{\varepsilon}^*)^{\rightarrow} : \ddot{\varepsilon}^*\right] \tag{32}$$

In numerical implementation we use (31) rather than the incremental form of (32). For this purpose the viscous stress $\sigma^{\mathrm{vis}\,n}$ from the previous increment need to be memorized. Given the updated stress $\sigma + \Delta\sigma^{\mathrm{HP}}$ we first subtract $\sigma^{\mathrm{vis}n}$ stored as a state variable and then we add the current viscous stress σ^{vis} from (31). The main argument for using

[3] The half-life of $\mathbf{e}$ is $\tau\ln(2)$.

[4] Hunt et al. [8] showed that two velocity ranges, originally proposed by Bagnold, are not necessary.

[5] These parameters are obtained from rough extrapolation of experiments on suspensions with very low density.

(31) is the accuracy upon sudden strain path reversals. Although such reversals are rare in reality, they may often appear in numerical simulations. Equation (32) may evoke artificial stress jump upon reversals due to $(\dot{\varepsilon}^*)^{\rightarrow} : \ddot{\varepsilon}^* \neq 0$, especially for small time increments. As an illustrative example let us consider a 180 reversal changing the sign of $\dot{\varepsilon}^*$ but keeping $\|\dot{\varepsilon}^*\| = const$. According to (32) the dispersive pressure will jump by $-\eta_{\mathrm{Bag}} k_{\mathrm{Bag}} \mathbf{1} (\dot{\varepsilon}^*)^{\rightarrow} : \ddot{\varepsilon}^* \Delta t$ although it is clear from (31) that it should remain unchanged. The viscous part of stress contributes to the Jacobian matrix as follows

$$\mathscr{D}^{\mathrm{vis}} = \frac{\partial \sigma^{\mathrm{vis}}}{\partial \Delta \varepsilon} = \frac{\eta_{\mathrm{Bag}}}{\Delta t} \left[\mathsf{J}^D - k_{\mathrm{Bag}} \mathbf{1} (\Delta \varepsilon^*)^{\rightarrow} \right] \tag{33}$$

with the tensor $J^D_{ijkl} = \delta_{ik}\delta_{jl} - \frac{1}{3}\delta_{ij}\delta_{kl}$ of deviatoric projection, $\sqcup^* = \mathsf{J}^D : \sqcup$.

It turns out that Bagnold viscosity can strongly influence the FEM simulations of the installation process of a vibro-injection pile. In an example calculation we tested an axisymmetric FE-model with a dynamic 34 Hz loading under undrained conditions. We used Bagnold to simulate the liquified soil material as an extremely dense suspension. The neohypoplasticity results in a much narrower liquefied zone and Bagnold viscosity provides a natural regularization, Fig. 5.

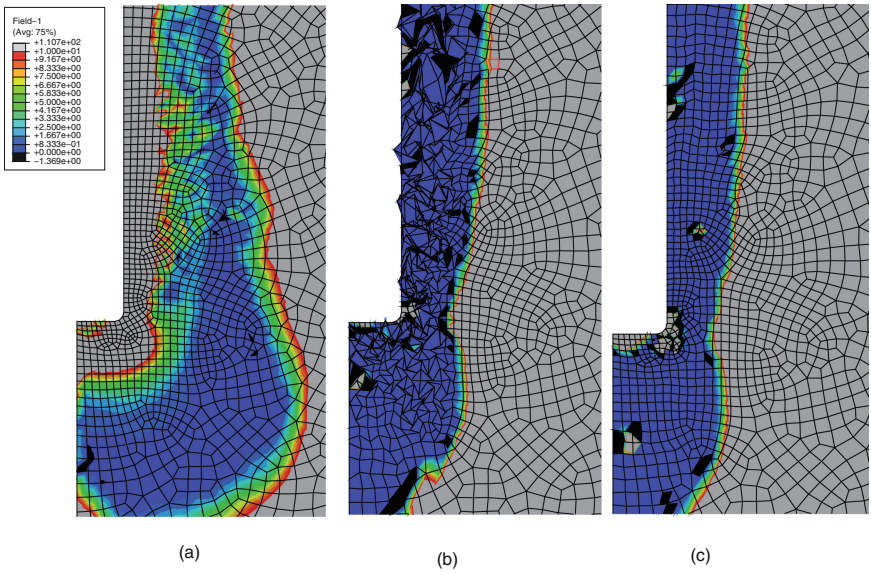

Fig. 5. Liquified zone around a vibrating pile (axial symmetry). The von Wolffersdorff hypoplastic [18] version (a) predicts excessive spreading [13, 14] of the this zone, compared to neohypoplasticity (b, c). A strong mesh distortion is observed in the liquefied zone if calculated with neohypoplasticity without viscosity (b). It is evident that the Bagnold viscosity can regularize the calculation with neohypoplasticity (c).

References

1. Bauer, E.: Zum mechanischen Verhalten granularer Stoffe unter vorwiegend öodometrischer Beanspruchung. Ph.D. thesis, Institut für Boden und Felsmechanik der Universität Karlsruhe (TH), Heft, Nr. 130 (1992)
2. Di Benedetto, H., Tatsuoka, F., Ishihara, M.: Time dependent shear deformation characteristics of sand and their constitutive modelling. Soils Found. **42**(2), 1–22 (2001)
3. Dafalias, Y.F., Manzari, M.T.: Simple plasticity sand model accounting for fabric change effects. J. Eng. Mech. **130**, 22–34 (2004)
4. Dafalias, Y.F.: Overview of constitutive models used in VELACS. In: Arulandan, K., Scott, R. (eds.) Verification of Numerical Procedures for the Analysis of Soil Liquefaction Problems, vol. 2, pp. 1293–1304. Balkema, Proceedings of the International Conference in Davis, California (1994)
5. Espino, E.: Quasi-statische Untersuchungen zur Elastizitt von Sand als Grundlage eines neuen hypoplastischen Stoffmodells. Masters thesis, Institut für Boden- und Felsmechanik, Karlsruher Institut für Technologie, Mai (2014)
6. Graham, J., Houlsby, G.T.: Anisotropic elsticity of a natural clay. Géotechnique **33**(2), 165–180 (1983)
7. Herle, I.: Hypoplastizität und Granulometrie einfacher Korngerüste. Ph.D. thesis, Institut füur Boden- und Felsmechanik der Universität Karlsruhe, Nr. 142 (1997)
8. Hunt, M.L., Zenit, R., Campbell, C.S., Brennen, C.E.: Revisiting the 1954 suspension experiments of R.A. Bagnold. J. Fluid Mech. **452**, 1–24 (2002)
9. Johnson, A.: A model for grain flow and debris flow. Technical report 96-728, U.S. Department of the Interior U.S. Geological Survey, Denver, Colorado (1996)
10. Knittel, L.J.: Fortgesetzte quasi-statische Untersuchungen zur Elastizitt von Sand als Grundlage eines neuen hypoplastischen Stoffmodells. Masters thesis, Institut für Boden- und Felsmechanik, Karlsruher Institut fr Technologie, September 2014
11. Matsuoka, H., Nakai, T.: Stress-strain relationship of soil base on the SMP constitutive equations of soils. In: Murayama, S., Schofield, A.N. (eds.) Proceedings of the 9th International Conference On Soil Mechanics and Foundation Engineering, Speciality Session 9. Japanese Society of Soil Mechanics and Foundation Engineering, IX ICSMFE, Tokyo (1977)
12. Niemunis, A., Grandas-Tavera, C.E., Wichtmann, T.: Peak stress obliquity in drained and undrained sands. Simulations with neohypoplasticity. In: Triantafyllidis, Th. (ed.) Holistic Simulation of Geotechnical Installation Processes. Numerical and Physical Modelling, vol. 80, pp. 85–114. Springer, Heidelberg (2016)
13. Osinov, V.A., Chisopoulos, S., Grandas-Tavera, C.E.: Vibration-induced stress changes in saturated soil: a high cyclic problem. In: Triantafyllidis, Th. (ed.) Holistic Simulation of Geotechnical Installation Processes. Numerical and Physical Modelling, pp. 69–84. Springer, Heidelberg (2016)
14. Chisopoulos, S., Osinov, V.A., Triantafyllidis, T.: Dynamic problem for the deformation of sturated soil in the vicinity of a vibratin pile toe. In: Triantafyllidis, Th. (ed.) Holistic Simulation of Geotechnical Installation Processes. Numerical and Physical Modelling, pp. 53–68. Springer, Heidelberg (2016)
15. Taiebat, M., Dafalias, Y.F.: SANISAND: simple anisotropic sand plasticity model. Int. J. Numer. Anal. Methods Geomech. **32**(8), 915–948 (2008)
16. Vermeer, P.: A five-constant model unifying well established concepts. In: Constitutive Relations for Soils, pp. 175–198. Balkema, Holland, Proceedings of the International Workshop in Grenoble (1982)
17. von Wolffersdorf, P.-A.: Verformungsprognosen für Stützkonstruktionen. Ph.D. thesis, Institut für Boden- und Felsmechanik der Universität Karlsruhe, Habilitationschrift, Heft Nr. 141 (1997)
18. von Wolffersdorf, P.-A.: Eine neue Version des erweiterten hypoplastischen Stoffgesetzes. Mech. Cohesive-Frictional Mater. **1**, 251–271 (1993)

On the Formulation of Multiphase Porous Geomaterials

Fusao Oka[1(✉)] and Sayuri Kimoto[2]

[1] Lab. 3, 138-1 Association for Disaster Prevention Research, Emeritus of Kyoto University, Tanakaasukai-cho, Sakyo-ku, Kyoto 606-8226, Japan
oka.fusao.38x@st.kyoto-u.ac.jp
[2] Department of Civil and Earth Resources Engineering, Kyoto University, Kyoto 615-8540, Japan
kimoto.sayuri.6u@kyoto-u.ac.jp

Abstract. For partially saturated soils, several stress variables have been used such as the net stress, Bishop stress, generalized Bishop stress and skeleton stress have been used. For elastic behavior of water saturated geomaterials, Biot developed a theory of porous media which is equivalent to the elastic water saturated model with the effective stress with the so-called Biot constant. On the other hand, for inelastic response, the applicability of the effective stress with Biot constant has not yet well been studied. In this study, the authors present the formulation of two phase and three-phase geomaterials based on the continuum thermodynamics with internal variables. It has been found that the effective stress with Biot coefficient is obtained for elastic two-phase materials, and the skeleton stress with Biot constant can be derived for three-phase materials such as partially saturated soil.

Keywords: Multi-phase geomaterials · Skeleton stress · Unsaturated soil

1 Introduction

It is well known Terzaghi's effective stress and the effective stress with Biot coefficient have been used for geomaterials. For partially saturated soils, several stress variables have been used such as the net stress, Bishop stress, generalized Bishop stress and skeleton stress. Biot [1] developed a theory of porous media which is equivalent to the elastic water saturated model with the effective stress having the so-called Biot constant. Kimoto et al. [2] showed that Biot type two-phase theory is applicable to the elastic behavior of dry soil, i.e., air filled sand, and the classical effective stress cannot be applied to the air-filled sand. However, for inelastic response, the applicability of the effective stress with Biot constant has not yet been well studied. This paper presents the constitutive equations for three-phase geomaterials based on the continuum thermodynamics with internal variables. The constitutive equation with full interaction between fluids and solid skeleton includes the matric suction and the saturation relation as well as the usual stress-strain relations. It has been found that the skeleton stress with Biot constant can be derived for three-phase materials such as partially saturated soil.

W. Wu (Ed.): *Desiderata Geotechnica*, SSGG, pp. 143–146, 2019.
https://doi.org/10.1007/978-3-030-14987-1_17

2 Thermodynamic Derivation of Constitutive Equation for Multi-phase Porous Material

Based on the first and second laws of thermodynamics, the constitutive equations for three-phase porous materials are obtained using the complementary energy per unit volume as

$$\eta = \frac{\partial \Psi}{\partial \theta}, \quad \varepsilon_{ij}^{\alpha} = \frac{\partial \Psi}{\partial \sigma_{ij}^{\alpha}} \tag{1}$$

where η is the entropy density per unit volume, θ is the temperature, $\sigma_{ij}^{(\alpha)}$ is the stress tensor and $\varepsilon_{ij}^{(\alpha)}$ is the strain rate tensor for α phase (α = *s, f, g*; *s, f* and *g* denote solid, water and air phase respectively), Ψ is the complementary energy function per unit volume.

Let us discuss the air-water-soil three-phase porous material. When the complementary energy is given by

$$\begin{aligned}\Psi = {} & A_{mnkl}\sigma_{mn}^{s}\sigma_{kl}^{s} + B_{mnkl}\sigma_{mn}^{s}\sigma_{kl}^{f} + C_{mnkl}\sigma_{mn}^{f}\sigma_{kl}^{f} + D_{mnkl}\sigma_{mn}^{s}\sigma_{kl}^{g} \\ & + E_{mnkl}\sigma_{mn}^{g}\sigma_{kl}^{g} + F_{mnkl}\sigma_{mn}^{f}\sigma_{kl}^{g} + H_{mnkl}\sigma_{mn}^{s}\xi_{kl}^{s},\end{aligned} \tag{2}$$

we have the stress-strain relations as:

$$\varepsilon_{ij}^{s} = \frac{\partial \Psi}{\partial \sigma_{ij}^{s}} = A_{mnkl}\delta_{mi}\delta_{nj}\sigma_{kl}^{s} + A_{mnkl}\delta_{ki}\delta_{lj}\sigma_{mn}^{s} + B_{mnkl}\delta_{mi}\delta_{nj}\sigma_{kl}^{f} + D_{mnkl}\delta_{mi}\delta_{nj}\sigma_{kl}^{g} + H_{mnkl}\delta_{mi}\delta_{nj}\xi_{kl}^{s} \tag{3}$$

$$\varepsilon_{ij}^{f} = \frac{\partial \Psi}{\partial \sigma_{ij}^{f}} = B_{mnkl}\delta_{ki}\delta_{lj}\sigma_{mn}^{s} + C_{mnkl}\delta_{mi}\delta_{nj}\sigma_{kl}^{f} + C_{mnkl}\delta_{ki}\delta_{lj}\sigma_{mn}^{f} + F_{mnkl}\delta_{ki}\delta_{lj}\sigma_{mn}^{g} \tag{4}$$

$$\varepsilon_{ij}^{g} = \frac{\partial \Psi}{\partial \sigma_{ij}^{g}} = D_{mnkl}\delta_{ki}\delta_{lj}\sigma_{mn}^{s} + E_{mnkl}\delta_{mi}\delta_{nj}\sigma_{kl}^{g} + E_{mnkl}\delta_{ki}\delta_{lj}\sigma_{mn}^{g} + F_{mnkl}\delta_{ki}\delta_{lj}\sigma_{mn}^{f} \tag{5}$$

It is assumed that A_{mnkl}, B_{mnkl}, C_{mnkl}, D_{mnkl}, E_{mnkl}, F_{mnkl}, and H_{mnkl} are the fourth order isotropic tensors.

In Eq. (3), we need an evolutional equation for the internal variables ξ_{ij}^{s} that may be given by the plastic flow rule or viscoplastic flow rule etc.

3 Constitutive Equations for Three-Phase Porous Materials

For the simplicity, we will discuss the air-water-solid elastic porous media. In the followings we assume that compression is positive. Extending the previous equations for water-saturated two-phase model given by Kimoto et al. [2], the volumetric elastic stress-strain increments can be written as:

$$\begin{aligned} d\sigma^{(s)} &= \alpha_b d\varepsilon^{(s)} + \alpha_c d\varepsilon^{(f)} + \alpha_d d\varepsilon^{(g)}, \\ d\sigma^{(f)} &= \alpha_c d\varepsilon^{(s)} + k_c d\varepsilon^{(f)} + h_c d\varepsilon^{(g)}, \\ d\sigma^{(g)} &= \alpha_d d\varepsilon^{(s)} + h_c d\varepsilon^{(f)} + k_d d\varepsilon^{(g)} \end{aligned} \tag{6}$$

where h_c is a volumetric interaction parameter between water and air of porous media such as the surface tension.

From Eq. (6), we obtain

$$d\sigma^{(s)} = A_1 d\varepsilon^{(s)} + B_1 d\sigma^{(f)} + C_1 d\sigma^{(g)}$$

$$A_1 = \alpha_b - \frac{\alpha_c(\alpha_c k_d - \alpha_d h_c) + \alpha_d(\alpha_d k_c - \alpha_c h_c)}{k_c k_d - h_c^2},\ B_1 = \frac{\alpha_c k_d - \alpha_d h_c}{k_c k_d - h_c^2},\ C_1 = \frac{\alpha_d k_c - \alpha_c h_c}{k_c k_d - h_c^2} \tag{7}$$

Considering the drained conditions, $d\sigma^{(f)} = d\sigma^{(g)} = 0$ and the unjacketed test conditions in water, i.e., in which the material is immersed in water; $d\sigma^{(f)} = ndu_w$, $d\sigma^{(s)} = (1-n)du_w$ and under the unjacketed test in the air, i.e., in which only the air pressure is applied to the dry material; $d\sigma^{(g)} = ndu_a$, $\sigma^{(s)} = (1-n)du_a$. du_w is the pore water pressure increment and du_a is the pore air pressure increment.

Since soils particles deform in the similar manner and the compressibility of soil particles is constant under both the unjacketed test conditions in water and air, it follows that $\alpha_c/\alpha_d = (k_c + h_c)/(k_d + h_c)$.

Finally we obtain the relationships between parameters as:

$$C_s = C_b((1-n) - B_1 n) \tag{8}$$

$$C_w = \left(-\frac{B_1}{A_1}(1-n) + \left(\frac{k_d}{k_c k_d - h_c^2} + \frac{B_1^2}{A_1}\right)n\right) \tag{9}$$

$$C_a = \left(-\frac{C_1}{A_1}(1-n) + \left(\frac{k_d}{k_c k_d - h_c^2} + \frac{C_1^2}{A_1}\right)n\right) \tag{10}$$

where C_b, C_s,C_w, and C_a are the compressibility of the solid skeleton, solid particles and water and air respectively.

For unsaturated geomaterials, partial stresses for water and air are given by

$$d\sigma^{(f)} = S_r n du_w \text{ and } d\sigma^{(g)} = (1 - S_r) n du_a, \tag{11}$$

where S_r is the saturation, and n is the porosity.

Then, the total stress increment becomes

$$\begin{aligned} d\sigma &= d\sigma^{(s)} + d\sigma^{(f)} + d\sigma^{(g)} = \frac{1}{C_b} d\varepsilon^{(s)} + B_1 S_r n du_w + C_1(1 - S_r) n du_a + S_r n du_w + (1 - S_r) n du_a \\ &= \frac{1}{C_b} d\varepsilon^{(s)} + \left(1 - \frac{C_s}{C_b}\right)(S_r du_w + (1 - S_r) du_a) = \frac{1}{C_b} d\varepsilon^{(s)} + \left(1 - \frac{C_s}{C_b}\right) dP_f \end{aligned} \tag{12}$$

where dP_f is the average pore pressure increment.

From the above equation, we can define the skeleton stress increment as:

$$d\sigma' = d\sigma - \left(1 - \frac{C_s}{C_b}\right) dP^f = \frac{1}{C_b} d\varepsilon^{(s)} \tag{13}$$

where $d\sigma'$ is the skeleton stress.

4 Conclusions

The elastic-inelastic constitutive relations were derived for multi-phase porous materials based on the continuum thermodynamics with internal variables. Then, it has been found that the effective stress with Biot coefficient is obtained for elastic two-phase materials, and the skeleton stress with Biot constant can be derived for three-phase materials such as partially saturated soil.

References

1. Biot, M.A., Willis, D.G.: The elastic coefficients of the theory of consolidation. J. Appl. Mech. **24**, 594–601 (1957)
2. Kimoto, S., Oka, F., Morimoto, Y.: The effective stress concept and the evaluation of changes in pore air pressure under jacketed isotropic compression tests for dry sand based on 2-phase porous theory. Int. J. Num. Anal. Methods Geomech. **41**, 1894–1907 (2017). https://doi.org/10.1002/nag.2705

Discrete Element Modeling of Free-Standing Wire Reinforced Jammed Granular Columns

Pavel S. Iliev, Falk K. Wittel, and Hans J. Herrmann(✉)

Institute for Building Materials, ETH Zurich, Zurich, Switzerland
{ilievp,fwittel}@ethz.ch, hans@ifb.baug.ethz.ch

Abstract. The use of fiber reinforcement in granular media is known to increase the cohesion and therefore the strength of the material. However, a new approach, based on layer-wise deployment of predetermined patterns of the fiber reinforcement has led self-confining and free-standing jammed structures to become viable. We have developed a model to simulate fiber reinforced granular materials, which takes into account irregular particles and wire elasticity and apply it to study the stability of unconfined jammed granular columns.

1 Introduction

Fiber reinforcement is widely used for different types of applications in various materials, such as reinforced polymer, concrete, and soil. A particularly interesting case is the use of fibers in combination with cohesionless granular materials, since the reinforcement acts as an additional "cohesion" to the material. Typical for reinforced granulates are the randomly distributed fibers inside the soil. Alternatively, the wire can be deployed along a predetermined path, creating strong anisotropies. Recently it was shown [1] that with the latter technique self-containing packings can be constructed allowing for load-bearing granular columns. This approach, named "3D rock printing" opens new opportunities for engineering and architectural applications since the structures behave like a solid and yet they are completely reversible - when the wire is removed the grains crumble into a pile [1,2].

Over the past few decades, reinforced soils have been studied extensively by numerical [3–5] and experimental [6,7] means. Several underlying mechanisms are known to be involved: tensioning of segments of wire, blocking between particles, friction induced sticking of wire wrapped around particles, and geometrical interlocking between individual grains. However, the mechanical behavior of such free-standing structures is not fully understood, since the reinforcement in this case does not only enhance the strength and the cohesion, but has also a confining function.

We present here a discrete numerical model for simulating wire reinforced granular materials that captures all the aforementioned mechanisms described

W. Wu (Ed.): *Desiderata Geotechnica*, SSGG, pp. 147–150, 2019.
https://doi.org/10.1007/978-3-030-14987-1_18

in detail in Ref. [8]. We apply it to study the stability of jammed, free standing granular columns under vertical load, see Fig. 1. Our discrete model incorporates two fundamentally different methods and couples them together, which allows us to capture the irregularities in grain shapes, the frictional interactions, and the elasticity of the wire. It should be noted that the proposed method has a very general scope of applicability, ranging from fiber [3] or geogrid [9] reinforced soils to rockfall protection [10] and beyond.

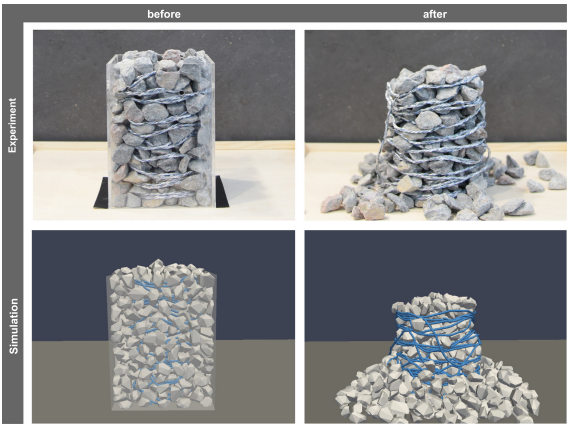

Fig. 1. Free standing fiber reinforced granular columns constructed by first depositing grains and wire inside a rectangular container and then removing the side walls of the container. Experiment (top row) and simulation (bottom row) showing the structure before (left) and after (right) the removal of the confining walls, source [8].

2 Numerical Modeling

In order to capture the effect of geometrical interlocking between the grains, the particles are represented by angular polyhedrons, or to be more precise spheropolyhedrons, which are a Minkowski sum of a polyhedron and a sphere [11]. The spherical dilation is needed to calculate the overlaps between the particles and the wire. Note that this modification does not change the contact calculation between the particles. The interactions between the particles are carried out by means of the Non-Smooth Contact Dynamics (NSCD) method, originally proposed by Moreau [12]. The main scope of applicability of this method is the modeling of dense packings of rigid frictional particles with lasting contacts. The NSCD method is based on the volume exclusion constraint and the Coulomb friction law without regularization. The equations of motion for the particles are integrated with an implicit Newton method. The forces and moments for each contact are resolved by an iterative Gauss-Seidel scheme for each time step, until a global convergence is achieved.

The wire is modeled as a chain of point-like masses connected by tensile spring elements and rotational springs attached to each node, which corresponds to a linear-elastic beam model in the continuum limit. Self-interaction of the wire is realized with the Soft Particle (SP) Discrete Element [13] method introduced by Cundall and Strack [14] with a linear spring-dashpot model. Each wire element has a spherocylinder attached to it in order to carry out the overlap computation [15]. The forces of a contact between two elements are distributed to the four involved nodes with weights inversely proportional to their distance from the closest point of contact. The equations of motion for the translational degrees of freedom of the wire nodes are integrated with an implicit Gear predictor-corrector method of 5-th order.

Since the NSCD method is implicit, it is unconditionally stable and therefore the time step can be significantly bigger than the one used for the explicit SP method. Hence, it is reasonable to have two different time steps for the two solvers: Δt^{NSCD} and Δt^{SP}. This leads to a sub-cycling procedure in which the positions of the wire nodes are updated n times for every update of the positions and orientation of the particles, where $n = \Delta t^{NSCD}/\Delta t^{SP}$. After the wire nodes are updated, the contact forces between the wire and the particles is averaged over the n wire time steps and added to the particles.

3 Results and Conclusions

Our simulations show a good qualitative as well as quantitative agreement with the laboratory experiments. For the experiment shown in Fig. 1 we have used railway ballast particles, while the wire is a standard textile string and the walls are made out of acrylic glass. The construction of the samples for both experiment and simulation is equivalent: layers of particles and wire are deposited sequentially inside a rectangular container. After the side walls are removed, the structure loses a part of the initial height, since crucial sections of the wire must be tensioned before it can start acting as a confinement and prevent the column from expanding in the transverse direction. This effect was confirmed by our numerical simulations from the time evolution of the elastic strain energy of the wire after the wall removal.

In order to gain a deeper understanding of the mechanical behavior of fiber reinforced jammed columns a large number of different simulations has been performed in order to investigate the behavior of the columns for a broad range of friction coefficients, wire stiffness, and particle size distributions. We observe from our numerical results that higher particle-wire friction can help to obtain higher columns as well as to increase the tension in the wire. In contrast, particle-particle friction does not influence the height of the columns or the fraction of retained particles inside the column, since the irregularities in the particles account for geometric interlocking between the grains. Nevertheless, higher friction between the particles leads to the reduction of the elastic energy on the wire as the forces are distributed on the particles instead of on the wire. Intuitively, wire stiffness also plays an essential role in the stability of the structures,

although the strain energy density has been found to decrease when strain resistance is increased. Furthermore, higher stiffness of the wire leads to a higher retained height of the column. We have shown also that larger variations in the particle sizes can be beneficial for the stability of free-standing wire reinforced granular columns.

Acknowledgements. We acknowledge financial support from the ETH Research Grant ETHIIRA Grant No. ETH-04 14-2 as well as from the ERC Advanced grant number FP7-319968 FlowCCS of the European Research Council. We also want to acknowledge the group of Gramazio/Kohler for the support and for the fruitful discussions.

References

1. Aejmelaeus-Lindström, P., Willmann, J., Tibbits, S., Gramazio, F., Kohler, M.: Jammed architectural structures: towards large-scale reversible construction. Granular Matter **18**, 28 (2016)
2. Keller, S., Jaeger, H.: Aleatory architectures. Granular Matter **18**, 29 (2016)
3. Laniel, R., Alart, P., Pagano, S.: Discrete element investigations of wire-reinforced geomaterial in a three-dimensional modeling. Comput. Mech. **42**, 67–76 (2008)
4. Villard, V., Chareyre, B.: Design methods for geosynthetic anchor trenches on the basis of true scale experiments and discrete element modelling. Can. Geotech. J. **41**, 1193–1205 (2004)
5. Fauconneau, M., Wittel, F.K., Herrmann, H.J.: Continuous wire reinforcement for jammed granular architecture. Granular Matter **18**, 27 (2016)
6. Michalowski, R.L., Zhao, A.: Failure of fiber-reinforced granular soils. J. Geotech. Eng. **122**, 226–234 (1996)
7. Gray, D.H., Ohashi, H.: Mechanics of fiber reinforcement in sand. J. Geotech. Eng. **109**, 335–353 (1983)
8. Iliev, P.S., Wittel, F.K., Herrmann, H.J.: Discrete element modeling of free-standing wire reinforced jammed granular columns. J. Comput. Part. Mech. **5**, 507–516 (2018). https://doi.org/10.1007/s40571-018-0186-7
9. Ferellec, J.R., McDowell, G.R.: Modelling of ballastgeogrid interaction using the discrete-element method. Geosynth. Int. **19**, 470–479 (2012)
10. Bertrand, D., Nicot, F., Gotteland, P., Lambert, S.: Discrete element method (DEM) numerical modeling of double-twisted hexagonal mesh. Can. Geotech. J. **46**, 1104–1117 (2008)
11. Alonso-Marroquin, F., Herrmann, H.J.: Calculation of the incremental stressstrain relation of a polygonal packing. Phys. Rev. E. **66**, 021301 (2002)
12. Moreau, J.J.: New computation methods in granular dynamics. In: Thornton, C. (ed.) Powders and Grains, pp. 227–232. Balkema, Rotterdam (1993)
13. Herrmann, H.J., Luding, S.: Modeling granular media on the computer. Contin. Mech. Thermodyn. **10**, 189–231 (1998)
14. Cundall, P.A., Strack, O.D.L.: A discrete numerical model for granular assemblies. Géotechnique **29**, 47–65 (1979)
15. Vetter, R., Wittel, F.K., Herrmann, H.J.: Packing model for elastic wires in ellipsoidal cavities. Eur. J. Mech. A. **37**, 160–171 (1998)

Fabric Evolution in Granular Materials Under Strain Probing

Mehdi Pouragha[1], Niels P. Kruyt[2], and Richard Wan[1(✉)]

[1] Civil Engineering Department, University of Calgary, Calgary, Canada
{mpouragh,wan}@ucalgary.ca
[2] Department of Mechanical Engineering,
University of Twente, Enschede, The Netherlands
n.p.kruyt@utwente.nl

Abstract. The fabric of granular materials, as the underlying internal contact network through which the interparticle forces transmit the stress, plays a key role in describing their elasticity, critical state, and dilatancy, to name a few. Just as response envelopes have been developed by Gudehus back in 1979 to get an overall picture of constitutive models and the nature of constitutive equations, herein, the evolution of contact fabric in granular materials when subjected to strain probes is explored through series of Discrete Element Method (DEM) simulations. As the first study of its kind, and also due to the richness of the observed responses, the scope of the study has been limited to isotropic configurations. The contribution of contact loss, gain, and reorientation mechanisms to the changes in the associated second order fabric tensor has been investigated as the proportion of vertical to horizontal strain changed during a strain probing procedure. Intriguingly, the evolution of fabric with strain probes shows a strong asymmetry in compression and extension, signalling an incrementally nonlinear relation between fabric and strain increments, despite the incrementally linear elastic stress-strain response. Such results suggest that the origins of the incrementally nonlinear stress-strain responses often observed in later stages of deviatoric loading of granular materials can be potentially traced back to characteristics of fabric evolution.

1 Introduction

The micromechanical study of granular materials encompasses the underlying connections between the microscopic-particle scales and the various characteristics at the macroscopic-continuum level with interparticle contacts as the main focus. Micromechanical descriptions of stress [1,9,19,30,36] and strain [2,14], and dilatancy in particular [4,15,16,35], show the important role that the internal contacts arrangement play in relating variables across the different scales. Therefore, having a detailed understanding of contact evolution during mechanical loading is essential in formulating micromechanics-based constitutive models for granular materials [10,17,18,32,37].

W. Wu (Ed.): *Desiderata Geotechnica*, SSGG, pp. 151–161, 2019.
https://doi.org/10.1007/978-3-030-14987-1_19

The internal contact configuration is often characterized by a second order fabric tensor [22,31] describing: the principal directions of contacts, the average number of contacts per particle, or coordination number, and the fabric anisotropy which quantifies the deviation of the fabric tensor from isotropy.

In fact, it is desirable to connect stress to strain through both coordination number and fabric anisotropy as worked out in [24,26] to arrive at so-called stress-strain-fabric relations for different stages of loading. The embedment of microstructural information can done through a statistical analysis of the micromechanical expression for the average stress tensor [9,19,36], relating interparticle contact forces to branch vectors that connect centroids of particles in contact as given by Rothenburg and coworkers [29,30], and the more recent studies on particle kinematics [13,15,23,34].

The question of how contact fabric evolves has been addressed in previous studies, see [13] for a thorough review. In general, two classes of studies can be recognized based on whether fabric evolution is related to stress [21] or to strain [6,13,27,28] increments. More recent studies suggest that a combination of stress and strain controls the evolution of fabric, with contact loss and gain being related to forces and deformations, respectively [25].

Nonetheless, the previous literature mostly studies the fabric evolution under simple conventional loading paths, such as in biaxial, triaxial, or isochoric tests. As such, the generality of such studies is considerably limited, recalling that the elasto-plastic response of granular materials is incremental in nature and generally depends upon the direction of loading [7,8,20,33]. Such a direction dependence, or incremental nonlinearity, is often studied via directional probing; a pioneer method also known as Gudehus envelope [11], where vertical and horizontal stress (or strain) increments in varying ratios are applied to the granular assembly, while the magnitude of the applied loading increment is kept constant [3,5].

The current study investigates the evolution of contact fabric in response to directional strain probes. As a first step toward this topic, the direction dependence of the fabric response is investigated herein for isotropic, two-dimensional granular assemblies with different initial coordination numbers. Discrete Element Method (DEM for short) simulations have been performed to measure various contributions to the evolution of the fabric tensor due to the contact loss, gain, and reorientation mechanisms. The results exhibit a strong *incrementally nonlinear* evolution of fabric tensor, that is in stark contrast with the accompanying elastic, linear stress-strain response. Such directional dependencies of fabric response, serves as a precursor for an elasto-plastic stress-strain response, normally reflected as the dependency of the stress response on the direction of loading.

2 Micromechanics

The internal structure of the interparticle contact network, is often characterized by a second-order fabric tensor $\boldsymbol{F}$ encompassing the density and the directional distribution of contact as [12,22,31]:

$$F_{ij} = \frac{2}{N_p} \sum_{c \in \mathbb{C}} n_i^c \, n_j^c \tag{1}$$

with N_p being the number of particles (excluding rattlers, i.e. particles with fewer than two contacts), $\mathbb{C}$ the set of all contacts, and $\boldsymbol{n}^c$ the contact normal vector at contact c.

The characteristics of the fabric tensor are herein studied in terms of two prominent variables: the coordination number, Z, defined as the average number of contacts per particle, and an anisotropy measure, A, both defined in terms of the principal values F_1 and F_2 of the fabric tensor $\boldsymbol{F}$:

$$Z = \frac{2N_c}{N_p} = \mathrm{tr}(\boldsymbol{F}) = F_1 + F_2, \quad A = F_1 - F_2 \tag{2}$$

where N_c is the total number of contacts. The commonly used fabric anisotropy, see e.g. [30], is related to these two variable by $2A = a_c \, Z$.

The change in fabric tensor can be decomposed into additive contributions from three mechanisms: contact gain, contact loss, and contact reorientation [13,25], i.e.

$$\begin{aligned} \Delta F_{ij} &= \frac{2}{N_p} \Big(\sum_{c \in \mathbb{C}^{\mathrm{final}}} n_i^c \, n_j^c - \sum_{c \in \mathbb{C}^{\mathrm{init}}} n_i^c \, n_j^c \Big) \\ &= \frac{2}{N_p} \sum_{c \in \Delta\mathbb{C}^g} n_i^c \, n_j^c - \frac{2}{N_p} \sum_{c \in \Delta\mathbb{C}^l} n_i^c \, n_j^c + \frac{2}{N_p} \sum_{c \in \mathbb{C}^r} \Delta(n_i^c \, n_j^c) \\ &= \quad \Delta F_{ij}^g \quad - \quad \Delta F_{ij}^l \quad + \quad \Delta F_{ij}^r \end{aligned} \tag{3}$$

with the sets of lost and gained contacts denoted by $\Delta\mathbb{C}^l$ and $\Delta\mathbb{C}^g$ respectively, while $\mathbb{C}^r$ is the set of persisting contacts.

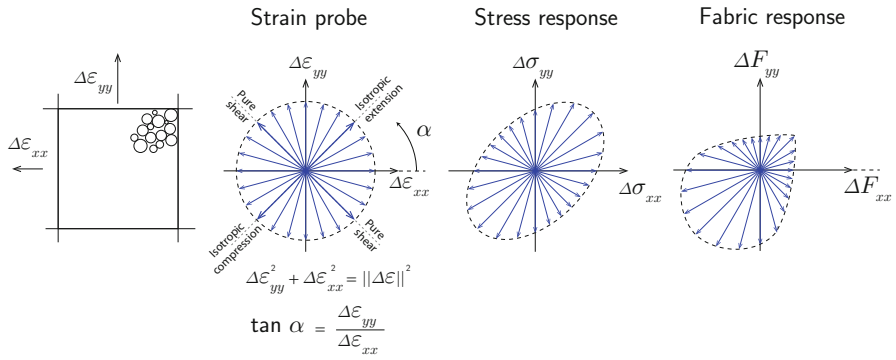

Fig. 1. Schematics of strain probe, stress response and fabric response.

As mentioned earlier, previous studies such as [13,25] have indeed provided insights as to how the fabric tensor changes due to these mechanisms along single monotonic loading (stress or strain) paths. The scope of the investigation is

broadened here by exploring the evolution of the fabric tensor in response to different proportional loading paths through strain probes, as illustrated schematically in Fig. 1. As a first step towards the study of more complex anisotropic systems, the current work is restricted to isotropic initial samples.

3 DEM Simulations

DEM simulations have been performed on two-dimensional square assemblies of 50,000 circular particles with uniformly distributed radii and a ratio of maximum to minimum particle radii of $r_{\max}/r_{\min} = 2$. Similar linear contact stiffnesses have been set for normal and tangential directions, $k_n = k_t$, with the relative stiffness of $k_n/p_0 = 5 \times 10^3$, where p_0 is the initial confining pressure. The interparticle friction has been set at $\mu = 0.5$.

In order to also investigate the effect of the initial coordination number, six initial samples, with varying coordination numbers, Z_0, and void ratios, e_0, were prepared, as listed in Table 1. The sample preparation method has been carefully chosen to yield initially isotropic samples with the initial fabric anisotropy remaining $|a_{c0}| \leq 10^{-4}$. After stabilizing the sample under the initial confining stress, strain probes with a magnitude of $||\Delta\boldsymbol{\varepsilon}|| = \sqrt{\Delta\varepsilon_{yy}^2 + \Delta\varepsilon_{xx}^2} = 2 \times 10^{-4}$ were applied to the samples.

Table 1. Coordination number Z_0 and void ratio e_0, after compaction, of the initial samples.

Z_0	4.53	4.21	4.10	3.87	3.76	3.68
e_0	0.157	0.173	0.179	0.196	0.204	0.211

Figure 2 presents the stress and fabric incremental responses to the imposed strain probes for the dense sample with initial coordination number of $Z_0 = 4.53$. Normal contact stiffness k_n has been used as a scaling factor to render stresses dimensionless.

While the common symmetry around $\alpha = 45°$, expected for an isotropic material, is observed, it is clear that the fabric response is incrementally nonlinear with respect to the strain increment as the symmetry breaks down around $\alpha = 135°$, i.e. contact loss in pure extension does not match the contact gain in pure compression.

The stress responses of samples to the strain probes of the same size are shown in Fig. 3. To avoid overcrowding, only the final states of strain and stress increments are plotted. Furthermore, the total strain was decomposed into elastic and plastic parts by repeating probes with an artificially large interparticle friction to suppress any sliding mechanism [26]. This showed that plastic deformations were insignificant (<1%), hence the total strains can be considered as elastic.

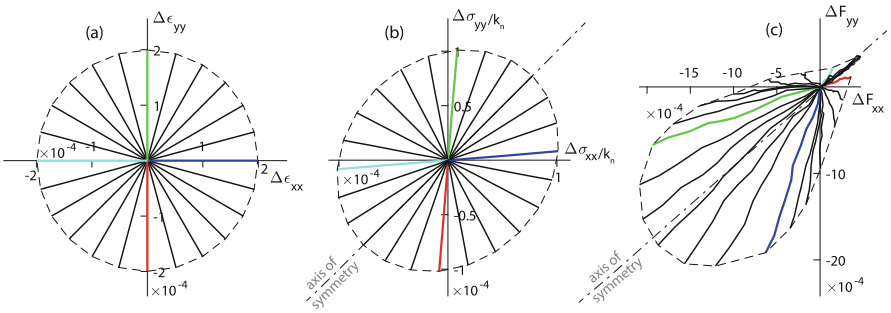

Fig. 2. (a) Imposed strain probes, (b) stress responses, and (c) fabric responses. Results for the dense sample with initial coordination number $Z_0 = 4.53$. Some characteristic probe directions are shown in colour for easy interpretation and clarity.

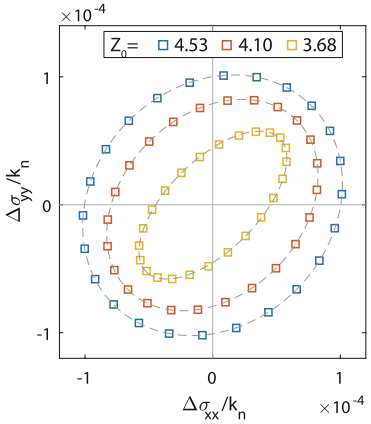

Fig. 3. Dimensionless stress responses to the strain probes with magnitude of $||\Delta\varepsilon|| = 2 \times 10^{-4}$ for samples with different (selected) initial coordination numbers Z_0. Only the final points of the stress response have been plotted. The dashed lines represent elliptical fits that correspond to an incrementally linear stress response.

The contact configuration at the beginning and at the end of the strain probes can be compared to compute the fabric change due contact loss, gain, and reorientation mechanisms, $\Delta\boldsymbol{F}^l$, $\Delta\boldsymbol{F}^g$, and $\Delta\boldsymbol{F}^r$, as defined in Eq. 3. While not presented here, the results indicate that the principal directions of these tensors are aligned with the horizontal and vertical directions. Therefore, the properties of these tensors are reduced to the sum of, and difference between their vertical and horizontal components (which are principal values). For generality, the results are normalized to the strain probe magnitude $||\Delta\boldsymbol{\varepsilon}||$ which presents the rate of change with respect to strain increment:

$$\Delta Z^{*m} = \frac{\Delta F^m_{yy} + \Delta F^m_{xx}}{||\Delta \boldsymbol{\varepsilon}||} = \Delta F^{*m}_{yy} + \Delta F^{*m}_{xx}$$
$$\Delta A^{*m} = \frac{\Delta F^m_{yy} - \Delta F^m_{xx}}{||\Delta \boldsymbol{\varepsilon}||} = \Delta F^{*m}_{yy} - \Delta F^{*m}_{xx} \tag{4}$$
$$m = l,\ g,\ r \quad \text{for contact loss, gain, and reorientation}$$

with the parameter ΔZ^{*m} in Eq. 4 denoting the rate of change in coordination number due to each mechanism, while ΔA^{*m} is related to the associated rate of change of fabric anisotropy. It should be noticed that the variable ΔA^{*m} in Eq. 4 is defined such that, depending on the direction of the maximum fabric change, it can assume both positive and negative values. Figure 4 shows the variation of ΔZ^{*m} and ΔA^{*m} with probe direction α for the probes presented in Fig. 3.

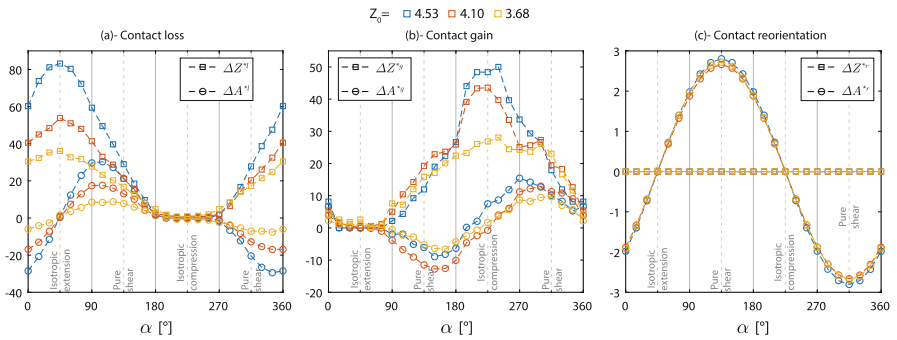

Fig. 4. Rate of change in contact fabric tensor due to (a) contact loss, (b) contact gain, and (c) contact reorientation, as defined in Eq. 3 for strain probes shown in Fig. 3. The square symbols show the sum of the vertical and horizontal (principal) components of the tensors, and the circles show the difference between these two values, as defined in Eq. 4.

The results in Fig. 4 indicate that the rate of contact loss in isotropic extension does not match the rate of contact gain in isotropic compression, which leads to the asymmetry of fabric change around $\alpha = 135°$, as already observed in Fig. 2(c). By definition, no coordination number change is associated with contact reorientation, i.e. $\Delta Z^{*r} = 0$. Moreover, the contribution of contact reorientation to fabric change remains negligible compared to contact loss and gain. While no clear dependency on initial coordination number is observed for the contact reorientation in Fig. 4(c), both variables ΔZ^{*m} and ΔA^{*m} for contact gain and loss mechanisms exhibit an increase as initial coordination number Z_0 increases, as shown in Fig. 4(a) and (b).

Furthermore, the results in Figs. 4(a) and (b) indicate that the maximum change in fabric anisotropy parameter, ΔA^{*m}, does not occur for the directions of pure shear, $\alpha = 135°$ and $315°$. Instead, the directions of these extrema are

shifted slightly towards the extension half region of the probes, i.e. $-45° < \alpha < 135°$. As such, it is concluded that the largest change in fabric anisotropy occurs for a strain probe direction that involves a combination of deviatoric and extension strain.

3.1 Analysis of DEM Results with Representation Theorem

Following the representation theorem for the functional dependence of a second-order tensor on another second-order tensor in two-dimensional isotropic systems, the change in fabric due to each mechanism can be readily expressed as:

$$\Delta F_{ij}^{*m} = \psi_1^m \delta_{ij} + \psi_2^m \Delta\varepsilon_{ij}^*, \quad m = l,\, g,\, r \tag{5}$$

where ψ_1^m and ψ_2^m are functions of the invariants of $\Delta\boldsymbol{\varepsilon}^*$ as well as the initial coordination number, Z_0. Assuming Fourier series expansion up to the second order of the probe direction, the expression in Eq. 5 can be reformulated in terms of ΔZ^*, ΔA^*, and the trigonometric functions:

$$\begin{aligned} \Delta Z^{*m} &= a_1^m + a_2^m(\cos\alpha + \sin\alpha) + a_3^m \cos\alpha \sin\alpha \\ \Delta A^{*m} &= a_4^m(\cos\alpha - \sin\alpha) + a_5^m(\cos^2\alpha - \sin^2\alpha) \\ m &= l,\, g,\, r \end{aligned} \tag{6}$$

with the total changes given as the sum over the contributing mechanisms:

$$\begin{aligned} \Delta Z^* &= -\Delta Z^{*l} + \Delta Z^{*g} = a_1 + a_2(\cos\alpha + \sin\alpha) + a_3 \cos\alpha \sin\alpha \\ \Delta A^* &= -\Delta A^{*l} + \Delta A^{*g} + \Delta A^{*r} = a_4(\cos\alpha - \sin\alpha) + a_5(\cos^2\alpha - \sin^2\alpha) \\ a_i &= -a_i^l + a_i^g + a_i^r \end{aligned} \tag{7}$$

The results in Fig. 5 verify the accuracy of the expressions in Eq. 6 in fitting the variation of ΔZ^{*m} and ΔA^{*m} with strain probe direction α for the sample with initial coordination number of $Z_0 = 4.10$. Only a single coefficient, E^r, with the relatively constant value of 2.7, is required to represent the variation of fabric tensor due contact reorientation ΔF_{ij}^r, since no coordination number change is associated with contact reorientation, and the variation of ΔA^{*r} is accurately fitted with the first-order harmonic term, as demonstrated in Fig. 5(c).

By definition, incremental linearity for fabric evolution is obtained where a symmetry around $\alpha = 135°$ is observed, i.e. $\Delta\boldsymbol{F}(\alpha) = -\Delta\boldsymbol{F}(-\alpha)$. Therefore, based on the expressions in Eq. 6, an incrementally linear fabric response is obtained whenever all the following conditions are met:

1. The rate of change in coordination number due to contact loss in isotropic extension is equal to the rate of change in coordination number due to contact gain in isotropic compression.
2. The rates of change in coordination number due to contact loss and contact gain are equal in pure shear.
3. The maximum rate of change of anisotropy is obtained in pure shear.

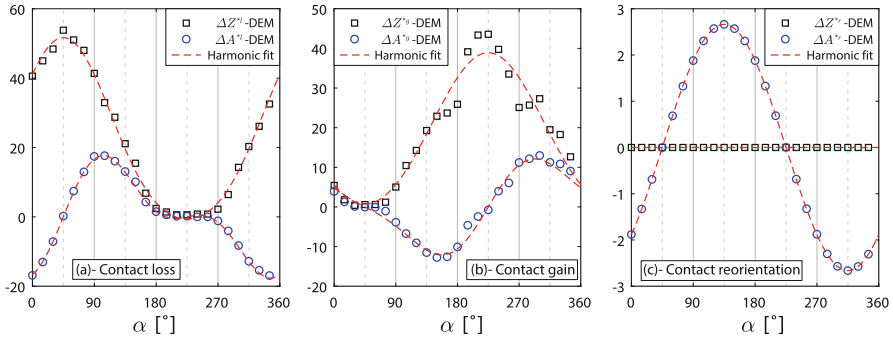

Fig. 5. Accuracy of the expressions in Eq. 6 in representing fabric change due to contact loss (left), contact gain (middle), and contact reorientation (right), for the sample with initial coordination number $Z_0 = 4.10$.

It is clear from the results in Fig. 4 that none of the above three conditions is satisfied, with the deviation from the first condition being the largest. The observed incrementally nonlinear evolution of fabric is particularly intriguing remembering that it occurs in a predominantly elastic deformation regime.

A more quantitative assessment of the incremental nonlinearity of fabric evolution is presented in Fig. 6 where the variation of coefficients in Eq. 7 with initial coordination number is given. Following the three above-mentioned requirements for incremental nonlinearity, the non-zero variables a_1, a_3, and a_5 point towards an incrementally nonlinear evolution of fabric with strain increments. Moreover, based on Eq. 7, the fact that $a_5 < a_3$ indicates that the deviation from incremental linearity is more significant for the deviatoric part of fabric tensor, ΔA^* compared to its spherical part, ΔZ^*. It is also important to notice that the changes in fabric scale with initial coordination number as suggested by the relatively linear trends in Fig. 6.

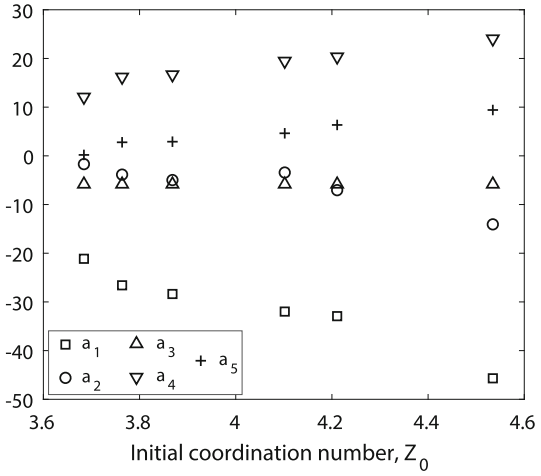

Fig. 6. Variation of coefficients describing the total fabric change in Eq. 7 with initial coordination number Z_0.

Such a dependency on the direction of loading further is consistent with the directional dependency of plastic flow rule [33] and constitutive models embedding such incremental nonlinearity [7,8,20].

4 Conclusions

Two-dimensional DEM simulations of initially isotropic systems have been performed to study the stress and fabric responses of granular media to strain probing. While the stress response remains incrementally linear and elastic, intriguingly, the fabric changes exhibit strong dependence on the strain probe direction, and hence incremental nonlinearity. Such an incrementally nonlinear evolution of the fabric response can only develop further to serve as a precursor to the elasto-plasticity of anisotropic granular assemblies.

To further explore the nature of fabric changes, the contributions of each of contact gain, loss, and reorientation mechanisms have been separately studied. As intuitively expected, the contribution of contact loss and gain are seen to be dominant in extensional and compressive probes, respectively. The contribution of contact reorientation is consistently negligible compared to the other two components.

As the main conclusions, the following qualitative observations have been made regarding the nature of fabric evolution:

1. In isotropic compression the rate of change in coordination number due to contact loss is very small, while the isotropic extension contact gain is very small.
2. The rate of change in anisotropy is not largest in pure shear, but in a probe direction that involves shear *and* extension.
3. The rate of contact loss in isotropic extension is larger than the rate of contact gain in isotropic compression. It is this difference that ultimately forms the primary origin of the incremental nonlinearity of fabric response to strain probing.
4. The parameters expressing the rate of change in the above-mentioned characteristic directions scale almost linearly with initial coordination number of the samples.

The results indicate that further studies, with wider ranges of conditions, are required to clearly explain the evolution of contact fabric and its role in driving the mechanical response of granular materials, especially in three-dimensional conditions. It will especially be interesting to study the fabric evolution in initially anisotropic configurations, for which, interrelations are expected between lost and gained contacts distributions, as our preliminary results show.

Finally, the observations in this study show that, as it stands, the issue of 'microstructure-motivated' elasticity is an open question, with more detailed investigations required to delineate the relation between fabric evolution and stress-strain response.

Acknowledgements. Research funding jointly provided by the Natural Sciences and Engineering Research Council of Canada and Foundation Computer Modelling Group (now Energi Solutions Ltd.) is gratefully acknowledged. This work was initiated during a short research visit at the University of Twente, the Netherlands, by the first author. Sincere gratitude is due to the University of Twente for providing an enriching and stimulating environment for this work, which has subsequently flourished into this manuscript.

References

1. Azéma, E., Radjai, F., Saussine, G.: Quasistatic rheology, force transmission and fabric properties of a packing of irregular polyhedral particles. Mech. Mater. **41**(6), 729–741 (2009)
2. Bagi, K.: Analysis of microstructural strain tensors for granular assemblies. Int. J. Solids Struct. **43**(10), 3166–3184 (2006)
3. Bardet, J.P.: Numerical simulations of the incremental responses of idealized granular materials. Int. J. Plast. **10**(8), 879–908 (1994)
4. Bashir, Y.M., Goddard, J.D.: A novel simulation method for the quasi-static mechanics of granular assemblages. J. Rheol. **35**(5), 849–885 (1991)
5. Calvetti, F., Viggiani, G., Tamagnini, C.: A numerical investigation of the incremental behavior of granular soils. Riv. Ital. Geotec. **37**(3), 11–29 (2003)
6. Calvetti, F., Combe, G., Lanier, J.: Experimental micromechanical analysis of a 2D granular material: relation between structure evolution and loading path. Mech. Cohesive-frictional Mater. **2**(2), 121–163 (1997)
7. Darve, F.: The expression of rheological laws in incremental form and the main classes of constitutive equations. In: Geomaterials: Constitutive Equations and Modelling, pp. 123–148 (1990)
8. Darve, F., Nicot, F.: On incremental non-linearity in granular media: phenomenological and multi-scale views (Part I). Int. J. Numer. Anal. Meth. Geomech. **29**(14), 1387–1409 (2005)
9. Drescher, A., De Jong, G.D.J.: Photoelastic verification of a mechanical model for the flow of a granular material. J. Mech. Phys. Solids **20**(5), 337–340 (1972)
10. Gao, Z., Zhao, J.: A non-coaxial critical-state model for sand accounting for fabric anisotropy and fabric evolution. Int. J. Solids Struct. **106–107**, 200–212 (2017)
11. Gudehus, G.: A comparison of some constitutive laws for soils under radially symmetric loading and unloading. Can. Geotech. J. **20**, 502–516 (1979)
12. Ken-Ichi, K.: Distribution of directional data and fabric tensors. Int. J. Eng. Sci. **22**(2), 149–164 (1984)
13. Kruyt, N.P.: Micromechanical study of fabric evolution in quasi-static deformation of granular materials. Mech. Mater. **44**, 120–129 (2012)
14. Kruyt, N.P., Rothenburg, L.: Micromechanical definition of the strain tensor for granular materials. J. Appl. Mech. **118**, 706–711 (1996)
15. Kruyt, N.P., Rothenburg, L.: Shear strength, dilatancy, energy and dissipation in quasi-static deformation of granular materials. J. Stat. Mech: Theory Exp. **2006**(07), P07021 (2006)
16. Kruyt, N.P., Rothenburg, L.: A micromechanical study of dilatancy of granular materials. J. Mech. Phys. Solids **95**, 411–427 (2016)
17. Li, X.S., Dafalias, Y.F.: Constitutive modeling of inherently anisotropic sand behavior. J. Geotech. Geoenvironmental Eng. **128**(10), 868–880 (2002)

18. Li, X.S., Dafalias, Y.F.: Anisotropic critical state theory: role of fabric. J. Eng. Mech. **138**(3), 263–275 (2011)
19. Love, A.E.H.: A Treatise on the Mathematical Theory of Elasticity. Cambridge University Press, Cambridge (1927)
20. Nicot, F., Darve, F.: Basic features of plastic strains: from micro-mechanics to incrementally nonlinear models. Int. J. Plas. **23**(9), 1555–1588 (2007)
21. Oda, M., Nemat-Nasser, S., Mehrabadi, M.M.: A statistical study of fabric in a random assembly of spherical granules. Int. J. Numer. Anal. Meth. Geomech. **6**(1), 77–94 (1982)
22. Oda, M.: Initial fabrics and their relations to mechanical properties of granular material. Soils Found. **12**(1), 17–36 (1972)
23. Pouragha, M., Wan, R.: Strain in granular media: a probabilistic approach to Dirichlet tessellation. J. Eng. Mech. **143**, C4016002 (2016)
24. Pouragha, M., Wan, R., Hadda, N.: A microstructural plastic potential for granular materials. In: Geomechanics from Micro to Macro, pp. 661–665 (2014)
25. Pouragha, M., Wan, R.: Non-dissipative structural evolutions in granular materials within the small strain range. Int. J. Solids Struct. **110**, 94–105 (2017)
26. Pouragha, M., Wan, R.: On elastic deformations and decomposition of strain in granular media. Int. J. Solids Struct. **138**, 97–108 (2018)
27. Radjai, F., Troadec, H., Roux, S.: Key features of granular plasticity. In Granular Materials: Fundamentals and Applications, pp. 157–184. Royal Society of Chemistry London, London (2004)
28. Rothenburg, L., Kruyt, N.P.: Critical state and evolution of coordination number in simulated granular materials. Int. J. Solids Struct. **41**(21), 5763–5774 (2004)
29. Rothenburg, L., Selvadurai, A.P.S.: A micromechanical definition of the Cauchy stress tensor for particulate media. In: Mechanics of Structured Media, pp. 469–486 (1981)
30. Rothenburg, L., Bathurst, R.J.: Analytical study of induced anisotropy in idealized granular materials. Géotechnique **39**(4), 601–614 (1989)
31. Satake, M.: Constitution of mechanics of granular materials through the graph theory. In: Proceedings of U.S.-Japan Seminar on Continuum Mechanical and Statistical Approaches in the Mechanics of Granular Materials Sendai, pp. 203–215 (1978)
32. Tobita, Y.: Fabric tensors in constitutive equations for granular materials. Soils Found. **29**(4), 91–104 (1989)
33. Wan, R., Pinheiro, M.: On the validity of the flow rule postulate for geomaterials. Int. J. Numer. Anal. Meth. Geomech. **38**(8), 863–880 (2014)
34. Wan, R., Pinheiro, M.: Fabric and connectivity as field descriptors for deformations in granular media. Continuum Mech. Thermodyn. **27**(1–2), 243–259 (2014)
35. Wan, R., Guo, J.: Drained cyclic behavior of sand with fabric dependence. J. Eng. Mech. **127**(11), 1106–1116 (2001)
36. Weber, J.: Recherches concernant les contraintes intergranulaires dans les milieux pulvérulents. Bul. Liaison P. et Ch **2**(64), 170 (1966)
37. Zhu, H.N., Mehrabadi, M.M., Massoudi, M.: Three-dimensional constitutive relations for granular materials based on the dilatant double shearing mechanism and the concept of fabric. Int. J. Plast. **22**(5), 826–857 (2006)

On How to Look Inside Geo-Materials

Alexander Scheuermann[1(✉)], Ling Li[2], Hans Muehlhaus[1], Thierry Bore[1], Sergio Galindo Torres[2], Dorival Pedroso[1], Farzin Hamidi[1], HMD Harshani[1], Tilman Bittner[1], Somayeh Behraftar[1], and Mohammad Aminpour[1]

[1] The University of Queensland, St Lucia, QLD 4072, Australia
a.scheuermann@uq.edu.au
[2] School of Engineering, Westlake University, Hangzhou, China

Abstract. The observation of structural changes inside geo-materials during testing is still uncommon in geotechnical engineering. New developments in imaging techniques and improved analysis methods allow us for the first time to observe structural changes inside geo-materials and to provide us with the required information for developing new knowledge and constitutive relationships. The presented paper introduces three approaches for observing structural changes in porous media: (1) Particle Imaging Velocimetry (PIV) in combination with transparent hydro-gel beads, (2) Spatial Time Domain Reflectometry (Spatial TDR) for observing porosity distributions during contact erosion testing, and (3) Ultra High Speed Camera (UHSC) imaging in combination with a brittle, low strength rock like material for investigating hydraulic fracturing.

Keywords: Imaging methods · Transparent soil · Electromagnetic methods

1 Introduction

It is the dreaming of every experimentalist working with geo-materials to have the chance to observe and quantify changes in the internal conditions of the specimen during testing. Whenever we analyze changes in macroscopic observations, such as deformation or discharge, we always look for explanations for these observations involving the internal structure of the specimen on the micro-scale without being able to provide the required evidence. Depending of the nature of the problem, these internal changes can be associated to water content changes and/or changes in the structural composition of the solid phase. New imaging techniques and analysis methods as well as other alternative observation methods allow us to capture additional information during testing and provide unique insights into the internal conditions of specimens. As examples, CT scanning techniques [1], X-Ray [2], acoustic emission [3], and the application of transparent soil as soil or rock substitute materials are mentioned. Less frequently used, but not less powerful, are electromagnetic measurement methods that are used e.g. in medicine or physical chemistry. Magnetic Resonance Imaging is probably the most powerful technique at hand. Simpler methods are dielectric spectroscopy and time domain reflectometry. This contribution introduces three methods used at the University of Queensland for capturing changes inside samples during testing.

W. Wu (Ed.): *Desiderata Geotechnica*, SSGG, pp. 162–168, 2019.
https://doi.org/10.1007/978-3-030-14987-1_20

2 Particle Imaging Velocimetry (PIV) for Quantifying Pore-Scale Flow

2.1 Motivation

The pore-scale flow conditions are causative for the onset of erosion. For example, in the case of contact erosion with water flow perpendicular to the interface from fine- to the coarse-grained soil fraction, the flow velocity changes dramatically and is concentrated in the constrictions formed by the coarse particles at the interface. This change in flow velocity needs to be known and characterized to enable the development of new erosion criteria and of computational models.

2.2 Approach

The development of an experimental set-up for investigating the flow conditions on the pore-scale based on PIV was one objective within a discovery project [4]. The application of PIV in porous media flow requires the usage of a solid and a liquid that are refractive-index matched. Frequently, glass beads are used in combination with glycerin mixtures or oil. The unique feature of the presented system is the use of 10 to 11 mm large hydrogel beads and water as the flowing liquid. The advantage of this combination is the possibility to use standard measurement methods for quantifying the flow conditions. A disadvantage is that the hydrogel beads are very soft, and their density is just a bit larger than the density of water. Therefore, there is a limitation in the flow forces that can be applied without deforming the beads, and no free surface of particles can be simulated. The experimental set-up allows the measurement of two-dimensional velocity fields within the illuminated plane by using seeding particles with neutral buoyance in the size of 20 μm. Out of plane movements of the water due to the three-dimensional nature of the water flow cannot be captured and can potentially falsify the measurement.

2.3 Measurement Example and Findings

Figure 1 shows an exemplary measurement result using the PIV system. Hydrogel beads of different sizes have been used to form two layers of finer and coarser grained materials. The cut through the sample was selected in a way to show the flow conditions in the constrictions formed by the particles. A coupled Lattice Boltzmann Method (LBM)/Discrete Element Method (DEM) model was used to simulate the measured flow conditions. The simulation results were analyzed in a way to allow a one-to-one comparison with the measurement results taking into account the out of plane movement of the water. An interesting and surprising finding of this investigation is the fact that the highest velocity is not observed within the base material, but in the constriction of the coarse particles just above the fine layer. This flow velocity was identified to be approximately four times larger than the filter velocity of the overall sample. This observation can be explained by taking into account the obstacle effect of coarse particles sitting on a layer of fine particles. Water flowing towards this obstacles get sidetracked and channelized into the constrictions producing a jet-like flow.

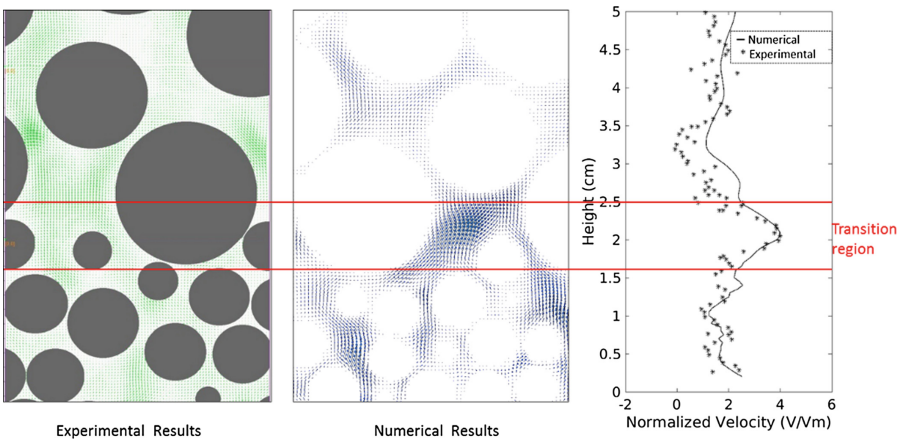

Fig. 1. Measurement example with the PIV system (left) in comparison with results from DEM/LBM simulations (middle) showing the flow conditions at the transition from a finer grained material into a layer of coarser grained material. The velocity profile normalized by the filter velocity (right) shows a comparison between the averaged velocities in the transition zone.

3 Spatial Time Domain Reflectometry (Spatial TDR) for Measuring Porosity Distributions During Erosion Testing

3.1 Motivation

Once a critical hydraulic gradient is reached within a geometrically unstable sample, erosion starts by mobilizing particles accompanied with porosity changes on the local scale. The porosity is the crucial parameter influencing the onset, but also the transient evolution of erosion. In various approaches for simulating erosion with continuum based computational models, the porosity is the main parameter of interest, and erosion is described as a process leading to changes in porosity. It is therefore obvious to observe changes in porosity during erosion and to identify where these changes take place.

3.2 Approach

Spatial TDR allows the measurement of the apparent dielectric permittivity along elongated sensors [5]. With suitable calibration functions, the porosity can be determined under the assumption of fully water-saturated conditions. A new experimental set-up was developed for determining porosity profiles using a large coaxial line cell that is used as sensor and sample holder [6]. The annulus of the coaxial cell allows the implementation of tests with particle sizes up to 11 mm. A Sequid SDTR-65 TDR device is used for capturing TDR measurements that are analysed using an inversion algorithm based on the approach of Schlaeger to compute the distribution of the apparent dielectric permittivity. This permittivity distribution can then be transferred into a porosity distribution by suitable mixing functions or material specific calibration formulas.

3.3 Measurement Example and Findings

Figure 2 shows an exemplary result of measured porosity distributions of a sample composed of glass beads during a contact erosion test with flow in upwards direction. The coaxial cell includes an observation window that allows the visual observation of changes in the heights of each material layer. As a consequence of erosion, coarse and fine particles mix together forming a new layer of material with a much reduced porosity. The development of this new layer is very well observed using the TDR measurement system. One important observation made with the new set-up concerns the nature of the progress of erosion. While erosion is frequently considered as a transport problem of fine particles, the observations in the new set-up revealed that once the critical gradient is reached fine particles get fluidized but are not transported away. It is rather the layer of coarse particles that starts to penetrate into the layer of fine particles due to the reduced shear strength of the uppermost fine particles. While penetrating into the matrix of fine particles, the coarse particles relocate and form a structure with an increased porosity.

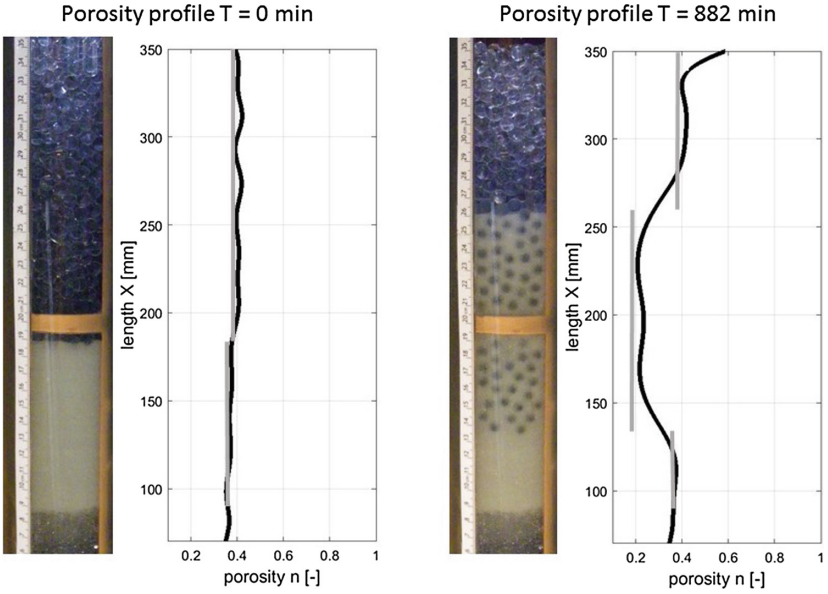

Fig. 2. Measured porosity distributions within a sample composed of glass beads at the beginning (left) and during a contact erosion test (right). The coarse fraction of 8 mm glass beads (nearly transparent) is placed on a layer of fine particles (appear in white) with a diameter of 0.3 to 0.4 mm. The grey columns represent the mean porosities measured from the mass and the height of the layer as observed through the window (left of each graph).

The new set-up involving Spatial TDR for porosity measurements allows for the first time continuous observations of porosity changes during erosion tests. The observations made with this system will help in future to better understand the transient

evolution of erosion and will lay the foundation for future developments of computational models that will allow in combination of field observation methods the development of monitoring and prediction tools.

4 Ultra High Speed Camera (UHSC) Recording for Characterizing Crack Evolution During Hydraulic Fracturing

4.1 Motivation

The use of PMMA in hydraulic fracturing investigation as substitute material for rock has already a long tradition. Within another discovery project, we have identified and characterized a new material showing better comparable parameters to rock than PMMA, but still being transparent [7]. The big advantages of this material, called Smash-It, is its low tensile strength and its capability to be melted at temperatures of around 120 °C. This allows casting samples of every kind, size and form. At the same time, many computational models have been developed by researchers mostly on particle based methods simulating hydraulic fracturing in 2D without being able to validate their model with experiments conducted at exactly the same conditions.

4.2 Approach

An experimental set-up was developed for the implementation of hydraulic fracturing tests with thin, thick-walled, circular samples with an injection hole in the middle. The aim of the set-up was to be able to conduct quasi-2D experiments in plain strain conditions to provide not only data for validating computational models, but also to have the unique opportunity to observe the various stages of the development of cracks as they evolve in one plane. For this purpose, a sandwich-like sample holder was developed with an upper steel head allowing the injection of a liquid and the application of a confining stress and a transparent bottom PMMA plate that allows the observation of the processes within the assembly. The Smash-It sample is placed in between these plates sealed with a thin silicon layer towards the both neighboring plates. By having dots marked on the sample in a regular pattern, UHSC observations can be used to observe deformations of the sample during the hydraulic fracturing test. At the same time, the evolution of the crack can be observed allowing the quantification of the crack velocity during the experiment.

4.3 Measurement Example and Findings

Figure 3 shows an example of UHSC observations during a hydraulic fracturing experiment conducted with the new set-up. Tests have been conducted for different confining stresses applied in vertical direction for samples with a notch-free injection hole. The circumference of the sample was stress-free. The main observations from these tests were that the crack velocity seems to be independent of the vertical confined stress while the breakdown pressure is. The crack velocity is highest at crack initiation

close to the theoretically possible terminal velocity. From this unstable crack propagation the crack development turns into a stable process at much lower velocities before it accelerates again towards the end of the sample. The new set-up provides the opportunity to look closer into the transient development of cracks induced by hydraulic fracturing.

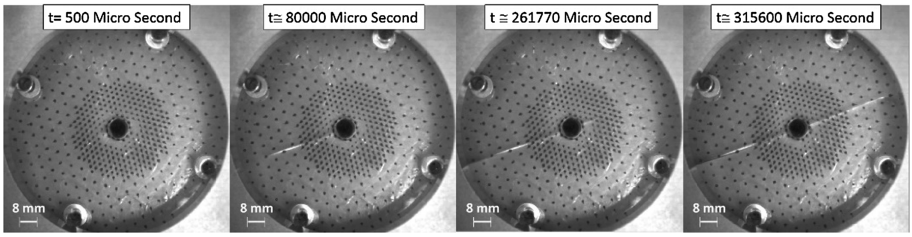

Fig. 3. Results of UHSC observations during hydraulic fracturing tests with the new set-up and using Smash-It as rock-similar test material.

5 Conclusion

The presented examples show the opportunities arising from the application of unconventional observation methods for investigating hydro-mechanically coupled process in and with geo-materials. The geotechnical community has identified the development of new measurement and observation methods as the key challenge for the future. It will be the task for research institutes to develop these techniques together with analysis procedures to be able to transfer these technologies into practical applications.

Acknowledgement. The presented research was funded by the Australian Research Council through the projects "Hydraulic erosion of granular structures" (DP120102188) and "Qualitative and quantitative modelling of hydraulic fracturing of brittle materials" (DP140100490) and supported by a Queensland Smart Futures Fellowship awarded to the first author.

References

1. Desrues, J., et al.: Void ratio evolution inside shear bands in triaxial sand specimens studied by computed tomography. Géotechnique **46**(3), 529–546 (1996)
2. Guillard, F., et al.: Dynamic X-ray radiography reveals particle size and shape orientation fields during granular flow. Sci. Rep. **7**(1), 8155 (2017)
3. Lockner, D.: The role of acoustic emission in the study of rock fracture. Int. J. Rock Mech. Min. Sci. **30**(7), 883–899 (1993)
4. Harshani, H.M.D., et al.: Experimental study of porous media flow using hydro-gel beads and LED based PIV. Meas. Sci. Technol. **28**(1), 015902 (2016)

5. Scheuermann, A., et al.: Spatial time domain reflectometry and its application for the measurement of water content distributions along flat ribbon cables in a full-scale levee model. Water Resour. Res. **45**(4) (2009)
6. Bittner, T., et al.: Development of a coaxial cell for porosity measurements during contact erosion experiments. Eurogroup Working Group on Int Erosion, vol. 48 (2017)
7. Hamidi, F., et al.: Synthetic low-strength materials as rock substitutes for physical model studies. Geomech. Geophys. Geo-Energy and Geo-Resour. **4**, 273–297 (2018)

The Biot Coefficient for a Low Permeability Geomaterial with a Heterogeneous Fabric

A. P. S. Selvadurai(✉)

McGill University, Montreal, QC H3A 0C3, Canada
patrick.selvadurai@mcgill.ca

Abstract. The paper describes a research methodology that can be adopted for estimating the Biot coefficient for a low permeability rock that has a heterogeneous internal fabric. Experimental techniques that address the requirements for a representative volume element can be combined with theoretical developments for multiphasic elastic materials to develop bounds for the Biot coefficient. The theoretical developments are used to estimate the Biot coefficient for a heterogeneous argillaceous limestone.

Keywords: Poroelasticity · Biot coefficient · Stress partitioning

1 Introduction

The theory of poroelasticity developed by Biot [1] is one of the key developments in geomechanics that deals with the mechanical behaviour of a porous elastic solid saturated by an ideal fluid [2–6]. Although the theory was developed for purposes of applications to geomaterials, the use of the theoretical concepts has reached beyond the initial objectives and the theory has been applied to the study of the mechanics of bone [7] and soft biological materials such as brain tissue and arterial materials [8–12]. The theory proposed by Biot [1], unlike that of the classical theory of Terzaghi [13], introduces a rational way of addressing stress partitioning between the porous skeleton and the pore fluid that takes into consideration the constitutive properties of the porous skeleton. In principle, the Biot coefficient can be determined provided the compressibility of the porous skeleton and the compressibility of the material composing the porous fabric can be accurately determined. While the estimation of the compressibility of the porous skeleton is straightforward, the estimation of the compressibility of the solid material composing the porous skeleton can be complicated, particularly when the porous rock fabric has a very low permeability [$K \in (10^{-23}, 10^{-20})$ m^2] and can be composed of a variety of rock minerals. This paper shows an approach that can be used to estimate the Biot coefficient, where the compressibility of the solid phase is determined by appeal to results developed for estimating the effective properties of multiphasic elastic media. The results of the experimental developments and theoretical research are used to develop bounds for the Biot coefficient for the argillaceous Cobourg limestone found in southern Ontario, Canada.

W. Wu (Ed.): *Desiderata Geotechnica*, SSGG, pp. 169–174, 2019.
https://doi.org/10.1007/978-3-030-14987-1_21

2 The Cobourg Limestone

The Cobourg limestone is an argillaceous rock formation that is found in southern Ontario and a geologic formation that is being investigated for the creation of a Deep Ground Repository (DGR) for the storage of low- and intermediate-level nuclear fuel waste. This DGR will be located approximately 680 m below ground level within the Cobourg limestone formation of the Paleozoic sedimentary sequence that rests on a Pre-Cambrian granitic gneiss basement rock. Despite its low clay content, the Cobourg limestone is referred to, nominally, as an argillaceous limestone. A characteristic feature of the Cobourg limestone is its heterogeneous fabric (Fig. 1), consisting of lighter nodular regions of calcite and dolomite separated by argillaceous partings of a similar composition but with quartz and a low clay content.

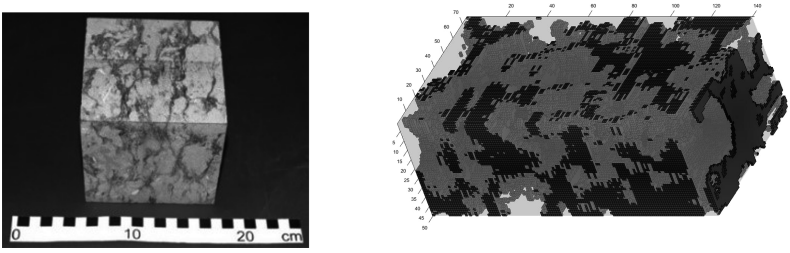

Fig. 1. The Cobourg limestone and its fabric.

Experimental results indicate that the basic physical and mechanical properties show some dependency on the fabric heterogeneity of the Cobourg limestone. The deformability characteristics in terms of the measured elastic modulus varied from 6.6 GPa (250 mm cube) to 17.7 GPa (200 mm cube) with an average of 13.5 GPa. These values are considerably lower than the Young's moduli estimated from triaxial tests on 85 mm diameter, 170 mm long cylindrical samples. A separate test on a 250 mm cube with bonded strain gauges gave a Young's modulus of 35 GPa, consistent with the triaxial test data [14]. These preliminary results indicate that to eliminate the influence of heterogeneity on the basic geomechanical characterizations, the sample dimensions should be larger than 100 mm, which is approximately *four times* the size of the larger nodular regions. The XRT images of the 85 mm diameter and 170 mm long Cobourg limestone cylinders lacked the RVE dimensions necessary to evaluate the relative volume fractions of the lighter gray nodular limestone and the darker argillaceous partings. These volume fractions were estimated using photographic images of thin slices (80 mm $\times$ 120 mm $\times$ 8 mm) obtained from a cuboidal prism. A composite image of the spatial distribution of the lighter grey limestone is shown in Fig. 1. The volume fraction of the lighter grey limestone region was approximately 0.475 and that of the darker argillaceous partings was 0.525. To further investigate the volume fractions, a 150 mm diameter by 300 mm long cylinder was cut into 13 discs of nearly equal thickness. An image analysis of the photographs of both faces of each disc was then used to reconstruct the spatial distribution of the lighter and

darker regions. These studies indicated that the area fraction of the darker grey argillaceous region exhibited wide variability, from 0.076 to 0.631 and the average area fraction of the darker argillaceous phase was approximately 0.36. The data obtained from the dissection of the cuboidal prism are considered more reliable due the smaller thickness of the slabs used in the image analysis. In view of the variability in the estimation of the volume fraction of the darker argillaceous partings (V_{DR}), it is prudent to assign plausible limiting values to the parameter: i.e. $V_{DR} \in (0.36, 0.53)$. The mineralogical composition of the two phases composing the Cobourg limestone can be summarized as follows:

The *Lighter Grey Nodular Phase*: *Calcite* ~ 86%; *Dolomite* ~ 5%; *Quartz* ~ 8%; *Clay* ~ 0.3%; *Porosity* ~ 0.001
The *Darker Argillaceous Partings*: *Calcite* ~ 51%; *Dolomite* ~ 16%; *Quartz* ~ 22%; *Clay* ~ 2.4%; *Porosity* ~ 0.006.

The Bulk and Shear Moduli Values: The values for the bulk moduli $(K_S)_i$ and shear moduli $(G_S)_i$ $(i = Calc, Dolm, Qrtz, Clay)$ of the basic minerals constituting the Cobourg Limestone can be obtained from published literature.

Calcite:$(K_S)_{Calc} = 76$ GPa; $(G_S)_{Calc} = 32$ GPa
Dolomite: $(K_S)_{Dolm} = 95$ GPa; $(G_S)_{Dolm} = 45$ GPa
Quartz: $(K_S)_{Qrtz} = 37$ GPa; $(G_S)_{Qrtz} = 45$ GPa
Clay: $(K_S)_{Clay} = 12$ GPa.

3 The Biot Coefficient

In principle, estimating the Biot coefficient for a geo-material is quite straightforward and requires only the estimation of the *bulk modulus of the porous skeleton* and the *effective bulk modulus of the solid phase constituting the porous skeleton*. The effective stress principle proposed by Biot [1] takes the form

$$\sigma_{ij} = \sigma'_{ij} + \alpha p \delta_{ij} \tag{1}$$

where σ_{ij} is the total stress tensor, σ'_{ij} is the effective stress tensor, p is the pore fluid pressure and δ_{ij} is Kronecker's delta function. Also in (1) α is the "Biot Coefficient", defined by

$$\alpha = 1 - (K_D/K_S) \tag{2}$$

where K_D and K_S are, respectively, the bulk moduli of the porous skeleton and the material composing the fabric of the porous skeleton. The accepted procedure for determining these bulk moduli values for an isotropic poroelastic medium is to conduct triaxial tests on the dry fabric of the porous medium to determine K_D and to conduct a fluid pressure compression of the entire fabric of the porous medium to determine K_S. The former procedure is straightforward but the latter is not. The primary reason for this is the extremely low permeability of the Cobourg Limestone, which inhibits both

the saturation process and the transmission of the externally applied pressure field to the interior of a sample; the larger the diameter of the sample (i.e. the smallest flow path) the larger will be the time required for the pressure pulse to migrate to the interior of the region and, based on the concept of the hydraulic pulse analysis [15–20], the pressure diffusion coefficient will be proportional to the permeability of the rock.

4 A Multi-phase Composites Approach for Estimating K_S

The alternative approach is to estimate the bulk modulus of the solid material constituting the porous skeleton by considering the bulk moduli of the constituents of the solid phases and their volume fractions. Excluding the voids, which constitute only a small fraction of the material space, there are four phases in the solid material. To the author's knowledge, there is no literature in the mathematical theory of multiphasic elastic solids that will allow the estimation of the bulk elastic properties of a multiphasic elastic solid that is composed of four separate constituents. The approach proposed in this research is to use the Voigt-Reuss-Hill (VRH) estimates (see. e.g. Hill [21]), for the light grey $[(\ )_{LR}]$ and the darker argillaceous $[(\ )_{DR}]$ phases as a prelude to the estimation of the bulk properties. The VRH estimate for the bulk modulus can be written as

$$(K_S)_I = \frac{1}{2}\left\{\sum_i^n V_i (K_S)_i + \left(\sum_i^n \frac{V_i}{(K_S)_i}\right)^{-1}\right\}; \quad I = LR, DR; \quad i = Calc,\ Dolm,\ Qrtz, Clay,\ Voids \tag{3}$$

Similarly, using the VRH estimate for the light grey $[(\ )_{LR}]$ and the darker argillaceous $[(\ )_{DR}]$ phases; the VRH estimate for the shear modulus can be written as

$$(G_S)_I = \frac{1}{2}\left\{\sum_i^n V_i (G_S)_i + \left(\sum_i^n \frac{V_i}{(G_S)_i}\right)^{-1}\right\}; \quad I = LR, DR; \quad i = Calc,\ Dolm,\ Qrtz, Clay,\ Voids \tag{4}$$

These estimates can now be used in conjunction with the bounds developed by Hashin and Shtrikman [22] to develop the *Upper* and *Lower* bound estimates for the bulk modulus of the multiphasic system: i.e.

$$(K_S)_L = (K_S)_{LR} + \frac{V_{DR}}{\frac{1}{(K_S)_{DR} - (K_S)_{LR}} + \left(\frac{3(1-V_{DR})}{3(K_S)_{LR} + 4(G_S)_{LR}}\right)} \tag{5}$$

and

$$(K_S)_U = (K_S)_{DR} + \frac{1 - V_{DR}}{\frac{1}{(K_S)_{LR} - (K_S)_{DR}} + \left(\frac{3\,V_{DR}}{3(K_S)_{DR} + 4(G_S)_{DR}}\right)} \tag{6}$$

These procedures have been used to estimate the effective bulk modulus of the solid material constituting the porous fabric of the Cobourg limestone and these values, in conjunction with triaxial experiments conducted on dry samples of the rock, have been used to develop estimates for the Biot efficient [23]; i.e. $0.655 \leq \alpha \leq 0.665$.

5 Concluding Remarks

The Biot coefficient is an important aspect of the theory of classical poroelasticity since it accounts for the rational estimation of effective stresses in a fluid-saturated porous media. The effective stresses ultimately control the deformations and failure of the skeletal fabric. In principle, the Biot coefficient can be estimated if the bulk moduli of the skeletal fabric and the bulk moduli of the rock minerals composing the porous fabric are known. With very low permeability materials, the ready determination of the latter is not feasible. The alternative involves the use of the results for the theory of multiphasic elastic composites to estimate the bulk modulus of the materials composing the porous structure. As the number of mineral species increase, appeal must be made to such developments to determine the effective bulk modulus of the material composing the porous skeleton.

Acknowledgements. The work described in this paper was supported by research grants awarded by the Natural Sciences and Engineering Research Council of Canada and the Nuclear Waste Management Organization of Ontario.

References

1. Biot, M.A.: General theory of three-dimensional consolidation. J. Appl. Phys. **12**, 155–164 (1941)
2. Selvadurai, A.P.S.: Mechanics of Poroelastic Media. Kluwer Academic Publishers, Dordrecht (1996)
3. Selvadurai, A.P.S., Yue, Z.Q.: On the indentation of a poroelastic layer. Int. J. Num. Anal. Methods Geomech. **18**, 161–175 (1994)
4. Selvadurai, A.P.S.: The analytical method in geomechanics. Appl. Mech. Rev. **60**, 87–106 (2007)
5. Cheng, A.H.-D.: Poroelasticity. Springer, Berlin (2016)
6. Selvadurai, A.P.S., Shi, L.: Biot's problem for a Biot material. Int. J. Eng. Sci. **97**, 133–147 (2015)
7. Cowin, S.C.: Bone Mechanics Handbook. Taylor and Francis, New York (2001)
8. Pence, T.J.: On the formulation of boundary value problems with incompressible constituent constraints in finite deformation poroelasticity. Math. Model. Methods Appl. Sci. **35**, 1756–1783 (2012)
9. Selvadurai, A.P.S., Suvorov, A.P.: Coupled hydro-mechanical effects in a poro-hyperelastic material. J. Mech. Phys. Solids **91**, 311–333 (2016)

10. Suvorov, A.P., Selvadurai, A.P.S.: On poro-hyperelastic shear. J. Mech. Phys. Solids **96**, 445–459 (2016)
11. Selvadurai, A.P.S., Suvorov, A.P.: On the inflation of poro-hyperelastic annuli. J. Mech. Phys. Solids **107**, 229–252 (2017)
12. Selvadurai, A.P.S., Suvorov, A.P.: On the development of instabilities in an annulus and a shell composed of a poro-hyperelastic material (in preparation)
13. Terzaghi, K.: Die Berechnung der Durchlassigkeitsziffer des Tones aus Dem Verlauf der Hydrodynamischen Spannungserscheinungen. Akad Wissensch Wien Sitzungsber Math-naturwissensch Klasse IIa **142**, 125–138 (1923)
14. Selvadurai, A.P.S.: Geomechanical characterization of the Cobourg limestone. Technical report, Nuclear Waste Management Organization (2018)
15. Selvadurai, A.P.S., Letendre, A., Hekimi, B.: Axial flow hydraulic pulse testing of an argillaceous limestone. Environ. Earth Sci. **64**, 2047–2058 (2011)
16. Selvadurai, A.P.S., Jenner, L.: Radial flow permeability testing of an argillaceous limestone. Ground Water **51**, 100–107 (2013)
17. Selvadurai, A.P.S., Najari, M.: On the interpretation of hydraulic pulse tests on rock specimens. Adv. Water Resour. **53**, 139–149 (2013)
18. Selvadurai, A.P.S., Najari, M.: Laboratory-scale hydraulic pulse testing: influence of air fraction in cavity on estimation of permeability. Géotechnique **65**, 126–134 (2015)
19. Selvadurai, A.P.S., Najari, M.: The thermo-hydro-mechanical behaviour of the argillaceous Cobourg limestone. J. Geophys. Res. (Solid Earth) **122** (2017). https://doi.org/10.1002/2016jb013744
20. Selvadurai, A.P.S., Głowacki, A.: Stress-induced permeability alterations in an argillaceous limestone. Rock Mech. Rock Eng. **50**, 1079–1096 (2017)
21. Hill, R.: The elastic behaviour of a crystalline aggregate. Proc. Phys. Soc. **65**, 349–354 (1952)
22. Hashin, Z., Shtrikman, S.: A variational approach to the elastic behavior of multiphase minerals. J. Mech. Phys. Solids **11**, 127–140 (1963)
23. Selvadurai, A.P.S.: The Biot coefficient for a low permeability heterogeneous limestone. Continuum Mech. Thermodyn. (2018). https://doi.org/10.1007/s00161-018-0653-7

Effective Stress and Effective Stress Equation

Longtan Shao(✉), Xiaoxia Guo, Tiande Wen, and Boya Zhao

State Key Laboratory of Structural Analysis for Industrial Equipment, Department of Engineering Mechanics, Dalian University of Technology, Dalian 116024, China
shaolongtan@l26.com

Abstract. The concept of effective stress and the effective stress equation is fundamental for establishing the theory of strength and the relationship of stress and strain in soil mechanics. However, up till now, the physical meaning of effective stress has not been explained clearly, and the theoretical basis of the effective stress equation has not been proposed. Researchers have not yet reached a common understanding of the feasibility of the concept of effective stress and effective stress equation for unsaturated soils. Focusing on these problems, new viewpoints for explicitly elucidating the effective stress and deriving the effective stress equation are given in this paper, including that the effective stress should be defined as the soil skeleton stress due to all the external forces excluding pore fluid pressure, and that the soil skeleton should include a fraction of pore water which can bears and passes the load together with soil particles. The relationship between the effective stress and the shear strength and the deformation of unsaturated soils is preliminarily verified by experiments and quoting test data from literature.

Keywords: Effective stress · Effective stress equation · Unsaturated soils · Soil skeleton stress · Pore fluid pressure

1 Introduction

The concept of effective stress and effective stress equation is very important to soil mechanics. However, there has always been controversial about what the effective stress is, whether the effective stress equation needs to be modified, and whether and what the effective stress equation for unsaturated soils is. To answer these controversial questions is the aim of this paper. It can be seen that the effective stress equation can be obtained easily in case of taking into account the effect of pore fluid pressure and external forces separately. And the effective stress has explicit physical meaning that is the skeleton stress induced by external forces excluding pore fluid pressure.

2 Skeleton Water

The soil skeleton may be defined as the structure consisting of the solid phase that can bear and transfer loadings [4]. Due to the strong absorption and the capillary effect to the water on the surface of soil particles, a fraction of pore water is tightly combined

W. Wu (Ed.): *Desiderata Geotechnica*, SSGG, pp. 175–192, 2019.
https://doi.org/10.1007/978-3-030-14987-1_22

with the particle and to bear and pass load incorporated with the particle. According to the definition of the skeleton, this fraction of pore water should be treated as a constituent of the soil skeleton, which is called skeleton water. The skeleton water may include strong bonding water and may also include a part of weak bonding water and capillary water. Discussion on the soil skeleton water illustrates that the pore water in soils is in general interconnected, even at low water content. In other words, as along as pore water exists, albeit at low water content, soil particles contact with each other with bonding water on their surfaces. So the bonding water on particles' surfaces is interconnected. There is molecule exchange between the connected bonding water, which does not need to transfer hydrostatic pressure. Only when the water content approaches or exceeds the residual water content will free water appear in the pores of soil, and will transfer hydrostatic pressure. Consequently, a soil with water content lower than residual water content (as maximum content of skeleton water approximately) should be "dry soil" in soil mechanics.

3 Derivation of the Effective Stress Equation

When separately considering the effect of pore fluid pressure and other external force, Terzaghi's effective stress equation for saturated soils and effective stress equation for unsaturated soils can be derived by various kinds of method.

3.1 Intergranular Force Analysis

Many textbooks of soil mechanics use intergranular force analysis to illustrate that Terzaghi's effective stress equation is not accurate and needs to be modified. As shown in Fig. 1(a), the equilibrium equation of the perpendicular inter-particle stress given in many soil mechanics books is

$$P = P_s + (A - A_s)u_w \tag{1}$$

And $\sigma_t = P/A$ is employed to denote the total stress, $\sigma' = P_s/A$ to denote the effective stress, and $a = A_s/A$ to represent the contact area ratio, Eq. (1) can be written as

$$\sigma_t = \sigma' + (1 - a)u_w \tag{2}$$

In consequence, it is considered that Terzaghi's effective stress equation is not accurate and needs to be modified in some circumstance.

In fact, Eq. (1) may be rewritten as

$$P = (P_s - u_w A_s) + u_w A \tag{3}$$

i.e.

$$P = P'_s + u_w A \tag{4}$$

Let $\sigma = P_s'/A$ denote the inter-particle stress excluding pore water pressure, a stress relationship equation can be obtained:

$$\sigma_t = \sigma + u_w \tag{5}$$

It should be noted that Eq. (5) is exactly the Terzaghi's effective stress equation. It can also be obtained by using equilibrium condition if the force on the contact induced by pore water pressure is excluded from the inter-particle forces, as presented in Fig. 1 (b), i.e. the Eq. (4), then Eq. (5).

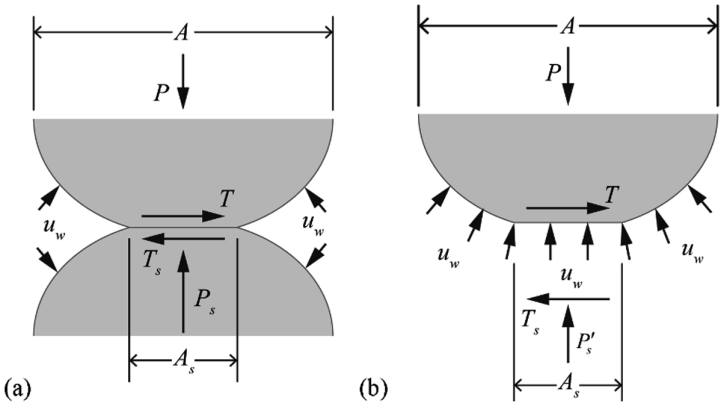

Fig. 1. Pore water pressure and the contact force between particles

This illustrates that the effective stress demonstrates the inter-particle stress generated by the external forces excluding pore water pressure. Based on such definition of effective stress, it could not draw the conclusion that Terzaghi's effective stress equation needs to be modified via inter-particle force analysis.

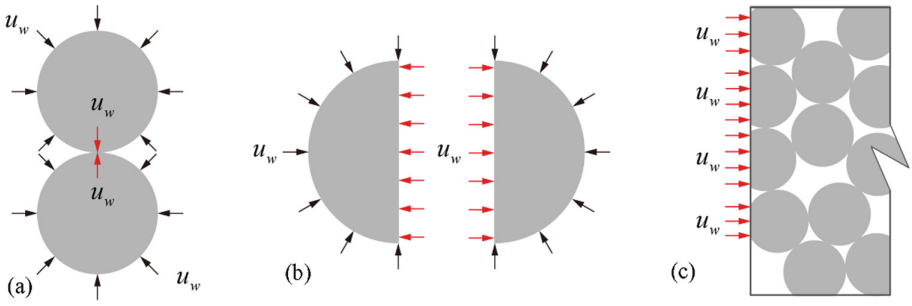

Fig. 2. The stresses on the soil particle and the soil skeleton induced by pore water pressure

Furthermore, Fig. 2 presents the internal force on the surface of a free body of soil skeleton induced by pore water pressure. When the pore water pressure alone acts on soil particles, the average intensity of the exposed stress on any section of the particle and the stress on the interface between particles are both equal to pore water pressure. Therefore, on the free body's surface of the soil skeleton, the internal force of the soil skeleton due to pore water pressure is equal to the product of pore water pressure and the area of the soil skeleton, $u_w(1 - n)A$, in which u_w is the pore water pressure, n is the porosity, A is the sectional area of soil, and $(1 - n)A$ represents the area of the soil skeleton. This analysis illustrates that pore water would result in exposed stress with an identical value of pore water pressure on the free body's surface of the soil skeleton when the soil skeleton and pore water are separated for stress analysis individually.

3.2 Derivation of the Effective Stress Equation from Equilibrium Differential Equation

The effective stress equation can be obtained from the equilibrium differential equation by taking each phase of the soil as an independent analysis object. The forces on the free body of the soil skeleton in a saturated soil can be sketched as in Fig. 3. For simplicity, only the forces on the plane are shown. The internal forces of the free body of soil skeleton include: (1) the soil skeleton stress due to pore water pressure, of which the action area is that of soil skeleton; (2) the soil skeleton stress due to external forces (including normal stress and shear stress), of which the action area is that of soil mass; (3) the self-weight of soil skeleton, equals to the product of the dry unit weight of the soil and the volume of soil mass; and (4) the interaction force between pore water and soil skeleton due to the gradient of water potential.

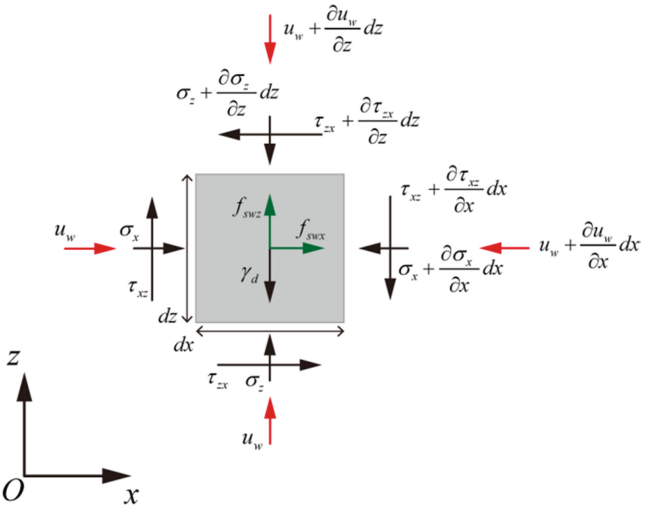

Fig. 3. Stress analysis on the free body of soil skeleton in a saturated soil

Figure 4 presents the force diagram of the free body of pore water in a saturated soil. The internal forces of the free body include (1) the pore water pressure on the free body's section which is perpendicular to the surface and acts on the area occupied by pore water; (2) the interaction force between pore water and soil skeleton of the free body; (3) the self-weight of pore water, which is equal to the unit weight of water multiplied by the volume of pore water.

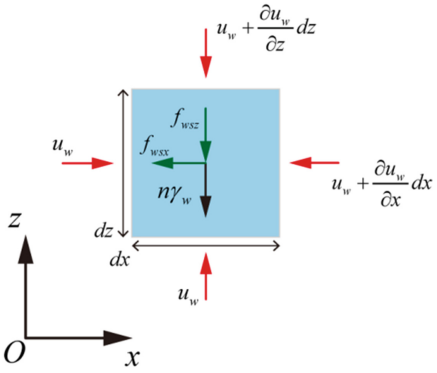

Fig. 4. Stress analysis on the free body of pore water in a saturated soil

Based on the equilibrium conditions for the free body, the equilibrium differential equations of soil skeleton and pore water can be obtained as

$$\sigma_{ij,j} + (1 - n_e)u_{w,i} + (1 - n_e)\rho_s g_i - f_i^{sw} = 0 \tag{6}$$

$$n_e u_{w,i} + n_e \rho_w g_i + f_i^{sw} = 0 \tag{7}$$

where n_e is the effective porosity that takes skeleton water into account, u_w is pore water pressure, σ_{ij} is the stress of soil skeleton due to external forces, f^{sw} is the action and reaction force between soil skeleton and pore water, ρ_s is the density of the soil particles, ρ_w is the density of water, and g is the gravitational acceleration.

The equilibrium differential equations for saturated soils without any interaction forces between phases can be obtained by adding Eqs. (6) and (7), i.e.

$$\sigma_{ij,j} + u_{w,i} + \rho_{sat} g_i = 0 \tag{8}$$

where ρ_{sat} is the saturated density of soil, and $\rho_{sat} = (1 - n_e)\rho_s + n_e \rho_w$.

For unsaturated soils, the forces diagrams of the free body of the skeleton is shown in Fig. 5. Based on equilibrium condition of the free body, the equilibrium differential equations of soil skeleton in unsaturated state can be obtained:

$$\sigma_{ij,j} + \frac{(1 - n_e)}{n_e}(n_{ew}u_w)_{,i} + \frac{(1 - n_e)}{n_e}(n_a u_a)_{,i} + (1 - n_e)\rho_s g_i - f_i^{sw} - f_i^{sa} = 0 \tag{9}$$

where f^{sw} is the action and reaction force between soil skeleton and pore water, f^{sa} is the action and reaction force between soil skeleton and pore air,n_e is the effective porosity of the soil, n_{ew} and n_a are the porosity corresponding to pore water and pore air, respectively. The sum of these two porosities is n_e. σ_{ij} is the stress of soil skeleton due to external forces.

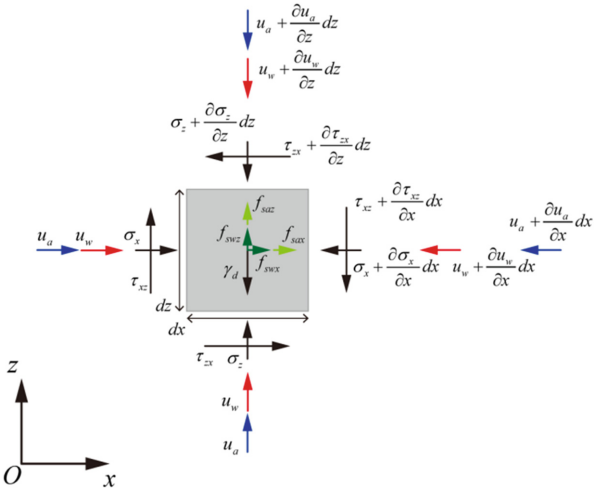

Fig. 5. Stress and force on the free body of unsaturated soil skeleton

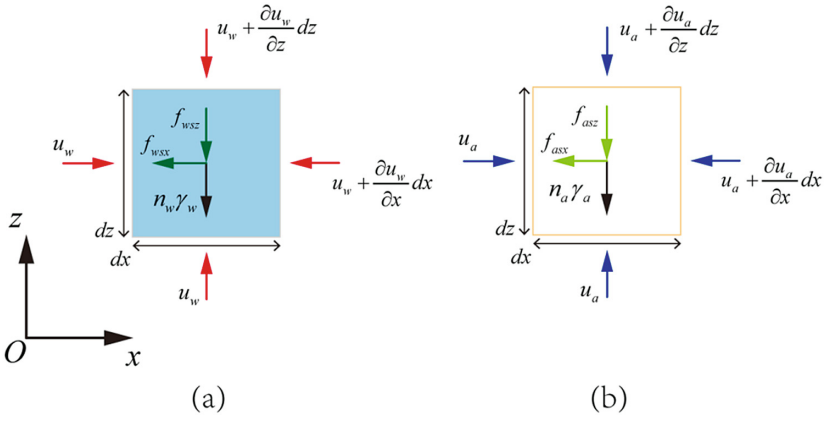

Fig. 6. Stress and force on the free body of (a) pore water (b) and pore air

The forces of the free body of pore water and pore air of unsaturated soils are shown in Fig. 6. The equilibrium equations of the pore water and pore air of unsaturated soils are obtained, respectively.

$$(n_{ew}u_w)_{,i} + f^{sw} + n_{ew}\rho_w g_i = 0 \tag{10}$$

$$(n_a u_a)_{,i} + f^{sa} + n_a \rho_a g_i = 0 \tag{11}$$

where n_w and n_a are the porosity corresponding to pore water and pore air, respectively; u_w is the pore water pressure; u_a is the pore air pressure; f^{sw} is the action and reaction force between soil skeleton and pore water, f^{sa} is the action and reaction force between soil skeleton and pore air, ρ_w is the density of pore water, and ρ_a is the density of pore air.

Adding Eqs. (9), (10) and (11), the equilibrium differential equation of unsaturated soils without interaction forces between phases can be obtained:

$$\sigma_{ij,j} + u_{a,i} - (S_e(u_a - u_w))_{,i} + \rho g_i = 0 \tag{12}$$

in which ρ is the density of soil, S_e is the effective degree of saturation,

$$S_e = \frac{n_{ew}}{n_e} = \frac{S - S_r}{1 - S_r} \tag{13}$$

where S is degree of saturation, S_r is residual degree of saturation.

Equation (12) is the equilibrium equations of unsaturated soils expressed by soil skeleton stress, pore water pressure and pore air pressure. By comparing them to equilibrium equation in total stress, i.e.

$$\sigma_{tij,j} + \rho g_i = 0 \tag{14}$$

The relationship between the soil skeleton stress induced by external force, total stress, pore water pressure and pore air pressure can be formulated as:

$$\sigma_{ij} = \sigma_{tij} - \delta_{ij}u_a + \delta_{ij}S_e(u_a - u_w) \tag{15}$$

It should be noted that Eq. (15) is exactly the same as Terzaghi's effective stress equation for saturated soils as $S_e = 1$, which can be obtained by comparing Eqs. (8) to (14).

3.3 Based on Force Analysis of Free Body of a Soil

Considering the effect of pore fluid pressure and other external loads separately, as shown in Fig. 7, taking a saturated soil as example, when analyzing the inner force of an infinitesimal section plane in the soil skeleton, separately considering the effect of pore water pressure and the other external forces, the stress on the skeleton plane due to the pore water pressure u_w should be u_w, and its action area should be the section area of the skeleton, i.e. $(1 - n)A$, in which A is cross section area of the plane, n is porosity (taking skeleton water into account). With σ_t representing the total normal stress in horizontal direction, then

$$N_t = \sigma_t A \tag{16}$$

where N_t is the total normal force in horizontal direction. With σ denoting the normal stress of the skeleton, which is produced by the external forces except for u_w, according to the equilibrium condition we have

$$N_t = \sigma A + u_w(1 - n_e)A + n_e u_w A \tag{17}$$

Substituting Eqs. (16) into (17), it can be obtained that

$$\sigma = \sigma_t - u_w \tag{18}$$

This is the Terzaghi's effective stress equation, but σ is the skeleton stress produced by all the external forces except for u_w. It indicates that the effective stress is the skeleton stress due to external forces except for pore water pressure, which may be called as skeleton stress by external force or skeleton stress for short.

For unsaturated soils as shown in Fig. 8, according to the equilibrium condition we have

$$N_t = \sigma A + \frac{n_{ew}}{n_e}(1 - n_e)u_w A + n_{ew}u_w A + \frac{n_a}{n_e}(1 - n_e)u_a A + n_a u_a A \tag{19}$$

Then

$$\sigma = \sigma_t - S_e u_w - (1 - S_e)u_a \tag{20}$$

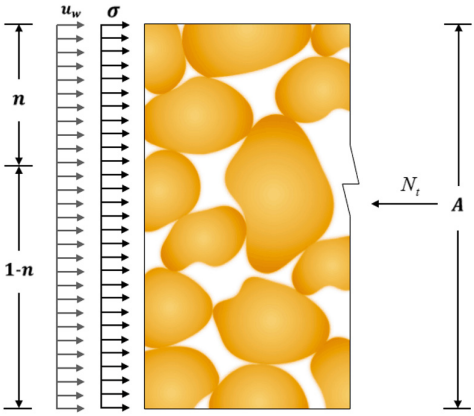

Fig. 7. Force analysis of a saturated soil separately considering the effect of pore water pressure and the other external forces

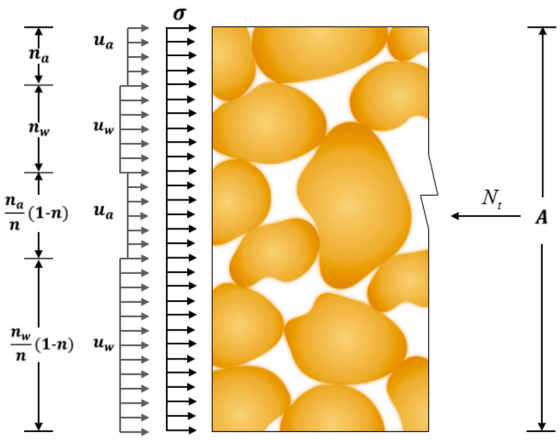

Fig. 8. Force analysis of an unsaturated soil separately considering the effect of pore fluid pressure and the other external forces

3.4 Based on the Definition of Effective Stress

Considering the effect of pore fluid pressure and other external loads separately, the effective stress can be defined as the soil skeleton stress due to all the external forces excluding pore fluid pressure. The effective stress expression can be obtained directly from the definition formula of effective stress.

$$\sigma = \frac{N_s^t - N_w - N_a}{A} \tag{21}$$

where N_s^t is the normal internal force of the soil skeleton, N_w represents the pore water pressure acting on the soil skeleton, and N_a represents the pore air pressure acting on the soil skeleton.

$$N_w = u_w \frac{n_{ew}}{n_e}(1 - n_e)A, \qquad N_a = u_a \frac{n_a}{n_e}(1 - n_e)A \tag{22}$$

All normal internal forces of soil mass (including soil skeleton, pore water and pore air) on the section includes the normal force acting on the soil skeleton and the normal force acting on the pore water and pore air, notes for the N_t, P_w and P_a represent the normal force on a section acting on the pore water area and on the pore air area, respectively.

$$P_w = u_w \frac{n_{ew}}{n_e} n_e A, \; P_a = u_a \frac{n_a}{n_e} n_e A \tag{23}$$

Furthermore,

$$N_t = N_s^t + P_w + P_a = \sigma A + N_w + N_a + P_w + P_a \tag{24}$$

When divided by A,

$$\frac{N_t}{A} = \sigma + u_w \frac{n_{ew}}{n_e}(1 - n_e) + u_a \frac{n_a}{n_e}(1 - n_e) + u_w n_{ew} + u_a n_a \tag{25}$$

Then the effective stress for unsaturated soils can be obtained.

$$\sigma = \sigma_t - u_a + S_e(u_a - u_w) \tag{26}$$

3.5 Based on the Equilibrium Equation of Pore Medium Mechanics

At present, the skeleton stress defined in pore medium mechanics includes the effect of pore fluid pressure. If the effective stress is defined as the soil skeleton stress due to the external forces excluding the pore fluid pressure, the relationship between the effective stress and the original skeleton stress can be obtained. By substituting it into the equilibrium equation of porous medium mechanics, the effective stress expressions can also be obtained.

The relationship between the skeleton stress and the effective stress:

$$(1 - n)\sigma_{ij}^s = \sigma_{ij} + (1 - n)S\delta_{ij}u_w + (1 - n)(1 - S)\delta_{ij}u_a \tag{27}$$

where the σ_{ij}^s is the skeleton stress. The equilibrium equation of the soil skeleton is

$$(1 - n)\sigma_{ij,j}^s + (1 - n)\rho_s g_i + f_i^{sw} + f_i^{sa} = 0 \tag{28}$$

Substituting Eqs. (27) into (28), the following equations can be obtained:

$$\sigma_{ij,j} + (1 - n)Su_{w,i} + (1 - n)(1 - S)u_{a,i} + (1 - n)\rho_s g_i + f_i^{sw} + f_i^{sa} = 0 \tag{29}$$

Adding Eq. (29), and equilibrium equations for pore water and pore air, we have

$$\sigma_{ij,j} + Su_{w,i} + (1 - S)u_{a,i} + \rho g_i = 0 \tag{30}$$

Comparison of Eqs. (30) to (14) may lead to the effective stress equation.

4 Preliminarily Verification of the Effective Stress Equation for Unsaturated Soils

We all know that the deformation and the strength of a soil are those of its skeleton, so it is logical that the deformation and the strength of a soil will be governed by its skeleton stress, i.e. the effective stress when the effect of pore pressure to the

deformation and strength can be neglected. This has been fully proven by test and practice for saturated soils. However, this has not been proven for unsaturated soils. But according to the definition and physical meaning of the effective stress we can believe that the effective stress also governs the deformation and strength of unsaturated soils.

4.1 Primary Verification of the Correlation Between Effective Stress and Shear Strength of Unsaturated Soils

A kind of kaolin is chosen to be tested for verifying that the effective stress governs its shear strength when it is in unsaturated state. The physic-mechanical index properties of the kaolin are listed in Table 1.

Table 1. The physic-mechanical index properties of kaolin

Specific gravity G_s	$\rho_{d,max}$ g/cm^3	Optimum moisture content/%	Liquid limit w_L/%	Plastic limit w_p/%	Plasticity index I_p/%
2.75	1.41	23.9	63.09	22.52	40.57

The axis-translation method with 1.5 MPa air entry porous ceramic plate and filter paper method is employed for the SWRC (Soil water retention curve) test of the kaolin. The results and the fitted SWRC with V-G model are shown in Fig. 9, from which the residual saturation was required as 14.3%.

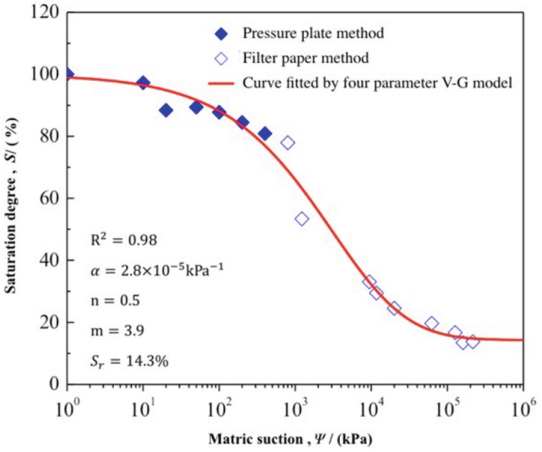

Fig. 9. SWRC for the kaolin fitting by four parameters VG model

Conventional triaxial tests have been conducted for specimens of the kaolin in dry density of 1.35 g/cm^3, and with setting initial water content, including saturated state. The water content in different layer of the specimen was monitored when test ended. It can be found that the variation of the average (gravimetric) water content of the specimen was less than 1.5%. Figure 10 shows the shear strength of the specimens in different initial water content, including saturated state. It can be seen that the shear strength of the kaolin in both saturated and unsaturated states expresses the same relationship with the effective stress. That is to say the shear strength of unsaturated kaolin is governed by the effective stress.

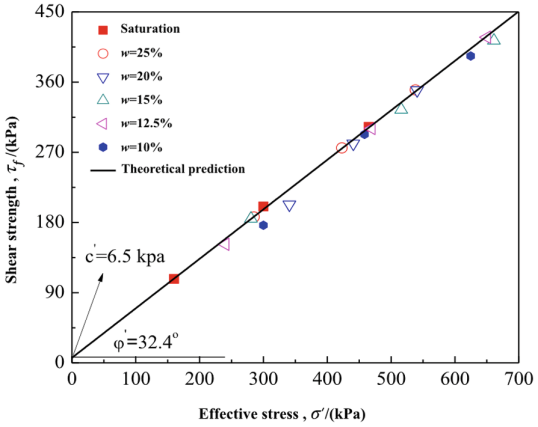

Fig. 10. The test results of the shear strength of the kaolin in saturated and unsaturated states

Some other test results of the shear strength of unsaturated soils which were found in literatures are reanalyzed in the concept of effective stress [1–3, 6, 7, 9, 11, 12]. The parameters of the test of unsaturated soils are all listed in Table 2. These tests were classified into groups of direct shear test and triaxial test. And the third group is triaxial tests considering the effect of net stress on SWRC, and on effective stress.

Table 2. Collection of the test of unsaturated soils founded in literatures

Reference	Soil type and preparation	Strength parameters		AEV & RWC@		
		c'(kPa)	$\varphi'(\circ)$	AEV(kPa)	$S_{res}(\%)$	$\theta_r(\%)$
Case 1 (Direct shear test)						
Zhan and Ng [12]	Compacted Expansive Clay	0	24	25	-	18
Aqtash and Bandini [1]	Adobe soil mixture (composed of natural soil, poorly graded sand and cut straw)	11.7	31.4	12.5	-	3.3

(*continued*)

Table 2. (*continued*)

Reference	Soil type and preparation	Strength parameters		AEV & RWC@		
		c'(kPa)	$\varphi'(\circ)$	AEV(kPa)	$S_{res}(\%)$	$\theta_r(\%)$
Escario et al. [3]	Madrid clay sand	40	39.5	-	32.64	-
Case 2 (Triaxial test)						
Khalili et al. [5]	Undisturbed soil samples form Hume Dam in Australia (SJ11)	5	30	200	-	4.5
Miao et al. [8]	Guangxi expansive soil (slurry sample)	50	19.8	100	13	-
Kayadelen et al. [6]	Residual clayey soil from Diyarbakirin Turkey (undisturbed)	14.82	21.9	40	35	-
Miao et al. [9]	Nanyang expansive soil (Middle grade soil)	32	21.3	25	-	3.5
Ye et al. [11]	Weekly expansive soil from Hubei: China	14.8	28.2	106	8.2	-
Cunningham et al. [2]	Silty clay reconstituted form a slurry	0	32	250	5	-
Case 3 (Influence of stress state)						
Lee et al. [7]	Weathered residual granite in Korea (silty sand)	12.45	30.48	2.5	12	-

It can be found that the shear strength of the soils in both saturated and unsaturated states fits the same formula with the same parameters, as shown in Fig. 11, in which the solid lines show the shear strength of the soils in saturated state. These reanalysis results verify that the effective stress also governs the shear strength of unsaturated soil.

4.2 Primary Verification of the Correlation Between Effective Stress and Deformation of Unsaturated Soils

On the other hand, it is on the way for us to verify that the effective stress governs the volume change (or the deformation) for unsaturated soils. Khalili et al. conducted a series of suction controlled confining compression tests [5]. Under the confining compression condition, the effective stress control the volumetric change of unsaturated soil.

$$\Delta\varepsilon_a = \frac{1}{E}\Delta\{(1-2v)[\sigma - u_a + S_e(u_a - u_w)]\} \tag{31}$$

in which $\Delta\varepsilon_a$ is the axial strain, v is Poisson's ratio, E is elastic modulus.

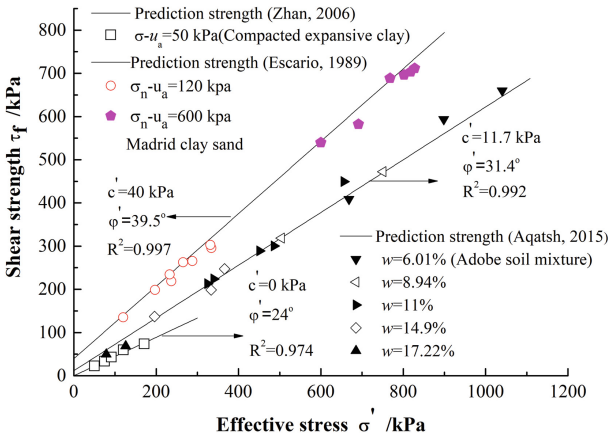

(a)

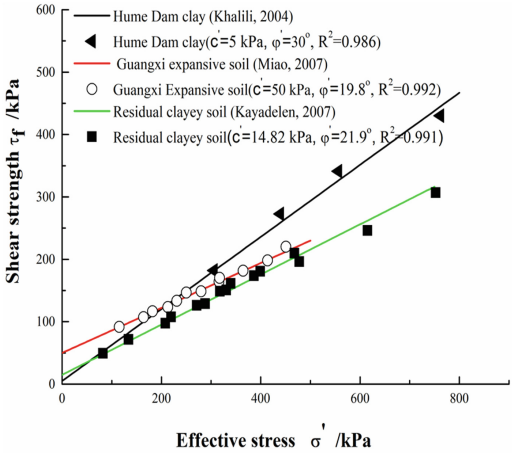

(b)

Fig. 11. Reanalysis of the test results of shear strength of unsaturated soils (test data from literatures)

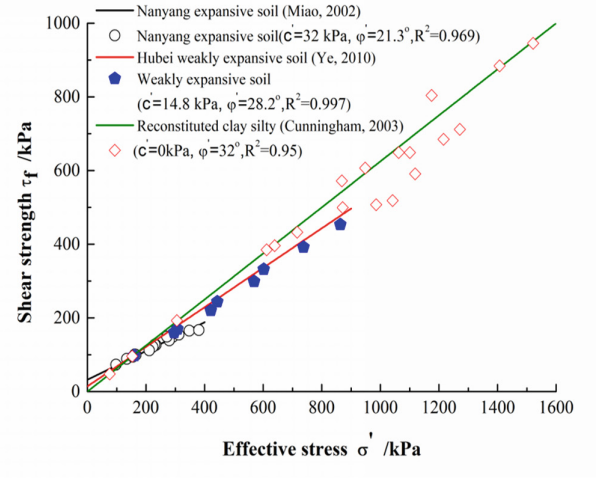

(c)

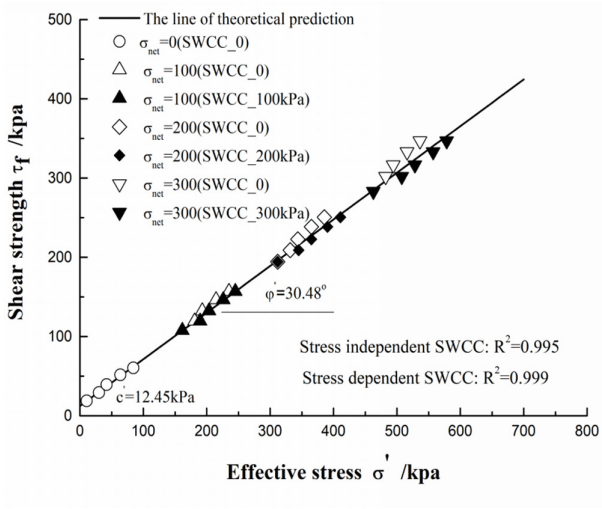

(d)

Fig. 11. (*continued*)

For the tested kaolin, the elastic modulus is 3.75 MPa and Poisson ratio is 0.4. The axial strain measured is compared with the formula, as shown in Fig. 12. For the tested Glenmore Park Silt, the elastic modulus is 55.75 MPa and Poisson ratio is 0.25. The axial strain measured is compared with the formula, as shown in Fig. 13. The experiment results of the two soil specimens show that the formula of volumetric change for unsaturated soil has an ideal prediction for the volumetric change of unsaturated soil when the deformation of soil is linear elastic.

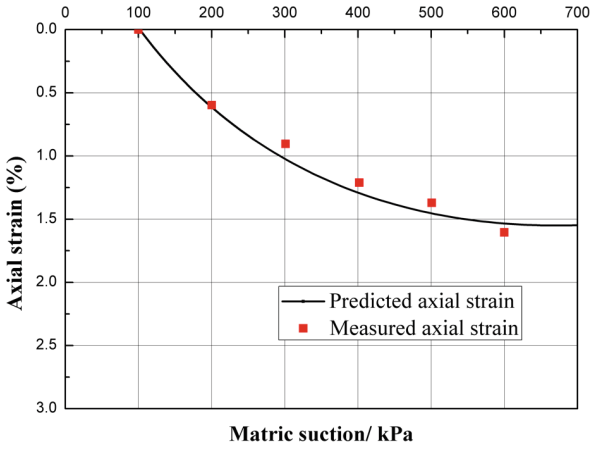

Fig. 12. Volumetric change of Kaolin (v = 0.4, E = 3.75 Mpa)

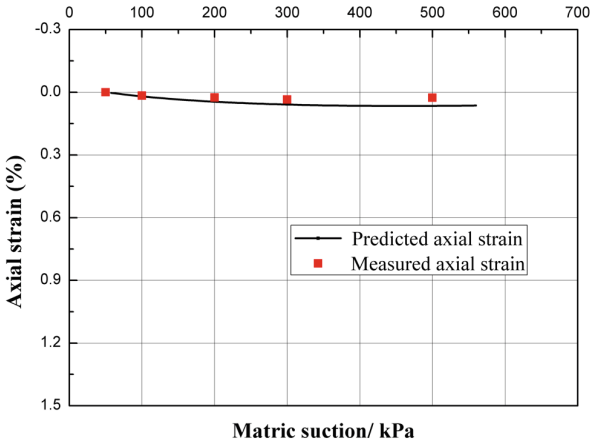

Fig. 13. Volumetric change of Glenmore Park Silt (v = 0.25, E = 55.75Mpa)

Because the effective stress controls the deformation of the soil, for both the saturated soil and unsaturated soil, the relationship between volumetric change and effective stress should be consistent. During drying shrinkage test, the specimens in the initial saturated state are subjected to isotropic contraction due to the equal suction in each direction. In the process of shrinkage, the specimen transits from the saturated state to unsaturated state. For the saturated specimen with the same initial dry density, the triaxial isotropic consolidation test are conducted. In drying shrinkage test, the effective stress of specimen is calculated in the process of contraction. By comparing the effective stress variation curves of saturated soil and unsaturated soil, the applicability of the unified effective stress equation is verified. The relationship between the pore ratio and effective stress is as shown in Fig. 14.

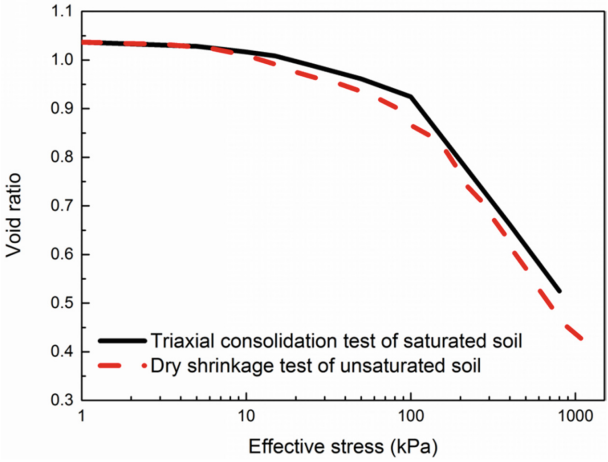

Fig. 14. Relationship between pore ratio and effective stress

From Fig. 14, it can be seen that the relation curves between the pore ratio and effective stress basically coincide for the saturated soil and unsaturated soil, which proves the applicability of the unified effective stress equation. The same inflection point appears on the two curves. Because of adopting the same specimen preparation methods for compaction method and pump suction saturation method, the specimens subject to the same pre-consolidation pressure.

For more contents please read the reference "Effective stress and equilibrium equation for soil mechanics" by Shao & Guo, etc. CRC [10].

References

1. Aqtash, U., Bandini, P.: Prediction of unsaturated shear strength of an adobe soil from the soil–water characteristic curve. Constr. Build. Mater. **98**, 892–899 (2015)
2. Cunningham, M.R., Ridley, A.M., Dineen, K., et al.: The mechanical behaviour of a reconstituted unsaturated silty clay. Geotechnique **53**(2), 183–194 (2003)
3. Escario, V., Juca, J.F.T., Coppe, M.S.: Strength and deformation of partly saturated soils. In: Proceedings of 12th ICSMFE, Rio de Janeiro, Brazil, vol. 11, pp. 43–46 (1989)
4. Herle, I., Gudehus, G.: Determination of parameters of a hypoplastic constitutive model from properties of grain assemblies. Mech. Cohesive-Frict. Mater. **4**(5), 461–486 (1999)
5. Khalili, N., Geiser, F., Blight, G.E.: Effective stress in unsaturated soils: review with new evidence. Int. J. Geomech. **4**, 115–126 (2004)
6. Kayadelen, C., Tekinsoy, M.A., Taskiran, T.: Influence of matric suction on shear behavior of a residual clayey soil. Environ. Geol. **53**, 891–901 (2007)
7. Lee, I.M., Sung, S.G., Cho, G.C.: Effect of stress state on the unsaturated shear strength of a weathered granite. Can. Geotech. J. **42**(2), 624–631 (2005)
8. Miao, L., Houston, S.L., Cui, Y., et al.: Relationship between soil structure and mechanical behavior for an expansive unsaturated clay. Can. Geotech. J. **44**(2), 126–137 (2007)

9. Miao, L., Liu, S., Lai, Y.: Research of soil–water characteristics and shear strength features of Nanyang expansive soil. Eng. Geol. **65**(4), 261–267 (2002)
10. Shao, L.T., Guo, X.X., Liu, S.Y., Zheng, G.F.: Effective Stress and Equilibrium Equation for Soil Mechanics. CRC Press, Boca Raton (2017)
11. Ye, W.M., Zhang, Y., Chen, B., et al.: Shear strength of an unsaturated weakly expansive soil. J. Rock Mech. Geotech. Eng. **2**(2), 155–161 (2010)
12. Zhan, L.T., Ng, C.W.: Shear strength characteristics of an unsaturated expansive clay. Can. Geotech. J. **43**, 751–763 (2006)

On the Use of the Finite Element Method for the Design of Offshore Wind Turbine Foundations

Hendrik Sturm(✉) and Lars Andresen

Norwegian Geotechnical Institute (NGI), Oslo, Norway
{hendrik.sturm,lars.andresen}@ngi.no

Abstract. This paper provides an introduction to the geotechnical design of *Offshore Wind Turbine* (OWT) foundations using the *Finite Element Method* (FEM). Procedures for incorporating the FEM in the design process are proposed under particular consideration of the practical application to commercial projects, where foundation design is done in a serial production. The proposed procedures allow to streamline the design process and enable to optimize the foundation geometries of OWTs under given time and resource constraints of typical *Offshore Wind Farm* (OWF) development projects. Advantages and disadvantages are discussed using the example of the design of Monopiles and Suction Caissons.

1 Introduction

It is well known and generally accepted that the *Finite Element Method* (FEM) can provide accurate results when used correctly, that means with appropriate constitutive soil models and within the given limitations. In fact, for some aspect of the foundation design, such as the prediction of the load-deformation response to general load conditions, the FEM is apparently the only procedure which can provide reasonable results.

However, despite the obvious advantages of the FEM, the design of *Offshore Wind Turbine* (OWT) foundations is typically done using simplified, analytical-based, methods. This may be surprising, since the *Offshore Wind Industry* (OWI) is, due to politically motivated reasons, forced to reduce costs more than any other energy producer.[1] At the same time, the OWI is aware of the potential cost savings when using more advanced methods, as measurements of actual built OWTs, which were designed using these conventional simplified methods, have shown, that the foundations perform considerable better than predicted; OWT foundations are often much stiffer and the (accumulated) deformations are

[1] Although political aspects shall not be the concern of this paper, the latest auctions in UK and other European countries have clearly shown that the offshore wind industry is already today considerably cheaper than most other energy sources including nuclear energy.

W. Wu (Ed.): *Desiderata Geotechnica*, SSGG, pp. 193–204, 2019.
https://doi.org/10.1007/978-3-030-14987-1_23

less than predicted in the design. However, the FEM has the reputation to be a time consuming procedure which requires considerable resources and by that potentially delays the typically very tight time schedules of commercial *Offshore Wind Farm* (OWF) development projects. Thus, the FEM has not found its way yet into the regular design routines, but is rather used as a complimentary tool to backup presumingly conservative assumptions.

Motivated by the expected cost savings, the OWI has initiated and (partially) financed several research projects with the objective to develop new and more advanced methodologies for the OWT foundation design. Particularly mentioned should be models and procedures developed within the PISA project [1,2] and the RedWin project [7]. Although the proposed methods are fundamentally different, they envisage the use of the FEM; primarily for the calibration of the input parameters. The advantage of these methods is, that the FEM can be used, but not necessarily has to be used. This allows to adjust the detailedness and comprehensiveness of the design process depending on the state of an OWF development project, i.e. feasibility, FEED or Detailed Design. As a result of this flexibility, the serial-production-design of an OWF can be streamlined, by means of a combination of FEM, normalizations and simplified calibrations.

This paper focuses primarily on the models developed in the RedWin project. The reason for that is due to the personal involvement of the authors in this project. Furthermore, foundation models for several foundation types were developed in the RedWin project, covering Monopiles, Suction Caissons and *Gravity Base Structures* (GBS), whereas only a model for the Monopile design was developed in the PISA project.

2 Foundation Concepts, Design Aspects and Design Approach

Figure 1 shows an illustration of typically foundation concepts used for bottom-fixed OWTs. Although the Monopile is used in most projects, also other concepts are applied frequently, including the GBSs and Jackets with Piles or Suction Caissons. Which concept is actually applied in an OWF project depends on numerous aspects such as site and soil conditions, loading conditions, supply chain, available resources, etc.

Outside Europe were developed other foundation concepts in order to cope with particular regional site conditions. For example, offshore China and Korea are found many sites comprising very soft clay overlying shallow bedrock. Other sites are exposed to extreme loads from earthquakes, typhoons and hurricanes. The foundation concepts developed for these areas are typically *hybrid* foundations, which are a mixture between shallow and deep foundations shown in Fig. 1.

Independent of the type of OWT foundation concept, the geotechnical design of OWT foundations comprises of three main aspects:

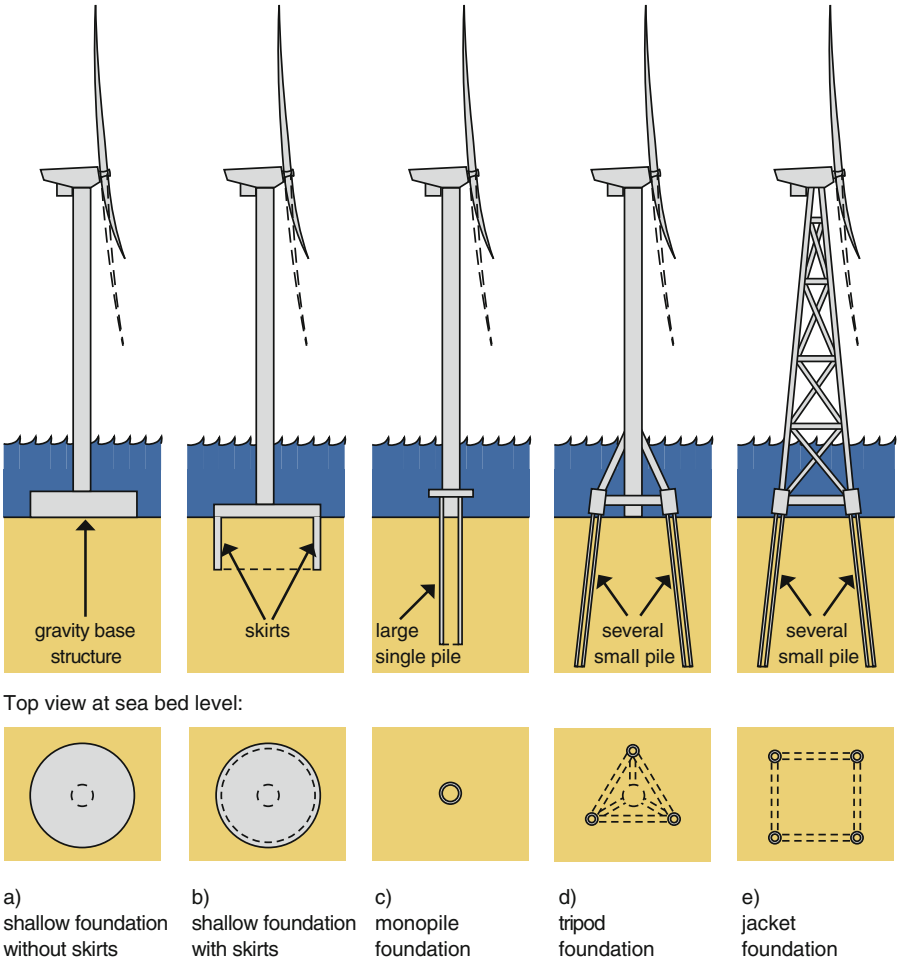

Fig. 1. Typical shallow and deep foundation concept used for bottom-fixed OWTs. (from Sturm [8])

- **ULS design**, i.e. Ultimate Limit State, is the foundation capacity assessment, which is typically done considering extreme load events combined with preceding cyclic load histories such as storm loading, which has potentially weaken the soil due to pore pressure accumulation.
- **FLS design**, i.e. Fatigue Limit State, is the assessment of the foundation stiffness and damping, which is typically determined for representative operational and extreme load events, and is used by the structural designer. Furthermore, the FLS design includes the assessment of the foundation stiffness and damping used in structural eigenmode analysis.

- **SLS design**, i.e. Serviceability Limit State, is the assessment of peak and accumulated deformations and rotations of the OWT foundation due to extreme load events and cyclic loads.

Occasionally, the stiffness analysis is considered as part of the SLS design, since fatigue limit states are not defined for geotechnical problems, but are relevant for structural design only. The cyclic loads considered in the structural FLS design, will yield, when subjected to a soil body, to accumulated deformations (SLS), or in the worst case a collapse (ULS).

A typical OWF may comprises of 50 to 100 OWT foundations. Each need to be designed separately. In order to optimize the workflow and by that reducing the number of analyses, an OWF is typically clustered by grouping locations with similar soil and load conditions. Depending on which design method used, the geotechnical input can be normalized, or upper and lower stiffness estimates may be used.

The overall OWT design approach is govern by the structural designer and load engineer. Traditionally the *Transition Piece* (TP), which is the interface between the tower and the support structure, serves as interface between the structural designer and the turbine manufacturer. Areodynamic loads are assessed by the latter one and are given to the structural designer. In order to avoid further interfaces, the foundation sizing is often included in the structural design of the support structure. That means the soil is in this traditional approach considered in a very simplified manner.

In order to optimize the OWT design by incorporating more advanced soil representations, another interface between structural and geotechnical designer needs to be introduced. However, an additional interface will yield to more load and stiffness iterations between both geotechnical, structural and turbine designer, which potentially requires a longer design period. In order to avoid that, the information exchanged in the interface needs to be more comprehensive but at the same time general enough to cover a wide range of loads and/or stiffness values. Therein, it is of fundamental importance to understand the nature of the loads and the structural design methodology, which is based on a very large number of integrated time domain analysis. Thus, the proposed methods for using the FEM needs to consider these constraints, as the FEM cannot be directly used in the time domain analysis without increasing the required calculation time unacceptably. In the following section are presented two approaches on how to cope with these challenges and requirements when using the FEM in the geotechnical design.

3 Using FEM in OWT Foundation Design

As detailed in Sect. 2, the FEM cannot be used directly in the design, but needs to be represented by a *tool* in order to use it in the structural design. We do not detail these tools in this paper, as these are already presented in other publications, but just introduce these in order to understand the proposed method for using the FEM.

3.1 Example: Monopile

The Monopile, which is literally a single pile with a diameter of typically 4 to 9 m and an aspect ratio of length to diameter of typically 3 to 6, has established itself as a standard foundation type in the current marketplace. Although the Monopile has the largest market share, the design is often done in a simplified manner. These conventional design models have proved unreliable and non-optimal. The industry has therefore commissioned intensive research efforts to develop improved design methodologies. These research projects have yielded significant advances, such as updated distributed soil-spring-models (e.g. PISA, [1,2]) and optimized macro-elements (e.g. RedWin, [7]).

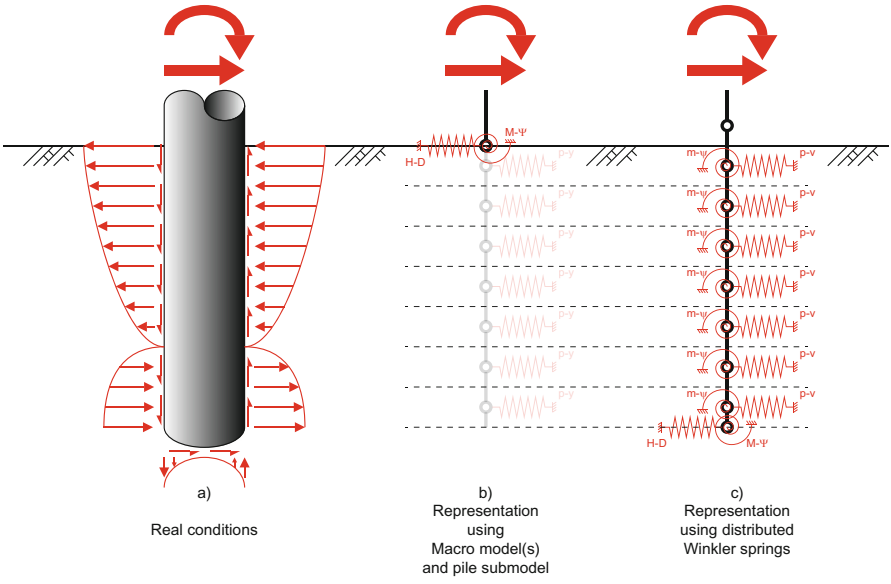

Fig. 2. Representation of the soil response in structural Monopile design.

Figure 2 shows how the soil response is typically represented in the structural design. The soil reactions are expressed by a lumped non-linear stiffness matrix at mudline (case (a)) or non-linear Winkler springs distributed over the length of the Monopile (case (b)).

Traditionally, API-type p-y curves were used for case (b). The input to these curves is based on soil test results and empirical correlations. This has been shown to be conservative by systematically under-predicting foundation stiffness and capacity. Thus the PISA project has developed a new set of distributed springs by introducing additional rotational springs. All springs are expressed by the same generic conic function illustrated in Fig. 3.

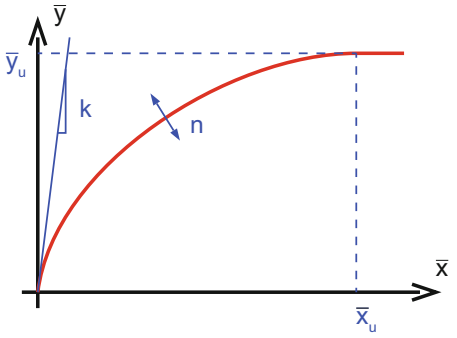

Fig. 3. Four parameter conic function employed to represent the soil reaction curves in the PISA model (after [1]).

In order to use these curves, the so-called soil reaction components need to be determined. In [2] is proposed to use either a rule-base method or a numerical based method, whereas the latter one is the preferred method. That requires to perform 3D FE analysis, as shown in Fig. 4, from which are extracted soil reaction curves over the height of the Monopile, which need to be fitted using the curve shown in Fig. 3. Since this is relatively time-consuming, the PISA design framework envisages a normalization procedure, which allows to the determine the Winkler springs based on representative Monopile geometries, load conditions and soil layers, and by that enables the structural designer to perform the actual Monopile sizing.

The advantage of the PISA model is, that it is very similar to the traditional design approach using API curves. However, as per today, the PISA model is calibrated for monotonic loading only and cannot be used under generalized cyclic load conditions when the load amplitudes exceed a small-deformation-range where the soil is often considered as elastic. Hysteresis needs to be captured indirectly using e.g. damping values, where the PISA springs represent a cyclic back-bone curve. Another disadvantage of the PISA model is, that the time required to perform the 3D FE analysis and calibration yield an increase of the time allocated for the design.

An alternative approach for the Monopile design is proposed by RedWin. The foundation response is represented by a macro-element placed at mudline. The macro-element combines the soil response with the response of the embedded Monopile. This is illustrated in Fig. 2 by case (b). The proposed macro-element is based on the theoretical formulation of multi-surface-plasticity. That allows not only to capture the Monopile response to monotonic loading, but also the response to general cyclic loading. By that, both the foundation stiffness and soil-foundation damping is described by the RedWin model.

Figure 5 shows a comparison of the Monopile response at mudline calculated using the macro-element with the response calculated using distributed monotonic springs, using the example of API. It becomes apparent, that for the two

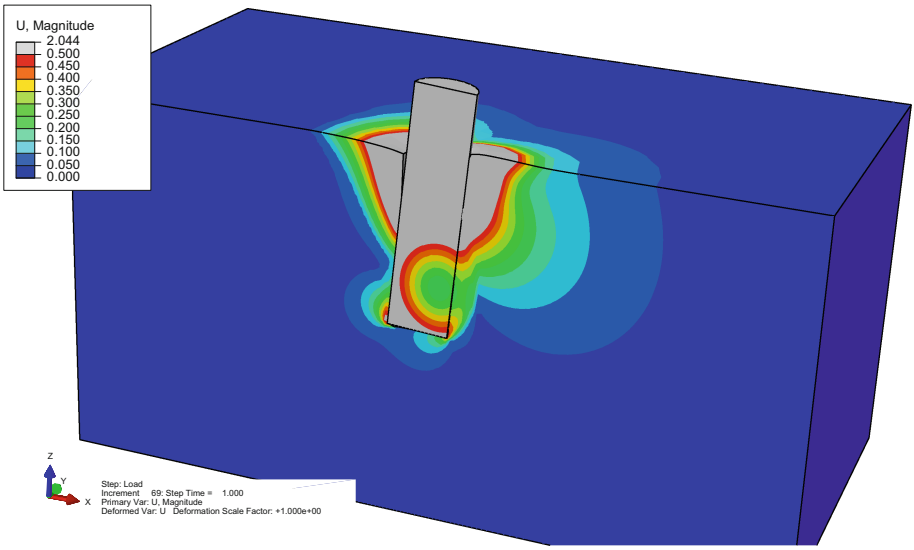

Fig. 4. Example of a 3D FE analysis of a Monopile using the commercial FE program ABAQUS.

cases, the macro-element predicts realistically the response to cyclic loading and also generates hysteretic damping, whereas the distributed monotonic springs describes only a non-linear elastic response whether loading or unloading.

Two types of input are required to the macro-element; (1) coefficients of elastic stiffness matrix, and (2) the moment, horizontal displacement, and rotation at mudline from non-linear analyses with $H = 0$. The latter one can be determined using FE analysis where a monotonic push-over response of the Monopile is modeled. The coefficients of the elastic stiffness matrix can be determined by either performing FEM with a linear elastic material for the soil, or by using empirical correlations for pile foundations.

The RedWin macro-element has several advantages compared to distributed springs as proposed for example by the PISA model. Although both utilize the same type FE analysis for the calibration, the extraction of the results is considerably easier and hence much faster for the macro-element. Only the output at mudline is required for the RedWin model, whereas the PISA model requires the extraction of several load-deflection and moment-rotation curves. As it is difficult to extract these curves along the complete Monopile length due to the low mobilization of the soil around the rotation point, ideally different pile geometries should be modeled. When considering the performance of the models in the structural time domain analysis, the macro-element will provide a more accurate response as it also captures the cyclic behavior.

Another advantage is the application of the RedWin model in layered soils. Winkler springs do not account for the interaction of the adjacent soil springs. The PISA project is currently extending the procedure to layered soils, as teh

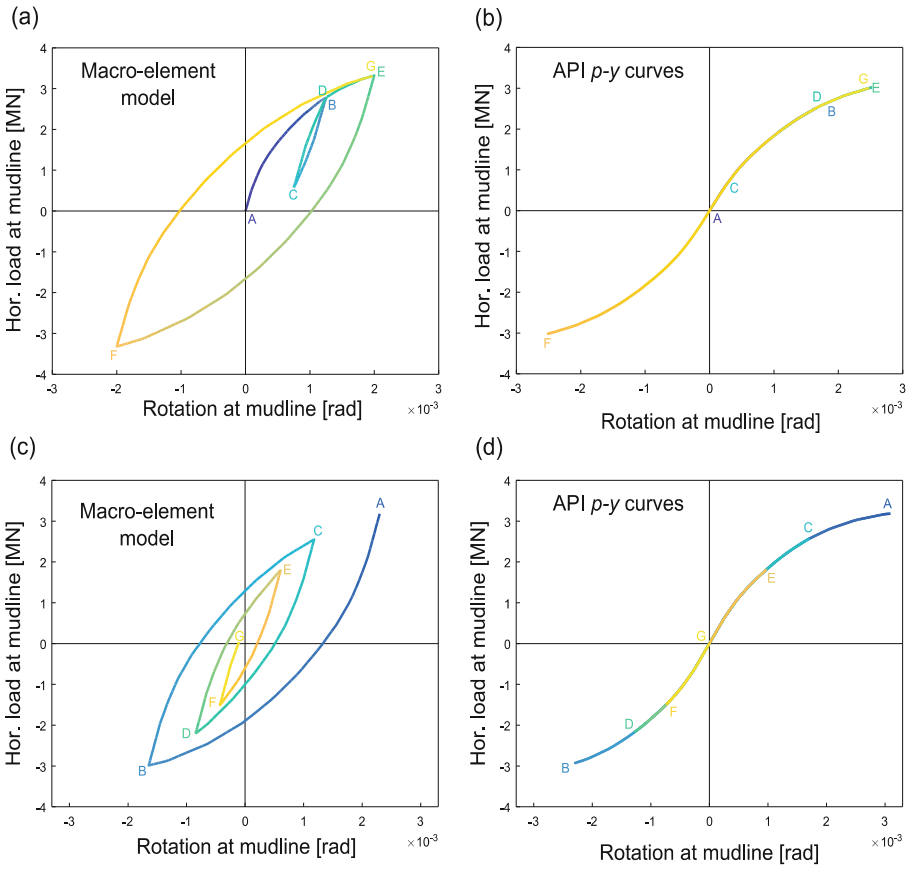

Fig. 5. Horizontal load-rotation response at mudline for two examples computed with different foundation models: (a) case 1 computed with the macro-element model calibrated by FEA; (b) case 1 computed with API p-y curves; (c) case 2 computed with the macro-element model calibrated by FEA; (d) case 2 computed with API p-y curves. (after [6]).

original model was developed and calibrated for homogeneous soil profiles only. Though results of the extended model are not yet published, it may be expected that soil layers may need to be divided into sub-layers to account for the effect of adjacent soil units, which in return will require – depending on the particular site and soil conditions – several more FE analyses and potentially a more detailed clustering of the OWF.

However, there are also disadvantages with the use of the RedWin model compared to the PISA model. As per today, the input to the macro-element is in absolute numbers and no normalization has been developed yet. That means parameters for every pile geometry at every location needs to be assessed separately, which thus requires considerable more FE analyses. NGI has developed

a fast and simplified 2D FE procedure for embedded pile-type foundations [4]. Numerical analysis have shown, that for aspect ratios between 2 and 5, the 2D FE model predicts very accurate results compared to full 3D FE analyses, given that appropriate side-shear factors are applied. The advantage of the 2D FE model is, that it is very fast (typically some few minutes) and the input of a large amount of geometries and soil conditions can be assessed in very short time. An automation of the 2D FE analyses allows to streamline the design process at the expense of affecting only slightly the time schedule of the design process.

3.2 Example: Suction Caissons for Jackets

The foundation design of suction caissons supporting a jacket is done considerably different compared to the Monopile design. Sturm [9] provides a detailed description of the design iterations and design requirements for both monocaissons and multi-legged support-structures founded on Suction Caissons. The design is done in an iterative manner as illustrated in Fig. 6.

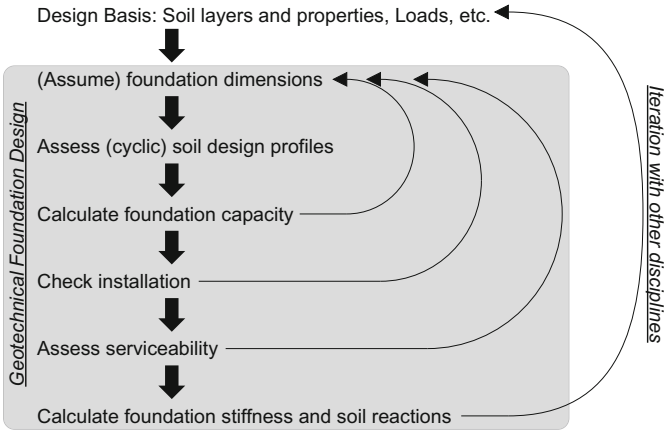

Fig. 6. Schematic presentation of the iterative and interdependent workflow of suction caissons design. (from Sturm [9])

As Suction Caissons for the foundation for OWTs have been applied first recently, the geotechnical design is typically much more comprehensive compared to the design of Monopiles. The first OWT designed followed a more traditional approach as applied in the Oil & Gas Industry. The caissons are designed by the geotechnical designer who provides to the structural designer stiffness in an interface point. Depending on the type of stiffness and load values used in the interface point, this procedure requires several iterations. It has been shown beneficial to provide stiffness ranges, i.e. high and low estimates. With each

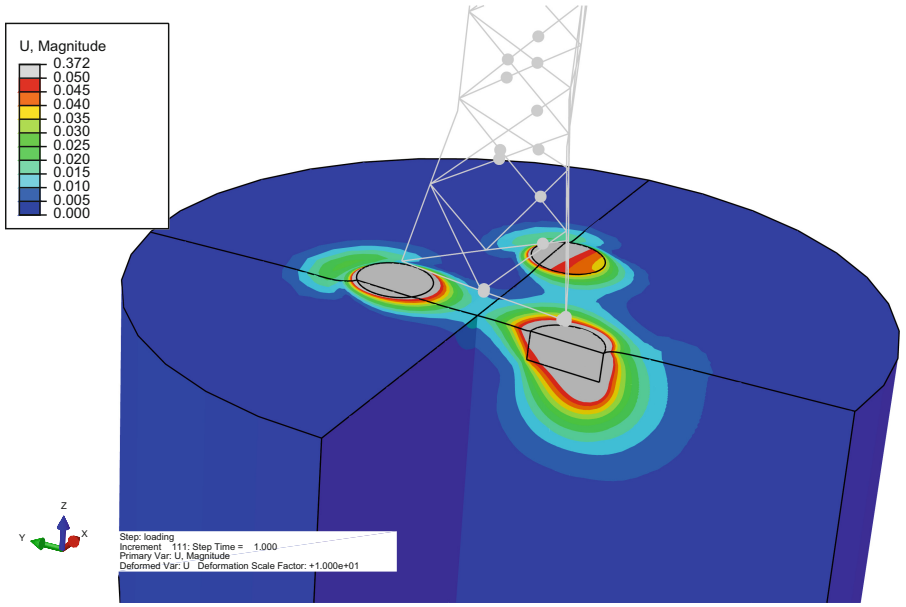

Fig. 7. Example of a global model used for assessing local foundation stiffness (from Sturm [9]).

iterations, the high and low estimate values approach each other, such that the range becomes smaller.

Therein, the FEM has been demonstrated to be a very efficient tool to reduce the number of iterations. An FE model including the soil, the caissons and the support-structure, shown in Fig. 7, enables to assess accurately the design loads for the sizing of the caissons and corresponding stiffness analysis. As the loads increase, the local foundation stiffness decreases causing a gradual redistribution of the loads, both locally at one leg, as well as globally between the different legs. This is captured by the FE model and hence reduces considerably the number of iterations between the structural and geotechnical designer.

For assessing the stiffness for operational load cases and eigenmode analysis, a macro-element has been developed in the RedWin project. Similar to the model presented for Monopiles, it is based on the theoretical formulation of multi-surface-plasticity. It also describes the foundation response to general cyclic loading. Calibration is done in the same way as detailed for the macro-element of the Monopile using the FEM.

Attempts have been made to introduce normalizations in order to reduce the number of analysis. However, the 2D FE procedure proposed by Jostad et al. [4] can be directly applied to Suction Caissons as well.[2]

[2] In fact, it has been actually developed for Suction Caissons and was just recently applied to other similar shaped foundations, such as Monopiles.

4 Summary and Outlook

The use of the FEM in the design of the OWTs was demonstrated using the example of a deep foundation – i.e. Monopile – and a shallow foundation – i.e. Suction Caisson. The proposed approaches are different for both foundation concepts, but both allow to benefit from the more advanced and potentially very accurate FE method, without suffering on the often very tight time schedule of OWF development project. The FEM cannot be directly used in the design, but requires a model capable to reproduce the relevant results from the FE analyses. Therein, it is essential that these models are as accurate as possible.

Although the proposed methods are promising and the respective authors have presented the impressing performance, there exist several open questions. Of particular relevance is the effect of cyclic loading. Neither the RedWin models nor the PISA model account for cyclic effects on the soil strength and stiffness. If cyclic effects are expected to be relevant, they have to be implicitly considered in the FE analysis. NGI has developed procedures for assessing the effect of cyclic loading, Jostad et al. [3,5]. However, these procedures are not yet fully integrated in a streamlined OWT design process, but have to be performed separately. Future development has to be done in order to incorporate these well established and proven procedure in the design process of OWTs in order to allow a further optimization.

Acknowledgements. The authors would like to thank the valuable contributions from Ana M. Page and Kristoffer Skau, which developed the RedWin models for Monopiles and Suction Caissons, respectively. The financial support by the Norwegian Research Council and the industrial partners Statoil, Vattenfall and Statkraft through the project 'Reducing cost of offshore wind by integrated structural and geotechnical design (REDWIN)', grant no. 243984, is gratefully acknowledged.

References

1. Burd, H.J., Byrne, B.W., McAdam, R.A., Houlsby, G.T., Martin, C.M., Beuckelaers W.J.A.P.: Proceedings of TC 209 Workshop (Foundation design of offshore wind structures): 19th International Conference on Soil Mechanics and Geotechnical Engineering, pp. 35-44 (2017)
2. Byrne, B.W., McAdam, R.A., Burd, H.J., Houlsby, G.T., Martin, C.M., Beuckelaers, W.J.A.P., Zdravkovic, L., Taborda, D.M.G., Potts, D.M., Jardine, R.J., Ushev, E., Liu, T., Abadias, D., Gavin, K., Igoe, D., Doherty, P, Skov, G.J., Pacheco, A.M., Muir, W.A., Schroeder, F.C., Turner, S., Plummer, M.A.L.: PISA: new design methods for offshore wind turbine monopiles. In: Proceedings of the 8th International Conference, 12–14 September 2017, pp. 142–161. Royal Geographical Society, London (2017)
3. Jostad, H.P., Grimstad, G., Andersen, K.H., Saue, M., Shin, Y., You, D.: A FE procedure for foundation design of offshore structures applied to study a potential OWT Monopile Foundation in the Korean Western Sea, Norway, pp. 153–172 (2014)

4. Jostad, H.P., Andersen, K.H.: Calculation of undrained holding capacity of suction anchors in clays. Geotech. Eng. **45**(4), 63–72 (2015). In: Frontiers in Offshore Geotechnics III, Oslo, Norway, pp. 263–268
5. Jostad, H.P., Grimstad, G., Andersen, K.H., Sivasithamparam, N.: A FE procedure for calculation of cyclic behaviour of offshore foundations under partly drained conditions. Front. Offshore Geotech. **III**(14), 153–172 (2015)
6. Page, A.M., Skau, K.S., Jostad, H.P., Eiksung, G.R.: A new foundation model for integrated analyses of monopile-based offshore wind turbines. Energy Procedia **137**, 100–107 (2017)
7. Skau, K.S., Page, A.M., Kaynia, A.M., Lvholt, F., Norn-Cosgriff, K., Sturm, H., Andersen, H.S., Nygard, T.A., Jostad, H.P., Eiksund, G.R., Havmller, O., Strm, P., Eichler, D.: REDWIN - REDucing cost in offshore WINd by integrated structural and geotechnical design. In: IOP Conference Series - Journal of Physics, EERA DeepWind 2018, Trondheim, Norway, 17–19 January 2018, Submitted for Publication
8. Sturm, H.: Stabilisation Behaviour of Cyclically Loaded Shallow Foundations for Offshore Wind Turbines. Universitatsverlag Karlsruhe, Karlsruhe (2009)
9. Sturm H.: Design aspects of suction caissons for offshore wind turbine foundations. In: Proceedings of TC 209 Workshop (Foundation design of offshore wind structures): 19th International Conference on Soil Mechanics and Geotechnical Engineering, pp. 45–63 (2017)

Fabric: A Missing Link Between Critical State and Critical State Theory

A. I. Theocharis[1(✉)], E. Vairaktaris[1], Y. F. Dafalias[1,2], and A. G. Papadimitriou[3]

[1] School of Applied Mathematical and Physical Sciences, Department of Mechanics, National Technical University of Athens, Athens, Greece
atheomec@mail.ntua.gr
[2] Department of Civil and Environmental Engineering, University of California Davis, Davis, CA, USA
[3] School of Civil Engineering, Department of Geotechnical Engineering, National Technical University of Athens, Athens, Greece

Abstract. The Critical State Theory of Roscoe et al. [1] and Schofield and Wroth [2], proposed two analytical conditions as necessary and sufficient for soil to reach and maintain Critical State. In this work the sufficiency of these two conditions is challenged by the results of a virtual experiment performed by means of the Discrete Element Method, where stress principal axes rotation is imposed at Critical State of a granular sample. The fabric emerges as the important entity that can explain the lack of sufficiency of the two conditions and serve as a link between Critical State Theory and Critical State as a physical event. The recently developed Anisotropic Critical State Theory includes an additional condition on fabric, that combined with the classical two provide a triplet of necessary and sufficient conditions for reaching and maintaining Critical State.

Keywords: Critical state · Fabric · DEM · Anisotropic critical state theory

1 Critical State and Critical State Theory

Critical State (CS) is the state where a granular material keeps deforming in shear at fixed stress and volume, analytically described by:

$$\dot{p} = 0, \;\; \dot{q} = 0, \;\; \dot{\varepsilon}_v = 0, \;\; \dot{\varepsilon}_q \neq 0 \tag{1}$$

where p is the hydrostatic pressure, q is the deviatoric stress, ε_v is the volumetric strain and ε_q is the deviatoric strain; a superposed dot indicates the material time derivative or rate. The deviatoric strain rate is implied to have a fixed direction, although not explicitly stated.

Roscoe et al. [1] and Schofield and Wroth [2] were the first to develop systematically a corresponding to CS theory, known as Critical State Theory (CST), that proposes two conditions as necessary and sufficient for reaching and maintaining CS, expressed by:

W. Wu (Ed.): *Desiderata Geotechnica*, SSGG, pp. 205–210, 2019.
https://doi.org/10.1007/978-3-030-14987-1_24

$$\eta = \eta_c = (q/p)_c = M, \quad e = e_c = e_c(p) \tag{2}$$

where η is the stress ratio, e is the void ratio, and subscript c denotes their CS values; the e_c is a unique function of p. As a precursor to the goal of this presentation it is crucial to underline the difference between the phenomenon of CS, expressed by Eq. (1), and the corresponding CST by means of Eq. (2).

Of particular interest is the question whether the CST conditions proposed in Eq. (2) are necessary and sufficient, as proclaimed. In order to answer it, the following thought experiment is set forward (Dafalias [3]): a soil sample is loaded in triaxial conditions until it reaches CS. Then, a rotation of stress principal axes (PA) takes place while keeping the stress principal values (PV) constant. The question then arises: will the sample remain at or abandon CS and why?

According to the definition of CST, fixed stress PV do not alter p and q, which enter Eq. (2); in addition, the void ratio is already at its CS value that is a unique function of the fixed p, thus, it should remain unchanged. As a result, the two CST conditions remain valid during the stress PA rotation and since they are claimed to be necessary and sufficient for reaching and maintaining CS, the sample should remain at CS. But maintenance of CS is conceived in conjunction with a change of strain rate direction due to stress PA rotation, in a transition from one CS to another with same fixed values of the invariants q, p and e. Is this possible? To find the answer one must execute the aforementioned thought experiment.

2 2D DEM Virtual Experiment

The requirements of the described experiment, reaching CS with a homogeneous sample and then applying stress PA rotation, make the experiment practically impossible to perform in a physical laboratory. The alternative, employed by the authors, is the use of the 2D Discrete Element Method (DEM, [4]), which can describe the material in its discrete nature; the DEM code PFC2D v4 has been used.

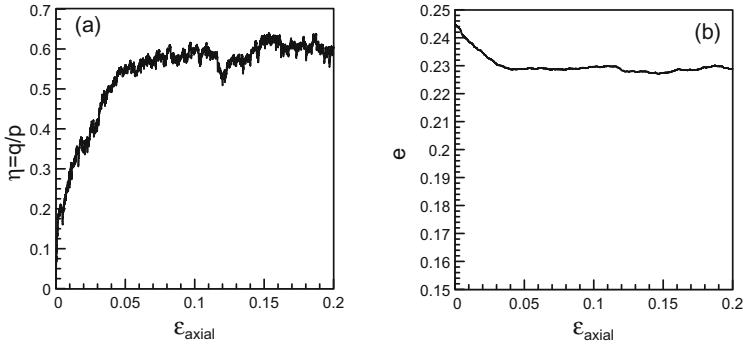

Fig. 1. Phase 1 biaxial test: (a) stress ratio η and (b) void ratio e.

The performed experiment has two phases. During phase one the sample is brought to CS by biaxial loading, and then during phase two a stress PA rotation is imposed at fixed stress PV. 20,000 particles were used with density 2600 kg/m^3, circular in shape and a uniform distribution from 0.5 to 1.5 mm. The mean pressure was kept constant at 200 kPa. The macroscopic results of the initial phase 1 loading are presented in Fig. 1a and b in terms of stress and void ratios, respectively. The choices of normal and tangential stiffness and micromechanical friction produce a macroscopic response for a loose soil sample, for which continuous hardening and volume reduction is observed. More details can be found in Theocharis et al. [5].

The sample deformation was stopped at 20% of vertical axial strain where it has undoubtedly reached Critical State and the two CST conditions are also fulfilled. This can easily be seen from Fig. 1a and b where both the stress ratio η and void ratio e have been stabilized at their CS values (in regard to the CS numerical values of η and e recall the experiment is two dimensional). At this point, the stress PA rotation was applied, with the stress PV kept constant.

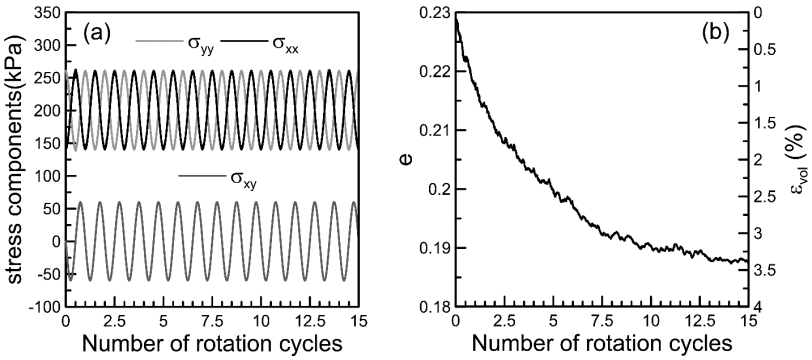

Fig. 2. Phase 2 stress PA rotation initiating at CS: (a) stress components and (b) void ratio e and volumetric strain ε_{vol}.

The results for the stress PA rotation (Phase 2 loading) are presented in Fig. 2. Figure 2(a) confirms that the stress PA rotation was successfully applied. Figure 2(b) is the key figure which shows that the sample contracts dramatically upon initiation of stress PA rotation, thus, CS is abandoned despite that none of the two CST condition was violated at rotation initiation. As a result, it becomes clear that the two conditions of classical CST given by Eq. (2), are necessary to reach but not sufficient to maintain CS, a feature attesting to some form of incompleteness.

3 Fabric Enhancement of CST

The conclusion drawn from the results of the experiment creates the need to re-examine the completeness of the CST conditions in Eq. (2). One would instinctively argue that stress PA rotation induced rotation of the (unit-norm) deviatoric plastic strain rate

direction tensor $\mathbf{n}$, in contrast to the (implied) CS observation of a fixed $\mathbf{n}$. Hence, imposing fixity of plastic strain rate direction as an additional condition for CS would seem to complete CST by excluding the stress PA rotation test. But the classical principle of invariance requirement for constitutive relations in Continuum Mechanics under superposed rigid body rotation with adjustment of body forces, would have allowed such change of $\mathbf{n}$ without abandonment of CS! Therefore, fixity of $\mathbf{n}$ must be related someway to the sample's orientation due to its existing, oriented microstructure, commonly called fabric.

The fabric of granular materials describes the orientation of microstructure and is related to various unit vectors along particles' orientation, contact normal vectors and void vectors. For the present analysis it suffices to consider the deviatoric contact normal fabric tensor $\mathbf{F}$ defined as the deviatoric part of the mean value of summation in a 2D scheme of the tensor products $\mathbf{n}_c^{k_c} \otimes \mathbf{n}_c^{k_c}$ [6], where $\mathbf{n}_c^{k_c}$ is the unit contact normal vector for the $k_c th$ contact.

Based on fabric observations Li and Dafalias [7] proposed the Anisotropic Critical State Theory (ACST) that is founded on the definition of the Fabric Anisotropy Variable (FAV) A according to:

$$A = \mathbf{F} : \mathbf{n} = F\mathbf{n}_F : \mathbf{n} = FN \tag{3}$$

where F is the fabric norm, $\mathbf{n}_F$ the unit-norm direction tensor of the fabric tensor $\mathbf{F}$ and $N = \mathbf{n}_F : \mathbf{n}$ measures the relative orientation of $\mathbf{F}$ and $\mathbf{n}$. The evolution of $\mathbf{F}$ can be monitored in DEM based on its definition and can serve for the development of a continuum rate equation of its evolution.

Previous DEM studies (e.g. [8, 9]) have indicated that, as the fabric tensor evolves during plastic deformation, its direction $\mathbf{n}_F$ tends to align with $\mathbf{n}$ and becomes identical to it at CS while the norm F normalized with respect to its value at CS, tends towards 1 at CS. Hence, at CS one has $N = N_c = \mathbf{n}_F : \mathbf{n} = \mathbf{n} : \mathbf{n} = 1$ (given the unit-norm feature of both $\mathbf{n}_F$ and $\mathbf{n}$), $F = 1$ and $\mathbf{F} = \mathbf{F}_c = \mathbf{n}$. Thus, based on the definition of A (Eq. (3)), the third CS condition $A = A_c = 1$ follows. Therefore, one can now re-write the three necessary and sufficient conditions of ACST for reaching and maintaining CS as:

$$\eta = \eta_c = (q/p)_c = M; \quad e = e_c = e_c(p); \quad A = A_c = 1 \tag{4}$$

4 The DEM Experiment Viewed Within ACST

The results presented in Fig. 2, arising from the DEM virtual experiment, can now be examined within ACST. Accordingly, Fig. 3 presents the results for the contact normal fabric norm F, the relative orientation N of fabric and plastic strain rate and the FAV A during the biaxial (Phase 1) loading and the stress PA rotation (Phase 2) loading. For the uniform presentation of the two loading phases, the cumulative deviatoric (directionless) plastic strain e_{eq} was used.

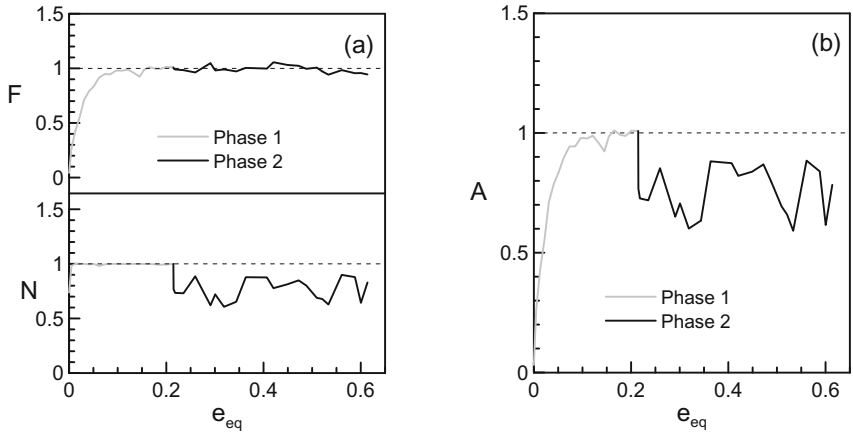

Fig. 3. Evolution of ACST variables for the biaxial and the stress PA rotation: (a) fabric norm and relative orientation of fabric and plastic strain rate (b) Fabric Anisotropy Variable.

Based on Fig. 3b, it is evident that the third ACST condition, which is the fabric condition that has enriched classical CST conditions, was fulfilled during the biaxial loading and was violated when stress PA rotation initiated. This violation of the extra ACST condition declares that CS was abandoned and as a result the change of the void ratio (shown in Fig. 2) is supported. Most importantly the reader is referred to Theocharis et al. [5] where it is shown that the densification present in Fig. 3b can actually be derived from a new dilatancy state parameter ζ defined within ACST as function of A, that substitutes for the classical state parameter ψ [10].

In closing note that the ACST has already been proven extremely useful in constitutive modeling of anisotropic granular materials [7]. The present work proves the validity of ACST as a complete theory that can remedy the incompleteness of and in fact substitute for the classical CST by enhancing the 2 classical CS conditions of the latter with a fabric-related 3rd condition.

5 Conclusions

In this paper the completeness of the classical CST has been investigated by means of a special virtual experiment, i.e. stress PA rotation initiating at CS while keeping stress PV constant, performed by 2D DEM. While CST would predict that the sample will remain at CS since its two conditions for CS are not violated, the DEM results show that the sample contracts and clearly abandons CS. Thus, the classical CST conditions were proven to be not sufficient for CS to be maintained, a feature attesting to some form of incompleteness.

The new ACST highlights fabric as a missing link between CST and CS and proposes a third fabric-based condition to be added to the initial two of classical CST that can explain the DEM results. The three conditions of ACST are proven to be necessary and sufficient for CS to be reached and maintained.

Acknowledgements. The research leading to these results has received funding from the European Research Council under the European Union's Seventh Framework Program (FP7/2007-2013)/ERC IDEAS Grant Agreement *n* 290963 (SOMEF) and partial support by NSF project CMMI-1162096. The paper is submitted on the occasion of the 80th birthday of Professor G. Gudehus.

References

1. Roscoe, K.H., Schofield, A.N., Wroth, C.P.: On the Yielding of Soils. Géotechnique **8**, 22–53 (1958)
2. Schofield, A.N., Wroth, C.P.: Critical State Soil Mechanics. McGraw-Hil, London (1968)
3. Dafalias, Y.F.: Must critical state theory be revisited to include fabric effects? Acta Geotech. **11**(3), 479–491 (2016)
4. Cundall, P.A., Strack, O.D.: A discrete numerical model for granular assemblies. Géotechnique **29**(1), 47–65 (1979)
5. Theocharis, A.I., Vairaktaris, E., Dafalias, Y.F., Papadimitriou, A.G.: Proof of incompleteness of critical state theory in granular mechanics and its remedy. J. Eng. Mech. **143**(2), 04016117 (2017)
6. Satake, M.: Fabric tensor in granular materials. In: Luger, H.J., Vermeer, P.A. (eds.) IUTAM Symposium on Deformation and Failure of Granular Materials, Delft, Amsterdam, pp. 63–68 (1982)
7. Li, X.-S., Dafalias, Y.F.: Anisotropic critical state theory: role of fabric. J. Eng. Mech. **138** (3), 263–275 (2012)
8. Li, X.S., Li, X.: Micro-macro quantification of the internal structure. J. Eng. Mech. **135**(7), 641–656 (2009)
9. Fu, P., Dafalias, Y.F.: Fabric evolution within shear bands of granular materials and its relation to critical state theory. Int. J. Numer. Anal. Methods Geomech. **35**, 1918–1948 (2011)
10. Been, K., Jefferies, M.G.: A state parameter for sands. Géotechnique **35**(2), 99–112 (1985)

Soils Under High- and Low-Cycle Loading - Experiments vs. Predictions by Constitutive Models

Torsten Wichtmann(✉)

Bauhaus-Universität Weimar, Coudraystraße 11c, Weimar, Germany
torsten.wichtmann@uni-weimar.de

Abstract. The behaviour of soils and foundation structures under a cyclic loading with either a high or a low number of cycles is discussed. Regarding the high-cycle loading, the validation of a high-cycle accumulation (HCA) model is demonstrated based on successful recalculations of element tests, model tests on monopile foundations with different scales and a full-scale test on a gravity base foundation for offshore wind turbines. The well-documented settlements of a ship lock over about two decades could be reproduced with the HCA model as well. Regarding the low-cycle loading, two databases with numerous undrained cyclic triaxial tests performed on either a coarse-grained or a fine-grained soil are introduced. The data for sand is used to inspect three constitutive models with a focus to low-cycle loading.

1 Introduction

Cyclic loading is of practical relevance for many problems in geotechnical engineering. A cyclic loading of non-endogenous nature may be caused by traffic (high-speed trains, magnetic levitation trains), industrial sources (crane rails, machine foundations), wind and waves (on-shore and off-shore wind turbines, coastal structures) or repeated filling and emptying processes (locks, tanks and silos). Furthermore, construction processes (e.g. vibration of sheet piles) and mechanical compaction (e.g. vibratory compaction) introduce cyclic loads into the soil. A cyclic loading may be also caused by endogenous sources, e.g. by the shear wave propagation during earthquakes.

If the repeated loading involves a large number of cycles ($N > 10^3$) with a relative small strain amplitude ($\varepsilon^{\mathrm{ampl}} < 10^{-3}$) one speaks of a high-cycle loading. Offshore wind turbine foundations under wind and wave action and infrastructure under traffic are typical examples for a high-cycle loading. In contrast, the cyclic shearing of the soil during earthquakes usually involves a rather low number of cycles, probably with a larger strain amplitude due to the relaxation of effective stress caused by the cycles.

In the following the results of various experimental and numerical studies with the focus on either high- or low-cycle loading are briefly summarized. This research has been done during the former work of the author at the Institute of Soil Mechanics and Rock Mechanics (IBF) at Karlsruhe Institute of Technology (KIT).

W. Wu (Ed.): *Desiderata Geotechnica*, SSGG, pp. 211–220, 2019.
https://doi.org/10.1007/978-3-030-14987-1_25

2 High-Cycle Loading

2.1 Element Tests vs. Prediction by HCA Model

In the laboratory the cumulative behaviour of sand can be studied in drained cyclic triaxial tests with a high number of cycles. Examples for the measured development of permanent strain ε^{acc} (with $\varepsilon = \sqrt{(\varepsilon_1)^2 + 2(\varepsilon_3)^2}$) with increasing number of cycles are provided in Fig. 1. These data from a test series on a medium coarse to coarse sand (d_{50} = 0.6 mm, $C_u = d_{60}/d_{10}$ = 2.5) with 10^5 cycles demonstrate the increase of the rate of permanent strain accumulation $\dot{\varepsilon}^{acc}$ with increasing stress amplitude q^{ampl}, decreasing initial relative density $I_{D0} = (e_{max} - e_0)/(e_{max} - e_{min})$ and growing average stress ratio $\eta^{av} = q^{av}/p^{av}$. The average mean pressure p^{av} has a minor effect on the curves $\varepsilon^{acc}(N)$ as long as the same amplitude-pressure ratio q^{ampl}/p^{av} is chosen in all tests. Further influencing factors (e.g. grain size distribution curve, fines content, shell fragment content, grain shape, sample preparation method, changes of average stress, frequently changing amplitude, multiple polarization changes, complicated multidimensional strain loops, sample geometry, saturation state) are discussed in detail in [12].

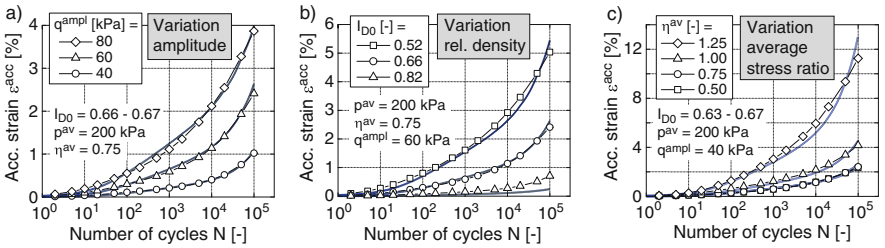

Fig. 1. Strain accumulation curves $\varepsilon^{acc}(N)$ measured in three series of drained cyclic triaxial tests with different (a) stress amplitudes q^{ampl}, (b) initial relative densities I_{D0} and (c) average stress ratios η^{av}. The blue curves stem from simulations with the HCA model using an optimum set of parameters for the tested sand.

In order to study the long-term behaviour of foundations subjected to high-cyclic loading so-called high-cycle accumulation (HCA) models (e.g. [6,9,10]) have been developed. The present paper concentrates on the model proposed by Niemunis et al. [9]. The determination of the parameters based on test series as those shown in Fig. 1 is explained in [17,18]. After such calibration the prediction of the HCA model can be checked by means of element test simulations. Such recalculations of the laboratory tests can be also used for an optimization of single parameters. The blue curves shown in Fig. 1 stem from such simulations using an optimum set of parameters for the tested sand. The numerical curves agree well with the measured ones. Based on these successful recalculations the HCA model can be regarded as validated on the element test level.

2.2 Model Tests vs. Numerical Simulations with HCA Model

In recent years considerable effort has been undertaken to validate the HCA model based on recalculations of model tests in different scales, full-scale tests on prototype foundations and measurements at real structures. Some of these efforts are described in this and the following section.

Model tests on shallow and monopile foundations for offshore wind turbines have been performed at the IBF using Karlsruhe fine sand (KFS) [20]. As an example, tests on a monopile with a diameter of 6.1 cm and a length of embedding of 60 cm subjected to a horizontal cyclic loading are discussed herein. The model test equipment is shown in Fig. 2a. The solid curves in Fig. 2c represent the measured development of the lateral pile displacement near the ground surface with increasing number of cycles for four different amplitudes of cyclic loading. The dashed curves in Fig. 2c stem from recalculations of the model tests with the FE model presented in Fig. 2b. A combination of hypoplasticity with intergranular strain (for the first two cycles) and the HCA model (for all further cycles) was used. The parameters of KFS for both constitutive models were determined from laboratory tests. Despite some differences in case of single tests, the overall congruence between the curves from the model tests and the simulations is quite satisfying.

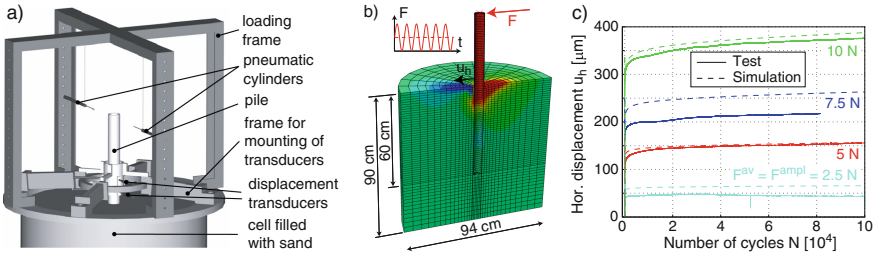

Fig. 2. Recalculation of model tests on monopiles performed at IBF: (a) Test equipment, (b) FE model and (c) development of lateral pile displacement near the ground surface with increasing number of cycles in the model tests and the FE calculations (modified from [20])

In a second step, model tests with a larger scale performed at TU Berlin [11] have been simulated [20]. The monopiles in these tests had diameters between 14 cm and 41 cm and lengths of embedding lying in the range from 1.6 m to 2.9 m. The parameters of hypoplasticity with intergranular strain and the HCA model for the Berlin sand used in the model tests were calibrated based on an extensive laboratory program performed at the IBF, including monotonic and cyclic tests. Furthermore, FE models of the tests performed at TU Berlin have been generated, including details of the experimental setup (e.g. the wooden construction at the sides of the pit used for an installation of displacement transducers, see Fig. 3a). Figure 3b presents a comparison of the lateral pile head displacement measured in one of the model tests with six packages of cycles with the curve obtained from the corresponding FE simulation. Also in this case the differences between measurement and simulation are acceptable.

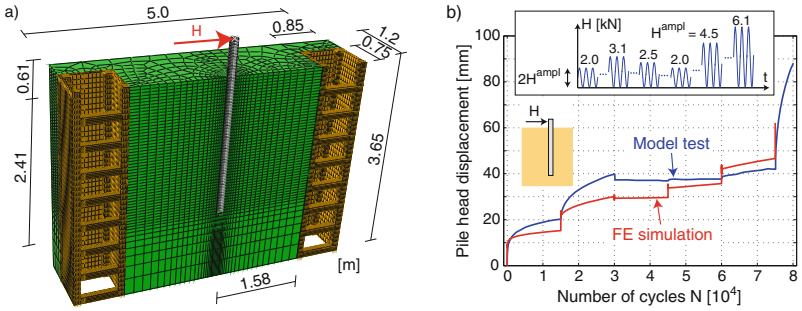

Fig. 3. Recalculation of model tests on monopiles at TU Berlin: (a) FE model and (b) development of lateral pile head displacement with increasing number of cycles in a test with six packages of cycles (modified from [20])

2.3 Full-Scale Tests and Measurements at Real Structures vs. Numerical Simulations with HCA Model

A full-scale test on the prototype of a gravity base foundation for offshore wind turbines has been performed by the Ed. Züblin AG near the shore of the North Sea in a flooded construction pit [5]. A cross-section of the test foundation is given in Fig. 4a. The foundation consisted of cross-shaped concrete box girders and a cylindrical shaft ballasted with sand and resting on four separate precast concrete plates. The foundation and the offshore-typical subsoil were extensively instrumented in order to measure settlements, soil pressures and pore water pressures. A cyclic loading simulating several strong storm events was applied by tension forces at the shaft. In the simulation with the HCA model [20] the subsoil of the test foundation was simplified to nine main layers based on core samples taken on site. For each of these sand layers the constitutive parameters have been derived from numerous laboratory tests with monotonic or cyclic loading. The initial relative density profile with depth $I_{D0}(z)$ has been derived from the results of CPT soundings following the procedure proposed in [1]. The FE model is shown in Fig. 4b. It also considers the construction stages. The cyclic loading up to the end of the first storm event has been simulated. The storm consists of several packages of cycles with amplitudes increasing to a peak value followed by a stepwise decrease (see scheme on the right-hand side of Fig. 4c). The measured and calculated settlements of the two plates A and C in the loading direction during this first storm event are compared in Fig. 4c. The predicted final settlement of plate C is very similar to the value measured in the field test. The settlement of plate A obtained from the simulation is, however, slightly lower than the measured value. This results in an underestimation of foundation tilting in the simulation. A possible influence of uncertainties in the initial density distribution is discussed in [20]. Generally, the HCA model prediction is very sensitive to changes in the relative density of the soil. Beside the settlements, the simulations with the HCA model could reproduce the development of excess pore water pressures in the soil (no accumulation) and the dangerous redistribution of contact pressures from foundation plates A and C lying in the main loading direction towards plates B and D lying aside during the high-cyclic loading [20].

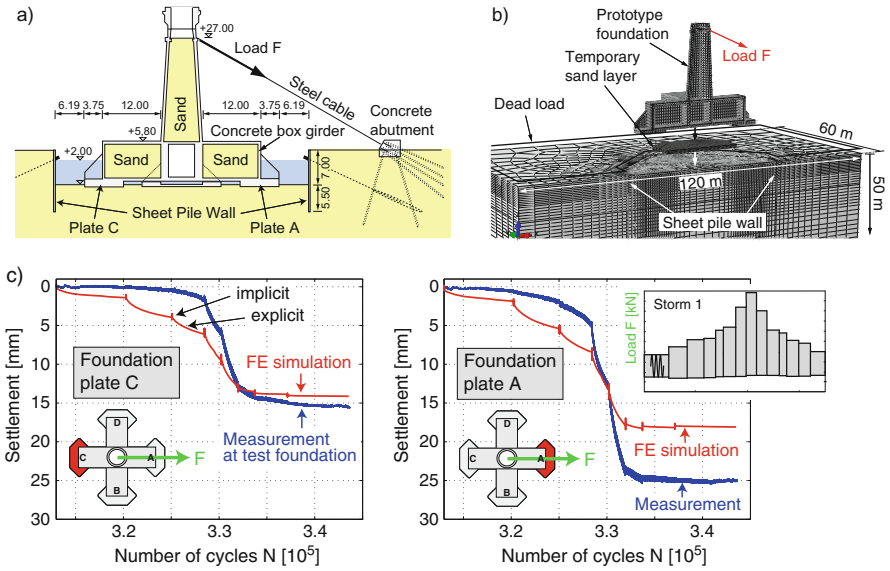

Fig. 4. (a) Cross-section and (b) FE model of the prototype foundation of the Ed. Züblin AG; (c) Comparison of the development of the settlements of plates A and B during the first simulated storm in the field test and the finite element calculation (modified from [20])

A ship lock is subjected to a high-cyclic loading due to the repeated filling and emptying of the lock chamber, possibly leading to the development of cumulative settlements. In [7] the well-documented example of the ship lock Uelzen I (part of Elbe-Seitenkanal) has been studied, for which settlement measurements over several decades are available. The ship lock has been investigated in finite element simulations with the HCA model. Due to the absence of samples from the subsoil of the ship lock, the stratified ground was represented by alternative or replicated sands with similar grain size distribution curve and grain shape. For each layer the parameters of the constitutive models have been derived from laboratory tests with monotonic or cyclic loading performed on these sands. For depths up to $-50\,\mathrm{m}$ the profile of the initial relative density with depth $I_{D0}(z)$ has been derived from CPT soundings. Since no CPT data was available for larger depths, two different assumptions regarding the continuation of the $I_{D0}(z)$ profile at those depths have been compared. Both a two-dimensional and a three-dimensional FE model were created and a sensitivity analysis was performed [7]. Figure 5a shows parts of the 3D model. The range of settlements measured for ten different blocks of the ship lock was somewhat overestimated by the results of the FE simulations (Fig. 5b). However, considering the uncertainties regarding the density profiles and the determination of the constitutive parameters based on laboratory tests performed on representative alternative or replicated sands, the congruence between field measurements and FE predictions can be judged as quite satisfying.

Despite some quantitative deviations between measured and predicted data in the various examples (under- or overestimation), the HCA model may be regarded as

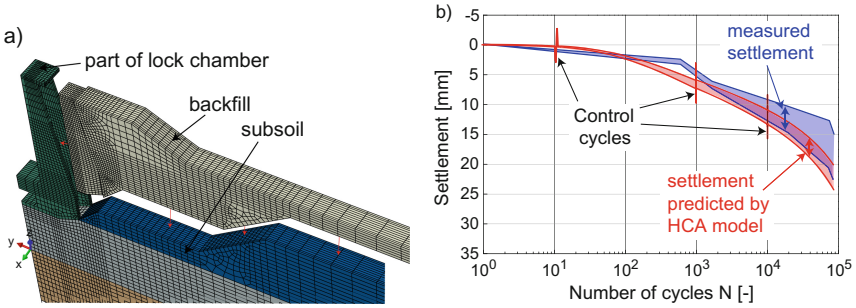

Fig. 5. (a) 3D FE model and (b) comparison of measured and predicted development of settlement of ship lock Uelzen I over two decades. The range of measured data comprises measurements at ten different blocks of the lock. The range of the curves from the FE simulations stems from the two different assumptions regarding the density profile $I_{D0}(z)$ at larger depths. (modified from [7])

approximately validated on different scales (element test, model test, full-scale test and field measurements). The advantages of the HCA model over simpler engineer-oriented approaches are obvious: Simulations with the HCA model are not restricted to a certain foundation type. Furthermore, beside a prediction of long-term deformations, the whole soil-structure interaction under high-cyclic loading can be investigated.

3 Low-Cycle Loading

3.1 Coarse-Grained Soils

A comprehensive data base with undrained cyclic triaxial tests performed on Karlsruhe fine sand has been published in [14,15]. The data of these tests are provided on the homepage of the author [13]. Some examples of effective stress paths for different densities and loading conditions are given in Fig. 6a–c. Tests with isotropic consolidation and stress cycles usually lead to butterfly-shaped effective stress paths in the final stage (cyclic mobility phase) for medium dense and dense samples (Fig. 6a). After initial liquefaction ($p = 0$ is reached for the first time), the axial strain amplitude progressively increases with each subsequent cycle until a chosen failure criterion (e.g. $|\varepsilon_1| = 10\%$) is reached. Loose samples fail due to large (in most cases extensional) strains within a single cycle after the effective stress path has come close to the failure line known from tests with monotonic loading.

If the stress cycles are started at an anisotropic stress ($q_0 \neq 0$) the shape of the final effective stress path and the stress-strain relationship depend on the position of the cycles with respect to the isotropic axis. Similar to the tests with isotropic consolidation, tests with an initial deviatoric stress $|q_0| > 0$ and a deviatoric stress amplitude $q^{\text{ampl}} > |q_0|$ end up in a butterfly-shaped effective stress path, temporarily passing $p = 0$. The accumulation of axial strain on the triaxial extension or compression side prevails, depending on whether the main portion of the stress path lies below or above the p-axis. If the stress cycles do not cross the p-axis, a zero effective stress ($p = 0$) is not reached.

After a certain number of cycles the accumulation of pore water pressure vanishes and the effective stress at the end of each subsequent cycle stays the same. In that phase the effective stress path repeatedly passes through the same lens-shaped loop in the p-q plane (Fig. 6b). The effective stress paths during cycles fully applied in the triaxial extension regime ($q_{\max} < 0$) show an opposite inclination to those observed for triaxial compression ($q_{\min} > 0$). The strain accumulation continues even when the accumulated pore water pressure has become stable.

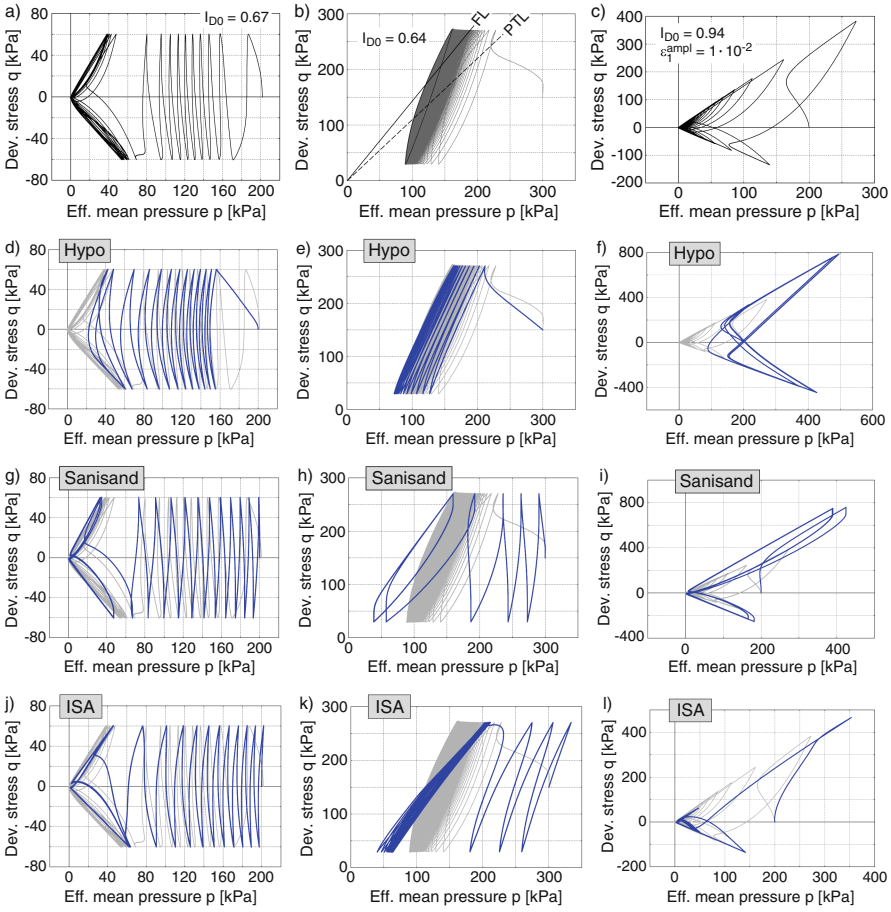

Fig. 6. Effective stress paths from tests on KFS with (a) isotropic initial stresses and stress cycles, (b) anisotropic initial stresses and stress cycles, (c) isotropic initial stresses and strain cycles [14, 15]; (d–l) simulations of these tests with hypoplasticity with intergranular strain, Sanisand (2004) or ISA (2014) (blue curves = simulations, gray curves = experimental data, modified from [12])

In tests with strain cycles a zero effective stress state ($p = q = 0$) is reached after a sufficiently large number of cycles, irrespective of the applied amplitude (a large range

$4 \cdot 10^{-4} \leq \varepsilon_1^{ampl} \leq 10^{-2}$ was tested) and the initial values of relative density I_{D0}, mean pressure p_0 or stress ratio $\eta_0 = q_0/p_0$. An example is given in Fig. 6c. It demonstrates that even very dense sand can reach a state of full liquefaction if the applied number of cycles is sufficiently large [15].

Three of the most sophisticated constitutive models for sand, namely hypoplasticity with intergranular strain [8,19], the Sanisand 2004 model [2,3] and the ISA (intergranular strain anisotropy) 2014 model [4] have been inspected based on selected tests from the experimental data base for KFS [13–15]. After a calibration of the material constants of the three models, simulations of the element tests with either monotonic or cyclic loading and various boundary conditions have been performed [12]. As an example, the results of recalculations of the three tests in Fig. 6a–c with the three constitutive models are given in Fig. 6d–l. In those diagrams the blue curves stem from the simulations, while the gray ones represent the effective stress paths measured in the tests. Each column of diagrams in Fig. 6 corresponds to a certain test. The comparison of the results of the simulations with the experimental data has demonstrated that all three inspected constitutive models have their strengths and weaknesses, delivering a satisfying prediction for some types of tests while some other ones are reproduced less well. Usually, a certain set of parameters works well for a certain type of test (e.g. tests with monotonic loading), while another set would fit better for some other experiments (e.g. tests with cyclic loading). For example, the simulations with hypoplasticity do not reach a state with zero effective stress (liquefaction, $p = q = 0$) in case of tests with isotropic initial stresses and stress cycles (Fig. 6d). The same applies to tests with large strain amplitudes ($\varepsilon_1^{ampl} = 10^{-2}$), in particular in case of dense samples (Fig. 6f). The Sanisand model nicely reproduces the butterfly-shaped effective stress paths for tests with isotropic initial stresses and stress cycles (Fig. 6g). For the test on dense sand with large strain cycles, however the butterfly predicted by Sanisand (Fig. 6i) is contrasted by the single point ($p = q = 0$) finally reached by the effective stress path in the experiments (Fig. 6c).

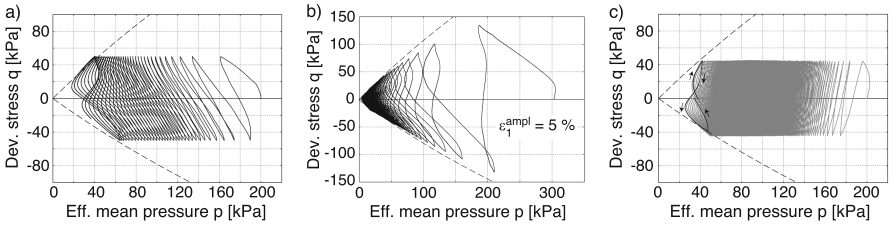

Fig. 7. Effective stress paths from tests on kaolin with isotropic initial stresses and (a) stress cycles, (b) strain cycles, (c) stress cycles applied on a sample cut out in the horizontal direction [16]

3.2 Fine-Grained Soils

An experimental study with numerous undrained monotonic and cyclic triaxial tests on kaolin (liquid limit w_L = 47.2 %, plasticity index I_P = 12.2 %) is documented in

[16]. The samples were pre-consolidated out of a slurry. Afterwards the triaxial samples were cut out of the centre of the pre-consolidated cylinders. The measured effective stress paths and stress-strain relationships resemble those obtained for sand with several exceptions. An accumulation of pore water pressure occurs also in case of the fine-grained soils, but a state with zero effective stress $p = q = 0$ is never reached. The effective stress path obtained from tests with isotropic initial stresses and stress cycles shows a strong inclination during the initial phase and is eight-shaped during the final phase of a test (Fig. 7a). An application of strain cycles results in fir-shaped effective stress paths (Fig. 7b), stopping at $p > 0$ after a sufficiently large number of cycles. The material response of the tested kaolin is slightly dependent on loading frequency. This effect is much more pronounced in case of materials with higher plasticity. The cumulative rates are strongly reduced by an overconsolidation. Furthermore, effects of anisotropy can be significant. Samples cut out of the preconsolidated cylinders in the horizontal direction showed an opposite inclination of the effective stress path (Fig. 7c) and could withstand a much larger number of cycles to failure than those taken conventionally in the vertical direction. The opposite inclination of the effective stress paths in the initial phase of the tests in Figs. 7a and c is a result of the anisotropy of stiffness.

References

1. Cudmani, R.: Statische, alternierende und dynamische Penetration in nichtbindige Böden. Ph.D. thesis, Publications of the Institute of Soil Mechanics and Rock Mechanics, University Karlsruhe, Issue No. 152 (2001)
2. Dafalias, Y.F., Manzari, M.: Simple plasticity sand model accounting for fabric change effects. J. Eng. Mech. **130**(6), 622–634 (2004)
3. Dafalias, Y.F., Manzari, M.: Sand plasticity model accounting for inherent fabric anisotropy. J. Eng. Mech. **130**(11), 1319–1333 (2004)
4. Fuentes, W.: Contributions in mechanical modelling of fill material. Ph.D. thesis. Publications of the Institute of Soil Mechanics and Rock Mechanics, Karlsruhe Institute of Technology, Issue No. 179 (2014)
5. Hartwig, U., Mayer, T.: Entwurfsaspekte bei Gründungen für Offshore-Windenergieanlagen. Bautechnik **89**(3), 153–161 (2012)
6. Karg, C., Francois, S., Haegeman, W., Degrande, G.: Elasto-plastic long-term behavior of granular soils: modeling and experimental validation. Soil Dyn. Earthq. Eng. **30**(8), 635–646 (2010)
7. Machaček, J., Wichtmann, T., Zachert, H., Triantafyllidis, T.: Long-term settlements of a ship lock: measurements vs. FE-prediction using a high cycle accumulation model. Comput. Geotech. **97**(5), 222–232 (2018)
8. Niemunis, A., Herle, I.: Hypoplastic model for cohesionless soils with elastic strain range. Mech. Cohesive-Frict. Mater. **2**, 279–299 (1997)
9. Niemunis, A., Wichtmann, T., Triantafyllidis, T.: A high-cycle accumulation model for sand. Comput. Geotech. **32**(4), 245–263 (2005)
10. Pasten, C., Shin, H., Santamarina, J.C.: Long-term foundation response to repetitive loading. J. Geotech. Geoenviron. Eng. **140**(4), 04013036 (2014)
11. Taşan, H.E., Rackwitz, F., Glasenapp, R.: Experimentelle Untersuchungen zum Verhalten von zyklisch horizontal belasteten Monopiles. Bautechnik **88**(2), 102–112 (2011)
12. Wichtmann T.: Soil behaviour under cyclic loading - experimental observations, constitutive description and applications. Habilitation thesis. Publications of the Institute of Soil Mechanics and Rock Mechanics, Karlsruhe Institute of Technology, Issue No. 181 (2016)

13. Wichtmann, T.: (2018). www.torsten-wichtmann.de
14. Wichtmann, T., Triantafyllidis, T.: An experimental data base for the development, calibration and verification of constitutive models for sand with focus to cyclic loading. Part I: Tests with monotonic loading and stress cycles. Acta Geotech. **11**(4), 739–761 (2016)
15. Wichtmann, T., Triantafyllidis, T.: An experimental data base for the development, calibration and verification of constitutive models for sand with focus to cyclic loading. Part II: tests with strain cycles and combined cyclic and monotonic loading. Acta Geotech. **11**(4), 763–774 (2016)
16. Wichtmann, T., Triantafyllidis, T.: Monotonic and cyclic tests on Kaolin - a database for the development, calibration and verification of constitutive models for cohesive soils with focus to cyclic loading. Acta Geotech. (2018). https://doi.org/10.1007/s11440-017-0588-3
17. Wichtmann, T., Niemunis, A., Triantafyllidis, T.: On the determination of a set of material constants for a high-cycle accumulation model for non-cohesive soils. Int. J. Numer. Anal Met. **34**(4), 409–440 (2010)
18. Wichtmann, T., Niemunis, A., Triantafyllidis, T.: Improved simplified calibration procedure for a high-cycle accumulation model. Soil Dyn. Earthq. Eng. **70**(3), 118–132 (2015)
19. von Wolffersdorff, P.-A.: A hypoplastic relation for granular materials with a predefined limit state surface. Mech. Cohesive-Frict. Mater. **1**, 251–271 (1996)
20. Zachert, H.: Zur Gebrauchstauglichkeit von Gründungen für Offshore-Windenergieanlagen. Ph.D. thesis. Publications of the Institute of Soil Mechanics and Rock Mechanics, Karlsruhe Institute of Technology, Issue No. 180 (2015)

Non-destructive Evaluation of Residual Tension of Ground Anchor Using Resonance Phenomenon

A. Yashima[1(✉)], H. Saito[2], K. Aoike[2], M. Yamazaki[3], Y. Sone[4], and T. Wachi[5]

[1] Gifu University, Gifu 501-1193, Japan
yashima@gifu-u.ac.jp
[2] OYO Corporation, Saitama 331-0812, Japan
[3] Central Nippon Highway Engineering Nagoya, Nagoya 460-0003, Japan
[4] Nagoya University, Nagoya 464-8601, Japan
[5] Nippon Expressway Research Institute, Machida 194-8508, Japan

Abstract. A new method of non-destructive evaluation for residual tension load of ground anchors was developed. If the tendon tension part of a ground anchor is approximated by a "string", the frequency of its free vibration is determined by line density and tension length of the PC steel and the operating tension. Although the free vibration of tendon tension part cannot be directly excited because it is in the ground, it is confirmed by a physical model experiment that the free vibration can be excited by applying a power at the extra length of anchor head. A series of field experiments was conducted by using a small vibrator and an accelerometer. A swept-frequency vibration was applied to the extra length of anchor head, and the vibration waveform was measured at the same position. The observed waveform was analyzed by running-spectrum analysis in order to find a resonance frequency which is used to calculate the residual tension load.

Keywords: Ground anchor · Monitoring · Resonance phenomenon

1 Introduction

Ground anchoring is one of the popular methods for maintaining the stability of slope. The ground anchoring method was introduced in Japan in 1957. Construction materials for ground anchors are easy to procure and construction is also simple compared with the preventive pile method. Many anchors are constructed every year as a way to stabilize cut slopes and prevent landslides. Periodic inspection of ground anchor are important to ensure the slope stability.

The anchors are constructed in natural ground. Therefore, the decrease in function caused by a variety of factors, such as the corrosion of steel and the effects of earth pressure is of primary concern. Initially, ground anchoring had been adopted as a temporary prevention method. Therefore, the protection against corrosion had not been sufficient, particularly on anchor heads boundary of tendon free part, and anchor fixed length. The ingress of water and air also contribute to the corrosion of anchors made of

W. Wu (Ed.): *Desiderata Geotechnica*, SSGG, pp. 221–226, 2019.
https://doi.org/10.1007/978-3-030-14987-1_26

steel. By the first-half of the 1980s, anchor failures caused by corrosion had been seen. We often observed jumping and lifting of the anchor head caused by rupture of the tendon free part. For these reasons, in 1988, the standard document was revised [1]. After that, the anchors protected against corrosion started to be adopted [2].

When anchors are installed, loadcells are set to some of the anchors. After that, the anchor tension is measured frequently to manage the anchor performance. After confirming the convergence of anchor tension, the frequency of measuring is reduced. Daily inspections and periodic inspections are conducted mainly visually. When an abnormality is observed, there is a concern that the cut slope may be destabilized due to the change in the anchor tension. The residual tensile load of anchor is usually confirmed by the lift-off tests, which typically require time and cost. In order to overcome this shortcoming of the lift-off test, recently, more advanced hydraulic jacks exclusively for the purpose of lift-off tests have been developed [3]. The functions of the test equipment have been improved dramatically [4]. Even if the function of one anchor deteriorates, it does not always lead to instability of the entire slope. Therefore, it is important to evaluate the health of the overall slope by monitoring the residual tension of a large number of anchors. Therefore, much more convenient as well as less expensive monitoring technique has been long awaited.

In this research, a non-destructive evaluation for residual tension load of ground anchors was developed. In the developing process, the tendon tension part of a ground anchor is assumed to be a "string". Therefore, the frequency of its free vibration can be determined by line density and tension length of the PC steel and the operating tension. A series of field experiments were conducted by using a proposed measuring equipment. The observed tendon tension values were compared with those measured by lift-off test.

2 Physical Phenomenon Focused

We assumed that the tendon tension part of a ground anchor is approximated by a "string" fixed at both ends. As the tendon tension part is thin and long, the assumption of "string" is considered to be appropriate. Based on this assumption, the frequency of the free vibration of "string" in Fig. 1 can be determined by line density, μ (density per unit length), tension length of the PC steel, L and the operating tension, T by Eq. (1).

$$f = \frac{1}{2L}\sqrt{\frac{T}{\mu}} \tag{1}$$

The residual tension can be determined by Eq. (2). However, the free vibration of tendon tension part cannot be directly excited because it is in the ground.

$$T = 4L^2 f^2 \mu \tag{2}$$

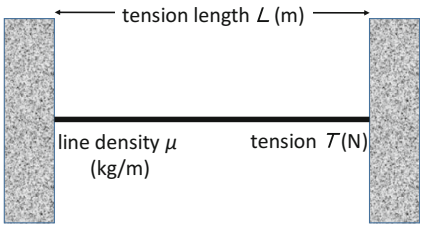

Fig. 1. "string" model fixed at both ends.

3 Field Test and Discussion

Anchors studied in this paper are the wedge-fixed type VSL ones which were most frequently built on expressway in Japan [5]. Those anchors have four PC steel bars, 3.096 kg/m of line density and 4.0 m of tendon tension part. The designed tension load was 341.9 kN for four anchors measured in this study. The residual tensile load for four anchors are 255 kN, 309 kN, 392 kN and 517 kN, respectively. Based on these residual load, the resonance frequencies of the tendon tension part were estimated between 36 to 51 Hz.

Firstly, we tried to generate the free vibration of the tendon tension part by hitting the anchor head with a hammer. However, the free vibration was not excited. Therefore, we added the vibration perpendicular to the extra length of the anchor head by attaching the small vibrator as shown in Fig. 2. A swept-frequency sinusoidal vibration from 10 to 200 Hz was applied to the extra length. Figure 3 shows the applied time history of swept-frequency vibration for 50 s with 60 s of measuring time. The vibration waveform was measured at the same position with a small accelerometer as also shown in Fig. 2. The acceleration was measured at 1 ms intervals and recorded through 16 bit A/D convertor.

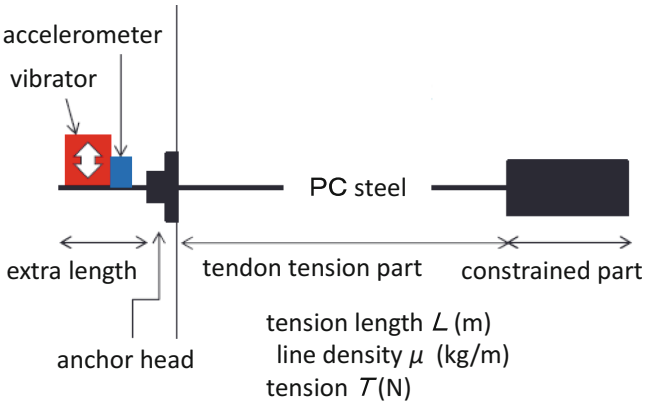

Fig. 2. Vibrator and accelerometer at extra length of anchor head.

When the applied frequency coincides with the resonance frequency of the tendon tension part, the response amplitude is expected to become large. We performed the running spectral analysis of the measured acceleration time history. Figure 4 shows an example of the analyzed result. The left figure in Fig. 4 shows the running spectrum. The luminance in the figure indicates the intensity of spectrum amplitude for each 0.512 s. In the right figure in Fig. 4, the Fourier spectrum for each time step is described. From this analysis, we can easily understand that there are two peaks of the spectrum amplitude at 37 Hz and 80 Hz. The former corresponds to the resonance frequency of the tendon tension part. On the other hand, the latter corresponds to the resonance frequency of the extra length of the anchor head.

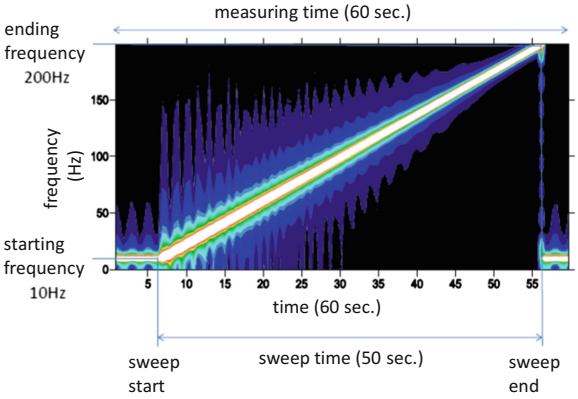

Fig. 3. Swept signal applied to vibrator.

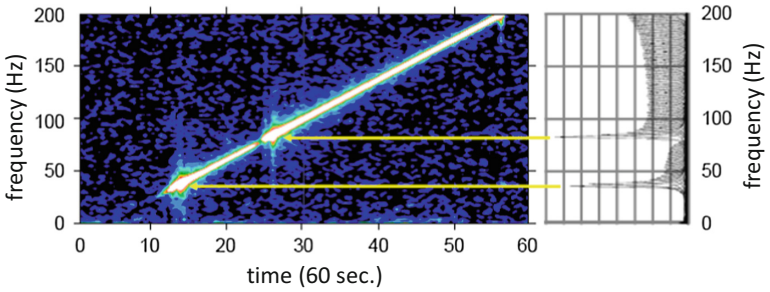

Fig. 4. Detection of resonance frequency by running spectral analysis.

The resonance frequency of the tendon tension part is easily estimated based on the residual tensile load. The relationship between observed resonance frequencies of four extra lengths of four anchor heads and the residual tensile loads of four anchors measured by lift-off tests are shown in Fig. 5. In this figure, the mean value of four resonance frequencies of four extra lengths and the theoretical resonance frequency calculated by the residual tensile load (see Eq. (1)) are also shown. The correlation between the resonance frequency and the residual tensile load is very clear. However, the divergence between the resonance frequency and the residual tensile load becomes larger as the residual load increases.

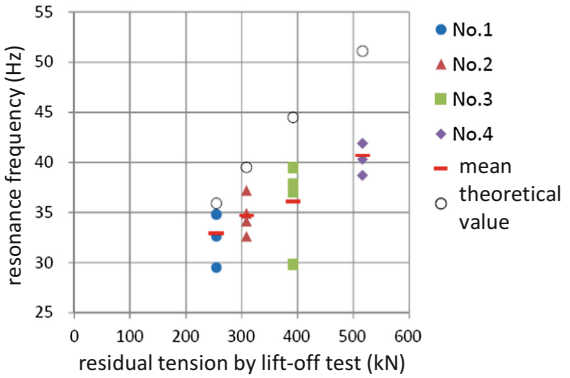

Fig. 5. Comparison between observed resonance frequency and the residual tensile load.

The comparison between the residual tensile load calculated by Eq. (2) and the measured residual tensile load by the lift-off test is summarized in Fig. 6. As each anchor has four extra length at the anchor head, the residual tensile load is calculated for each extra length. Therefore, the horizontal axis of the lift-off result is described as one fourth of the real residual load. As the lengths of tendon tension part of four anchors are same as 4.0 m, the tendency shown in Fig. 6 is just same as that in Fig. 5. There is a clear correlation between estimated residual loads in this study and observed ones by lift-off tests. However, the divergence between the estimated residual load and the observed load becomes larger as the observed residual load increases. This tendency is also same as the finding in Fig. 5. The cause of this deviation is under consideration. There is a possibility that the assumption of "string" for 4 m long tendon tension part is not correct. There needs to be a lot of experiment and field measurements further.

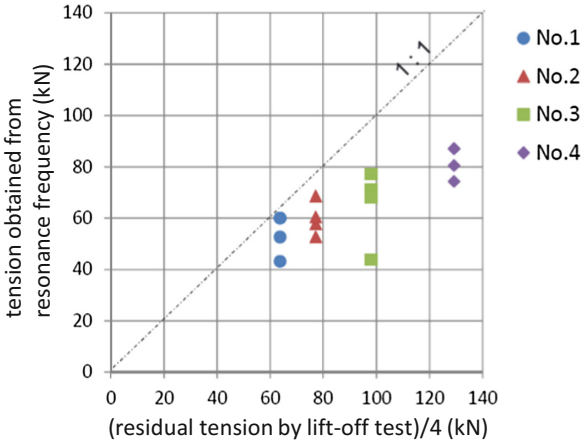

Fig. 6. Comparison between estimated residual load by Eq. (2) and measured one by lift-off test.

4 Concluding Remarks

We have proposed a new method of non-destructive evaluation for residual tension load of the ground anchor based on the assumption of "string" of tendon tension part. It is summarized as follows the features of the proposed technique.

(1) measuring point: extra length of anchor head
(2) measurement principle: change in vibration frequency of tendon tension part
(3) frequency band of interest: from some Hz to tens of Hz.

Based on the proposed technique, it is easily possible to indicate the magnitude of the residual tensile load of the ground anchor. At least, the comparison of the residual load of large and small is possible.

In this study, we only carried out the field test for the wedge-fixed type VSL anchors. The wedge-nut-fixed type KTB anchors and the nut-fixed type SEEE anchors have been also widely used in Japan. We have to carry out field tests for other type anchors as well as old type anchors to investigate the applicability of our proposed method to those anchors. We also plan model tests for three different type anchors to confirm the assumption of "string" of tendon tension part. We look forward to introducing further results in the near future.

References

1. Okubo, K., et al.: On the ground anchor in Expressway. Jpn. Road Assoc. Misc. **27**, 15 (2007)
2. Japanese Society of Soil Mechanics and Foundation Engineering: Ground anchor design and construction standards, the commentary, pp. 13–15 (1988)
3. Sakai, T., et al.: The development of compact and lightweight maintenance jack and the investigation as the plane of ground anchor tension. Found. Work **38**(9), 79–82 (2010)
4. Sakai, T., et al.: The evaluation of investigation of ground anchor slope as the plane by using SAAM jack. In: Proceedings of 65th Annual Scientific Society of Civil Engineers Conference, pp. 123–124 (2010)
5. Fujiwara, Y., Sakai, T.: A study of a lift-off test method for ground anchors. J. JSCE **4**, 106–117 (2016)

Multi-hazard Risk Assessment

Limin Zhang(✉)

Hong Kong University of Science and Technology, Kowloon, Hong Kong
cezhangl@ust.hk

Abstract. This paper presents a brief summary of multi-hazard risk assessment, focusing on cascading landslide hazards. It starts by presenting the multi-hazard processes an engineering system may face, and possible interactions among the separate hazards and between the vulnerabilities of elements at risk to these hazards. Then a framework for analyzing the flooding, landslide and debris flow processes in a rainstorm is introduced. Multi-hazard risk assessment requires more comprehensive physical analyses than what are needed in conventional geotechnical design. Stability analysis, flow analysis and impact analysis are all required. The outcomes of such physical analyses form the basis for evaluating the risks associated with these multi-hazardous processes. The multi-risk analysis can be performed using a HKUST five-step procedure, which describes the hazardous processes in an explicit probabilistic framework and identifies key parameters that govern the success of a risk mitigation effort. Rational engineering decisions and emergency management policies can be made based on such physically-based risk analysis.

Keywords: Multi-hazard risk assessment · Landslide · Risk management

1 Multi-hazard Processes and Hazard Interactions

1.1 Multi-hazard Processes

A large engineering system may be exposed to several hazards. Two types of multi-hazard processes prevail: those with separate causes such as earthquakes, floods, and volcanic eruptions; and those from interrelated causes such as floods, landslides and debris flows. The former hazards are often analyzed separately while the latter hazards can be treated as a hazard chain that lasts a certain period.

Figure 1 shows an evolving multi-hazard chain in the epicentral area of the Wenchuan earthquake (Zhang et al. 2014b, 2016; Zhang and Zhang 2017a). The strong earthquake in May 2008 caused numerous landslides and the landslide debris was retained on the steep terrain. Such deposits were at a quasi-stable state at normal weather conditions but might reactivate during rainstorms, turning into catastrophic landslides and debris flows. The landslide or debris flow materials sometimes blocked the river, forming landslide dams and posing flood risks that affected greater areas both upstream and downstream the dam. The sediment or soil that entered the river system also caused a significant rise in the riverbed, aggravating the flood risk.

W. Wu (Ed.): *Desiderata Geotechnica*, SSGG, pp. 227–236, 2019.
https://doi.org/10.1007/978-3-030-14987-1_27

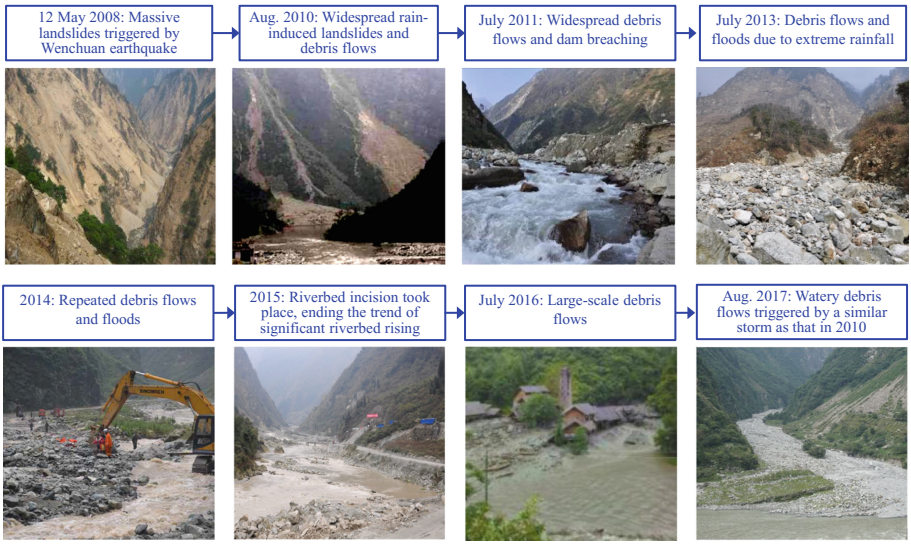

Fig. 1. An evolving multi-hazard chain in the epicentral area of the Wenchuan earthquake.

1.2 Interaction Effects in Dealing with Landslide Hazards

Landslide hazards, which include various slides, falls and flows, can interact in many ways:

1. Domino effects or cascading landslides, in which an initiating event causes a chain of disaster events, the outcome of one event being the cause of other events. Figure 1 shows a chain of landslide hazards.
2. Overlapping of several hazards of the same type or different types. The impact areas and volumes of several slides or rock falls will be larger, affecting both the destructive power of the hazards and the vulnerability to the hazards. During a severe storm, a particular area may be concurrently impacted by flooding, rain-induced landslides and debris flows.
3. Merging of numerous smaller debris flows of various origins into a larger debris flow (Gao et al. 2018).
4. When an element at risk is subject to multiple hazards concurrently or consecutively, the vulnerability to these hazards will be higher than that to an individual hazard. After the occurrence of one hazard, the ability of the element at risk to resist the subsequent hazards will decline gradually. Figure 2 shows two buildings that were damaged during the Wenchuan earthquake. The buildings were later impacted by repeated debris flows, with debris material inundating two floors of the rear building and breaking the wall into the first floor of the building. The integrity and functionality of the buildings deteriorated further after the earthquake.

Fig. 2. Declining resistance of two buildings after subject to a strong earthquake and several debris flows.

2 Approaches to Multi-hazard Risk Assessment

2.1 Multi-risk Assessment

Engineers need to answer the following questions in managing multi-hazard risks:

(1) What might happen?
(2) How likely is it?
(3) What is the damage or injury if it happens?
(4) What can be done about it?

A simple expression for defining 'landslide risk' follows

$$R = P(L) \times P(T{:}L) \times P(S{:}T) \times V(D{:}T) \times E \quad (1)$$

where E = number of persons at risk (PAR), or economic worth; P(L) = annual probability of the landslide; P(T:L) = probability of the landslide reaching the highway; P(S:T) = probability of PAR present at locations impacted by the landslide; V(D:T) = vulnerability of the PAR to the landslide event.

Equation (1) clearly indicates the need for more comprehensive physical analyses than what is needed in conventional geotechnical design. In addition to stability analysis for hazard identification, flow analysis is needed to simulate the movements of the landslide debris, and impact analysis is required to evaluate the damage to the facilities concerned due to landslide impact.

Recently Zhang (2014), Chen et al. (2016) and Zhang and Zhang (2017b) proposed a framework of multi-hazard risk assessment for evaluating the risks posed by cascading landslide hazards considering the interactions among the hazards and the possible cascading effects on human vulnerability. Attention is paid to the quantification of the amplification and overlapping effects due to the interactions among two or more hazards. The framework consists of five phases, including definitions, multi-hazard assessment, exposure assessment, multi-vulnerability assessment, and multi-risk assessment:

(1) Definition of the time and space scales for hazard analysis, the risk sources, and the initiating events.
(2) Multi-hazard assessment, which includes identifying the hazard scenarios and links among these scenarios, and quantifying their occurrence probabilities.
(3) Assessment of interactions among the elements at risk considering the overlapping or amplification effects.
(4) Multi-vulnerability assessment, which quantifies the vulnerability of the elements at risk in each affected area to one or multiple hazards.
(5) Multi-risk assessment, in which the risk of the cascading hazards is expressed as the sum of all risks posed by these hazards, as well as new hazards derived from the hazard interactions, in a pre-defined area.

Cascading hazards may occur in sequence in time, and interact with each other in space. Hence one should consider the lifecycle of these hazards in defining the time and space scales for risk assessment. Starting from an initiating hazard, one should investigate each individual hazard over its entire lifecycle from the formation of the hazard to the cessation of further evolution, for instance from the formation of a landslide dam to the breaching of the dam, from the formation of a loose soil deposit to the cessation of reactivation and erosion in the deposit, and from sedimentation to the incision of a stream. Some of the cascading hazards can be considered as one "event" that stretches over a certain period (Zhang et al. 2014a).

2.2 Characterizing Multi-hazard Processes

Intense rainfall in mountainous regions can trigger debris flows from loose soil deposits on hill slopes or in channels. A conceptual model for rain-induced landslides, debris flows and likely initiation mechanisms are shown in Fig. 3. Debris flows can be initiated by three mechanisms: transformation from landslides, surface erosion and dam breaching. Due to rainfall infiltration, the hill slope gradually becomes saturated, and the soil loses its strength, causing shallow seated slope failures (Zhang et al. 2011). During a rainstorm, slope failures can occur at different times in space within a catchment. Some of the detached material may move into channels and form landslide dams, and some may transform into debris flows directly. As the surface runoff accumulates, the landslide dam formed earlier in the channel may break, initiating a channelized debris flow (e.g. Chen and Zhang 2015; Shen et al. 2017). At the same time, the surface runoff may cause bed erosion and initiate hillslope debris flows. Some of the separate debris flows may merge in the main channel of the drainage basin, forming a larger catastrophic debris flow event (Zhang et al. 2014a, b, c). The final magnitude of a debris flow could be many times of its initial volume due to entrainment of materials along the path from additional slope failures, bed erosion or bank collapses (Chen and Zhang 2015; Shen et al. 2017). If reaching a flat residential area downstream the basin, the developed debris flow can cause severe loss of lives and properties.

Based on the conceptual model in Fig. 3, an integrated model for simulating the multi-hazard processes including two debris-flow initiation mechanisms (i.e. bed erosion and transformation from landslides) is shown in Fig. 4. The integrated model consists of a digital terrain module, a rainfall module, an infiltration module, an

overland flow module, a slope stability module, a surface erosion module, a debris flow dynamics module and a deposition module. Extensive field tests have been performed to determine the erodibility of bare soil and vegetated soil (Chang et al. 2014; Zhu and Zhang 2016). The model was applied to simulate the multi-hazard processes in Xiaojiagou Gully during the 13 August storm. The storm triggered widespread slope failures and debris flows in the study area. The simulated instability scars, erosion scars and debris flow channels agree very well with those revealed on remote sensing images (Fig. 5).

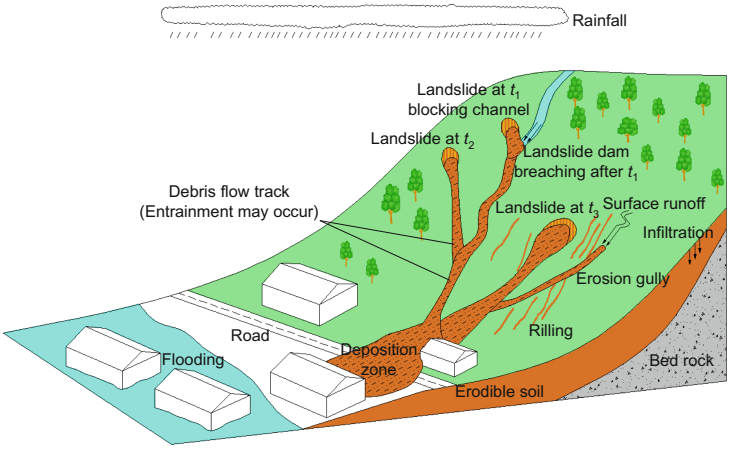

Fig. 3. Conceptual model for the initiation of flooding, surface erosion, landslides and debris flows in a rainstorm event.

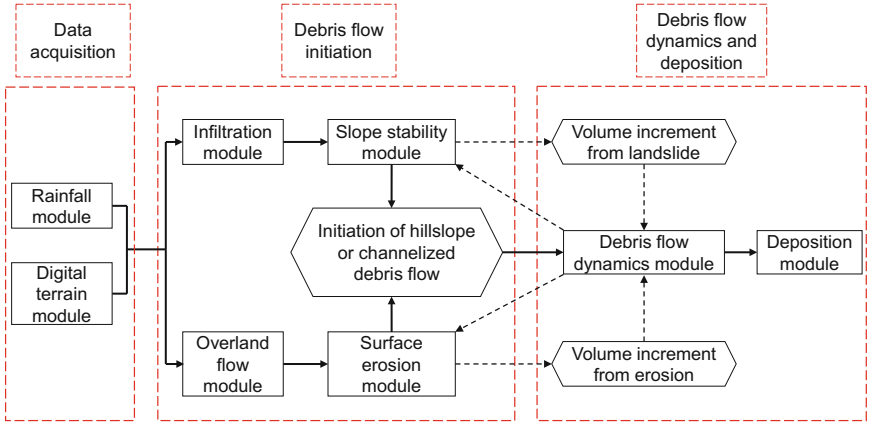

Fig. 4. Framework of integrated simulation of debris flows.

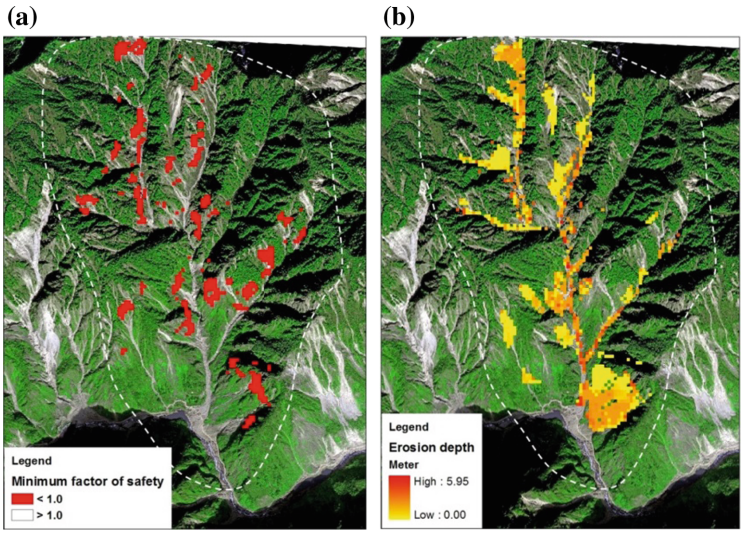

Fig. 5. Simulation results of the Xiaojiagou debris flow: (a) final shape and depth of the erosion zone; (b) maximum flow velocity.

A simpler version of the integrated model can be applied to serve different purposes (Chen and Zhang 2014; Chen et al. 2015). For instance, the infiltration module and the slope stability module can be combined to form a distributed cell model for simulating regional shallow landslides and their movements on a three-dimensional digital terrain. The locations and volumes of landslides are analyzed first through rainfall infiltration and slope stability analyses. The detached material is assumed to move along the steepest path from one cell to a lower cell. Empirical equations that are developed based on local landslide inventories are adopted as a landslide movement cessation criterion. The movement analysis method is applied to a 165 km^2 hilly terrain (Fig. 6) in the Wenchuan earthquake zone to test its performance in presenting regional shallow landslide movement. The method predicts the volume of landslides reasonably well.

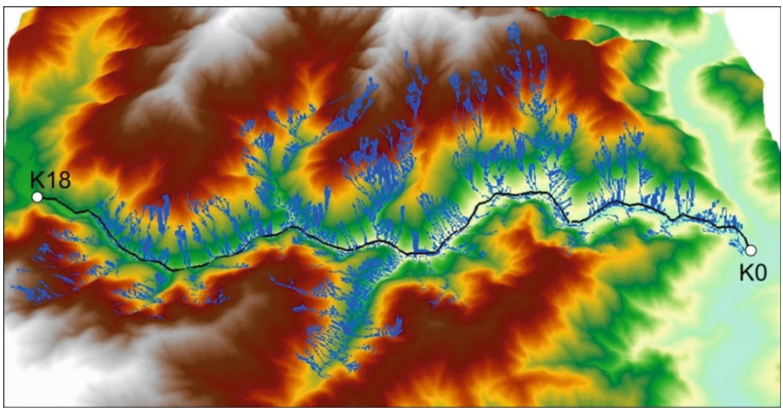

Fig. 6. Movement traces of the detached materials at the end of the storm.

2.3 Multi-vulnerability Assessment

Vulnerability to landslides covers a broad spectrum of issues including physical vulnerability (i.e. buildings and bridges), environment, human life, and socio-economic aspects (Bell and Glade 2012). Vulnerability to a landslide is defined as the level of potential damage, or degree of loss of a given element subjected to the landslide of a given intensity. Various approaches to estimating the human vulnerability have been discussed qualitatively and quantitatively (e.g., Bell and Glade 2012; Lacasse and Nadim 2011; Lacasse et al. 2012).

Vulnerability can be formulated as a reliability problem. Figure 7 shows an example dealing with the chance of people escaping from being impacted by a landslide or a flood wave. In the general framework, the available time, T_L, and the demand time, T_F, are assumed to be two independent random variables, whose schematic probability distributions can be determined. The flight is considered as successful if the evacuees arrive at safe places before the landslide debris or flood front reaches them, i.e. $T_L \geq T_F$, and unsuccessful when $T_L < T_F$.

Similarly, the physical vulnerability, namely degree of damage of the physical facility (building and bridges etc.) can be evaluated by establishing the probability distributions of the load Q and resistance R for the facility and evaluating the failure probability of the facility when exposed to one or multiple hazards. The failure probability values at different load levels then form a fragility curve.

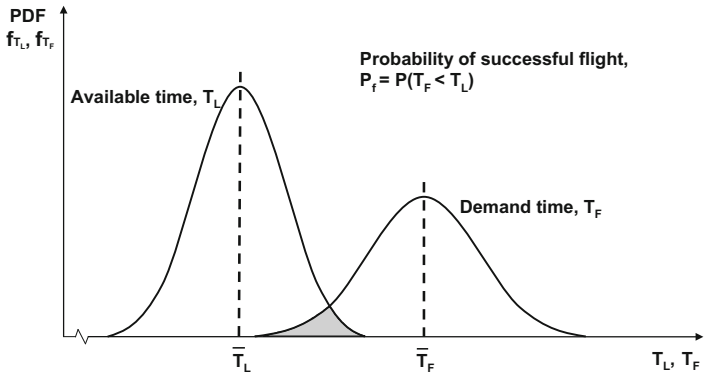

Fig. 7. Probability of successful flight from a landslide (Zhang and Zhang 2014).

3 Risk-Based Engineering Decision

The conventional factor of safety approach addresses the issue of component safety but not system safety and risk. The use of unsystematic engineering measures may result in a false sense of safety, and "unexpected" engineering failures when exposed to high intensity hazardous events. Examples are the failure of the New Orleans hurricane protection system during Hurricane Katrina in August 2005 and the severe damage of several major highway reconstruction projects in the Wenchuan earthquake zone.

Risk-based engineering decision, on the other hand, leads to greatly reduced landslide risk in Hong Kong, less than 25% of that in 1977 (Ho et al. 2016). This was achieved by identifying sources of risk, minimizing risks arising from new developments, reducing risks by improving the stability of existing slopes, and reducing risks by minimizing the possible consequences of landslides.

The risk-based approach has also fundamentally changed the highway design and construction practice in seismic hilly terrain in western China. Ten years after the Wenchuan earthquake, landslide risk management has become top priority in selecting highway alignments and elevations, aiming at bypassing major landslide-prone areas using long tunnels, minimizing river crossing and adopting sufficiently high road elevations to allow for long-term evolution of hazard chains (Zhang et al. 2012).

4 Risk-Based Decision and Emergency Management

Risk analysis is the science behind risk-based decisions for disaster preparedness and emergency management. By formulating an evacuation model based on rigorous reliability theory (Fig. 8), the role of local administration, political aspects and population training can be reflected in determining the probability distributions of the times required to respond to an idealized landslide, make evacuation decisions, and move to safe places. For instance, the response time, delay time and movement time are influenced by preparedness and evacuation training. Sensitivity of human vulnerability to the key influence factors can be analyzed by varying one factor a time while keeping other factors constant in the model in Fig. 7, or in a Bayesian network. The key influence factors, particularly those related to local administration, political aspects and population training can be ranked according to their sensitivities. Figure 8 ranks the key factors that affect successful flight of people from a landslide. Network analysis for factors that influence the emergency management of flood risks has been presented by Peng et al. (2012a, b; 2013a, b).

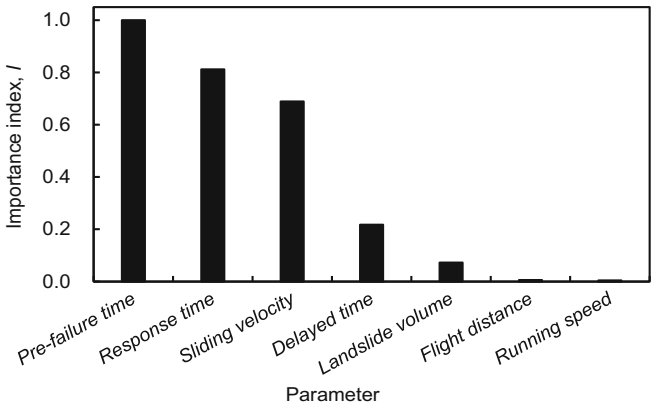

Fig. 8. Sensitivity analysis of human flight from a landslide.

5 Summary

An engineering system may face a chain of hazards which occur concurrently or consecutively. These hazards evolve over time and have a lifecycle. How to assess their initiation, propagation and societal impacts is a very challenging issue that goes beyond conventional engineering design. We developed a HKUST five-step procedure for multi-hazard risk assessment, focusing on landslide risks. Attention has been made to include the interactions between hazards and between vulnerabilities to the hazards. The procedure has been successfully applied to assist engineering design decision making and emergency management. Much more effort is needed to advance multi-hazard analysis and instill risk governance in engineering planning, design, construction and operation.

Acknowledgments. I would like to thank Prof. Gerd Gudehus on the special occasion of his 80th birthday, for hosting me as a senior visiting scholar in 1995 at Institute for Soil and Rock Mechanics of Karlsruhe University, and for his insight in teaching and research in soil mechanics and geotechnical engineering. The research reported in this paper was supported by the Research Grants Council of the Hong Kong SAR Government (Projects No. C6012-15G, T22-603/15N and 16206217).

References

Bell, R., Glade, T.: Multi-hazard analysis in natural risk assessments. In: Mambretti, S. (ed.) Landslides, pp. 1–11. WIT Press (2012)

Chang, D.S., Zhang, L.M., Xu, Y., Huang, R.Q.: Field testing of erodibility of two landslide dams triggered by the 12 May Wenchuan earthquake. Landslides **8**(3), 321–332 (2014)

Chen, H.X., Zhang, L.M.: A physically-based distributed cell model for predicting regional rainfall-induced slope failures. Eng. Geol. **176**, 79–92 (2014)

Chen, H.X., Zhang, L.M.: EDDA 1.0: integrated simulation of debris flow erosion, deposition and property changes. Geosci. Model Dev. **8**, 829–844 (2015)

Chen, H.X., Zhang, L.M., Gao, L., Zhu, H., Zhang, S.: Presenting regional shallow landslide movement on three-dimensional digital terrain. Eng. Geol. **195**, 122–134 (2015)

Chen, H.X., Zhang, S., Peng, M., Zhang, L.M.: A physically-based multi-hazard risk assessment platform for regional rainfall-induced slope failures and debris flows. Eng. Geol. **203**, 15–29 (2016)

Gao, L., Zhang, L.M., Cheung, R.W.M.: Relationships between natural terrain landslide magnitudes and triggering rainfall based on a large landslide inventory in Hong Kong. Landslides **15**, 727–740 (2018)

Ho, K.S.S., Cheung, R.W.M., Wong, Y.S.: Managing landslide risk systematically using engineering works. Proc. Inst. Civ. Eng.-Civ. Eng. **169**(6), 25–34 (2016)

Lacasse, S., Nadim, F.: Learning to live with geohazards: from research to practice. In: ASCE Geotechnical Conference Georisk-2011, GSP No. 224, pp. 64–116. ASCE, Reston (2011)

Lacasse, S., Nadim, F., Hoeg, K.: Risk assessment and mitigation in geo-practice. In: Keynote Lecture, GeoCongress 2012, GSP No. 226, pp. 729–764. ASCE, Reston (2012)

Peng, M., Zhang, L.M.: Analysis of human risks due to dam break floods - part 1: a new model based on Bayesian networks. Nat. Hazards **64**(1), 903–933 (2012a)

Peng, M., Zhang, L.M.: Analysis of human risks due to dam break floods - part 2: application to Tangjiashan landslide dam failure. Nat. Hazards **64**(2), 1899–1923 (2012b)

Peng, M., Zhang, L.M.: Dynamic decision making for dam-break emergency management - part 1: theoretical framework. Nat. Hazards Earth Syst. Sci. **13**, 425–437 (2013a)

Peng, M., Zhang, L.M.: Dynamic decision making for dam-break emergency management - part 2: application to Tangjiashan landslide dam failure. Nat. Hazards Earth Syst. Sci. **13**, 439–454 (2013b)

Shen, P., Zhang, L.M., Chen, H.X., Fan, R.L.: EDDA 2.0: integrated simulation of debris flow initiation and dynamics, considering two initiation mechanisms. Geosci. Model Dev. Discuss. (2017). https://doi.org/10.5194/gmd-2017-204

Zhang, L.L., Zhang, J., Zhang, L.M., Tang, W.H.: Stability analysis of rainfall-induced slope failures: a review. Proc. Inst. Civ. Eng. Geotech. Eng. **164**(5), 299–316 (2011)

Zhang, L.M., Zhang, S.: Approaches to multi-hazard landslide risk assessment. In: Proceedings of ASCE GeoRisk 2017, GSP No. 286, pp. 312–323. ASCE, Reston (2017b)

Zhang, L.M., Zhang, S., Huang, R.Q.: Multi-hazard scenarios and consequences in Beichuan, China: the first five years after the 2008 Wenchuan earthquake. Eng. Geol. **180**, 4–20 (2014a)

Zhang, S.: Assessment of human risks posed by cascading landslides in the Wenchuan earthquake area. Ph.D. thesis, The Hong Kong University of Science and Technology, Hong Kong (2014)

Zhang, S., Zhang, L.M.: Human vulnerability to quick shallow landslides along road: fleeing process and modelling. Landslides **11**(6), 1115–1129 (2014)

Zhang, S., Zhang, L.M.: Impact of the 2008 Wenchuan earthquake in China on subsequent long-term debris flow activities in the epicentral area. Geomorphology **276**(1), 86–103 (2017a)

Zhang, S., Zhang, L.M., Peng, M., Zhang, L.L., Zhao, H.F., Chen, H.X.: Assessment of risks of loose landslide deposits formed by the 2008 Wenchuan earthquake. Nat. Hazards Earth Syst. Sci. **12**, 1381–1392 (2012)

Zhang, S., Zhang, L.M., Glade, T.: Characteristics of earthquake- and rain-induced landslides near the epicentre of Wenchuan Earthquake. Eng. Geol. **175**, 58–73 (2014b)

Zhang, S., Zhang, L.M., Chen, H.X.: Relationships among three repeated large-scale debris flows at the Pubugou Ravine in the Wenchuan earthquake zone. Can. Geotech. J. **51**(9), 951–965 (2014c)

Zhang, S., Zhang, L.M., Nadim, F., Lacasse, S.: Evolution of mass movement near epicentre of Wenchuan earthquake, the first eight years. Sci. Rep. **6**, 36154 (2016)

Zhu, H., Zhang, L.M.: Field investigation of erosion resistance of common grass species for soil-bioengineering in Hong Kong. Acta Geotech. **11**(5), 1047–1059 (2016)

Deformation and Strength of Transversely Isotropic Rocks

Yang Zhao and Ronaldo I. Borja(✉)

Stanford University, Stanford, CA 94305, USA
{yangz16,borja}@stanford.edu

Abstract. Transverse isotropy is characterized by a plane of isotropy and an axis of anisotropy. For rocks, the plane of isotropy is associated with the bedding plane, whereas the axis of anisotropy is the normal to the bedding plane. Transversely isotropic rocks are known to exhibit strength that depend on the orientation of the bedding plane relative to the direction of load. In this work, we present a constitutive framework for predicting the deformation and strength of transversely isotropic rocks. The model is based on anisotropic critical state plasticity with thermal softening. We conduct numerical simulations of boundary value problems to demonstrate the impact of bedding plane orientation on the deformation and strength of a transversely isotropic rock.

1 Introduction

In a recent publication [13], a thermoplastic constitutive model for rocks with distinct bedding planes based on anisotropic critical state plasticity has been presented. The model consists of anisotropic elasticity characterized by five independent constants, anisotropic plasticity characterized by a yield surface in the form of a rotated ellipsoid of modified Cam-Clay theory [5], and a softening response that depends on temperature [10]. Anisotropy results from the existence of bedding planes defining a rock's microstructure [4,6,12,16,17], such as those encountered in shale [3,11] and synthetic transversely isotropic rocks [14,15]. The model presented in [13] has been used to predict the onset of deformation band through stress-point calculations [7–9]. The objective of the present paper is to demonstrate the important features of this aforementioned constitutive model beyond the stress-point calculations. To this end, we implement the constitutive model into a nonlinear finite element code and solve boundary-value problems to demonstrate the impact of bedding plane orientation on the deformation and strength of transversely isotropic rocks.

2 Computational Framework

A nonlinear finite element framework with Newton iteration is developed in this study. The constitutive model is presented by Semnani et al. [13] and provides

W. Wu (Ed.): *Desiderata Geotechnica*, SSGG, pp. 237–241, 2019.
https://doi.org/10.1007/978-3-030-14987-1_28

a robust description of the impact of bedding plane orientation on the material response. Plastic anisotropy is represented by a rotated ellipsoidal yield surface of modified Cam-Clay theory [5]. The model is developed in such a way that the rotation of the ellipsoid is consistent with the orientation of the bedding plane. The model is further enhanced to include thermal softening using the Laloui and Cekerevac softening law [10]. Stress-point integration is based on a fully implicit return mapping scheme.

3 Numerical Simulations

We conduct plane strain nonlinear finite element simulations to investigate the deformation and bearing capacity of a layer of transversely isotropic rock subjected to strip loading σ_L. A schematic diagram of the problem is shown in Fig. 1. The rock layer is 20 m wide and 10 m thick, with a surcharge pressure σ_E acting on top of it. The strip load σ_L spans 2 m wide and is located in the middle of the rock layer.

Assuming 1 as the axis of anisotropy and 23 as the plane of transverse isotropy, the five elastic constants are: $E_1 = 12860$ MPa, $E_2 = 21900$ MPa, $\nu_{12} = 0.15$, $\nu_{23} = 0.17$, and $G_{12} = 6510$ MPa, while the plasticity parameters are: $M = 1.07$, $\lambda^p = 0.0026$, $\alpha = 0.94$, $\beta = 0.7$, $\gamma = 1.0$, and $p_{c0} = 40$ MPa (the reader is referred to [13] for a more detailed description of these parameters). These values have been calibrated for Tournemire shale [11,13]. Assuming the rock is normally consolidated, we set $\boldsymbol{\sigma}_E$ equal to p_{c0}. Gravity has been taken into account in the simulations, with the density of rock assumed to be 2600 kg/m^3. The intensity of the strip load $\boldsymbol{\sigma}_L$ is set equal to 400 MPa. Results for two different bedding plane orientations, $\theta = 0°$ (horizontal bedding plane) and $\theta = 30°$ (inclined bedding plane) are illustrated in the following.

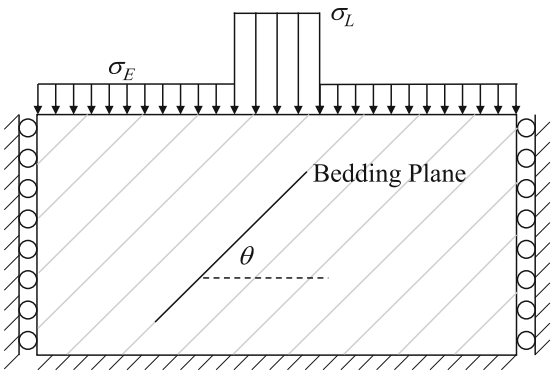

Fig. 1. Schematic diagram of the simulated problem. Anisotropic rock layer is 20 m wide by 10 m thick.

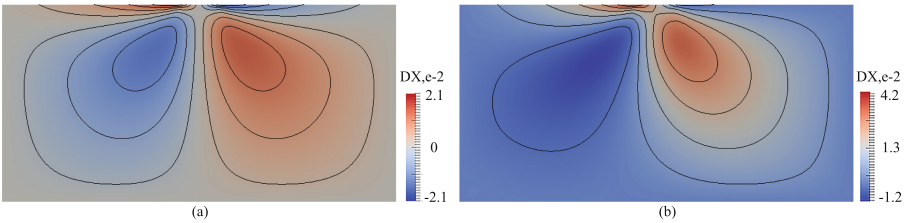

Fig. 2. Contours of horizontal displacement for: (a) $\theta = 0°$; (b) $\theta = 30°$. Color bars in meters.

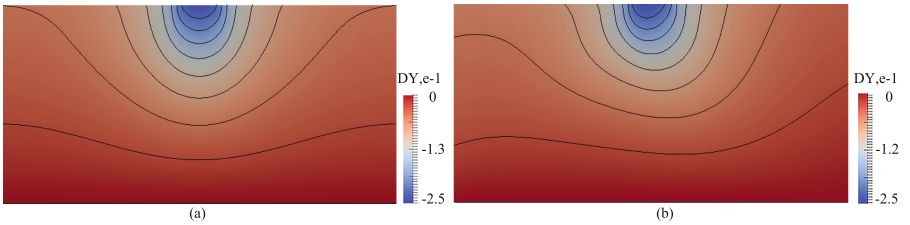

Fig. 3. Contours of vertical displacement for: (a) $\theta = 0°$; (b) $\theta = 30°$. Color bars in meters.

When the bedding plane is horizontal, the axis of anisotropy is parallel to the central vertical axis, which guarantees that the displacement field is also symmetric with respect to the central vertical axis, as revealed in Figs. 2(a) and 3(a). However, when the bedding plane is inclined, the displacement field is no longer symmetric, as indicated in Figs. 2(b) and 3(b). The lack of symmetry in the displacement field could cause serious problem to engineering practice: Foundations built on a rock layer with inclined bedding plane could experience uneven settlement and tilting of the building above it. Although horizontal bedding planes are more commonly encountered due to the nature of sediment deposition, inclined bedding planes are also common due to complex geology resulting from tectonic deformation.

A similar comparison may be made of the resulting plastic strain field. When the bedding plane is horizontal, the plastic deformation tends to localize equally from the two edges of the strip loading and evolve downward in a symmetric fashion, as indicated in Fig. 4(a). But when the bedding plane is inclined, the plastic deformation prefers to localize along the path that crosses the bedding plane, as shown in Fig. 4(b). Such preference agrees with the bifurcation analysis conducted by Semnani et al. [13], and validated by the laboratory results of Niandou et al. [11] and Tien et al. [15], which suggest that the cross bedding plane direction is generally weaker for transversely isotropic rocks.

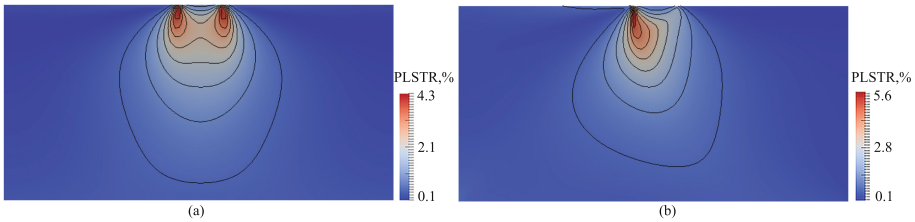

Fig. 4. Contours of plastic strain $\|\boldsymbol{\varepsilon}^p\|$ for: (a) $\theta = 0°$; (b) $\theta = 30°$.

4 Closure

Deformation and strength of a transversely isotropic rock are functions not only of the bed-normal and bed-parallel deformation and strength properties, but also of the orientation of the bedding plane with respect to the direction of load. An inclined bedding plane relative to the direction of load could result in strength that is even lower than either the strength in the bed-normal or bed-parallel directions [18]. In this work, we have shown how bedding plane orientation can impact the solution of a boundary-value problem. Even if the loading is symmetric and the geometry of the problem is equally symmetric, the deformation could be unsymmetric due to anisotropy in the mechanical properties. It is thus natural to expect that fracture and damage propagation can also be influenced by the anisotropy of a rock [1,2], although we have not covered these topics in the present work due to space limitation.

Acknowledgments. This material is based upon work supported by the U.S. Department of Energy, Office of Science, Office of Basic Energy Sciences, Geosciences Research Program, under Award Number DE-FG02-03ER15454. Support for materials and additional student hours were provided by the National Science Foundation under Award Number CMMI-1462231.

References

1. Bennett, K.C., Borja, R.I.: Hyper-elastoplastic/damage modeling of rock with application to porous limestone. Int. J. Solids Struct. **143**, 218–231 (2018). https://doi.org/10.1016/j.ijsolstr.2018.03.011
2. Bennett, K.C., Regueiro, R.A., Borja, R.I.: Finite strain elastoplasticity considering the Eshelby stress for materials undergoing plastic volume change. Int. J. Plast. **77**, 214–245 (2016)
3. Bennett, K.C., Berla, L.A., Nix, W.D., Borja, R.I.: Instrumented nanoindentation and 3D mechanistic modeling of a shale at multiple scales. Acta Geotech. **10**, 1–14 (2015)
4. Borja, R.I., Rahmani, H.: Computational aspects of elasto-plastic deformation in polycrystalline solids soils. J. Appl. Mech. **79**(3), 031024 (2012)
5. Borja, R.I.: Plasticity Modeling & Computation. Springer, Heidelberg (2013)
6. Borja, R.I., Rahmani, H.: Discrete micromechanics of elastoplastic crystals in the finite deformation range. Comput. Methods Appl. Mech. Eng. **275**, 234–263 (2014)

7. Borja, R.I., Aydin, A.: Computational modeling of deformation bands in granular media, I: geological and mathematical framework. Comput. Methods Appl. Mech. Eng. **193**(27–29), 2667–2698 (2004)
8. Borja, R.I.: Computational modeling of deformation bands in granular media, II: numerical simulations. Comput. Methods Appl. Mech. Eng. **193**(27–29), 2699–2718 (2004)
9. Borja, R.I.: Bifurcation of elastoplastic solids to shear band mode at finite strain. Comput. Methods Appl. Mech. Eng. **191**(146), 5287–5314 (2002)
10. Laloui, L., Cekerevac, C.: Thermo-plasticity of clays: an isotropic yield mechanism. Comput. Geotech. **30**(8), 649–660 (2003)
11. Niandou, H., Shao, J.F., Henry, J.P., Fourmaintraux, D.: Laboratory investigation of the mechanical behaviour of Tournemire shale. Int. J. Rock Mech. Min. Sci. **34**(1), 3–16 (1997)
12. Semnani, S.J., Borja, R.I.: Quantifying the heterogeneity of shale through statistical combination of imaging across scales. Acta Geotech. **12**, 1193–1205 (2017)
13. Semnani, S.J., White, J.A., Borja, R.I.: Thermo-plasticity and strain localization in transversely isotropic materials based on anisotropic critical state plasticity. Int. J. Num. Anal. Methods Geomech. **40**, 2423–2449 (2016)
14. Tien, Y.M., Kuo, M.C.: A failure criterion for transversely isotropic rocks. Int. J. Rock Mech. Min. Sci. **38**(3), 399–412 (2001)
15. Tien, Y.M., Kuo, M.C., Juang, C.H.: An experimental investigation of the failure mechanism of simulated transversely isotropic rocks. Int. J. Rock Mech. Min. Sci. **43**(8), 1163–1181 (2006)
16. Tjioe, M., Borja, R.I.: On the pore-scale mechanisms leading to brittle and ductile deformation behavior of crystalline rocks. Int. J. Num. Anal. Methods Geomech. **39**(11), 1165–1187 (2015)
17. Tjioe, M., Borja, R.I.: Pore-scale modeling of deformation and shear band bifurcation in porous crystalline rocks. Int. J. Num. Methods Eng. **108**(3), 183–212 (2016)
18. Zhao, Y., Semnani, S.J., Yin, Q., Borja, R.I.: On the strength of transversely isotropic rocks. Int. J. Num. Anal. Methods Geomech. **42**, 1917–1934 (2018). https://doi.org/10.1002/nag.2809

Numerical Simulation of a CAES Pile with Hypoplasticity

Wei Wu[1(✉)], Shun Wang[1], Guofang Xu[2], Jilin Qi[3], Dichuan Zhang[4], and Jong-Ryeol Kim[4]

[1] Institute of Geotechnical Engineering,
University of Natural Resources and Life Sciences, Vienna,
Feistmantelstraße 4, 1180 Vienna, Austria
wei.wu@boku.ac.at
[2] Institute of Rock and Soil Mechanics, Chinese Academy of Sciences, Wuhan, China
[3] College of Civil and Transportation Engineering,
Beijing University of Civil Engineering and Architecture, Beijing, China
[4] Department of Civil Engineering, Nazarbayev University, Astana, Kazakhstan

Abstract. In this paper, we investigate the mechanical behaviour of a compressed air energy storage (CAES) pile through finite element analyses. A simple hypoplastic constitutive model is used for the soil surrounding the pile. The analyses are carried out on two numerical models, namely a plane-strain model and an axisymmetric model. The numerical results show that the internal pressure of the pile has only minor influence on the stress state in the surrounding soil. The radial deformation around the pile is much smaller than the vertical deformation during the pressurization. Moreover, an increase of the internal pressure induces pile expansion around a neutral point in middle of the pile. This gives rise to relative displacement at the pile-soil interface, leading to upward slip at the pile head and downward slip at pile tip. The shear stress between pile and soil is also considered.

1 Introduction

Utilization of renewable energy sources such as solar and wind power suffers from an intermittency issue, which thus requires efficient energy storage options. This issue however can be addressed by storing excess energy during off-peak hours to accommodate high demands later [2]. Pile foundations have been employed as ground heat exchangers (energy piles) using fluid circulation in the foundations and built structures to save energy. This idea can be explored to develop the CAES pile system by compressing air in underground piles to store excess energy. The compressed air is then released to drive gas turbines to produce electricity during peak demand hours [3,4].

Hollow steel piles are suitable for storing compressed air because they are commonly-used in foundation engineering. Moreover, hollow steel piles have high strength and large internal spaces; therefore, they are easy to install and do

W. Wu (Ed.): *Desiderata Geotechnica*, SSGG, pp. 242–249, 2019.
https://doi.org/10.1007/978-3-030-14987-1_29

not require additional process to create internal space [8]. Compared with conventional piles, the main difference of CAES piles in loading condition is that they have high internal air pressure. Therefore, the influence of the internal air pressure on the mechanical behaviour of the soil surrounding the pile needs to be considered. Particularly, the critical internal pressure which may result in unneglectable stress and displacement changes in the surrounding soil is of interest in engineering practice. To continue pursuing the idea of using pile foundation system as an energy storage vessel, we need to analyse the mechanical behaviour of the CAES pile under internal pressurization. In this paper, we investigate the stress state in the surrounding soil and the displacement patterns of a single CAES pile through finite element analyses. The analyses are carried out on two numerical models, namely a plane-strain model and an axisymmetric model, in which the pile is considered as an elastic medium while the surrounding soil is modelled using a simple hypoplastic constitutive model.

2 Constitutive Model and Implementation

The hypoplastic constitutive model used in this paper is an improved one of an early version by Wu [6], while a new critical state function is incorporated to account for the effects of density and stress level of granular materials.

$$\mathring{\boldsymbol{\sigma}} = C_1(\mathrm{tr}\boldsymbol{\sigma})\dot{\boldsymbol{\varepsilon}} + C_2(\mathrm{tr}\dot{\boldsymbol{\varepsilon}})\boldsymbol{\sigma} + C_3\frac{\mathrm{tr}(\boldsymbol{\sigma}\cdot\dot{\boldsymbol{\varepsilon}})}{\mathrm{tr}\boldsymbol{\sigma}}\boldsymbol{\sigma} + f_d\cdot C_4(\boldsymbol{\sigma}+\boldsymbol{\sigma}^*)\|\dot{\boldsymbol{\varepsilon}}\|, \tag{1}$$

where C_i $(i = 1, 2, 3, 4)$ are dimensionless parameters. $\boldsymbol{\sigma}$ is the Cauchy stress tensor, and $\|\dot{\boldsymbol{\varepsilon}}\| = \sqrt{\mathrm{tr}(\dot{\boldsymbol{\varepsilon}}^2)}$ stands for the Euclidean norm of the stretching tensor. The deviatoric stress tensor $\boldsymbol{\sigma}^*$ in Eq. (1) is defined by $\boldsymbol{\sigma}^* = \boldsymbol{\sigma} - 1/3(\mathrm{tr}\boldsymbol{\sigma})\mathbf{I}$ with $\mathbf{I}$ being the second order unity tensor. The critical state function f_d reads:

$$f_d = \left(\frac{e}{e_{crt}}\right)^{\alpha} \tag{2}$$

where e and e_{crt} refer to the current void ratio and the critical state void ratio, respectively, and α controls the degree of non-linearity of the strain-stress relation. The critical state void ratio is expressed as:

$$e_{crt} = e_{co}\exp\left[-\lambda\left(\frac{p}{p_a}\right)^{\xi}\right] \tag{3}$$

where e_{co}, λ, and ξ are parametric constants, and $p = -\mathrm{tr}\boldsymbol{\sigma}/3$ and p_a denote the hydrostatic pressure and atmospheric pressure, respectively. In addition, the constitutive model can be used for cohesive soil by replacing the stress tensor $\boldsymbol{\sigma}$ with a translated stress tensor $\boldsymbol{\sigma_c} = \boldsymbol{\sigma} - p_t\boldsymbol{\delta}_{ij}$ with the translated scale being $p_t = c/\tan\phi_c$ and the parameters c and ϕ_c being respectively the cohesion and critical friction angle of the cohesive soil.

The constitutive Eq. (1) can be regarded as an ordinary differential equation, for which the general time integration over an increment step $t \in [t_n, t_{n+1}]$ can

be written as:

$$\boldsymbol{\sigma}_{n+1} = \boldsymbol{\sigma}_n + \int_{t_n}^{t_{n+1}} h(\boldsymbol{\sigma}_n, e_n, \boldsymbol{\varepsilon}_n)dt = \boldsymbol{\sigma}_n + \mathbf{D}\Delta\boldsymbol{\varepsilon}_n, \quad n = 1, 2, \ldots \tag{4}$$

where $\mathbf{D}$ denotes the tangent stiffness matrix. The void ratio is evaluated as: $e_{n+1} = (1+e_n)\exp(\Delta\varepsilon_v) - 1$. The stress and void ratio can be evaluated using an adaptive explicit integration method with a stress correction treatment detailed in [5].

3 Numerical Simulation

The analyses are carried out on two numerical models, namely a plane strain model and an axisymmetrical model, using the commercial finite element software Abaqus standard. In the simulations, we consider a single steel pile for simplicity. The pile is close-end, circular in cross section, and vertically pre-installed in the ground at a depth of 20 m below the ground surface. In the numerical model the pile has a dimension of 20 m in length, 500 mm in outer diameter, and 15 mm in thickness with an inner volume of 3.47 m^3. In the analyses, the pile is considered as an elastic medium while the surrounding soil is modelled using the aforementioned hypoplastic model. In addition, a frictional interface is adopted between the pile and soil to simulate the pile-soil interaction. The parameters of the steel pile and surrounding soil are listed in Table 1.

3.1 Plane-Strain Analysis

The finite element mesh shown in Fig. 1 is used in the plane-strain analysis. During the simulation, the CASE pile is linearly pressurized from the atmospheric pressure of $p_0 = 0.1$ MPa to the maximum pressure $p_{max} = 10,000p_0$, which

Table 1. Material parameters used in the finite element simulations

Mechanical parameters	Steel pile	Saturated cohesive soil
Mass density: ρ, kg/m^3	7800	1600
Yound's modulus: E, MPa	210000	100
Poission's ratio: υ	0.3	0.33
Critical friction angle: ϕ_c, /°	-	25
Cohesion: c /kPa	-	30
Initial void ratio: e	-	0.78

Note: The corresponding parameters C_i $(i = 1, 2, 3, 4)$ for constitutive Eq. (1) are $C_1 = -25.07$, $C_2 = -260.25$, $C_3 = -349.56$, $C_4 = -93.60$, which can be identified by a procedure proposed by Wu and Bauer [7]. In addition, the parameters for the critical state function f_d ($e_{co} = 0.957$, $\lambda = 0.022$, $\xi = 0.061$, $\alpha = 1.0$) are gained from literature [5].

is much higher than the service pressure of CAES piles [3]. The computation is performed to find the actual pressure, p_{int}, applied to the surrounding soil. The relation between the internal pressure and the actual interface stress is shown in Fig. 2. The normal stress acting on the interface between the outer surface of pile and the surrounding soil remains as p_0 until the internal air pressure rises to $100p_0$. The interface stress increases from p_0 to $3.46p_0$ with the internal air pressure increasing from $100p_0$ to $10{,}000p_0$. This implies that pressurization of the CAES pile to 10 Mpa has only minor influence on the stress state of the surrounding soil.

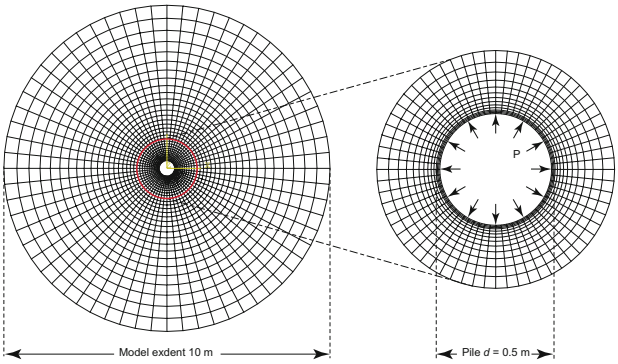

Fig. 1. Plane strain model with FE meshes

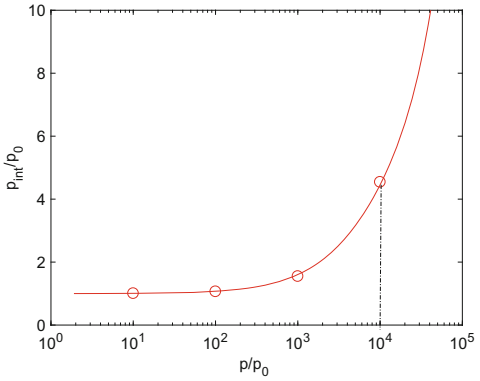

Fig. 2. The relation between the internal pressure of the CAES pile and the stress acting on the surrounding soil

Total strains in the soil in response to the internal pressure increasing from p_0 to $10{,}000p_0$ are shown in Fig. 3(a). The radial strains in the soil occur as a result of the pressurization on the pile face as well as the Poisson effects due

to the constraint along the out-of-plane direction. The soil surrounding the pile exhibits compressional radial strains within a distance approximately two times of the pile diameter with the maximum compressional strain occurring at the interface. Presumably, the maximum compressional strain increases 10 times with 10 times increase of the the internal air pressure.

The calculated radial stresses in the soil are compressive and they increase with the internal pressure of the pile (see Fig. 3(b)). Obviously, the maximum stress occurs at the pile—soil interface. For the internal pressure less than $1000p_0$, the compressional stresses reduce to negligible values at about 1.5 m away from

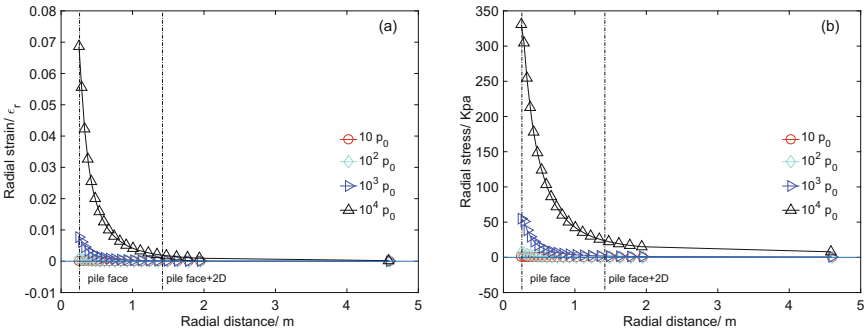

Fig. 3. Radial strain (a) and radial stress (b) over radial distance in the surrounding soil of the CAES pile.

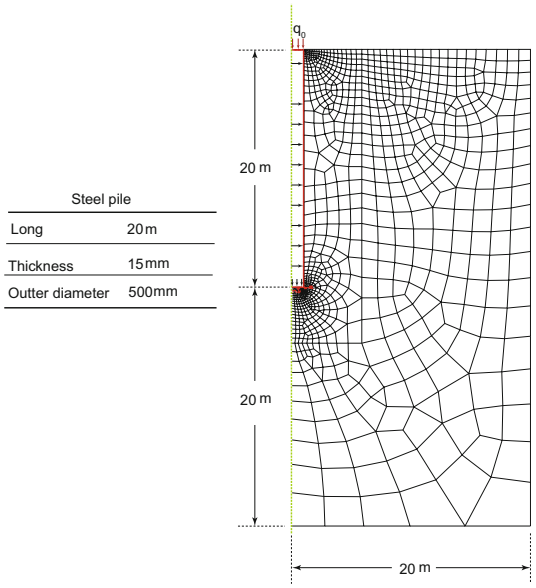

Fig. 4. Axisymmetric model with FE meshes

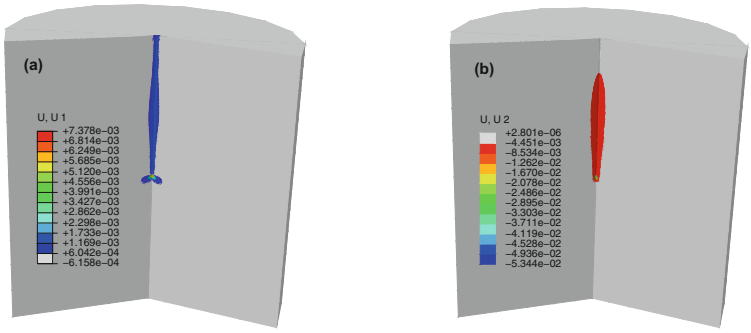

Fig. 5. (a) Radial displacement, and (b) vertical displacement in the soil surrounding the CAES pile with 10 Mpa internal pressure

the pile face. However, the maximum stress increases significantly when increasing the internal pressure to $10{,}000p_0$, and it drops to 7 kPa at about 4.7 m away from the pile face.

3.2 Axisymmetric Analysis

In this section, the discussion is extended to an axisymmetric analysis, which enables us to assess both radial and vertical displacements of a CAES pile as well as the slip at the pile-soil interface. The model has a domain of 20 m far from the axis of symmetry and 40 m deep from the ground surface to avoid boundary effects. The dimension and FE meshes of this model is shown in Fig. 4.

Prior to this simulation, a pile load test is numerically analysed and the ultimate capacity is determined to be roughly 10 Mpa based on Davisson's criterion [1]. To mimic the structural loads, an axial load $q_0 = 1.3$ Mpa is applied on the top of the steel pile, as shown in Fig. 4. Meanwhile, the geostress is applied by taking the gravity effect into account. Similar to the previous plane strain model, the internal pressure is monotonically increased from $p_{min} = 0.1$ MPa to $p_{mid} = 1$ MPa, and $p_{max} = 10$ MPa in the axisymmetric model.

With the effect of the internal pressure of the CAES pile, both radial and vertical displacements of the surrounding soil change with depth (see Fig. 5 in 3D view). However, The radial displacement is smaller than the vertical displacement (see dash lines in Fig. 6(a)) that is in excellent agreement with the result obtained from the plane-strain analysis. This agreement suggests that the radial deformation has minor contribution to the structure stability. We also investigate the slip occurred at the pile-soil interface, as shown in Fig. 6(b). The increase of the internal pressure induces pile expansion around a neutral point in the middle of the pile. This gives rise to relative displacement at the pile-soil interface, leading to upward slip at the pile head and downward slip at pile tip. The slip increases from the neutral point to a position near the pile base, and then decreases significantly at the pile base. Consequently, the pile base attains the largest shear stress change at the interface, see Fig. 6(c).

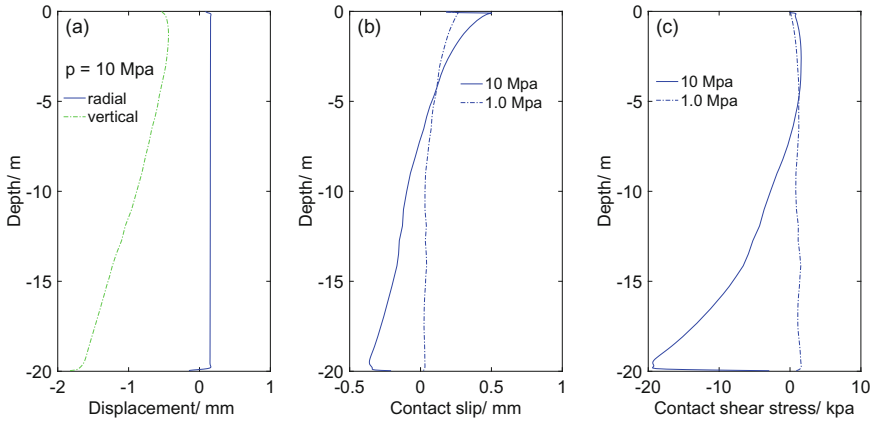

Fig. 6. Axisymmmetric analysis of the pile-soil system (a) depth profile of radial and vertical displacements (b) pile-soil interface slip and (c) shear stress.

4 Conclusions

The internal pressure in a CAES pile leads to changing stress and displacement in the pile and the surrounding soil. It can, in turn, influence the serviceability and limit state of CAES piles. This paper numerically examines the effect of pressurization induced lateral stress and strain, and the vertical load—displacement behaviour of CAES pile. The major results are summarized as follows.

- The plane strain analysis reveals that the normal pressure acting on the interface between outer surface of pile and the surrounding soil is a function of internal air pressure. The pressurization can influence the stress state of the surrounding soil only when the internal pressure is larger than a threshold value.
- The axisymmetric analysis confirms that the internal pressure induces much greater vertical deformation than the radial deformation around the CAES pile. The pile expands around a neutral point in the middle of the pile. This gives rise to relative displacement at the pile-soil interface, leading to upward slip at the pile head and downward slip at pile tip. In addition, shear stress is observed at the pile-soil interface during the pressurization of the CAES pile.

Some features are not considered in our analyses, such as the influence of pressurization on the bearing capacity of a pile and the stability of the while system, the long-term behaviour of CAES pile under the loading-unloading cycles, and degradation of soil-pile interface property. Moreover, the thermal effect due to elevated internal pressure is not considered. This will require a constitutive model for the mechanical-thermal behaviour of soil.

References

1. Davisson, M.T.: High capacity piles. In: Lecture Series on Innovations in Foundation Construction, pp. 81–112. American Society of Civil Engineers, Chicago (1972)
2. Kim, S., Ko, J., Seo, H., Tummalapudi, M.: Investigation of a small-scale compressed air energy storage pile as a foundation system. In: Geotechnical Frontiers 2017, pp. 103–112 (2017)
3. Kim, S., Kim, S., Seo, H., Jung, J.: Mechanical behavior of a pile used for small-scale compressed air energy storage. In: Geo-Chicago 2016, pp. 135–143 (2016)
4. Luo, X., Wang, J., Krupke, C., Wang, Y., Sheng, Y., Li, J., Xu, Y., Wang, D., Miao, S., Chen, H.: Modelling study, efficiency analysis and optimisation of large-scale adiabatic compressed air energy storage systems with low-temperature thermal storage. Appl. Energy **162**, 589–600 (2016)
5. Wang, S., Wu, W., Peng, C., He, X.Z., Cui, D.S.: Numerical integration and FE implementation of a hypoplastic constitutive model. Acta Geotechnica **13**(6), 1265–1281 (2018)
6. Wu, W., Lin, J., Wang, X.T.: A basic hypoplastic constitutive model for sand. Acta Geotechnica **12**(6), 1373–1382 (2017)
7. Wu, W., Bauer, E.: A simple hypoplastic constitutive model for sand. Int. J. Numer. Anal. Meth. Geomech. **18**(12), 833–862 (1994)
8. Zhang, L.Y., Ahmari, S., Sternberg, B., Budhu, M.: Feasibility study of compressed air energy storage using steel pipe. In: GeoCongress 2012: State of the Art and Practice in Geotechnical Engineering, pp. 4272–4279 (2012)

Epilogue

The repeated revision of hypotheses, notions, relations and methods is needed for geomechanics as for any rational science. So I welcomed Wu Wei's proposal of a workshop on behalf of my 80th birthday, and to publish invited papers in a book afterwards. Differently from a Festschrift this volume is entitled DESIDERATA GEOTECHNICA, and I contribute a paper. The workshop inspired me to add some remarks in this epilogue. They refer first to the stable range for which fractal relics of critical phenomena do not refute concepts with geomaterials, then to losses of stability for which geomatter cannot be captured without fractality.

In physical terms soil and rock are solids with a fractal pore system. They are per-meable ($\pi o \rho o \varsigma$ = passage), but not in Darcy's sense as pore water is diffused in an anomalous way. Fabrics of grains are often called skeleton, but have no hinges. Terzaghi's effective pressure is $p' = p - p_w$ for full saturation as the solid state is not changed by changes of pore water pressure p_w if they equal changes of total pressure p. As this holds true likewise for rock p' could be called solid pressure p_s. In a stable range total and solid stresses may be considered as force densities with gradients despite rather fractal force chains.

Although the fractality matters already for the propagation of waves in the elastic range movements of geomatter may be captured with gradients of velocity for the stable range, whereas deformations make sense only for solid structures interacting with geomatter. Spatial fluctuations of void ratio and stress, ever-present as relics of former critical phenomena, require a hidden variable which eludes precise determination. As a way out of this indeterminacy I proposed cyclic attractors for judging constitutive relations, in particular butterfly- and lense-shaped solid stress cycles for cyclic deformation and ratcheting, respectively. This is a precise substitute of 'cyclic mobility' and works also with cyclically moving structures at or in the ground. Despite such asymptotes one should keep in mind the inevitable incertainty due to relics of critical phenomena.

'Failure' is a legal and a technical notion, not a physical one. Structures at or in the ground can fail due to excessive deformations although the adjacent geomatter remains in a stable range after the installation. This can happen with thermally,

W. Wu (Ed.): *Desiderata Geotechnica*, SSGG, pp. 251–252, 2019.
https://doi.org/10.1007/978-3-030-14987-1

seismically or hydraulically activated dislocations between molecules, clay particles, grains, rock fractions and embedded structures. We all know that this variety implies indeterminacy and requires judgment. So-called plastic limit states are often empirically justified for geotechnical design, but should not be mixed up with failure. As outlined in my contribution to this volume, such states cannot really be reached so that their boundary is fuzzy. Only if they are justified partial safety factors can suffice to avoid a loss of stability. A better understanding of the range of validity is needed, then macro-elements an be legitimate because of an almost parallel ground reaction. The well-posedness of numerical equation systems requires a stable range, therefore the stability of geotechnical systems cannot be proven with such approaches.

My main desideratum is to clarify losses of stability beyond plastic limit states. There are more critical phenomena than the ones outlined in my own contribution. E.g., seismically induced cascades of blockades and collapses can occur with dams or natural slopes. Gas enclosed in macropores after flooding enhances the collapse into a mud. This kind of phase transition may be called liquefaction although flowing geomatter is not a liquid. Geotechnical operations can fail due to a loss of control with critical phenomena: quasi-static ones can prevent further driving along an intended path, kinetic ones can run off so fast and wide that an evacuation is impossible. This can occur with excavations and tunneling, and likewise with slopes and offshore structures. Localized internal erosion can enhance successive collapses, in particular with breakouts of water, gas, mud and/or petrol.

Geotechnical engineers have to imagine such and other worst cases in order to keep damages acceptably low. Although scenarios with critical phenomena elude as yet mathematical treatment they have to be estimated alongside with probabilities. The wild randomness implies that extreme events can matter as much as smaller ones altogether. Damage data are scarce and big experiments are hardly feasible. I could clarify some catastrophic mechanisms, but was not always allowed to publish them. Probabilities of such events cannot be estimated intuitively nor calculated with combinatorics. Stable Lévy processes enable a way out of this dilemma, but the physical interpretation of this mathematical concept has only just begun. Seismo-hydraulic monitoring can help to reduce the risk (i.e. the expected value of damage) with critical phenomena if these are properly understood, while usual extrapolations in observational methods fail.

As always our research is motivated by Richard Feynman's 'pleasure of finding things out', Ernst Mach's pursuit of mental economy or parsimony, and a sense of responsibility. Thanking Wu Wei for his initiative, I hope that the present book will enhance the progress of geomechanics.

August 2018 G. Gudehus

Author Index

W. Wu (Ed.): *Desiderata Geotechnica*, SSGG, pp. 253–254, 2019.
https://doi.org/10.1007/978-3-030-14987-1